

THEORETICAL STUDY OF PRESSURE-INDUCED PHASE TRANSITIONS AND THERMAL  
PROPERTIES FOR MAIN-GROUP OXIDES AND NITRIDES

Except where reference is made to the work of others, the work described in this dissertation is my own or was done in collaboration with my advisory committee. This dissertation does not include proprietary or classified information.

---

Bin Xu

Certificate of Approval:

---

Minseo Park  
Associate Professor  
Physics

---

Jianjun Dong, Chair  
Associate Professor  
Physics

---

Yu Lin  
Professor  
Physics

---

Satoshi Hinata  
Professor  
Physics

---

George T. Flowers  
Dean  
Graduate School

THEORETICAL STUDY OF PRESSURE-INDUCED PHASE TRANSITIONS AND THERMAL  
PROPERTIES FOR MAIN-GROUP OXIDES AND NITRIDES

Bin Xu

A Dissertation

Submitted to

the Graduate Faculty of

Auburn University

in Partial Fulfillment of the

Requirements for the

Degree of

Doctor of Philosophy

Auburn, Alabama  
August 10, 2009

THEORETICAL STUDY OF PRESSURE-INDUCED PHASE TRANSITIONS AND THERMAL  
PROPERTIES FOR MAIN-GROUP OXIDES AND NITRIDES

Bin Xu

Permission is granted to Auburn University to make copies of this dissertation at its  
discretion, upon the request of individuals or institutions and at  
their expense. The author reserves all publication rights.

---

Signature of Author

---

Date of Graduation

## VITA

Bin Xu, son of Qingshan Xu and Xiufen Cai, was born on April 21, 1980 in Shijiazhuang, Hebei, P. R. China. He attended University of Science and Technology of China (USTC) in 1998, and graduated with a Bachelor of Science in Physics in 2003. He entered Graduate School at Auburn University to pursue a Doctoral degree in Physics in September 2003. He was married to Shi Chen, daughter of Taixuan Chen and Junhua Wang, on April 25, 2007 in China.



DISSERTATION ABSTRACT

THEORETICAL STUDY OF PRESSURE-INDUCED PHASE TRANSITIONS AND THERMAL  
PROPERTIES FOR MAIN-GROUP OXIDES AND NITRIDES

Bin Xu

Doctor of Philosophy, August 10, 2009  
(B.S., University of Science and Technology of China, 2003)

211 Typed Pages

Directed by Jianjun Dong

Main group nitrides and oxides are important solid compounds with applications in fields ranging from structural ceramics to catalysts and electronic materials. We have theoretically investigated the pressure-induced phase transitions and thermal properties for a series of oxides, nitrides and oxynitrides of IIIB, IVB and IIIB group, including  $\text{Al}_2\text{O}_3$ ,  $\text{AlN}$ ,  $\text{Si}_3\text{N}_4$ ,  $\text{Ga}_2\text{O}_3$ , and  $\text{Ga}_3\text{O}_3\text{N}$ .

In this dissertation, thermodynamic potentials at finite temperatures were calculated within the quasi-harmonic approximation (QHA). Structural optimization and total energy calculation of unit cell models were carried out based on first-principles density functional theory (DFT) within the local density approximation (LDA). Vibrational spectra were calculated using the real-space supercell force-constant (SC-FC) method. For pressure-induced phase transitions, we have studied the equilibrium transition conditions, as well as the kinetic process, including the investigation of transition pathways, kinetic barriers and the softening-phonon induced displacive transitions.

In our studies of equilibrium transition conditions, we calculated the  $T$ - $P$  phase diagrams for  $\text{Al}_2\text{O}_3$ ,  $\text{AlN}$ ,  $\text{Si}_3\text{N}_4$ , and  $\text{Ga}_2\text{O}_3$ . Our predicted transition pressures are 84 and 134 GPa at 300 K for corundum $\rightarrow$ Rh $_2$ O $_3$ (II) $\rightarrow$ postperovskite transitions in  $\text{Al}_2\text{O}_3$ , 9.9 GPa at

0 K for wurtzite→rocksalt transition in AlN, 7.5/7.0 GPa at 300 K for  $\beta/\alpha\rightarrow\gamma$  transitions in  $\text{Si}_3\text{N}_4$  and 0.5 and 39 GPa at 300 K for  $\beta\rightarrow\alpha\rightarrow\text{Rh}_2\text{O}_3(\text{II})$  transitions in  $\text{Ga}_2\text{O}_3$ .

In our studies of the pressure-induced reconstructive phase transition pathways, we examined the corundum-to- $\text{Rh}_2\text{O}_3(\text{II})$  transition in  $\text{Al}_2\text{O}_3$  and the wurtzite-to-rocksalt transition in AlN. We showed that the rhombohedral corundum phase and the orthorhombic  $\text{Rh}_2\text{O}_3(\text{II})$  phase are related by intermediate structures with monoclinic symmetry ( $P2/c$ ). Using the proposed transition pathway, we calculated the kinetic barriers for the forward (C-to-R) and backward (R-to-C) transitions and further predict the meta-stabilities of the two phases. For AlN, different transition pathways were previously proposed. We reinterpreted the bond-preserving paths with long-range patterns of the “transition units”, and our calculated kinetic barriers indicate that the long-range pattern is less important. We also showed that the bond-breaking paths are not energetically favored. In addition, based on the pressure dependencies of the barrier heights we explained the discrepancy of transition pressure between the room temperature observation and the calculated equilibrium result.

In our studies of displacive transitions in  $\text{Si}_3\text{N}_4$ , although  $\beta$  phase is dynamically stable at low pressure, two competing phonon-softening mechanisms are found under high pressure. If the  $\beta\rightarrow\gamma$  transition is bypassed due to kinetic reasons at lower temperatures, the  $\beta$  phase is predicted to undergo a first-order  $\beta\rightarrow P3$  transition at about 38.5 GPa. This predicted metastable high-pressure  $P3$  phase is structurally related to  $\beta\text{-Si}_3\text{N}_4$ .

We have also calculated the thermodynamic and elastic properties of these systems, and selected results are presented. Our predictions are in good agreement with available experimental and other theoretical data.

Furthermore, we studied the shifted Raman scattering and its correlation with the growth direction in  $\text{Ga}_2\text{O}_3$  nanowires. And collaborated with an experimental study that synthesized spinel-structured gallium oxynitride from  $\text{Ga}_2\text{O}_3+\text{GaN}$  mixtures at high pressure and high temperature, we showed that the optimal synthesis pressure is predicted to be close to the  $\beta$ -to- $\alpha$  transition pressure of  $\text{Ga}_2\text{O}_3$ .

## ACKNOWLEDGMENTS

Although only my name appears as the author of this dissertation, its completion is truly contributed from many great people. I would like to thank everyone and everything came along into my life, even without mentioning here.

I express my sincere gratitude to my research advisor, Dr. Jianjun Dong, for his continuous encouragement, support and advice throughout my graduate years. Dr. Dong taught me not only the knowledge and techniques in this field, but also how to question thoughts and express ideas. I enjoy the great benefit from his instruction, especially the emphasis on details. His tolerance and being understanding is greatly appreciated.

I would like to thank Dr. An-Ban Chen, who introduced me to Auburn University. He is always there to help with my research and career. And I appreciate the helpful suggestions from the committee members, Dr. Yu Lin, Dr. Satoshi Hinata, Dr. Minseo Park, and the outside reader, Dr. Orlando Acevedo. When I was working as a TA, Dr. Satoshi Hinata gave me great advice on how to teach as a first-time lecturer. And I thank Dr. Robert Boivin for our discussion about recitations and labs.

I am also thankful to our IT management professional Philip Forrest. He ensured the computational ability of the computer cluster which is important for my research. And I would like to acknowledge my graduate friend Xiaoli Tang, for the research discussion and the influence of her diligent attitude, Zengjun Chen for his knowledge on Latex.

Beyond all the above gratitude, the support and care from my family is invaluable. I especially would like to thank my parents and my wife, Shi Chen, for all their understanding and care.

Finally, I appreciate the financial support from DOE (DE-FG02-03ER46060) and NSF (HRD-0317741) that funded part of the research in this dissertation.

Style manual or journal used Bibliography follows American Physical Society (APS)  
style

---

Computer software used The document preparation package T<sub>E</sub>X (specifically L<sup>A</sup>T<sub>E</sub>X)  
together with the departmental style-file `auphd.sty`.

---

## TABLE OF CONTENTS

LIST OF FIGURES	xii
LIST OF TABLES	xviii
1 INTRODUCTION	1
1.1 Pressure-Induced Phase Transitions and Thermodynamic Properties of Main-Group Oxides and Nitrides . . . . .	1
1.1.1 $\text{Al}_2\text{O}_3$ . . . . .	1
1.1.2 $\text{AlN}$ . . . . .	3
1.1.3 $\text{Si}_3\text{N}_4$ . . . . .	4
1.1.4 $\text{Ga}_2\text{O}_3$ . . . . .	8
1.1.5 $\text{Ga}_3\text{O}_3\text{N}$ . . . . .	9
1.2 First-Principles Theoretical Studies . . . . .	10
1.3 Outline of Dissertation . . . . .	13
2 THEORY OF PHASE TRANSITIONS IN SOLIDS	15
2.1 Phases and Crystal Symmetries . . . . .	15
2.2 Equilibrium Thermodynamic Theory of Phase Transitions . . . . .	19
2.2.1 Thermodynamic Stability . . . . .	19
2.2.2 Phase Diagram and Classification of Phase Transitions . . . . .	21
2.3 Landau Theory for Phase Transitions of Second Kind . . . . .	25
2.3.1 The Order Parameter and Landau Free Energy . . . . .	25
2.3.2 Dynamic Lattice Stability and Soft Phonon Modes . . . . .	27
2.4 Transition Paths of Reconstructive Phase Transitions . . . . .	28
3 FIRST-PRINCIPLES CALCULATIONS OF THERMODYNAMIC PROPERTIES OF CRYSTALS	33
3.1 First-Principles Total Energy Theory . . . . .	33
3.1.1 Density Functional Theory (DFT) . . . . .	33
3.2 Statistical Theory of Bulk Crystals . . . . .	36
3.2.1 Phonon Theory of Lattice Dynamics . . . . .	36
3.2.2 Statistical Harmonic Approximation . . . . .	41
3.2.3 First-Principles Phonon Calculations . . . . .	42
3.3 Thermodynamic Properties . . . . .	46
3.3.1 Quasi-Harmonic Approximation . . . . .	46
3.3.2 Equation of State (EOS) Models . . . . .	50
3.3.3 Case Study: $\text{MgO}$ . . . . .	54

4	PRESSURE-INDUCED PHASE TRANSITIONS IN ALUMINIUM OXIDE AND ALUMINIUM NITRIDE	59
4.1	Aluminium Oxide: $\text{Al}_2\text{O}_3$	59
4.1.1	Introduction	59
4.1.2	Crystal Structures, Total Energies and Vibrational Properties	62
4.1.3	$T$ - $P$ Phase Diagram	70
4.1.4	Transition Pathways in the $\alpha$ -to- $\text{Rh}_2\text{O}_3(\text{II})$ Transition	72
4.1.5	Thermal Properties	80
4.1.6	High Pressure Elasticity	83
4.1.7	Conclusions	87
4.2	Aluminum Nitride: $\text{AlN}$	90
4.2.1	Introduction	90
4.2.2	Total Energy and Equilibrium Phase Transition	94
4.2.3	Microscopic Mechanism for the Wurtzite-to-Rocksalt Transition	95
4.2.4	Conclusions	101
5	STUDY OF HIGH-PRESSURE PHASE TRANSITIONS IN SILICON NITRIDE	102
5.1	Introduction	102
5.2	Crystal Structures, Static Binding Energies, and Vibrational Spectra	106
5.3	Equilibrium Thermodynamic Stability and Phase Transitions	114
5.4	Phonon-Softening Induced Structural Instability in $\beta$ - $\text{Si}_3\text{N}_4$ at High Pressures	116
5.5	Room Temperature Metastable $P3$ Phase	121
5.6	Thermodynamic Properties	126
5.7	Conclusions	130
6	FIRST-PRINCIPLES STUDY OF GALLIUM OXIDE AND GALLIUM OXYNITRIDE	132
6.1	Gallium Oxide: $\text{Ga}_2\text{O}_3$	132
6.1.1	Introduction	132
6.1.2	Total Energy and Vibrational Properties	136
6.1.3	$T$ - $P$ Phase Diagram	139
6.1.4	Blue-Shifted Raman Scattering in Gallium Oxide Nanowires	141
6.1.5	Conclusions	144
6.2	Gallium Oxynitride: $\text{Ga}_3\text{O}_3\text{N}$	145
6.2.1	Introduction	145
6.2.2	Total Energy Calculations of $\text{GaN}$ and $\text{Ga}_3\text{O}_3\text{N}$	147
6.2.3	Theoretical Study of the Synthesis, Structure, and Stability of $\text{Ga}_3\text{O}_3\text{N}$ Spinel	148
6.2.4	Electronic Properties	154
6.2.5	Phonon Spectrum	155
6.2.6	Conclusions	157
7	CONCLUSIONS AND FUTURE WORK	159
	APPENDICES	180

A	TOTAL ENERGY CALCULATION WITH VASP	181
B	ELASTICITY CALCULATION	182
C	BEYOND HARMONIC APPROXIMATION: PERTURBATION THEORY OF LATTICE ANHARMONICITY	188

LIST OF FIGURES

1.1	Photo of recently constructed departmental computer cluster. . . . .	12
2.1	Phase diagram with two solid phases, one liquid phase and one gas phase. Two triple points and one critical point are present. . . . .	23
2.2	Variation of the Landau free energy with positive and negative $A$ coefficients. . . . .	26
3.1	LDA (with US-PP) calculated (a) phonon dispersion relation, (b) vibrational density of states of $\alpha$ -Al <sub>2</sub> O <sub>3</sub> at zero pressure. High symmetry points are A: $(0, \frac{1}{2}, 0)$ , $\Gamma$ : $(0, 0, 0)$ Z: $(\frac{1}{2}, \frac{1}{2}, \frac{1}{2})$ , and D: $(\frac{1}{2}, 0, \frac{1}{2})$ . Lines denote theoretical spectrum and discrete squares denote experimental data. . . . .	47
3.2	Potential energy vs. interatomic distance curve. Dashed line denotes harmonic potential curve. Minimum potential energy is provided at $r = a$ . . . .	48
3.3	LDA calculated thermal free energy at several volume points. (a) At $T = 0$ K. (b) At $T = 2000$ K. . . . .	55
3.4	LDA calculated $F_{vib} - V$ data at $T = 2000$ K are fitted to several EOS models. . . . .	55
3.5	Thermal expansion of MgO at zero pressure. Lines represent this work from LDA calculation. Discrete symbols are reported measurements. . . . .	56
3.6	Thermal expansion of MgO at zero pressure. Solid line denotes our calculation with Debye model. Discrete symbols are reported measurements. . . . .	58
4.1	Crystal structures of four polymorphs of Al <sub>2</sub> O <sub>3</sub> : (a) Corundum, (b) Rh <sub>2</sub> O <sub>3</sub> -(II), (c) $Pbnm$ perovskite and (d) post-perovskite. . . . .	63
4.2	LDA calculated phonon dispersion curves and vibrational density of state of $\alpha$ -Al <sub>2</sub> O <sub>3</sub> at zero pressure using (a) US-PP and (b) PAW. Discrete squares denote experimental data <sup>172</sup> . . . . .	66
4.3	Calculated Raman-active frequencies of $\alpha$ -Al <sub>2</sub> O <sub>3</sub> as a function of pressure. (a) US-PP, (b) PAW. Solid and dashed lines represent $E_g$ and $A_{1g}$ modes from linear fitting with data sets below 20 GPa. . . . .	67



4.4	Calculated IR-active frequencies of $\alpha$ -Al <sub>2</sub> O <sub>3</sub> as a function of pressure. (a) TO modes with US-PP, (b) TO modes with PAW, (c) LO modes with US-PP, (d) LO modes with PAW. Solid and dashed curves denote $E_u$ and $A_{2u}$ modes from 2 <sup>nd</sup> order polynomial fitting. . . . .	69
4.5	Calculated Raman-active frequencies of Rh <sub>2</sub> O <sub>3</sub> (II)-Al <sub>2</sub> O <sub>3</sub> as a function of pressure. (a), (c), (e), (g) US-PP, (b), (d), (f), (h) PAW. Solid curves are from 2 <sup>nd</sup> order polynomial fitting. . . . .	71
4.6	Calculated Raman-active frequencies of pPV-Al <sub>2</sub> O <sub>3</sub> as a function of pressure. (a) US-PP, (b) PAW. Solid, dashed, dotted and dash-dotted curves represent $A_g$ , $B_{1g}$ , $B_{2g}$ and $B_{3g}$ modes from 2 <sup>nd</sup> order polynomial fitting. . . . .	72
4.7	Static enthalpies of Al <sub>2</sub> O <sub>3</sub> polymorphs as a function of pressure relative to that of corundum phase using (a) US-PP and (b) PAW. The static $\alpha \rightarrow$ Rh <sub>2</sub> O <sub>3</sub> (II) and Rh <sub>2</sub> O <sub>3</sub> (II) $\rightarrow$ pPV transition pressure are present. The PV phase is metastable at all pressures considered among the four polymorphs.	73
4.8	Calculated $T$ - $P$ phase diagram of Al <sub>2</sub> O <sub>3</sub> . (a) US-PP, (b) PAW. Dashed lines denote possible phase boundaries. . . . .	74
4.9	Comparison of structures of (a) corundum and (b) Rh <sub>2</sub> O <sub>3</sub> (II)-Al <sub>2</sub> O <sub>3</sub> . The corundum phase is viewed from an angle in which it appears “orthorhombic”-like. The differences between two polymorphs are highlighted. . . . .	75
4.10	Al-O bond lengths as a function of the transition parameter at 84.0 GPa. As the transition parameter changes from 0 to 1, corundum structure transforms smoothly to the Rh <sub>2</sub> O <sub>3</sub> (II) phase. There are 12 distinct bonds and only one bond breaks and reforms during the transformation. . . . .	77
4.11	Volume per atom for the corundum $\rightarrow$ Rh <sub>2</sub> O <sub>3</sub> (II) transformation at several pressures. Same volume ranges are used to illustrate the pressure effect. . .	77
4.12	Enthalpies for the corundum $\rightarrow$ Rh <sub>2</sub> O <sub>3</sub> (II) transformation at several pressures.	78
4.13	Enthalpy barrier height for the corundum $\rightarrow$ Rh <sub>2</sub> O <sub>3</sub> (II) and Rh <sub>2</sub> O <sub>3</sub> (II) $\rightarrow$ corundum transformations as a function of pressure. . . . .	79
4.14	Calculated phonon dispersion curves of corundum-Al <sub>2</sub> O <sub>3</sub> at 204 GPa. . . .	79
4.15	Calculated phonon dispersion curves of Rh <sub>2</sub> O <sub>3</sub> (II)-Al <sub>2</sub> O <sub>3</sub> at 0 GPa. . . . .	79
4.16	Comparison of the present theoretical calculation with measured thermal expansion coefficients of $\alpha$ -Al <sub>2</sub> O <sub>3</sub> as a function of temperature at zero pressure. Solid and dashed lines represent our LDA calculations using US-PP and PAW method, respectively. Discrete symbols are reported experimental data. <sup>16-21</sup>	81

4.17	Theoretical thermal expansion coefficients of $\alpha$ -Al <sub>2</sub> O <sub>3</sub> as a function of temperature at several pressures from using (a) US-PP, (b) PAW. . . . .	82
4.18	Comparison of the present LDA predicted adiabatic bulk modulus as a function of temperature of $\alpha$ -Al <sub>2</sub> O <sub>3</sub> with Voigt-Ruess-Hill data by Teffet <sup>23</sup> , by Goto <i>et al.</i> <sup>25</sup> and the polycrystalline data by sound velocity measurements by Chung and Simmons <sup>24</sup> . . . . .	82
4.19	Comparison of calculated isobaric heat capacity and entropy as a function of temperature of $\alpha$ -Al <sub>2</sub> O <sub>3</sub> with experimental data at zero pressure. Discrete open circles denote measured data from Furukawa <sup>22</sup> . . . . .	83
4.20	LDA calculated thermal expansion coefficients of Rh <sub>2</sub> O <sub>3</sub> (II)-Al <sub>2</sub> O <sub>3</sub> at several pressures as a function of temperature up to 3000 K. (a) US-PP, (b) PAW .	84
4.21	LDA calculated thermal expansion coefficients of pPV-Al <sub>2</sub> O <sub>3</sub> at several pressures as a function of temperature up to 3000 K. (a) US-PP, (b) PAW . . .	84
4.22	Pressure dependence of the elastic constants of corundum. (a) US-PP, (b) PAW. Discrete symbols represent directly calculated data. Curves are from the 2 <sup>nd</sup> -order polynomial fitting. . . . .	85
4.23	Pressure dependence of the elastic constants of Rh <sub>2</sub> O <sub>3</sub> (II)-Al <sub>2</sub> O <sub>3</sub> . (a) US-PP, (b) PAW. Discrete symbols represent directly calculated data. Curves are from the 2 <sup>nd</sup> -order polynomial fitting. . . . .	87
4.24	Pressure dependence of the elastic constants of pPV-Al <sub>2</sub> O <sub>3</sub> . (a) US-PP, (b) PAW. Discrete symbols (except crosses) represent directly calculated data from this work. Crosses denote GGA calculation from Stackhouse <i>et al.</i> <sup>36</sup> at 136 GPa. Curves are from the 2 <sup>nd</sup> -order polynomial fitting. . . . .	88
4.25	Phase transformation along TP1. (a) Unit cell of B4 structure, (b) Unit cell of B1 structure, (c), (d) Transformation pattern of “transition units” in B4 and B1 phases. Dashed lines denote primitive unit cell. (Origin shifted onto the position of an atom for better illustration of the unit cell.) . . . . .	92
4.26	Phase transformation along TP2, TP3, TP4 and TP5. (a) Unit cell of B4 structure, (b) Unit cell of B1 structure, (c), (d) Transformation pattern of “transition units” in B4 and B1 phases. (Origin shifted onto the position of an atom for better illustration of unit cell.) . . . . .	93
4.27	Four-atom “transition unit” from B4 to B1 structure. . . . .	94
4.28	Cohesive energy per atom as a function of volume for B4 and B1-AlN. Enthalpy variation of both phases as a function of pressure is also shown. . . .	96

4.29	Enthalpy as a function of transition parameter relative to B4 phase for five TPs at six pressures. (a) at 0 GPa, (b) at 5 GPa, (c) at the predicted transition pressure 9.85 GPa, (d) at 15 GPa, (e) at 20 GPa and (f) at 30 GPa.	100
4.30	Forward (B4-to-B1) and backward (B1-to-B4) activation barrier height (enthalpy) as a function of pressure for five TPs. . . . .	101
5.1	Polymorphs of $\text{Si}_3\text{N}_4$ and synthesis conditions . . . . .	104
5.2	Crystal structures of (a),(b) $\alpha$ -, (c),(d) $\beta$ -, and (e),(f),(g) $\gamma$ - $\text{Si}_3\text{N}_4$ . In the panel of $\alpha$ - and $\beta$ - $\text{Si}_3\text{N}_4$ , the first graph illustrates the unit-cell model and the second graph is the $2 \times 2 \times 1$ supercell model viewed in the direction of $c$ axis. In the panel of $\gamma$ - $\text{Si}_3\text{N}_4$ , the first graph shows the conventional cubic cell of the spinel structure and the following two graphs show the fourfold and sixfold coordinated Si units( $\text{SiN}_4$ and $\text{SiN}_6$ ) with tetrahedra and octahedra, respectively. . . . .	108
5.3	Energy-volume curves for $\alpha$ -, $\beta$ - and $\gamma$ - $\text{Si}_3\text{N}_4$ in the scale of per atom. $\beta$ phase has an equilibrium energy of 3 meV lower than that of $\alpha$ phase. $E_0$ of $\gamma$ phase is 93 meV higher than $\beta$ phase. . . . .	110
5.4	Phonon dispersion curves and vibrational density of states (VDOS) of (a) $\alpha$ -, (b) $\beta$ -, and (c) $\gamma$ - $\text{Si}_3\text{N}_4$ at zero pressure. . . . .	112
5.5	Calculated dispersion curves (scattered circles) of mode Grüneisen parameter of (a) $\alpha$ -, (b) $\beta$ -, and (c) $\gamma$ - $\text{Si}_3\text{N}_4$ at zero pressure. Red horizontal line is present to separate the positive and negative values. . . . .	113
5.6	Gibbs free energy of $\alpha$ - $\text{Si}_3\text{N}_4$ relative to that of $\beta$ phase as a function of temperature. Solid, dashed and dotted lines represent the pressure of 0, 5 and 10 GPa, respectively. . . . .	114
5.7	$T$ - $P$ phase diagram of $\text{Si}_3\text{N}_4$ . Solid curve denotes the phase boundary between $\beta$ - and $\gamma$ - $\text{Si}_3\text{N}_4$ . Dashed curve denotes the phase boundary between $\alpha$ - and $\gamma$ - $\text{Si}_3\text{N}_4$ . . . . .	116
5.8	(a) Raman, (b) IR and (c) silent mode frequencies as a function of pressure up to 60 GPa for $\beta$ - $\text{Si}_3\text{N}_4$ . Experimental pressure dependence of Raman modes up to 30 GPa is also presented in discrete symbols as a comparison <sup>200</sup> . Solid squares denote measurements upon pressure increase and open squares denote measurements upon pressure decrease. Several low-frequency modes are found to decrease with increasing pressure. One $B_u$ branch of silent modes is found dropping to zero at about 60 GPa. . . . .	117

5.9	Phonon dispersion of $\beta$ -Si <sub>3</sub> N <sub>4</sub> at a pressure of 48 GPa. Two competing soft phonon modes are found: one TA branch at M point and one optic branch at $\Gamma$ point. No LOTO splitting correction is added for the interests of low-frequency modes only. . . . .	118
5.10	The square of vibration frequency ( $\omega^2$ ) as a function of pressure for two competing soft phonon branches: one TA branch at M point and one B <sub>u</sub> branch at $\Gamma$ point. Solid squares and circles represent data from calculation. Solid and dashed lines are from a linear fitting. . . . .	119
5.11	Ball-stick models of (a) $P6_3/m$ , (b) $P\bar{6}$ , (c) $P2_1/m$ and (d) $P3$ structures viewed along the $c$ axis. Balls in dark color represent N atoms and Si atoms are in light color. . . . .	122
5.12	The total energy of $P6_3/m$ ( $\beta$ ), $P\bar{6}$ , $P2_1/m$ and $P3$ structures as a function of volume. . . . .	122
5.13	Enthalpy landscape and its contour plot as a function of $f_{xy}$ and $f_z$ at the transition pressure of 38.5 GPa. . . . .	124
5.14	Enthalpy barrier (relative to $\beta$ phase) as a function of linearly interpreted transition parameter at 30 GPa (thinner) and the transition pressure of 38.5 GPa (thicker). Solid curves denote the $\beta \rightarrow P3' \rightarrow P3$ path and the dashed curves denote direct $\beta \rightarrow P3$ path. Horizontal axis is defined as qualitative structural similarity. The left end represents $\beta$ structure and the right end represent $P3$ structure. . . . .	125
5.15	Temperature dependence of volume thermal expansion coefficient of bulk $\beta$ -Si <sub>3</sub> N <sub>4</sub> at zero pressure. Solid and dashed lines show present work with static energies fitted to the 2 <sup>nd</sup> -order BM-EOS and 3 <sup>rd</sup> -order BM-EOS, respectively, and both thermal free energies fitted to the 2 <sup>nd</sup> -order BM-EOS. Discrete symbols denote experimental data <sup>83-86</sup> . . . . .	127
5.16	Temperature dependence of bulk Grüneisen parameter of $\beta$ -Si <sub>3</sub> N <sub>4</sub> at zero pressure. Solid and dashed lines show present work with static energies fitted to the 2 <sup>nd</sup> -order BM-EOS and 3 <sup>rd</sup> -order BM-EOS, respectively, and both thermal free energies are fitted to the 2 <sup>nd</sup> -order BM-EOS. Discrete symbols denote experimental data <sup>85</sup> . . . . .	128
5.17	Temperature dependence of volume thermal expansion coefficient of bulk $\beta$ -Si <sub>3</sub> N <sub>4</sub> at pressures of 0, 10, 20 and 30 GPa. . . . .	129
5.18	Temperature dependence of isobaric heat capacity of $\beta$ -Si <sub>3</sub> N <sub>4</sub> at zero pressure. Solid and dashed lines show present work with static energies fitted to the 2 <sup>nd</sup> -order BM-EOS and 3 <sup>rd</sup> -order BM-EOS, respectively, and both thermal free energies are fitted to the 2 <sup>nd</sup> -order BM-EOS. Discrete symbols denote experimental data <sup>85-88</sup> . . . . .	130

5.19	Temperature dependence of volume thermal expansion coefficient of $\alpha$ -, $\beta$ - and $\gamma$ - $\text{Si}_3\text{N}_4$ at zero pressure. Discrete symbols represent experimental data <sup>89,90</sup> . . . . .	131
6.1	Crystal structure of monoclinic $\beta$ - $\text{Ga}_2\text{O}_3$ phase. Note that $\text{Ga}^{3+}$ cations (light color) occupy both tetrahedral and octahedral interstices within the ccp lattice of $\text{O}^{2-}$ ions (dark color). . . . .	133
6.2	Enthalpy differences relative to $\alpha$ phase for $\alpha$ , $\beta$ and $\text{Rh}_2\text{O}_3(\text{II})$ - $\text{Ga}_2\text{O}_3$ as a function of pressure up to 60 GPa. The $\beta$ and $\alpha$ curves cross at 0.5 GPa, the $\alpha$ and $\text{Rh}_2\text{O}_3(\text{II})$ curves cross at 40.9 GPa. . . . .	137
6.3	$T$ - $P$ phase diagram for $\beta$ , $\alpha$ and $\text{Rh}_2\text{O}_3(\text{II})$ - $\text{Ga}_2\text{O}_3$ polymorphs. . . . .	140
6.4	LDA-calculated formation enthalpy $\Delta H$ (i.e., Gibbs free energy of formation $\Delta G_{\text{formation}}$ at zero temperature) as a function of pressure using (a) LDA methods and (b) the GGA approach. The calculated positive $\Delta H$ suggests an endothermic formation. The solid plots are calculated assuming the oxynitrides are synthesized from $\beta$ - $\text{Ga}_2\text{O}_3$ and wurtzite GaN, and the dashed plots are calculated assuming the oxynitrides are synthesized from $\alpha$ - $\text{Ga}_2\text{O}_3$ and wurtzite GaN. The solid plot and the dashed plot cross at the pressure of the $\beta$ -to- $\alpha$ phase transition in $\text{Ga}_2\text{O}_3$ (predicted to be 0.5 and 6.6 GPa by LDA and GGA methods, respectively). . . . .	151
6.5	(a) Electronic band structure and (b) Electronic density of states for $\text{Ga}_3\text{O}_3\text{N}$ calculated using first-principles (DFT) methods within the LDA. . . . .	155
6.6	Photoluminescence spectrum of the $\text{Ga}_{2.8}\text{N}_{0.64}\text{O}_{3.24}$ sample obtained via high- $P,T$ synthesis in the multianvil experiments, using UV laser excitation (325 nm) . . . . .	156
6.7	(a) Raman spectrum collected for the $\text{Ga}_{2.8}\text{N}_{0.64}\text{O}_{3.24}$ sample at an excitation wavelength of 514.5 nm. The bold solid lines on the frequency scale below indicate the positions of the Raman bands for the analogous spinel form of $\gamma$ - $\text{Ge}_3\text{N}_4$ . (b) Phonon density of states (VDOS) calculated for the $R\bar{3}m$ pseudocubic $\text{Ga}_3\text{O}_3\text{N}$ phase, predicted as “model I” in the enthalpy calculations (Table 6.7 ). The dashed lines indicate the Raman-active modes for that phase. . . . .	157

LIST OF TABLES

2.1	Point and space groups of Bravais lattices and crystal structures . . . . .	17
4.1	Space groups, formula units per primitive unit cell $Z$ and Wyckoff sites of four polymorphs of $\text{Al}_2\text{O}_3$ : Corundum, $\text{Rh}_2\text{O}_3$ -(II), $Pbnm$ perovskite and post-perovskite. . . . .	63
4.2	Third-order BM-EOS parameters for $\text{Al}_2\text{O}_3$ polymorphs . . . . .	65
4.3	The theoretical data of Raman frequencies at zero pressure and their pressure dependencies, and comparison with other reported experimental results on corundum . . . . .	68
4.4	IR-active frequencies of corundum at zero pressure . . . . .	69
4.5	Elastic constants of corundum at zero pressure and their pressure dependencies	86
4.6	Comparison of elastic moduli between corundum and $\text{Rh}_2\text{O}_3$ (II) phase. The corundum phase is treated as a monoclinic crystal with 20 atoms per unit cell.	88
4.7	Third-order BM-EOS parameters, zero pressure structural parameters for B4 and B1-AlN and B4-to-B1 transition pressure $P_t$ . Parameters listed for B1 phase is for the 8-atom conventional cubic unit cell. . . . .	95
4.8	Bond-preserving TPs for the B4-to-B1 phase transition. $G$ denotes the space group of two end structures and $G'$ denotes the common subgroup. $Z$ represents the number of formula units per unit cell along the TP. The transformation matrices are given with respect to the primitive unit cell lattice vectors and the fractional atomic coordinates are in terms of the setting of $G'$ . $u \approx 3/8$ . . . . .	96
5.1	Space groups, formula units per primitive unit cell and Wyckoff sites of hexagonal $\alpha$ -, $\beta$ - $\text{Si}_3\text{N}_4$ and cubic $\gamma$ - $\text{Si}_3\text{N}_4$ . . . . .	102
5.2	Summary of calculated and measured crystal parameters of $\alpha$ -, $\beta$ - and $\gamma$ - $\text{Si}_3\text{N}_4$ . $V_0$ is the equilibrium volume per atom, $B$ is the bulk modulus and $B'$ is the first-order pressure derivative. Measurements were made at room temperature. . . . .	111

5.3	Summary of phase transition pressure and temperature for synthesizing $\gamma$ - $\text{Si}_3\text{N}_4$	115
6.1	Third-order BM-EOS parameters for $\text{Ga}_2\text{O}_3$ polymorphs . . . . .	136
6.2	Calculated and experimental zone-center Raman peak positions and Grüneisen parameter for the $\beta$ - $\text{Ga}_2\text{O}_3$ phase . . . . .	138
6.3	Calculated and experimental zone-center Raman peak positions for the $\alpha$ - $\text{Ga}_2\text{O}_3$ . . . . .	139
6.4	Estimated internal strains . . . . .	143
6.5	Raman mode frequencies and frequency shifts in $\beta$ - $\text{Ga}_2\text{O}_3$ nanowires with the $[40\bar{1}]$ and $[110]$ growth directions. Overall, excellent agreement between the observed and calculated shifts is seen for all mode frequencies except the one marked with an *. . . . .	144
6.6	Third-order Birch-Murnaghan EOS parameters, zero pressure structural parameters for wurtzite GaN . . . . .	148
6.7	Parameters of the third-order Birch-Murnaghan equation of states of three unit-cell-based atomic models of the spinel-structured $\text{Ga}_3\text{O}_3\text{N}$ that have the lowest energy calculated within the LDA. . . . .	150
6.8	Analysis of local coordination ordering schemes within the three unit-cell models of the spinel-structured $\text{Ga}_3\text{O}_3\text{N}$ in terms of the ratio of various types of $\text{AX}_4$ tetrahedral and $\text{AX}_6$ octahedral units. . . . .	153
A.1	Value and meaning of ISIF tag . . . . .	181
B.1	Independent components of $C_{ij}$ for all the crystal classes . . . . .	184
B.2	Correction term to $C_{ij}$ due to pressure . . . . .	187

CHAPTER 1  
INTRODUCTION

**1.1 Pressure-Induced Phase Transitions and Thermodynamic Properties of Main-Group Oxides and Nitrides**

Main group nitrides and oxides are important solid compounds with applications in fields ranging from structural ceramics to catalysts and electronic materials. In this dissertation, I report our studies of five material systems of these groups:  $\text{Al}_2\text{O}_3$ ,  $\text{AlN}$ ,  $\text{Si}_3\text{N}_4$ ,  $\text{Ga}_2\text{O}_3$ , and  $\text{Ga}_3\text{O}_3\text{N}$ .

**1.1.1  $\text{Al}_2\text{O}_3$**

Aluminium oxide ( $\text{Al}_2\text{O}_3$ ) is often referred to as alumina, sapphire or aloxite in the ceramic, mining and materials science communities. It is commonly used as an abrasive due to its hardness and as a refractory material due to its high melting point. The naturally-occurring crystalline form of  $\text{Al}_2\text{O}_3$  at ambient condition is primarily corundum. Rubies ( $\text{Cr}^{+3}$  doped) and sapphires are gem-quality forms of corundum. In high-pressure experiments, ruby usually serves as a standard pressure gauge (ruby scale) in diamond anvil cell (DAC)<sup>1</sup> and sapphire is used as window material in shock wave experiments<sup>2</sup>.  $\text{Al}_2\text{O}_3$  is also one of the major constituents of the Earth's lower mantle. High-pressure behaviors and thermal properties of alumina are important for both experimental research and better understanding of the interior of the earth.

At ambient conditions, The crystalline form of  $\text{Al}_2\text{O}_3$  is corundum ( $\alpha\text{-Al}_2\text{O}_3$ , space group  $R\bar{3}c$ ). This structure is known to exist over a wide range of pressure and temperature conditions. In the past twenty years theoretical<sup>3-7</sup> and experimental<sup>8-11</sup> studies showed that  $\alpha\text{-Al}_2\text{O}_3$  transforms into the  $\text{Rh}_2\text{O}_3(\text{II})$  structure (space group  $Pbcn$ ) around



90 GPa, and further transforms into the post-perovskite structure (space group  $Cmcm$ ) at  $\sim 130$  GPa. Several calculations predicted a transition from  $\text{Rh}_2\text{O}_3(\text{II})$  structure to the orthorhombic perovskite (PV) structure (space group  $Pbnm$ ) at even higher pressures<sup>5,12</sup>. However, it has never been observed in experiments. Recent calculations showed that  $Pbnm$  perovskite is not thermodynamically favored with respect to the corundum,  $\text{Rh}_2\text{O}_3(\text{II})$  and post-perovskite phases<sup>6,7</sup>. Here we report our LDA calculated equilibrium  $T$ - $P$  phase diagram with both ultra-soft pseudopotentials (US-PP) and PAW method. The results are compared with other reported calculations<sup>3-6,6,7,13</sup>.

In the corundum $\rightarrow$  $\text{Rh}_2\text{O}_3(\text{II})$  transformation, *in situ* heating is found necessary. At room temperature, X-ray diffraction experiments showed that corundum phase is stable up to 175 GPa<sup>14,15</sup>, which implies the existence of a large kinetic barrier for the corundum to transform into the  $\text{Rh}_2\text{O}_3(\text{II})$  phase. On the other hand, Lin *et al.* found that the high-pressure  $\text{Rh}_2\text{O}_3(\text{II})$  phase can be seen as low as 85 GPa ( $P_t = 96$  GPa) on decompression after laser heating<sup>10</sup>, indicating the  $\text{Rh}_2\text{O}_3(\text{II})\rightarrow$ corundum transition is also sluggish. No experiment has quenched the  $\text{Rh}_2\text{O}_3(\text{II})$  phase to ambient conditions. We proposed a transformation pathway for the corundum $\rightarrow$  $\text{Rh}_2\text{O}_3(\text{II})$  transition and evaluate the kinetic barrier based on the proposed pathway. We further predict the meta-stability of two phases.

Thermodynamic properties, such as thermal expansion coefficient (TEC), heat capacity  $C_P$ , entropy and adiabatic bulk modulus have long been studied experimentally<sup>16-25</sup>. Almost a decade ago Hama *et al.* calculated the thermal properties of corundum phase by extending the formalism of Thomsen and combining the results with the Vinet model and the Debye model for lattice vibrations<sup>26</sup>. To date, no first-principles studies have been reported to predict the thermodynamic properties of  $\text{Al}_2\text{O}_3$ . And, both experimental and theoretical data of thermal properties of the high-pressure phases are lacking. We thus present our calculated high-pressure TEC and bulk modulus for  $\text{Rh}_2\text{O}_3$  (II) and pPV phases as a function of temperature up to 3000 K.

Before 2004, experimental elastic constants of  $\alpha$ - $\text{Al}_2\text{O}_3$  were reported from as early as 1950s<sup>25,27-29</sup>. And many efforts of *ab initio* calculations were made to predict the elastic

constants independently<sup>30,31</sup>. However, some calculations showed conflict in the sign of  $C_{14}$ <sup>32</sup>. In 2004, Gladden *et al.*<sup>33</sup> reported their reexamination of the elasticity of  $\alpha$ -Al<sub>2</sub>O<sub>3</sub> using resonance ultrasound spectroscopy (RUS) and confirmed that  $C_{14}$  is positive rather than negative. Gladden’s conclusion was later confirmed by both measurement with a different technique<sup>34</sup> and first-principles calculations<sup>35</sup>. Although measurements of  $C_{ij}$  for the high-pressure phases of Al<sub>2</sub>O<sub>3</sub> are still lacking, Duan *et al.*<sup>31</sup> and Stackhouse<sup>36</sup> have calculated the elastic constants of Rh<sub>2</sub>O<sub>3</sub>(II) (from 75 GPa to 300 GPa) and post-perovskite phases (at 136 GPa), respectively. Here we report our predicted  $C_{ij}$  of  $\alpha$ -, Rh<sub>2</sub>O<sub>3</sub>(II)- and pPV-Al<sub>2</sub>O<sub>3</sub> with pressure dependencies, which will be compared with other available results. Elastic properties of both corundum and Rh<sub>2</sub>O<sub>3</sub>(II) phases have been studied, but a direct comparison between the two phases is not accessible due to different crystal classes. Here we compare the elastic properties of corundum and Rh<sub>2</sub>O<sub>3</sub>(II) phase by treating both phases as the common-subgroup monoclinic lattices.

### 1.1.2 AlN

AlN is an important semiconductor primarily due to its wide band-gap and thermal properties. The structural changes and properties at high pressures are of special interests. Experiments<sup>37–40</sup> and calculations<sup>41–46</sup> revealed that a pressure-induced first-order phase transition from wurtzite (B4) structure to rocksalt (B1) structure happens for AlN. On the experimental side, without heating, the lowest pressure at which the rocksalt structure started to show up is 14 GPa<sup>39</sup> and the B4-to-B1 transition was observed to complete at 20–31.4 GPa<sup>39,40</sup>. Xia *et al.* also found that the rocksalt phase is quenchable to ambient conditions<sup>39</sup>. However, theoretical calculations consistently predicted a transition pressure that is lower than the experimental values. Most of the recent first-principles predicted static  $P_t$  is less than 10 GPa. The discrepancy implies the existence of a hysteresis for the forward and backward transitions which is caused by the activation barrier at the transition.

To calculate the activation barrier, we first examine the previously proposed transition paths. Using the computer program *COMSUBS*<sup>47</sup>, Stokes *et al.* proposed five TPs by

preserving the nearest neighbors along the transition pathway and limiting the size of unit cell to no more than four different Wyckoff positions<sup>48</sup>. He also found a common bilayer sliding mechanism along five paths, which had been pointed out by Zahn *et al.*<sup>49</sup> and Sowa<sup>50</sup>. Another work adopted the systematic approach is from Capillas *et al.*<sup>51</sup>, which was performed using the databases and tools provided by the *Bilbao Crystallographic Server*<sup>52</sup>. They proposed eight possible paths with different orthorhombic and monoclinic symmetries by setting the maximum  $k$ -index equal to 4, strain tolerance  $S_{tol} < 0.15$  and maximum atomic displacement  $\Delta_{tol} < 2 \text{ \AA}$ . The intermediate structures along all the eight paths have eight atoms per unit cell. The difference between these two reports is that the nearest neighbours are not preserved along all the eight paths proposed by Capillas *et al.*

DFT calculations from Shimojo *et al.* showed that the enthalpy barrier of transformation is independent of the three paths ( $Cmc2_1$ ,  $Pna2_1$  and  $P2_1$ ) for CdSe. Cai suggested, without calculation, that the B4-to-B1 transition is characterized by the transformation of the four-atom “transition unit”, while the long-range pattern may be less important. On the other hand, using MD simulations, Zahn *et al.* pointed out that the favored paths have a tendency to avoid excess strains during the transformation.

It would be interesting to investigate the proposed TPs with another material via first-principles method. Previous studies<sup>53–55</sup> suggested that the energetically favored TPs are bond preserving. In this paper, we studied all five bond-preserving TPs proposed by Stokes *et al.* and one bond-breaking TP proposed by Capillas *et al.* from an energetic point of view for the B4-to-B1 transition in AlN. The correlation of the enthalpy barrier with different TPs and strains will be discussed. We also relate the bilayer sliding mechanism to the long-range patterns of “transition units”, and Cai’s hypothesis will be examined.

### 1.1.3 Si<sub>3</sub>N<sub>4</sub>

For Si<sub>3</sub>N<sub>4</sub>, it is widely used in cutting tools and anti-friction bearings due to its excellent mechanical properties, low mass density, and thermal stability<sup>56</sup>. It is also used as an insulator layer or as an etch mask because of its dielectric properties and a better diffusion

barrier against impurities in microelectronics<sup>57</sup>. For its technological importance, the mechanical and thermal properties of silicon nitride at ambient pressure has been investigated extensively by both experiment and theory<sup>56,57</sup>. In contrast, its properties at high-pressure is less known.

$\alpha$  ( $P3_1c$ ) and  $\beta$  ( $P6_3/m$ ) phases are the only two bulk polymorphs of  $\text{Si}_3\text{N}_4$  known at ambient pressure. Both phases can be synthesized by nitriding pure silicon. In 1999,  $\gamma$ - $\text{Si}_3\text{N}_4$  (or  $c$ - $\text{Si}_3\text{N}_4$ ,  $Fd\bar{3}m$ ) with the cubic spinel structure was synthesized at high pressure and high temperature<sup>58</sup>. Despite intensive research efforts in searching the “post-spinel” phases in Group-IVB nitrides, the spinel structured  $\gamma$  phase remains as the only experimentally identified high-pressure phase.

Phase transitions in  $\text{Si}_3\text{N}_4$  have drawn extensive attention for more than a decade. The relative phase stability between  $\alpha$  and  $\beta$  phases has been a topic of investigation for many years. Direct measurements of energetics of  $\text{Si}_3\text{N}_4$  were reported by Liang *et al.*<sup>59</sup>. However, the difference in formation enthalpies between  $\alpha$ - and  $\beta$ - $\text{Si}_3\text{N}_4$  was founded to be less than the intrinsic experimental uncertainty of  $\pm 22$  kJ/mol ( $\pm 32.6$  meV/atom). Nevertheless, the  $\beta$  phase is believed to be the ground state in  $\text{Si}_3\text{N}_4$  because no  $\beta \rightarrow \alpha$  transition is ever observed. The stability condition for  $\alpha$  phase has been experimentally studied at temperatures of  $1300^\circ$ – $1800^\circ\text{C}$  and pressures up to 60 GPa<sup>60–67</sup>. A solution-precipitation mechanism was proposed for the  $\alpha \rightarrow \beta$  transformation<sup>67</sup>. The observed liquid phase on the  $\alpha$ - $\text{Si}_3\text{N}_4$  surfaces was believed to lower the activation energy of atomic transportation. The stability of pristine  $\alpha$ - $\text{Si}_3\text{N}_4$  at high temperatures is ascribed to the extremely high value of the activation energy with clean surfaces. On the theory side, several studies confirmed that the static bonding energy of  $\alpha$  phase is slightly higher than that of  $\beta$  phase<sup>68–71</sup>. Wendel *et al.*<sup>70</sup> and Kuwabara *et al.*<sup>71</sup> carried out statistical QHA calculations, and they both found that the  $\alpha$  phase remains metastable in the temperature range from 0 to 2000 K at ambient pressure. Yet, pressure effects on the relative thermodynamic stability between  $\alpha$  and  $\beta$  phases was not addressed in previous studies. Our study is to understand the relative thermodynamic stability at high pressures.

The spinel structured  $\gamma$ - $\text{Si}_3\text{N}_4$  was first synthesized by Zerr *et al.* with laser-heated diamond anvil cell (LH-DAC)<sup>58</sup>. Later experiments showed that  $\gamma$ - $\text{Si}_3\text{N}_4$  can be obtained from both  $\alpha$  and  $\beta$ - $\text{Si}_3\text{N}_4$  upon compression and simultaneous *in-situ* heating<sup>58,72-75</sup>. We predict the equilibrium phase boundaries for the  $\alpha \rightarrow \gamma$  and  $\beta \rightarrow \gamma$  transitions. The transition pressures for the  $\alpha \rightarrow \gamma$  transition is about 0.5 GPa lower than that of  $\beta \rightarrow \gamma$  transition. The  $\gamma$  phase is quenchable to the ambient condition, and it remains stable at temperatures ranging up to about 1670 K at ambient pressure<sup>76,77</sup>. When  $\gamma$ - $\text{Si}_3\text{N}_4$  “decomposes” at ambient pressure upon heating, the samples may consist of both  $\alpha$  and  $\beta$ - $\text{Si}_3\text{N}_4$ <sup>76</sup>.

The *in-situ* heating to high temperature is found to be necessary to form the  $\gamma$ - $\text{Si}_3\text{N}_4$  at high pressures. At room temperature the  $\beta \rightarrow \gamma$  transition is, however, by-passed. Zerr found that  $\beta$ - $\text{Si}_3\text{N}_4$  exists up to 34 GPa and it then transforms into a new phase (labeled as  $\delta$ -phase) under further compression<sup>78</sup>. This phase transition was identified by Raman spectroscopy and energy dispersive X-ray powder diffraction (EDXD). But the structure of  $\delta$  phase was not fully determined. Zerr proposed three possible unit-cells based on the EDXD pattern: two tetragonal and one orthorhombic. He further suggested that the  $\delta$ - $\text{Si}_3\text{N}_4$  should be considered as a metastable intermediate stage in the  $\beta \rightarrow \gamma$  transition. Kroll has proposed a metastable willemite-II- $\text{Si}_3\text{N}_4$  phase which is an intermediate between  $\beta$  and  $\gamma$ - $\text{Si}_3\text{N}_4$  in both energetics and density<sup>79</sup>. However, the wII phase is unlikely to be the experimentally observed unknown phase at high pressure and room temperature. Because 1) the wII phase, which is structurally closely related to the spinel  $\gamma$ - $\text{Si}_3\text{N}_4$ , has been shown to have a significantly lower activation barrier for the  $\gamma \rightarrow$ wII transformation, comparing to that of  $\gamma \rightarrow \beta$  transformation<sup>79</sup>. Although the activation barrier of the  $\beta \rightarrow$ wII transformation is unknown, it is more likely to be high enough to exclude the room temperature transition. 2) The calculated Raman frequencies of wII- $\text{Si}_3\text{N}_4$  could not match many strong peaks appeared in the measurements, e.g., two observed peaks at about  $500 \text{ cm}^{-1}$  and  $550 \text{ cm}^{-1}$  are absent in the calculation. A recent experimental work from McMillan *et al.* reproduced Zerr’s findings on  $\delta$ - $\text{Si}_3\text{N}_4$ , but excluded the wII cubic structure<sup>80</sup>.

Meanwhile,  $\beta$ -Ge<sub>3</sub>N<sub>4</sub> is found to transform into the metastable polymorph  $\delta$ -Ge<sub>3</sub>N<sub>4</sub> with hexagonal  $P3$  symmetry at room temperature by Soignard *et al.*<sup>81</sup> *Ab initio* calculation from Dong *et al.* showed that a  $\beta \rightarrow P\bar{6} \rightarrow P3$  transition sequence could occur in Ge<sub>3</sub>N<sub>4</sub> at the pressure of about 20 GPa and 28 GPa<sup>82</sup>, which are of second-order that driven by soft phonons. If  $\beta$ -Ge<sub>3</sub>N<sub>4</sub> directly transforms into the  $P3$  structure, the transition was predicted to be first-order and  $P_t = \sim 23$  GPa. Dong also pointed out that the  $\beta \rightarrow P\bar{6}$  transition is originated from a soft silent  $B_u$  mode. Room temperature experimental study by Soignard *et al.* confirmed the direct  $\beta \rightarrow P3$  transition associated with a 5-7% volume reduction<sup>81</sup>. The Raman data they observed excludes the intermediate  $P\bar{6}$  structure. Based on the density consideration, Soignard *et al.* suggested that the new polymorph is a “post-phenacite” phase, in stead of “post-spinel”. Comparison of the X-ray diffraction and Raman data between Ge<sub>3</sub>N<sub>4</sub> and Si<sub>3</sub>N<sub>4</sub> shows similarity which may suggest a  $P3$  structure for  $\delta$ -Si<sub>3</sub>N<sub>4</sub>. It is still unclear whether there are intrinsic differences between the HP-RT behaviors of Si<sub>3</sub>N<sub>4</sub> and Ge<sub>3</sub>N<sub>4</sub>, or the experimental results may be interpreted differently. Our study is to theoretically investigate structural instabilities and possible metastable phase transitions in  $\alpha$ - and  $\beta$ -Si<sub>3</sub>N<sub>4</sub> at high pressures and room temperature. We found no sign of dynamical instability in the  $\alpha$  phase at high-pressure. On the other hand, we predicted a phonon-softening related first-order phase transition at about 38.5 GPa in  $\beta$  phase. At this pressure, the density of the proposed high-pressure phase is 4.16 g/cm<sup>3</sup> which is larger than that of  $\beta$ -Si<sub>3</sub>N<sub>4</sub> (3.71 g/cm<sup>3</sup>), yet smaller than that of  $\gamma$ -Si<sub>3</sub>N<sub>4</sub> (4.53 g/cm<sup>3</sup>, calculated). We further estimated the kinetic barrier heights for our proposed  $\beta \rightarrow P3$  transition, which is only 67.23 meV/atom at 38.5 GPa. Despite being of first-order phase transition, the small barrier height suggests that the  $P3$  phase is unlikely to be recovered below 38.5 GPa.

We also performed a series of systematical calculations of thermodynamic properties of Si<sub>3</sub>N<sub>4</sub>, such as thermal expansion coefficient (TEC), heat capacity and bulk Grüneisen parameter, and compared our results with available experimental data<sup>83-90</sup> and some previous calculations<sup>70,71,91,92</sup>. The overall good agreement with experiment validates the

adopted statistical quasi-harmonic approximation (QHA) and the Birch-Murnagahn equation of states (EOS) models. Our results support the prediction from Kuwabara *et al.*<sup>71</sup> on the negative TEC of  $\alpha$  and  $\beta$  phases at temperatures below 100 K. We attributed the origin of the negative TEC to the low-frequency phonon modes with the negative mode Grüneisen ratios in the two phases.

#### 1.1.4 Ga<sub>2</sub>O<sub>3</sub>

Monoclinic gallium oxide (Ga<sub>2</sub>O<sub>3</sub>) is usually known as a wide-band-gap semiconductor ( $E_g = 4.9$  eV); however, the conductivity can be varied from insulating to conducting behavior depending upon the preparation conditions<sup>93</sup>. It is well known that Ga<sub>2</sub>O<sub>3</sub> can exist in several forms, including  $\alpha$ ,  $\beta$ ,  $\gamma$ ,  $\delta$ , and  $\epsilon$  polymorphs that all have different structure types<sup>94</sup>. Of these, the most stable form at ambient conditions is determined to be  $\beta$ -Ga<sub>2</sub>O<sub>3</sub>. It is of great interest to determine the pressure-induced phase transformations among Ga<sub>2</sub>O<sub>3</sub> polymorphs in order to establish the stable and metastable phase relations between different crystalline modifications, and to evaluate their production under different synthesis conditions. The relative densities of  $\beta$ - and  $\alpha$ -Ga<sub>2</sub>O<sub>3</sub> are 5.94 and 6.48 g·cm<sup>-3</sup>, respectively<sup>95</sup>, indicating that a  $\beta \rightarrow \alpha$  transformation should occur at high pressure. Nanocrystalline  $\beta$ -Ga<sub>2</sub>O<sub>3</sub> particles embedded in a glassy matrix were also studied at high pressure using energy-dispersive x-ray diffraction<sup>96</sup>. In that work, a  $\beta$ -to- $\alpha$  phase transformation was found to be initiated at 6 GPa, but the process was not completed by 15 GPa, the highest pressure achieved in the study. However, it is known that the silica glass host matrix undergoes important structural and density changes within this pressure range<sup>97,98</sup>, so that it is not yet known if the structural changes are intrinsic to the  $\beta$ -Ga<sub>2</sub>O<sub>3</sub> material presumably influenced by the nanocrystalline nature of the sample, or are promoted by anomalous densification among the SiO<sub>2</sub> matrix. These results prompted us to theoretically investigate the high-pressure behavior of the phase-pure bulk  $\beta$ -Ga<sub>2</sub>O<sub>3</sub>.

One-dimensional nanostructured forms of  $\beta$ -phase of gallium oxide ( $\beta$ -Ga<sub>2</sub>O<sub>3</sub>) such as nanotubes, nanobelts, and nanowires, have attracted recent interest due to enhanced

optical properties<sup>99,100</sup>. Recently, Choi *et al.*<sup>101</sup> synthesized  $\beta$ -Ga<sub>2</sub>O<sub>3</sub> nanowires (diameter range of 15–45 nm) with a [001] growth direction using an arc-discharge method. Gao *et al.*<sup>102</sup> synthesized [40 $\bar{1}$ ]  $\beta$ -Ga<sub>2</sub>O<sub>3</sub> nanowires with diameters ranging from  $\sim$ 10–100 nm in a vertical radio-frequency furnace. Interestingly, the Raman mode frequencies of the [001]  $\beta$ -Ga<sub>2</sub>O<sub>3</sub> nanowires coincide with the corresponding frequencies in bulk  $\beta$ -Ga<sub>2</sub>O<sub>3</sub><sup>101</sup>. On the other hand<sup>102</sup>, the Raman mode frequencies of the [40 $\bar{1}$ ]  $\beta$ -Ga<sub>2</sub>O<sub>3</sub> nanowires are redshifted relative to corresponding frequencies in bulk  $\beta$ -Ga<sub>2</sub>O<sub>3</sub> by 4–23 cm<sup>-1</sup>. Using plasma-enhanced chemical vapor deposition, Rao *et al.* have synthesized  $\beta$ -Ga<sub>2</sub>O<sub>3</sub> nanowires whose growth is along the [110] direction<sup>103</sup>, and the Raman spectrum is significantly blueshifted in frequency<sup>104</sup>. Here we focus on the first-principles calculations of the Raman mode frequencies under internal strains. Our calculated Raman frequency shifts suggest that the observed shifts in the nanowires with the [40 $\bar{1}$ ] and [110] growth directions can be explained in term of different internal strains, in contrast to the previously suggested quantum confinement effects and defect-induced effects.

### 1.1.5 Ga<sub>3</sub>O<sub>3</sub>N

The group 13 oxynitride materials have many useful properties related to their electronic structure.  $\alpha$ -Ga<sub>2</sub>O<sub>3</sub> with the corundum structure is conveniently alloyed with Al<sub>2</sub>O<sub>3</sub> to provide selective reduction catalysts for gaseous NO<sub>x</sub><sup>105</sup>, and various other Ga<sub>2</sub>O<sub>3</sub> phases have been proposed as gas sensors, and in nanoscale structures as electron emitters and magnetic memory materials<sup>106</sup>. Within the Al<sub>2</sub>O<sub>3</sub>–AlN system, several important Al<sub>x</sub>O<sub>y</sub>N<sub>z</sub> ceramic alloys and compounds are known. At high AlN contents, layered forms based on hexagonal/cubic intergrowths are present. As the Al<sub>2</sub>O<sub>3</sub> content is increased, cubic spinel-structured materials begin to appear. A large family of defect spinels ( $\gamma$ -Al<sub>2</sub>O<sub>3</sub>, Al<sub>x</sub>O<sub>y</sub>N<sub>z</sub>) contain vacancies on both cation and anion sites<sup>107</sup>. A stoichiometric oxynitride spinel-structured compound is obtained at the Al<sub>3</sub>O<sub>3</sub>N composition, in which Al<sup>3+</sup> ions are present on the octahedral and tetrahedral sites, and O<sup>2-</sup> and N<sup>3-</sup> occupy tetrahedral anion sites<sup>108,109</sup>. Among the related nitride compounds Si<sub>3</sub>N<sub>4</sub> and Ge<sub>3</sub>N<sub>4</sub>, high-pressure



synthesis has recently resulted in formation of a new class of spinel structures, that contain  $\text{Si}^{4+}$  and  $\text{Ge}^{4+}$  cations on both tetrahedral and octahedral sites<sup>110-114</sup>. Gallium oxynitride ( $\text{Ga}_3\text{O}_3\text{N}$ ) has been predicted to form a new spinel-structured compound within the  $\text{Ga}_2\text{O}_3$ - $\text{GaN}$  system, with potentially useful electronic properties<sup>115,116</sup>. It is predicted to be a direct wide bandgap semiconductor, comparable with  $\text{GaN}$ <sup>115</sup>. There has previously been an experimental report of a cubic gallium oxynitride phase with composition close to  $\text{Ga}_{2.8}\text{O}_{3.5}\text{N}_{0.5}$ , that formed metastably during  $\text{GaN}$  thin film synthesis from chemical precursors<sup>117,118</sup>. Here, we report our first-principles theoretical study of the formation energetics, stability, and electronic properties of the  $\text{Ga}_3\text{O}_3\text{N}$  spinel-structured phase, combined with experiments using a combination of high pressure-high temperature techniques to establish the formation and stability of spinel-structured  $\text{Ga}_3\text{O}_3\text{N}$  from  $\text{Ga}_2\text{O}_3$ + $\text{GaN}$  mixtures, and to determine the chemical composition, structure and properties of the resulting materials.

## 1.2 First-Principles Theoretical Studies

Simulation of macroscopic properties of a physical system typically involves solving an ordinary or partial differential equation over large numbers of degrees of freedom. Even if a precise mathematical theory is available, it is only in very few cases that analytical solutions are possible. Computational physics is the study and implementation of numerical algorithm to solve problems in physics where a quantitative theory exists. Before the prevalence of powerful computers, empirical and semi-empirical approaches are often adopted, which rely on the phenomenological model or parameters fitted from measured data. Nowadays, *ab initio* (or first-principles) calculations are routinely performed in the fields of computational physics and chemistry. Compared with the empirical approach, predictions from first-principles method can provide unbiased comparison and interpretation to the experimental data. It is also advantageous in calculating properties of materials at conditions where no or limited experimental data is available, and designing novel materials with promising properties. As one of the *ab initio* approaches, density function theory (DFT) is extremely successful in the electronic structure calculations for solids, which results from the work

of Hohenberg, Kohn and Sham<sup>119,120</sup>. Beside bulk systems, density functional theory has also become popular for complex materials such as nanostructures. In this dissertation, within the DFT, the many-electron exchange-correlation is approximated with the local density approximation (LDA). For part of the study that is associated with small energy differences, the LDA results are compared with calculations using the generalized gradient approximation (GGA). To improve numerical efficiency, core electrons were approximated with ultrasoft pseudopotentials (US-PP)<sup>121</sup>. In the case of  $\text{Al}_2\text{O}_3$ , we also conducted a parallel comparative study using Projector Augmented-Wave (PAW) method.

As mentioned above, the DFT based calculation is only possible and useful with the rapid development of high performance computer technologies, especially the parallel computing techniques. Considering the current computational efficiency, the DFT calculation can only deal with atomistic models of no more than a few hundred atoms on a single-core CPU. Our calculations are performed on the departmental computational resource, a distributed memory computer system (Beowulf cluster). This cluster is comprised of 96 AMD Athlon MP CPUs running Red Hat Enterprise Linux 5. A photo of our recently constructed cluster system is shown in Figure 1.1. We have implemented *parallel* algorithms to distribute each job into a set of calculations. Each corresponds to one DFT calculation. The most computationally expensive part in this study is to calculate the real-space force-constant matrix using supercell models of  $\sim 100$ -200 atoms.

I have been focused on adopting and further developing computational methods based on density functional theory and statistical theory to study the behavior of materials, in particular the pressure induced solid-solid phase transitions and thermodynamic properties, over a wide range of temperature-pressure ( $T$ - $P$ ) conditions. To predict the equilibrium transition pressure at a finite temperature and thermodynamic properties (such as thermal expansion coefficient (TEC), heat capacity, entropy and bulk modulus, etc.), the calculation of free energy is required. We adopt quasiharmonic approximation (QHA) to model the lattice dynamics. Our approach of calculating phonon frequencies belongs to a method of the direct approach: a first-principles real-space supercell force-constant (SC-FC) method



Figure 1.1: Photo of recently constructed departmental computer cluster.

which calculates the phonon frequencies from the forces obtained via the Hellmann-Feynman theorem. This technique is proved to be efficient and successful in predicting the full phonon spectra of many materials<sup>122–129</sup>.

For pressure-induced phase transitions, we are interested in investigating both equilibrium transition conditions and the kinetic process. Regarding reconstructive transitions with no group-subgroup relation, the equilibrium phase boundary is determined by equating the Gibbs free energy of the two phases. However, in general, there exists a kinetic barrier at the transition, which can be overcome by the thermal activation energy from the environment (small barrier) or heating process (large barrier). Based on the pressure dependencies of the forward and backward barrier heights, we can predict the metastability of polymorphs. The kinetic barrier can be estimated from the knowledge of the microscopic mechanism of the transition. For transformations with a group-subgroup relation, a transition path (TP) can be easily defined by a set of continuous atomic displacements

and/or lattice strains that the system transforms from one phase into another. For some simple reconstructive transformations with no group-subgroup relation, although nucleation processes may occur, diffusionless collective atomic displacements can still characterize the transformation on a local basis. The concept of transition pathway is then possible to describe the transformation from the starting phase to the ending phase in a continuous manner. Among the infinite number of ways to transform one structure into another, the theoretical studies are restricted only to those most possible paths, e.g., preservation of bonds, less strains, etc.

The pressure dependence of phonon spectrum can also reveal the information of structural stability under compression. In the case when soft phonon happens, a vanishing phonon frequency indicates the disappearance of the restoring forces related to the corresponding normal mode, and the structure consequently undergoes a continuous transition to a lower-symmetry phase, which can be found according to the vibrational pattern based on the associated eigenvectors. However, the transition happened at room or higher temperatures is often first-order, where no phonon has become soft yet. But this first-order phase transition is driven by the phonon mode with softening tendency.

### **1.3 Outline of Dissertation**

The rest of this dissertation is organized as follows. In Chapter Two I first review the fundamental theory of solid-solid phase transitions, which include the reconstructive phase transitions and the soft-phonon driven continuous transitions. Then our computational approaches of investigating the transformation mechanism and phase metastability/instability are introduced. In Chapter Three I discuss the first-principles methodologies we adopted in this study, i.e., total energy calculation based on density functional theory and our methods to calculate the finite-temperature thermodynamic potentials. The influence of equation of state models on the prediction of thermal properties is also presented. In Chapter Four we show our first-principles studies on the pressure-induced phase transitions in  $\text{Al}_2\text{O}_3$  and  $\text{AlN}$ . Our focus is on the microscopic mechanism of the transition from an energetic point

of view. The thermal and elastic properties of  $\text{Al}_2\text{O}_3$  are also studied. In Chapter Five we predict a metastable high-pressure transition for  $\beta\text{-Si}_3\text{N}_4$ . We also predict the thermodynamic properties of three known polymorphs of  $\text{Si}_3\text{N}_4$ . In Chapter Six I present our study of pressure-induced phase transitions in bulk  $\text{Ga}_2\text{O}_3$  and the blue-shifted Raman frequencies in  $\text{Ga}_2\text{O}_3$  nanowires, as well as the theoretical optimal synthesis condition, electronic properties and phonon spectrum of the spinel-structured gallium oxynitride ( $\text{Ga}_3\text{O}_3\text{N}$ ). Finally in Chapter Seven we summarize our key results and discuss the future works.

CHAPTER 2  
THEORY OF PHASE TRANSITIONS IN SOLIDS

### 2.1 Phases and Crystal Symmetries

Before we discuss the phase transitions, it is necessary to elucidate the concept of phase. The word “phase” may have different meanings in different disciplines. In thermodynamics, a phase of a macroscopic system refers to a type of internal structure of the system when the composition of the system is specified. Throughout a single phase, all the physical properties of the system is uniform at the macroscopic level. These properties include chemical composition, density, heat capacity, index of refraction and so on. For a material system, the internal structure is simply its atomic configuration if magnetic or electronic degrees of freedom can be ignored. A macroscopic solid material is composed of numerous atoms or molecules, usually in the order of  $\sim 10^{23}$ . The atoms or molecules that compose the solid are closely packed together and the chemical bonds between them are relatively strong. The short-range structural orders are largely controlled by the chemistry of the constituent elements, while statistics affects the long-range structural order. According to their long-range atomic order/disorder, solids are divided into two categories: crystals and amorphous solids. Real solids contain imperfections, such as surfaces, grain boundaries, and defects. In this dissertation, my study is limited to only ideal crystals, which are good approximations to real bulk crystalline materials that contain only small amount of defects and impurities.

Symmetry is an essential character of crystals. Atoms in a crystal vibrate around their equilibrium positions, which form a periodical and ordered pattern in the three dimension space. The pattern is made up of a group of equilibrium positions of atoms, which is called the *atomic basis*. The collection of repetition of identical structural units with translational

symmetry is called *Bravais lattice*.

$$\text{crystal structure} = \text{Bravais lattice} + \text{atomic basis} \quad (2.1)$$

The location of each Bravais lattice point, in another word, the origin of each repeated unit in a crystal, can be described by

$$\mathbf{R} = n_1 \mathbf{a}_1 + n_2 \mathbf{a}_2 + n_3 \mathbf{a}_3 \quad (2.2)$$

where the 3-D vectors  $\mathbf{a}_i$  ( $i = 1, 2, 3$ ) are linearly independent unit-cell vectors.  $n_1$ ,  $n_2$  and  $n_3$  are integers. The smallest repeatable unit cell of a lattice is called *primitive unit cell*, and the corresponding unit vectors are *primitive unit-cell vectors*. Note that the choice of unit-cells in a crystal is not unique.

There are seven distinct crystal systems, i.e., cubic, hexagonal, rhombohedral (also known as trigonal), tetragonal, orthorhombic, monoclinic, and triclinic. By considering additional possible lattice points at body centers, face centers, or base centers, whereas not to reduplicate, there are precisely 14 distinct Bravais lattices, e.g., the orthorhombic system includes four different Bravais lattices, i.e., simple orthorhombic, body-centered orthorhombic, face-centered orthorhombic, and base-centered orthorhombic lattices; and for the cubic system, there are three distinct Bravais lattices, i.e., simple cubic (sc), body-centered cubic (bcc), and face-centered cubic (fcc) lattices. In the case of body-centered, face-centered, or base-centered Bravais lattice, the primitive unit cell is different from its conventional unit cell. And accordingly, the primitive unit vectors are different from those conventional unit vectors. As an example, for face-centered cubic lattice (fcc), the conventional unit cell is constructed by having atoms on the corners of a cube and an atom at the center of each

Table 2.1: Point and space groups of Bravais lattices and crystal structures

	Bravais lattice (Basis of spherical symmetry)	Crystal structure (Basis of arbitrary symmetry)
Number of point group	7 crystal systems	32 crystallographic point group
Number of space group	14 Bravais lattices	230 space groups

face. The conventional unit vectors and primitive unit vectors are

$$\left\{ \begin{array}{l} \mathbf{a}_1 = (a, 0, 0) \\ \mathbf{a}_2 = (0, a, 0) \\ \mathbf{a}_3 = (0, 0, a) \end{array} \right. \quad \text{and} \quad \left\{ \begin{array}{l} \mathbf{a}_1 = \left(0, \frac{a}{2}, \frac{a}{2}\right) \\ \mathbf{a}_2 = \left(\frac{a}{2}, 0, \frac{a}{2}\right) \\ \mathbf{a}_3 = \left(\frac{a}{2}, \frac{a}{2}, 0\right) \end{array} \right. \quad (2.3)$$

respectively. The volume of the fcc primitive unit cell is 1/4 of the conventional cubic cell.

In addition to translational symmetry as described by the Bravais lattice, a crystal is also invariant under a set of point group symmetry operations, such as rotation, reflection and inversion. There are totally 32 crystallographic point groups. Each point group can be classified into one of the 7 crystal systems. Point group is also called crystal class. The combination of translational symmetry operations and point group operations in a crystal is referred as the crystal's *space group* symmetry. There are a grand total of 230 space groups<sup>130</sup>. Table 2.1 shows the relation between point and space groups of Bravais lattices and crystal structures.

The nomenclature of space group is not unique. One commonly adopted notation is listed in the International Union of Crystallography, which assigns each space group with a number (#1 to #230). The Hermann-Mauguin notation and Schönflies notation are also commonly used in crystallography community. For example,  $\alpha$ -Al<sub>2</sub>O<sub>3</sub> belongs to the space group #167, which can be equivalently noted as  $R\bar{3}C$  or  $D_{3d}^6$ .

Experimentally, the crystal structure can be determined by either atomic scale imaging or diffraction techniques, such as X-ray diffraction (XRD). To understand the general principles involved in solving diffraction data, it is necessary to introduce the concept of the reciprocal lattice. The reciprocal lattice plays a fundamental role in studies of functions



with the periodicity of a Bravais lattice. Once a Bravais lattice in real space is given, one can construct the reciprocal lattice correspondingly. The primitive unit vectors in reciprocal space are defined as

$$\begin{cases} \mathbf{b}_1 = 2\pi \frac{\mathbf{a}_2 \times \mathbf{a}_3}{\mathbf{a}_1 \cdot (\mathbf{a}_2 \times \mathbf{a}_3)} \\ \mathbf{b}_2 = 2\pi \frac{\mathbf{a}_3 \times \mathbf{a}_1}{\mathbf{a}_2 \cdot (\mathbf{a}_3 \times \mathbf{a}_1)} \\ \mathbf{b}_3 = 2\pi \frac{\mathbf{a}_1 \times \mathbf{a}_2}{\mathbf{a}_3 \cdot (\mathbf{a}_1 \times \mathbf{a}_2)} \end{cases} \quad (2.4)$$

where  $\mathbf{a}_i$  ( $i = 1, 2, 3$ ) are primitive unit vectors of real space Bravais lattice. Under this definition,  $\mathbf{a}_i \cdot \mathbf{b}_j = 2\pi\delta_{ij}$  ( $i, j = 1, 2, 3$ ). Any reciprocal lattice vector can be written as

$$\mathbf{G} = k_1\mathbf{b}_1 + k_2\mathbf{b}_2 + k_3\mathbf{b}_3 \quad (2.5)$$

where  $k_i$  ( $i = 1, 2, 3$ ) are integers. Then

$$\mathbf{G} \cdot \mathbf{R} = 2\pi (n_1k_1 + n_2k_2 + n_3k_3) \quad (2.6)$$

and

$$e^{i\mathbf{G} \cdot \mathbf{R}} = 1 \quad (2.7)$$

where  $\mathbf{R} = n_1\mathbf{a}_1 + n_2\mathbf{a}_2 + n_3\mathbf{a}_3$  is any real space lattice vector. For any family of lattice planes separated by a distance  $d$ , there are reciprocal lattice vectors normal to the planes. The shortest one has a length of  $2\pi/d$ . It is convenient to describe the orientation of lattice planes based on this relation. The commonly used notation is *Miller indices*. The Miller indices for a family of lattice planes are the integral coefficients of the shortest reciprocal lattice vector perpendicular to the planes in terms of the primitive unit vectors in reciprocal space, e.g., the reciprocal lattice vector  $h\mathbf{b}_1 + k\mathbf{b}_2 + l\mathbf{b}_3$  determines a family of planes with Miller indices  $(h, k, l)$ .

The diffraction pattern of X-rays incident on a crystal provides information on interplanar spacing, and ultimately the space group and structure of the crystal. Generally, there are two equivalent ways to explain the phenomenon of X-ray diffraction by a perfect

crystal, i.e., the Bragg law and von Laue condition. W. L. Bragg simply treated the crystal as parallel planes of atoms and the incident waves are specularly (mirror-like) reflected from these planes. The condition for a constructive interference leads to the famous Bragg law

$$2d \sin \theta = n\lambda \quad (2.8)$$

where  $d$  is the distance between two adjacent parallel planes,  $\theta$  is the angle measured from the plane ( $90^\circ$  minus angle of incidence), integer  $n$  is the order of interference and  $\lambda$  is the wavelength of incident radiation. The total deflected angle measured from the incident light is  $2\theta$ .

The von Laue approach regards the crystal as identical lattice points (a set of atoms) which can reradiate the incident wave in all directions. Sharp peaks will be observed at directions where constructive interference happens. The Laue condition can be written as

$$\Delta \mathbf{k} = \mathbf{G} \quad (2.9)$$

i.e., the change in wave vector equals to a reciprocal lattice vector. Under the assumption of elastic scattering (the magnitude of the wave vector does not change), the Laue condition yields Bragg law. The practical and detailed experimental methods to determine the crystal structure are beyond the scope of this dissertation.

## **2.2 Equilibrium Thermodynamic Theory of Phase Transitions**

### **2.2.1 Thermodynamic Stability**

The occurrence of phase transitions can be interpreted synonymous to changes of atomic structures of matters. This phenomenon has long been studied and many natural forms of transitions are well observed in our everyday life, e.g., water freezes into ice below freezing temperatures. Here we focus our attention to the solid-solid phase transitions, especially the

pressure-induced structural phase transitions. Within this limitation, some important aspects of the complete theory of phase transitions, such as critical phenomena, melting, glass transition, ferromagnetism, superconductivity, etc., are not considered in this dissertation.

The first set of questions are: (1) *why* does a phase transition happen? (2) *when* does it happen? and (3) *how* does it happen? The first question is related to the interactions between a solid and its surrounding media. For simplicity, we ignore magnetic and electric interactions, and focus only on mechanical and thermal interactions. According to the 1<sup>st</sup> and 2<sup>nd</sup> law of thermodynamics, the most thermodynamically stable state of an isolated state is the state that minimizes the energy ( $E$ ). When the system is interacting with the surrounding media through mechanical work, the system reaches a mechanical equilibrium with the media when its pressure ( $P$ ) equals the pressure of the media, and it becomes thermodynamically stable against any spontaneous fluctuations when its enthalpy ( $H$ ), defined as  $H = E + PV$ , becomes minimized. Here,  $V$  represents the volume of the system. Similarly, when the system exchanges its energy with the media through heating, the thermal equilibrium is reached when the temperature ( $T$ ) of the system equals the temperature of the media, and it becomes thermodynamically stable when its Helmholtz free energy  $F$ , defined as  $F = E - TS$ , becomes minimized. Here,  $S$  is the entropy of the system.

In our studies, a solid is considered to be in a thermal equilibrium at temperature  $T$  and a mechanical equilibrium at pressure  $P$  with the surrounding media. At a given  $(T, P)$  condition, the thermodynamically stable state is reached when:

$$\Delta E + P\Delta V - T\Delta S \geq 0 \tag{2.10}$$

where  $\Delta E$ ,  $\Delta V$ , and  $\Delta S$  are virtual variations of total internal energy, volume, and entropy respectively. Given a sufficiently long period of time and allowing all possible fluctuations, a solid at a given  $(T, P)$  condition should reach its thermodynamically stable state, which minimizes its Gibbs free energy  $G$ , defined as  $G = E + PV - TS$ . Equation 2.10 is the Gibbs-Duhem stability criterion which is equivalent to  $\Delta G \geq 0$ .

A thermodynamically stable phase of a solid at a given  $(T, P)$  condition corresponds to a global minimal of Gibbs free energy for all atomic configurations. Correspondingly, metastable phases are referred to those associated local minimums of  $G$ . Altering  $T$  or  $P$  will change the Gibbs free energy landscapes and may in turn shuffle the relative orders among the local  $G$  minimums. The emergence of a new global minimal of  $G$  will lead to a phase transition in the solid.

The answer of when and how a phase transition happens requires detailed knowledge of not only the thermodynamic properties of individual phases but also the kinetic process that connect the initial and final phases. At equilibrium condition, a phase transition becomes possible when a new phase has lower Gibbs free energy than the initial phase. The initial phase then can be considered as a metastable phase at the new  $(T, P)$  condition. However, the lifetime of a metastable state is controlled by its local kinetic barrier heights. In reality, metastable states can exist for a long period of time and an equilibrium phase transition can be hindered when there exist large kinetic barriers that against the fluctuations. A well-known example is the two crystalline forms of element carbon: diamond and graphite. Graphite is known to be the ground state at ambient conditions whereas diamond is also “stable” in a wide range of usual environment unless enough activation energy (such as heating) is provided.

### 2.2.2 Phase Diagram and Classification of Phase Transitions

When two phases of a single-component system coexist at equilibrium, three conditions must be satisfied between two phases:

1. The temperatures of the two phases must be equal.

$$T_1 = T_2 \tag{2.11}$$

2. The pressures in two phases must be equal.

$$P_1 = P_2 \tag{2.12}$$

3. The chemical potentials of the two phases must be equal.

$$\mu_1 = \mu_2 \tag{2.13}$$

Since the chemical potential is the molar Gibbs free energy, we can rewrite the phase equilibrium conditions in the following form if both phases have the same number of atoms.

$$G_1(T, P) = G_2(T, P) \tag{2.14}$$

The basic concepts of an equilibrium phase diagram is sketched in Figure 2.1. Each point in the two-dimensional  $(T, P)$  space denotes one equilibrium state of the system. In most the  $T$ - $P$  region of the phase diagram, only a single phase is thermodynamically stable. At the boundary of two adjacent regions, two phases are equally stable along the  $T$ - $P$  phase boundary lines. Phase transitions happen when the phase boundaries are crossed. At triple points, such as the  $(T_1, P_1)$  and  $(T_2, P_2)$  points in the plot, three phases coexist. For a single component system, no more than three phases can reach simultaneous thermodynamic equilibria. There is a special point C where the phase boundary curve between the liquid and gas phases come to an end. This point is named as critical point, at and beyond which the liquid and gas phases become identical. It should be mentioned that the critical point can exist only for phases which are quantitatively different, e.g., a liquid and a gas. On the contrary, solid phases have certain internal symmetries. The difference between two solid phases of a substance, or between the liquid and solid phases, are qualitatively different.

During a quasi-static process of phase transition, the system may absorb or release the so-called *latent heat* ( $L$ ). The latent heat is associated with the change of entropy of the

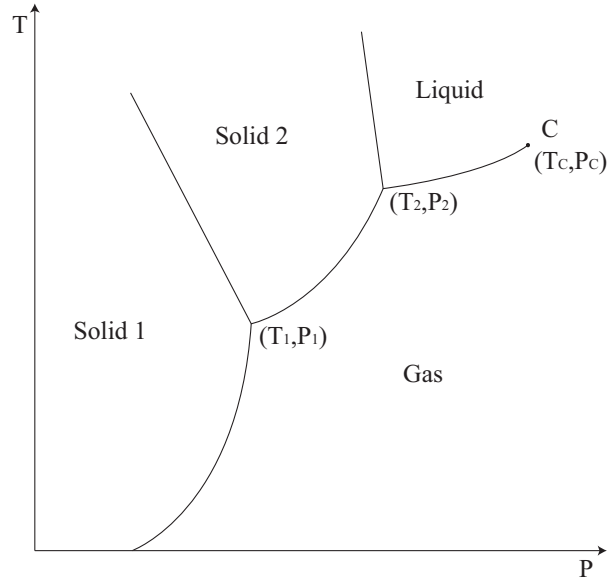


Figure 2.1: Phase diagram with two solid phases, one liquid phase and one gas phase. Two triple points and one critical point are present.

system.

$$L = T\Delta S \tag{2.15}$$

where  $\Delta S$  is the entropy difference between the final and initial phases.  $\Delta S$  may be zero in continuous phase transitions.

If we differentiate both sides of equation 2.14 with respect to temperature, the *Clapeyron-Clausius* equation can be derived.

$$\frac{dT}{dP} = \frac{V_2 - V_1}{S_2 - S_1} = \frac{T\Delta V}{L} \tag{2.16}$$

Clapeyron-Clausius equation gives the slope of the phase boundary in the phase diagram which is directly related to the change of volume and latent heat. We can estimate the amount of heat being absorbed/released during the transition from equation 2.16, nevertheless both  $\Delta V$  and  $L$  are zero for continuous phase transitions (see below).

As discussed above, while Gibbs free energy is always continuous during equilibrium phase transitions, other thermodynamic variables might be discontinuous. I now introduce the concept of order of a phase transition based on the Gibbs free energy.

1. First-order transitions are accompanied with a discontinuous change in the first-order derivatives of the thermodynamic potentials, such as volume and entropy. Thus a density jump and a latent heat are presented during a first-order phase transition. Transitions of this type is referred as the first kind or discontinuous phase transitions.

$$V = \left( \frac{\partial G}{\partial P} \right)_T \quad S = - \left( \frac{\partial G}{\partial T} \right)_P \quad (2.17)$$

2. In second-order transitions, the first-order derivatives of Gibbs free energies are continuous. Yet, the transitions are accompanied with discontinuity in second-order derivatives of thermodynamic potentials, such as isobaric specific heat capacity  $C_P$  and isothermal compressibility  $\kappa_T$ .

$$C_P = T \left( \frac{\partial S}{\partial T} \right)_P = -T \left( \frac{\partial^2 G}{\partial T^2} \right)_P \quad (2.18)$$

$$\kappa_T = -\frac{1}{V} \left( \frac{\partial V}{\partial P} \right)_T = -1/V \left( \frac{\partial^2 G}{\partial P^2} \right)_T \quad (2.19)$$

Higher order transitions can be specified in a similar fashion. Within the framework of Landau theory, second and higher order transitions belong to the second-kind (continuous). For these transitions, system continuously passes from one phase to another without any abrupt changes in volume, entropy and consequently no latent heat.

In the case of solid-solid phase transitions in crystals, reconstructive transitions reform the crystal lattices from one type to a distinctly different one without any direct structural relations, e.g., no group-subgroup relations. This type of transitions are always first-order. On the other hand, during displacive phase transitions, atoms gradually deviate from their original equilibrium positions to their corresponding new positions in the final phase in

a collective fashion. Although the displacements might be small, crystal symmetry is altered. Since the displacements happen in a continuous manner, one structure must have a higher symmetry and the other structure has a lower symmetry which is a subgroup of the spacegroup of the high-symmetry phase. The displacive transitions can be any order

## 2.3 Landau Theory for Phase Transitions of Second Kind

### 2.3.1 The Order Parameter and Landau Free Energy

Landau theory is a general phenomenological theory for phase transitions of second kind. Landau introduced a quantity *order parameter* to describe the changes in structure during the phase transition. The order parameter is zero in the high symmetry phase and takes non-zero value in the low-symmetry phase. For displacive phase transitions, the order parameter can be easily chosen as the atomic displacement from the equilibrium sites of the initial high-symmetry phase. Usually the free energy is independent of the sign of the order parameter that it only contains even-power terms.

$$G(T, P, \eta) = G_0 + A\eta^2 + B\eta^4 + \dots \quad (2.20)$$

where  $G_0$  is the free energy of the high symmetry phase. Apparently this expansion is valid only for small values of the order parameter, i.e., close to the transition point. For simplicity, we consider equation 2.20 up to the fourth-order term, the sign of coefficient  $A$  will determine whether it leads to a single minimum at  $\eta = 0$  or a local maximum at  $\eta = 0$ . Plot of the free energy as a function of order parameter is shown in Figure 2.2 for these two cases. If  $A > 0$ , the global minimum is at  $\eta = 0$  which corresponds to the high symmetry phase, while if  $A < 0$ , the high symmetry phase becomes energetically unstable and the system is stable at non-zero values of the order parameter ( $\pm\eta_0$ ).

In this dissertation, we have studied the pressure induced displacive phase transition from phenacite to post-phenacite phase in  $\text{Si}_3\text{N}_4$ . Because the transition is largely pressure driven, we neglect the temperature dependence of the Landau free energy. Therefore at the



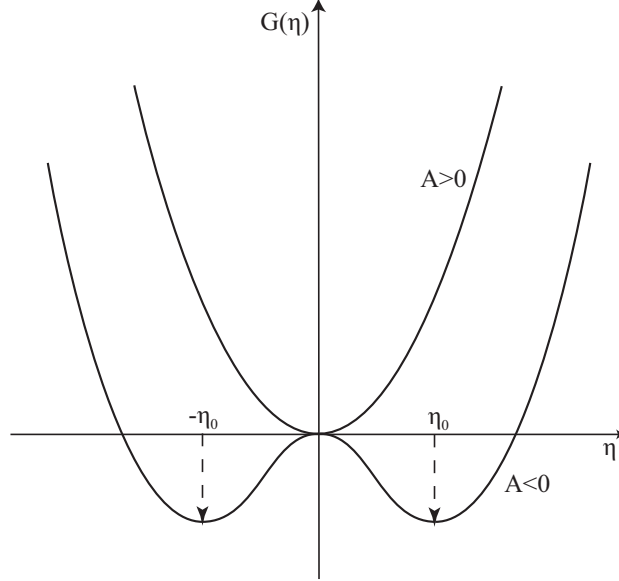


Figure 2.2: Variation of the Landau free energy with positive and negative  $A$  coefficients.

transition pressure the coefficient  $A$  changes sign, so that it is positive for the high symmetry phenacite phase below the transition pressure and is negative for the post-phenacite phase above the transition pressure. The simplest form of this condition is

$$G(P, \eta) = G_0 + a(P_t - P)\eta^2 + b\eta^4 \quad (2.21)$$

where  $a$  and  $b$  both have positive values. We assume  $A = a(P_t - P)$  where  $P_t$  is the transition pressure, and  $B = b$ . When  $P > P_t$ , the equilibrium condition  $\frac{\partial G}{\partial \eta} = 0$  leads to the non-zero value of the order parameter.

$$\eta_0 = \sqrt{\frac{a(P - P_t)}{2b}} \quad (2.22)$$

Note that the first order derivative of Gibbs free energy with respect to pressure is continuous at  $P = P_t$ .

### 2.3.2 Dynamic Lattice Stability and Soft Phonon Modes

As a phenomenological approach, Landau theory is mathematically simple and flexible as the theoretical background of many studies of phase transitions. However, from the *ab initio* simulation point of view, the new low-symmetry phase is determined from a different approach. For instance, the low-symmetry structure can be derived by relaxing the high-symmetry structure to equilibrium at the conditions where it is unstable. Usually a slight distortion is needed to break the symmetry. For phonon instability (elastic instability is less common), the distortion is a set of collective atomic displacements, which is associated with the soft phonon theory.

At finite temperature, atoms inside a solid never “freeze” at their equilibrium positions. Instead, they oscillate around their respective equilibrium positions. The atomic displacements of atoms can be analyzed in term of the vibrational normal modes. The quasi-particle representation of quantization in harmonic lattice vibration is phonon. The squares of phonon (vibrational) frequencies are normally positive. A vanishing  $\omega^2$  indicates that the restoring forces related to that normal mode disappear. The corresponding vibration is called *soft mode* or *soft phonon*. A crystal structure containing soft phonon modes are considered as dynamically unstable because atomic displacements along the eigenmode pattern will lead to a new structure with lower energy. Note that the new structure belongs to a lower symmetry whose space group is a subgroup of the original space group, and the eigenmodes of soft phonons are often adopted as the order parameters in Landau theory discussed above.

The simplest case of soft phonon modes is that only one phonon mode becomes softened. If the soft mode drops to zero at  $\Gamma$ -point (center of Brillouin zone), the periodicity of the low symmetry structure will be of the same size of unit cell as the high symmetry phase. If phonon softening happens at the zone boundary, the periodicity of the new phase will be different from the high symmetry phase. The unit cell of the low symmetry phase, in general, is a super cell of the previous primitive unit cell. The size of the super cell is determined by the symmetry of the system and the  $\mathbf{k}$ -point that has soft phonon, e.g., if the soft phonon

happens at  $X$ -point  $(1, 0, 0)$ , the new structure will have a double-sized primitive unit cell vector along  $\mathbf{a}_1$  compared to the previous phase. Real space displacements of atoms from high symmetry equilibrium sites can be obtained based on the eigenvector of the soft mode. By breaking the symmetry with atomic displacements (usually small), the low-symmetry structure can be found by relaxing the distorted high-symmetry configuration energetically at the condition that it is unstable.

In the case that more than one mode (at different  $\mathbf{k}$ -points) involve soft phonons, in principle, the real space atomic displacements that lead to the low-symmetry stable phase can be derived from a linear combination of the eigenvectors of the soft modes. In practice, we usually treat the soft phonon modes in serial. For each soft phonon, a new low-symmetry structure can be derived from total energy calculation by imposing its symmetry. In the next step, we calculate the phonon dispersion for the new phase. We repeat the process until all soft phonon modes disappear. The energetically favored structure among these stable or metastable phases is the one with the lowest energy, which can be determined from the  $E$ - $V$  curves.

## 2.4 Transition Paths of Reconstructive Phase Transitions

Many structural phase transitions in solids belong to the first-order reconstructive category, i.e., the symmetries of the two structures have no group-subgroup relation and typically bonds breaking/forming process occurs during the transition. The dynamics of reconstructive phase transitions is not yet well understood for most known solid-solid phase transitions. It is known that for some transitions of this kind, an interface forms between the initial and final phases, and atoms go through a long range diffusion process during the transformation. In our study, we examine the transformation mechanism from a different angle, assuming the initial and final structures are related by a diffusionless transition path (TP). Intermediate structures along the path can be given with a crystalline character approximately. Transition pathway studies are helpful for understanding the mechanism of transitions at a microscopic level, and predicting the kinetic barrier height of the proposed

path(s) from the energy landscape. However, there are in principle an infinite number of pathways for one structure to transform into another. If neglecting defects and surface effects that exist in reality, we assume a certain symmetry is maintained when atoms are displaced collectively along the TP. For diffusionless reconstructive transitions, it is known that the nucleation free path is defined by is a common subgroup of both end structures<sup>131–134</sup>. Although the number of common subgroups is infinite, it is possible to obtain a finite set of common subgroups with certain constrains, such as the size of unit cell, bonds preserving, maximum strains etc. Among these TPs, the energetically favorable path(s) is/are that/those associated with the lowest kinetic energy barrier(s).

From the theoretical point of view we could investigate the most possible paths and find the one(s) with the least barrier height. Stokes and Hatch have implemented a computer program called COMSUBS which systematically finds maximal common subgroups of two structures. The major constraint for COMSUBS is the bond condition, since many studies suggested that the most energetically favored TPs are those preserve the number of bonds<sup>53–55</sup>. Other constrains that affect the number of common subgroups are the minimum and maximum size of unit-cell, strain tolerance, maximum atomic displacement, minimum distance allowed between nearest neighbors, etc. This method has been adopted in the studies of B1-to-B2 transitions in sodium chloride (NaCl) and lead sulfide (PbS)<sup>135</sup>, zinc-blende to rocksalt transitions in silicon carbide (SiC)<sup>136</sup>, and wurtzite-to-rocksalt transition<sup>48</sup>.

For each possible transition path, in principle, the energy barrier height is determined by the calculated  $n$ -dimensional potential-energy surface (PES), where  $n$  is the degree of freedom of the intermediate state. For example, in the case of wurtzite-to-rocksalt transition in AlN, the degree of freedom is 6 for the  $Pna2_1$  path, i.e., there are 6 free parameters that can be adjusted independently. The complete information of the wurtzite-to-rocksalt transformation path can be revealed from a 6-dimensional PES. However, first-principles calculation of a 6D PES is not an easy task. To calculate the barrier height, two reasonable approaches have been investigated. The first approach is named as bow-function method, as adopted in the study of zinc-blende to rocksalt transition in SiC<sup>136</sup>. The first step within

this method is to calculate the enthalpy along a linear TP. Here “linear” means that all the structural parameters, including both external parameters (lattice parameters) and internal coordinates, vary according to a single transition parameter.

$$x_m = (1 - \xi) x_{mi} + \xi x_{mf} \quad (2.23)$$

where  $\xi$  is the transition parameter which varies from 0 to 1,  $x_{mi}$  and  $x_{mf}$  are the initial and final  $m^{th}$  structural parameter, respectively. In many cases we have studied, the peak of the barrier height locates at around  $\xi = 0.5$ . In this way, although we obviously overestimate the enthalpy barrier, it is efficient for eliminating some TPs that give much larger barriers. With the number of TPs being reduced, we further develop a numerical algorithm to possibly lower the barrier height. On the basis of previous linear TP, we assume the saddle point (which gives the enthalpy barrier height) of the “true” TP is not far from the maximum point of the linear one. By adding a quadratic term to equation 2.23 we change the linear function to a bow function.

$$x_m = (1 - \xi) x_{mi} + \xi x_{mf} + w_m \xi (1 - \xi) \quad (2.24)$$

where  $w_m$  is the “weight” of the bow function for the  $m^{th}$  structural parameter. Then we minimize the enthalpy barrier height with respect to  $w_m$ . This is done by searching for the lowest height of the peak with different weights (positive or negative) for each structural parameter. If more than one peak are present, we will track the highest peak across the entire TP. If the change on  $w_m$  decreases the barrier height, we keep the change, otherwise we undo the change. This process is done when no changes on  $w_m$  will further lower the height of the peak. At this situation, saddle point of the true TP is found and so for the true barrier height. We should stress that our aim is to find the barrier height and our proposed TP only matches the saddle point and two end points of the true TP. The quadratic bow function that links these three points is generally different from the true TP.

However, the bow-function algorithm may fail if the landscape of the enthalpy function is complex, e.g., if the saddle point is surrounded by peaks and the true path is off the linear path, the barrier height found by bow function can be higher than the saddle point. In all the concerns our estimated enthalpy barrier height will always be an upper limit compared to the true barrier.

Besides the bow function method, sometimes a reconstructive phase transition can be characterized by only a few structural parameters. In this case a proper choice of the structural parameter is essential. Other “unimportant” parameters will be fully relaxed during the DFT calculation. In the simplest case, if only one structural parameter is primarily responsible during the transition, the transition parameter is defined based on the changes of this parameter. If two equally important structural parameters both cause significant changes in enthalpy from one structure to the other, we can calculate the enthalpies as a function of two transition parameters (a 2D PES). Calculations involve more than two transition parameters can be cumbersome in the sense of both computational load and analysis.

Let’s take the single parameter case as an example to illustrate the procedure of transition pathway calculations. The particular structural parameter can be found either by comparison of two end structures or by a testing calculation as follows. If we choose the transition parameter at values which are uniform samplings between two end phases (equation 2.23), the saddle point normally locates at  $\xi = 0.5$  or nearby (this testing is not applicable to the case where a metastable state exists around  $\xi = 0.5$ ). A series of total energy calculation can be done by fixing only one structural parameter at a time and fully relaxing the others starting with  $\xi = 0.5$ . If the parameter we fixed is unimportant, the resulting energy will be close to the energy of one end phase, whereas the important structural parameter will yield an energy apparently different from the end phases. Next we sample the transition parameter in the  $[0, 1]$  region and calculate the energies at each sampling point by fixing the chosen parameter and relaxing the other parameters. To get the enthalpy under a given pressure, we perform the energy calculations at several volume

points and obtain the enthalpy based on the equation of states,  $H = E + PV$ . Finally a relative enthalpy as a function of transition parameter can be plotted and the barrier height is estimated from that. We emphasize that the calculated barrier height is approximate and should be understood as an upper limit of the true one.

For technical reason, it is easy to fix the internal parameter(s), however, difficult to do so for the external ones. So the second approach currently only works for transitions that characterized by changes in the internal structural parameter(s).

CHAPTER 3  
FIRST-PRINCIPLES CALCULATIONS OF THERMODYNAMIC  
PROPERTIES OF CRYSTALS

### 3.1 First-Principles Total Energy Theory

#### 3.1.1 Density Functional Theory (DFT)

Atomic-scale theory and simulation of solids rely on accurate evaluation of the total energy of an N-atom system with a specified atomic configuration. Many theories, evolving from simple empirical models in early years to quantum Monte Carlo method, have been developed to estimate the total electronic energy of a given system. Benefiting from the increasing power of computational technology and to our purpose, in this study, we adopt *density functional theory* (DFT). DFT is one of the most successful first-principles quantum mechanical theories for atoms, molecules and solids. Nowadays, DFT calculations are routinely performed in the fields of materials physics and chemistry.

In quantum mechanics, a system is described by the wave function  $\Psi$  of its Hamiltonian. Within Born-Oppenheimer approximation<sup>137</sup> (adiabatic approximation), one assumes that the electrons are in their ground state for the instantaneous ionic configuration at any moment. Therefore, we are able to treat ionic motion with classical mechanics, and only the electronic Hamiltonian is treated with quantum mechanics. A stationary electronic state of a N-electron Hamiltonian is described by a wave function  $\Psi(\mathbf{r}_1, \dots, \mathbf{r}_N)$  satisfying the Schrödinger equation:

$$\hat{H}\Psi = \left[ \hat{T} + \hat{V} + \hat{U} \right] \Psi = \left[ \sum_i^N -\frac{\hbar^2}{2m} \nabla_i^2 + \sum_i^N v(\mathbf{r}_i) + \sum_{i<j} U(\mathbf{r}_i, \mathbf{r}_j) \right] \Psi = E\Psi \quad (3.1)$$



where  $U(\mathbf{r}_i, \mathbf{r}_j)$  is the electron-electron coulomb interaction. Exact solution to this Schrödinger equation even for a system with 100 atoms is computationally forbidden. DFT provides an exact way to map the many-body problem onto an effective single-body problem. This is done by replacing the many-body electronic wavefunction with the electron density as the basic quantity.

The predecessor to DFT is the simple Thomas-Fermi model<sup>138</sup> which neglects the exchange and correlation energy. Hohenberg and Kohn<sup>119</sup> proved two celebrated theorems (HK theorems) stating that (1) the nondegenerate ground-state wave function is a unique functional of the ground-state electron density and (2) the ground-state electron density minimizes the total energy of the system. According to HK theorems, the system's wavefunction only depends on the particle density which is a function of three spatial variables whereas a many-body wavefunction is dependent on  $3N$  variables (three degrees of freedom for each of the  $N$  electrons). Since the electron density  $n(\mathbf{r})$  is given by:

$$n(\mathbf{r}) = N \int d^3r_2 \int d^3r_3 \cdots \int d^3r_N \Psi^*(\mathbf{r}, \mathbf{r}_2, \dots, \mathbf{r}_N) \Psi(\mathbf{r}, \mathbf{r}_2, \dots, \mathbf{r}_N) \quad (3.2)$$

The ground-state wavefunction is a unique functional of  $n_0$ , i.e.,  $\Psi_0 = \Psi_0[n_0]$ . Thus all the observables are also functionals of  $n_0$ , in particular the ground-state energy.

$$E_0 = E[n_0] = \langle \Psi_0[n_0] | \hat{T} + \hat{V} + \hat{U} | \Psi_0[n_0] \rangle \quad (3.3)$$

In practice, for a specific system ( $v(\mathbf{r})$  is known), all one need to do is to minimize the sum of kinetic, potential and interaction energies.

$$E_v[n] = T[n] + U[n] + V[n] = T[n] + U[n] + \int d^3r n(\mathbf{r})v(\mathbf{r}) \quad (3.4)$$

Exact form of  $E[n]$  functional is unknown. Most commonly adopted approach in DFT is the Kohn-Sham method<sup>120</sup>. The kinetic energy functional of interacting electrons  $T[n]$

can be treated as a summation of two parts.

$$T[n] = T_S[n] + T_C[n] \quad (3.5)$$

where  $S$  and  $C$  represent “single-particle” and “correlation”.  $T_S[n]$  is the kinetic energy density functional of noninteracting particles and  $T_C[n]$  is the remainder.  $T_S[n]$  is an explicit function of the single-particle wavefunctions  $\phi_i(\mathbf{r})$ , where  $\phi_i(\mathbf{r})$  is a density functional, so  $T_S[n]$  is an implicit functional of the electron density.

$$T_S[n] = T_S[\{\phi_i[n]\}] \quad (3.6a)$$

$$T_S[n] = -\frac{\hbar^2}{2m} \sum_i^N \int d^3r \phi_i^*(\mathbf{r}) \nabla^2 \phi_i(\mathbf{r}) \quad (3.6b)$$

Without any approximation, the energy can be written as:

$$E[n] = T[n] + U[n] + V[n] = T_S[\{\phi_i[n]\}] + U_H[n] + E_{xc}[n] + V[n] \quad (3.7)$$

where  $U_H = \frac{q^2}{2} \int d^3r \int d^3r' \frac{n(\mathbf{r})n(\mathbf{r}')}{|\mathbf{r}-\mathbf{r}'|}$ , which is the electrostatic interacting Hartree energy of the charge distribution  $n(\mathbf{r})$ . And  $E_{xc}[n]$  is the exchange-correlation ( $xc$ ) energy which has contributions from  $T - T_S$  and  $U - U_H$ . This term can be decomposed as  $E_{xc} = E_x + E_c$ , where  $E_x$  is the exchange energy due to Pauli principle and  $E_c$  is the correlation energy. An effective potential energy can be defined as:

$$V_S(\mathbf{r}) = V(\mathbf{r}) + U_H(\mathbf{r}) + E_{xc}(\mathbf{r}) \quad (3.8)$$

Consequently, the Schrödinger equation is:

$$\left[ -\frac{\hbar^2}{2m} \nabla^2 + V_S(\mathbf{r}) \right] \phi_i(\mathbf{r}) = \epsilon_i \phi_i(\mathbf{r}) \quad (3.9)$$

By solving the charge density of this equation of noninteracting single-body system in potential  $V_S(\mathbf{r})$ , one can obtain the density of the interacting many-body system in

potential  $V(\mathbf{r})$ .

$$n(\mathbf{r}) = n_S(\mathbf{r}) = \sum_i^N f_i |\phi_i(\mathbf{r})|^2 \quad (3.10)$$

where  $f_i$  is the occupation of the  $i^{\text{th}}$  orbital.

The above three equations are called Kohn-Sham (KS) equations. The purpose of KS equations is to solve a noninteracting Schrödinger equation to replace the problem of minimizing the total energy  $E[n]$ . With an initial guess of the density  $n(\mathbf{r})$ , an iterative process is performed until convergence is reached (e.g., convergence in energy, density, or some other observables). In numerical calculations, the KS orbital is typically expanded using a set of basis functions. There are different ways to construct a suitable basis function. Our DFT based calculations are implemented in the Vienna *ab initio* Simulation Package (VASP)<sup>139</sup>, which uses a planewave expansion<sup>140,141</sup>.

Because the core electrons are bounded to the nuclei and their orbitals typically do not change much, it is a good approximation that the Hartree and  $xc$  terms in  $V_S(\mathbf{r})$  are evaluated only for the valence electron density  $n_v$ , and the core electrons are treated with a pseudopotential (PP)  $V_{ext}^{PP}$ . The pseudopotentials that are adopted in our VASP calculations are Vanderbilt Ultra-Soft Pseudopotentials (US-PP)<sup>121,142</sup> or Projector Augmented Wave (PAW)<sup>143,144</sup> method.

Further approximation is needed to evaluate the exchange-correlation functional  $E_{xc}[n]$ . Unless stated otherwise, this study is performed with local density approximation (LDA)<sup>145,146</sup> which is a local functional. A semilocal, gradient dependent functional, generalized gradient approximation (GGA)<sup>147–151</sup> is sometimes used as a comparison.

## 3.2 Statistical Theory of Bulk Crystals

### 3.2.1 Phonon Theory of Lattice Dynamics

Equilibrium positions of atoms in a crystal are determined by the minimum total energy. However, the atoms are not fixed at their equilibrium positions. Because the interatomic chemical bonds are not infinitely strong, nor do the atoms have infinite masses,

the atoms may oscillate about their equilibrium locations at a finite temperature. According to statistical mechanics, the equilibrium energy at a given temperature is the ensemble average over all the possible atomic configurations of the system. If we denote by  $E_i$  the static energy of the  $i^{\text{th}}$  stationary configuration of the crystal and  $\beta = 1/k_B T$ , the total energy can be written as:

$$E = \frac{\sum_i E_i e^{-\beta E_i}}{\sum_i e^{-\beta E_i}} \quad (3.11)$$

However, exact evaluation of the total energy is a formidable task. Here we make two assumptions which are valid for most crystals at equilibrium conditions below melting temperature:

1. We assume the mean equilibrium position of each atom is a Bravais lattice site and the atom oscillates about this position.
2. We assume the deviation from the equilibrium position is small compared with the interatomic distance.

The potential energy of a crystal is a function of the instantaneous atomic positions. If we let  $u_{\alpha,i}(\ell)$  denote the  $\alpha$  cartesian component of the displacement of the  $i^{\text{th}}$  atom in the  $\ell^{\text{th}}$  primitive unit cell ( $\mathbf{x}(\ell) = \ell_1 \mathbf{a}_1 + \ell_2 \mathbf{a}_2 + \ell_3 \mathbf{a}_3$ , where  $\ell$  collectively denotes  $\ell_1, \ell_2$  and  $\ell_3$ ) from its equilibrium position, under the two assumptions, we may expand the potential energy in power series of these components:

$$\begin{aligned} V = & V_0 + \sum_{\ell,i,\alpha} \left( \frac{\partial V}{\partial u_{\alpha,i}(\ell)} \right)_0 u_{\alpha,i}(\ell) \\ & + \frac{1}{2} \sum_{\ell,i,\alpha} \sum_{\ell',j,\beta} \left( \frac{\partial^2 V}{\partial u_{\alpha,i}(\ell) \partial u_{\beta,j}(\ell')} \right)_0 u_{\alpha,i}(\ell) u_{\beta,j}(\ell') \\ & + \frac{1}{6} \sum_{\ell,i,\alpha} \sum_{\ell',j,\beta} \sum_{\ell'',k,\gamma} \left( \frac{\partial^3 V}{\partial u_{\alpha,i}(\ell) \partial u_{\beta,j}(\ell') \partial u_{\gamma,k}(\ell'')} \right)_0 u_{\alpha,i}(\ell) u_{\beta,j}(\ell') u_{\gamma,k}(\ell'') \\ & + \dots \end{aligned} \quad (3.12)$$

In this expansion,  $V_0$  is the potential energy of the static crystal when all the atoms are at their equilibrium positions. The subscript “0” indicates that the derivatives are evaluated with atoms at the equilibrium positions. Since there is no net force on any atom in the equilibrium configuration, the first order derivative  $\left(\frac{\partial V}{\partial u_{\alpha,i}(\ell)}\right)_0$  vanishes and the second term in the expansion is zero. It will be convenient to use different symbols to replace those derivatives as follows:

$$\Phi_{\alpha i, \beta j}(\ell, \ell') = \left( \frac{\partial^2 V}{\partial u_{\alpha,i}(\ell) \partial u_{\beta,j}(\ell')} \right)_0 \quad (3.13a)$$

$$A_{\alpha i, \beta j, \gamma k}(\ell, \ell', \ell'') = \left( \frac{\partial^3 V}{\partial u_{\alpha,i}(\ell) \partial u_{\beta,j}(\ell') \partial u_{\gamma,k}(\ell'')} \right)_0 \quad (3.13b)$$

$$B_{\alpha i, \beta j, \gamma k, \lambda l}(\ell, \ell', \ell'', \ell''') = \left( \frac{\partial^4 V}{\partial u_{\alpha,i}(\ell) \partial u_{\beta,j}(\ell') \partial u_{\gamma,k}(\ell'') \partial u_{\lambda,l}(\ell''')} \right)_0 \quad (3.13c)$$

The first nonvanishing contribution to the constant equilibrium static potential energy is the quadratic term and this is the only term being kept in the harmonic approximation. Those higher order terms are known as anharmonic terms which are considerably responsible for many physical properties. Typically they are treated as perturbations to the dominant harmonic term. If we denote  $p_{\alpha,i}(\ell)$  the  $\alpha$  cartesian component of the momentum of the  $i^{th}$  atom in the  $\ell^{th}$  primitive unit cell and  $m_i$  is the mass of the  $i^{th}$  atom in the primitive unit cell, the total kinetic energy of the system is:

$$T = \sum_{\ell, i, \alpha} \frac{p_{\alpha,i}^2(\ell)}{2m_i} \quad (3.14)$$

Consequently the vibrational Hamiltonian can be written as:

$$H = H_0 + H_A \quad (3.15)$$

where

$$H_0 = \sum_{\ell, i, \alpha} \frac{p_{\alpha, i}^2(\ell)}{2m_i} + \frac{1}{2} \sum_{\ell, i, \alpha} \sum_{\ell', j, \beta} \Phi_{\alpha i, \beta j}(\ell, \ell') u_{\alpha, i}(\ell) u_{\beta, j}(\ell') \quad (3.16a)$$

$$H_A = \sum_{n=3}^{\infty} \frac{1}{n!} \sum_{\ell_1, i_1, \alpha_1} \cdots \sum_{\ell_n, i_n, \alpha_n} \left( \frac{\partial^n V}{\partial u_{\alpha_1, i_1}(\ell_1) \cdots \partial u_{\alpha_n, i_n}(\ell_n)} \right)_0 u_{\alpha_1, i_1}(\ell_1) u_{\alpha_n, i_n}(\ell_n) \quad (3.16b)$$

The Hamiltonian  $H_0$  is the harmonic part of the vibrational Hamiltonian. The Hamiltonian  $H_A$  is the anharmonic part of the vibrational Hamiltonian. In the harmonic approximation, the anharmonic contribution has been neglected. In order to solve the vibrational energy, it is convenient to introduce the normal coordinates.

$$Q_{\xi}(\mathbf{q}) = \frac{1}{\sqrt{N}} \sum_{\ell, i, \alpha} \sqrt{m_i} e_{\alpha, i}^*(\mathbf{q}, \xi) \cdot u_{\alpha, i}(\ell) e^{-i\mathbf{q} \cdot \mathbf{x}(\ell)} \quad (3.17)$$

$$P_{\xi}(\mathbf{q}) = \frac{1}{\sqrt{N}} \sum_{\ell, i, \alpha} \frac{1}{\sqrt{m_i}} e_{\alpha, i}(\mathbf{q}, \xi) \cdot p_{\alpha, i}(\ell) e^{i\mathbf{q} \cdot \mathbf{x}(\ell)}$$

where  $\xi = 1, 2, \dots, 3n$  that labels the index of branch and  $n$  is the number of atoms in a primitive unit cell.  $N$  is the total number of atoms in the crystal.  $\mathbf{q}$  is the wave vector in the reciprocal space and it has  $s$  discrete values which is the number of primitive unit cells in the crystal ( $n \cdot s = N$ ). Usually a bulk crystal consists of a very large number of primitive unit cells which allows  $\mathbf{q}$  to change quasi-continuously. And  $e_{\alpha, i}(\mathbf{q}, \xi)$  is the  $\alpha$  cartesian component of the eigenvector of the  $i^{\text{th}}$  atom at reciprocal space point  $\mathbf{q}$  from the  $\xi^{\text{th}}$  branch. It has the property as follows:

$$\sum_{i, \alpha} e_{\alpha, i}(\mathbf{q}, \xi) \cdot e_{\alpha, i}^*(\mathbf{q}, \eta) = \delta_{\xi\eta} \quad (3.18)$$

Derivation shows that with normal coordinates the kinetic energy and the harmonic potential energy can be expressed as summations of square terms, which transform the

Hamiltonian  $H_0$  into the Hamiltonian of  $3n$  independent harmonic oscillators.

$$H_0 = \frac{1}{2} \sum_{\xi} P_{\xi}^2(\mathbf{q}) + \frac{1}{2} \sum_{\xi} \omega_{\xi}^2(\mathbf{q}) Q_{\xi}^2(\mathbf{q}) \quad (3.19)$$

where  $\omega_{\xi}(\mathbf{q})$  is determined by solving the following secular equation

$$\sum_{j,\beta} D_{\alpha i, \beta j}(\mathbf{q}) \cdot e_{\beta, j}(\mathbf{q}, \xi) = \omega_{\xi}^2(\mathbf{q}) \cdot e_{\alpha, i}(\mathbf{q}, \xi) \quad (3.20)$$

In equation 3.20  $\mathbf{D}(\mathbf{q})$  is often called dynamical matrix which can be obtained from the real space force constant matrix.

$$D_{\alpha i, \beta j}(\mathbf{q}) = \frac{1}{\sqrt{m_i m_j}} \sum_{\mathbf{h}} \Phi_{\alpha i, \beta j}(0, \mathbf{h}) \cdot e^{-i\mathbf{q} \cdot \mathbf{h}} \quad (3.21)$$

where  $\mathbf{h} = \mathbf{x}(\ell') - \mathbf{x}(\ell)$ . Without losing generality, it is convenient to set  $\mathbf{x}(\ell)$  as the reference lattice point. The vibrational frequency  $\omega$  is a function of the wave vector  $\mathbf{q}$  and this dependence is often called the dispersion relation. For each  $\mathbf{q}$ , there are  $3n$  normal modes, and the normal modes are identical for wave vectors differ by reciprocal lattice vectors. For crystals have one atom in its primitive unit cell ( $n = 1$ ), only three acoustic modes exist. Otherwise ( $n \geq 2$ ) there are three acoustic modes and  $3n - 3$  optical modes.

Within the harmonic approximation, the hamiltonian is expressed as  $3N$  independent oscillators, whose energy levels are well known in quantum mechanics. The total vibrational energy is simply the summation of the energies of individual oscillators

$$E_{vib} = \sum_{\mathbf{q}\xi} \left( n_{\xi}(\mathbf{q}) + \frac{1}{2} \right) \hbar \omega_{\xi}(\mathbf{q}) \quad (3.22)$$

where  $n_{\xi}(\mathbf{q})$  is the occupation number of the normal mode, which takes the values of  $0, 1, 2, \dots$ .  $\frac{1}{2} \hbar \omega_{\xi}(\mathbf{q})$  is the zero-point vibrational energy of the normal mode. And equivalently, one usually says there are  $n_{\xi}(\mathbf{q})$  phonons with wave vector  $\mathbf{q}$  in the  $\xi$  branch instead

of the  $n_\xi(\mathbf{q})^{th}$  excited state of the normal mode. Using equation 3.11, one can show that

$$n_\xi(\mathbf{q}) = \frac{1}{e^{\beta\hbar\omega_\xi(\mathbf{q})} - 1} \quad (3.23)$$

The calculation of phonon dispersion relation is the major part of our computation and is necessary to further study the thermodynamic properties. Our techniques of calculating the phonon dispersion and the corresponding vibrational density of state are described in the next subsection.

### 3.2.2 Statistical Harmonic Approximation

We have discussed the equilibrium vibrational energy of a harmonic crystal in Section 3.2.1. Based on statistical ensemble theory, the canonical partition function is  $Z = \sum_i e^{-\beta E_i}$  where  $i$  represent any possible state of the system. The total energy within harmonic approximation is:

$$E = E_0 + \sum_{\mathbf{q}\xi} \left( n_\xi(\mathbf{q}) + \frac{1}{2} \right) \hbar\omega_\xi(\mathbf{q}) \quad (3.24)$$

where  $E_0$  is the static equilibrium energy and the second term is the vibrational energy which has been shown earlier in equation 3.22. Thus the partition function can be written as:

$$\begin{aligned} Z &= \sum_{n_\xi(\mathbf{q})=0}^{\infty} e^{-\beta \left( E_0 + \sum_{\mathbf{q}\xi} \left( n_\xi(\mathbf{q}) + \frac{1}{2} \right) \hbar\omega_\xi(\mathbf{q}) \right)} \\ &= e^{-\beta E_0} \prod_{\mathbf{q}\xi} \left( \sum_{n_\xi(\mathbf{q})=0}^{\infty} e^{\beta \left( n_\xi(\mathbf{q}) + \frac{1}{2} \right) \hbar\omega_\xi(\mathbf{q})} \right) \\ &= e^{-\beta E_0} \prod_{\mathbf{q}\xi} \frac{e^{\frac{1}{2}\beta\hbar\omega_\xi(\mathbf{q})}}{e^{\beta\hbar\omega_\xi(\mathbf{q})} - 1} \end{aligned} \quad (3.25)$$



From the partition function, we can further derive all the thermodynamic potentials and their derivatives which are measurable thermal properties.

$$E = -\frac{\partial \ln Z}{\partial \beta} = E_0 + \sum_{\mathbf{q}\xi} \frac{1}{2} \hbar \omega_{\xi}(\mathbf{q}) + \sum_{\mathbf{q}\xi} \frac{\hbar \omega_{\xi}(\mathbf{q})}{e^{\beta \hbar \omega_{\xi}(\mathbf{q})} - 1} \quad (3.26a)$$

$$F = -k_B T \ln Z = E_0 + \sum_{\mathbf{q}\xi} \left[ \frac{1}{2} \hbar \omega_{\xi}(\mathbf{q}) + k_B T \ln \left( 1 - e^{-\frac{\hbar \omega_{\xi}(\mathbf{q})}{k_B T}} \right) \right] \quad (3.26b)$$

$$S = -\left( \frac{\partial F}{\partial T} \right)_V \quad (3.26c)$$

In equation 3.26, summation over all the  $\mathbf{q}$  points and phonon branches is needed to evaluate each thermal quantity. Although the  $\mathbf{q}$  points in principle take discrete values, the typical size of a real crystal consists of a great number of primitive unit cells, which will make the  $\mathbf{q}$  points quasi-continues. Using the concept of phonon density of state (DOS), the Helmholtz free energy can be calculated from the Brillouin zone integration

$$F(T, V) = E_0(V) + \int_0^{\infty} \left[ \frac{1}{2} \hbar \omega_{\xi}(\mathbf{q}) + k_B T \ln \left( 1 - e^{-\frac{\hbar \omega_{\xi}(\mathbf{q})}{k_B T}} \right) \right] g(\omega) d\omega \quad (3.27)$$

where  $g(\omega)$  is the phonon DOS. There is an upper limit of the phonon frequencies, above which the phonon DOS is zero. As a good approximation, we can also evaluate the vibrational free energy as a summation and being normalized to a primitive unit cell if the  $\mathbf{q}$  point sampling is dense enough.

$$F_{vib} = \frac{1}{N_{\mathbf{q}}} \sum_{\mathbf{q}\xi} \left[ \frac{1}{2} \hbar \omega_{\xi}(\mathbf{q}) + k_B T \ln \left( 1 - e^{-\frac{\hbar \omega_{\xi}(\mathbf{q})}{k_B T}} \right) \right] \quad (3.28)$$

### 3.2.3 First-Principles Phonon Calculations

In *ab initio* calculations, there are basically two approaches to obtain the phonon spectrum, namely the *linear response theory*<sup>152–154</sup> (density-functional perturbation theory, DFPT) and the *direct method*. The DFPT approach assumes that the interatomic force-constant matrix is determined by the linear response of electron density to the periodic

lattice perturbation. The dynamical matrix may be obtained from the inverse dielectric matrix. The major advantage of DFPT method is one can calculate phonon frequencies at arbitrary  $\mathbf{q}$  point without using supercell. It also directly provides the *Born effective charge* (BEC) and dielectric constant which are necessary in predicting the LO-TO splitting for ionic crystals. However, The implementation of DFPT calculation requires complex coding and the dielectric matrix is obtained from the eigenfunctions and eigenvalues of the unperturbed system, which demands summations over unoccupied conduction bands. The computational cost for DFPT calculation is in the order of  $3N^4 \times R_{IFC}^3$ , where  $N$  is the number of atoms and  $R_{IFC}$  is the range of interatomic force constants.

The direct approach falls into two classes. In *frozen-phonon* method<sup>155</sup>, the phonon frequencies can be calculated from energy differences between displaced system and relaxed system. This method is limited as wave vector  $\mathbf{q}$  must be the reciprocal lattice vector of the supercell, but too large supercell is not computationally affordable. Our calculations belong to another method of the direct approach: a first-principles real-space supercell force-constant (SC-FC) method which calculates the phonon frequencies from the forces obtained via the Hellmann-Feynman theorem. This technique is proved to be efficient and successful in predicting the full phonon spectrum of many materials<sup>122-129</sup>. The major limitation of this method comes from the range of the interatomic force constants  $R_{IFC}$ . This type of error can be reduced by using a large supercell. The computational cost of a complete interatomic force constants calculation is in the order of  $N \times R_{IFC}^9$ . For systems with a relatively small  $R_{IFC}$ , SC-FC method will be efficient by using a suitable size of supercell to balance the accuracy and computational workload. To predict the phonon dispersion for ionic solids, which involves induced Born effective charges  $Z^*$  due to lattice vibration, a separate calculation proposed by Kunc and Martin<sup>156</sup> need to be performed to take care of the LO-TO splitting as a correction.

Start from here I will describe the detailed procedure of our phonon calculation. Within this subsection, we are restricted to the harmonic approximation. At a fixed volume, a relaxed structure model is provided by the previous static total energy calculation, i.e., no

net force on each atom at this configuration. Then a finite small displacement is made to a single atom and all the atomic positions are not allowed to change. According to Hellmann-Feynman theorem,  $\alpha$  component of the force on the  $i^{th}$  atom in the  $\ell^{th}$  unit cell is:

$$F_{\alpha,i}(\ell) = -\frac{\partial E}{\partial u_{\alpha,i}(\ell)} = -\left\langle \Psi \left| \frac{\partial H}{\partial u_{\alpha,i}(\ell)} \right| \Psi \right\rangle \quad (3.29)$$

where  $H$  is the total hamiltonian and  $\Psi$  is the electronic ground-state wavefunction. In the Born-Oppenheimer approximation, ionic displacement is the parameter. Assuming the amount of single displacement is  $\Delta$ , using equation 3.16 and keeping up to the  $4^{th}$  order term in the hamiltonian expansion, the Hellmann-Feynman (H-F) forces is

$$F_{\alpha,i}(\ell) = -\Phi_{\alpha i, \beta j}(\ell, \ell') \cdot \Delta - \frac{1}{2} A_{\alpha i, \beta j, \gamma k}(\ell, \ell', \ell'') \cdot \Delta^2 - \frac{1}{6} B_{\alpha i, \beta j, \gamma k, \lambda l}(\ell, \ell', \ell'', \ell''') \cdot \Delta^3 \quad (3.30)$$

Note that all the other atoms are held in their equilibrium positions. The reason to keep up to the  $4^{th}$  order term is to better estimate the harmonic force constant  $\Phi_{\alpha i, \beta j}(\ell, \ell')$  from the first-principles calculated H-F forces. A simple displacement scheme is applied in order to eliminate the anharmonic terms. If we calculate the H-F forces for the  $j^{th}$  atom deviates in the  $\beta$  direction by  $\Delta$  from its equilibrium position, we also do calculations with the displacements of  $-\Delta$ ,  $2\Delta$ , and  $-2\Delta$ , where the negative sign implies the displacement is in the opposite direction. Provided an label to each of the four forces, we have

$$\left\{ \begin{array}{l} F_{\alpha,i}^+(\ell) = -\Phi_{\alpha i, \beta j}(\ell, \ell') \cdot \Delta - \frac{1}{2} A_{\alpha i, \beta j, \gamma k}(\ell, \ell', \ell'') \cdot \Delta^2 - \frac{1}{6} B_{\alpha i, \beta j, \gamma k, \lambda l}(\ell, \ell', \ell'', \ell''') \cdot \Delta^3 \\ F_{\alpha,i}^-(\ell) = \Phi_{\alpha i, \beta j}(\ell, \ell') \cdot \Delta - \frac{1}{2} A_{\alpha i, \beta j, \gamma k}(\ell, \ell', \ell'') \cdot \Delta^2 + \frac{1}{6} B_{\alpha i, \beta j, \gamma k, \lambda l}(\ell, \ell', \ell'', \ell''') \cdot \Delta^3 \\ F_{\alpha,i}^{2+}(\ell) = -2\Phi_{\alpha i, \beta j}(\ell, \ell') \cdot \Delta - 2A_{\alpha i, \beta j, \gamma k}(\ell, \ell', \ell'') \cdot \Delta^2 - \frac{4}{3} B_{\alpha i, \beta j, \gamma k, \lambda l}(\ell, \ell', \ell'', \ell''') \cdot \Delta^3 \\ F_{\alpha,i}^{2-}(\ell) = 2\Phi_{\alpha i, \beta j}(\ell, \ell') \cdot \Delta - 2A_{\alpha i, \beta j, \gamma k}(\ell, \ell', \ell'') \cdot \Delta^2 + \frac{4}{3} B_{\alpha i, \beta j, \gamma k, \lambda l}(\ell, \ell', \ell'', \ell''') \cdot \Delta^3 \end{array} \right. \quad (3.31)$$

It is straightforward to show that

$$\Phi_{\alpha i, \beta j}(\ell, \ell') = \frac{-8F_{\alpha,i}^+(\ell) + 8F_{\alpha,i}^-(\ell) + F_{\alpha,i}^{2+}(\ell) - F_{\alpha,i}^{2-}(\ell)}{12\Delta} \quad (3.32)$$

We currently use a simplified version to calculate the FC matrix that we ignore the typically small 4<sup>th</sup> order term and cancel all the odd order anharmonic terms.

$$\Phi_{\alpha i, \beta j}(\ell, \ell') \approx -\frac{1}{2} \left( \frac{F_{\alpha, i}^+(\ell)}{\Delta} + \frac{F_{\alpha, i}^-(\ell)}{-\Delta} \right) \quad (3.33)$$

In this way we can further reduce the computational cost by half. If each atom needs to be displaced in one direction (including positive and negative directions) by 4 times, i.e., 4 total energy calculations, a supercell with  $N$  atoms requires  $12N$  calculations. The typical size of the supercell in phonon calculation is in the order of  $\sim 100$  atoms. However, the number of direct calculations can be greatly reduced based on the crystal symmetry.

First we go through the full point group operations and possible gliding vectors to find all the spacegroup symmetry operations for a fully relaxed crystal structure (code *FindSG.x*). Then an one-on-one mapping is established to find the independent and dependent atoms (code *Find1on1.x*). The mapping and operations relate them are saved in the file named as *1on1map.dat*. The next code is called *FindIR.x* which reads in *1on1map.dat* and find the irreducible directions of independent atoms. We call it “moves” to specify which atom to displace, in which direction to displace, and by what amount. It should be mentioned that the direction of displacement can be in terms of either the cartesian coordinates or the primitive unit vectors which is called “direct” format. We also save the information to obtain the H-F forces of the dependent moves from the results of the independent ones.

In our calculations an absolute amount of  $\Delta = 0.015 \text{ \AA}$  is usually chosen for cartesian moves and a relative amount of  $\Delta = 0.002$  for direct moves. The amount of displacement should be applied with care. Too large deviation will include more anharmonic effect while too small deviation may worsen the results due to numerical errors. For the irreducible moves, the H-F forces are calculated directly and the corresponding FC matrix elements are derived from these forces. For other reducible moves, the FC matrix element can be obtained by applying the one-on-one spacegroup symmetry operation to the irreducible

ones. Both cartesian and direct transformation matrices are saved so we can handle either case. With the fully reconstructed FC matrix, we can get the dynamical matrix based on equation 3.21. Note that in equation 3.21, the subscript of the phase factor is  $-i\mathbf{q}\cdot\mathbf{h}$ , where  $\mathbf{h}$  is the difference of real-space lattice vectors. Another implementation is by using the phase factor of  $e^{-i\mathbf{q}\cdot(\mathbf{x}_j(\mathbf{h})-\mathbf{x}_i(0))}$  where  $\mathbf{x}_i(0)$  and  $\mathbf{x}_j(\mathbf{h})$  are the positions of the  $i^{th}$  atom in the reference primitive unit cell and the  $j^{th}$  atom in the primitive unit cell with a lattice vector  $\mathbf{h}$  relative to the reference unit cell, respectively. These two variants are equivalent with a difference in the phase factor. The corresponding dynamical matrices are related by a unitary transformation so that there is no influence on the phonon frequencies.

By solving the secular equation 3.20, phonon frequencies at arbitrary  $\mathbf{q}$  point can be calculated. To illustrate the dispersion relation, the  $\mathbf{q}$  points are generated along some high symmetry directions. The frequency changes in certain LO modes caused by BEC in the lattice vibration will be further considered for ionic crystals.

Phonon density of state (DOS) is imperative for Brillouin zone integrations. We adopted the tetrahedron method<sup>157,158</sup> for DOS calculation. Using a uniformly generated coarse grids in the reciprocal space, we calculate the phonon frequencies at these  $\mathbf{q}$  points. In the tetrahedron method, the first Brillouin zone is divided into small tetrahedrons and density of state is evaluated within each tetrahedron. The integration of DOS over the full phonon spectrum is normalized to  $3n$  where  $n$  is the number of atoms per primitive unit cell. Figure 3.1 is an example of our calculated phonon dispersion and density of state, together with experimental data as a comparison.

### 3.3 Thermodynamic Properties

#### 3.3.1 Quasi-Harmonic Approximation

Many properties of real crystals, such as thermal expansion and transport properties, can only be explained with lattice anharmonicity. If the real crystal is purely harmonic, the phonon frequencies will be the same at any volume, which is not the case. To illustrate the

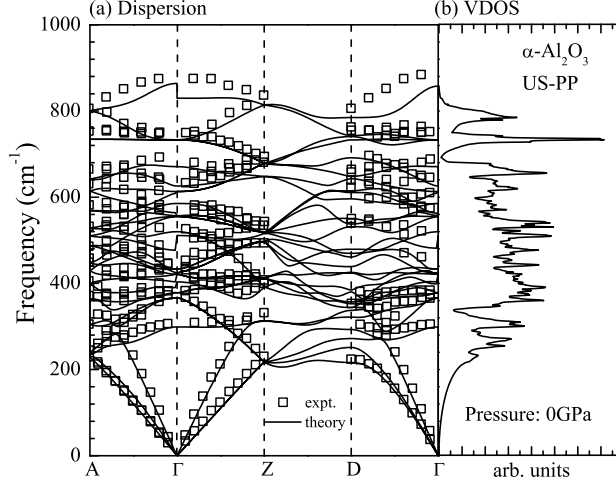


Figure 3.1: LDA (with US-PP) calculated (a) phonon dispersion relation, (b) vibrational density of states of  $\alpha\text{-Al}_2\text{O}_3$  at zero pressure. High symmetry points are A:  $(0, \frac{1}{2}, 0)$ ,  $\Gamma$ :  $(0, 0, 0)$  Z:  $(\frac{1}{2}, \frac{1}{2}, \frac{1}{2})$ , and D:  $(\frac{1}{2}, 0, \frac{1}{2})$ . Lines denote theoretical spectrum and discrete squares denote experimental data.

anharmonic effect, a qualitative plot of the potential energy as a function of the interatomic distance is shown in Figure 3.2.

The interatomic distance gets smaller with decreasing volume. At a volume less than the equilibrium volume  $V_0$  one can see that the true potential curve is steeper than the harmonic curve, which provides a higher phonon frequencies. And, at a volume larger than  $V_0$ , the true curve is flatter than the harmonic one, which makes the phonon frequencies relatively lower. For a volume that is in the vicinity of  $V_0$ , the anharmonic effect is comparatively small. In this case the anharmonicity can be approximated with the quasi-harmonic approximation (QHA). Within this approximation, we treat the crystal harmonically at a fixed volume, whereas the phonon frequencies are volume dependent. A quantity  $\gamma_{\mathbf{q},\xi}$ , known as the *mode Grüneisen parameter*, describe this dependence, i.e.,

$$\gamma_{\xi}(\mathbf{q}) = -\frac{V}{\omega_{\xi}(\mathbf{q})} \frac{\partial \omega_{\xi}(\mathbf{q})}{\partial V} = -\frac{\partial (\ln \omega_{\xi}(\mathbf{q}))}{\partial (\ln V)} \quad (3.34)$$

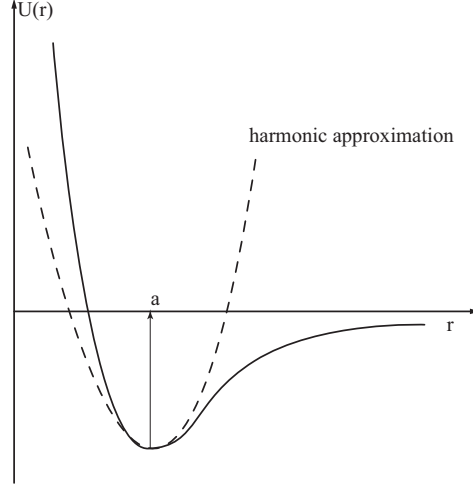


Figure 3.2: Potential energy vs. interatomic distance curve. Dashed line denotes harmonic potential curve. Minimum potential energy is provided at  $r = a$

and the overall *Grüneisen parameter* is defined as:

$$\gamma = \frac{\sum_{q,\xi} \gamma_{\xi}(\mathbf{q}) c_{v,\xi}(\mathbf{q})}{\sum_{q,\xi} c_{v,\xi}(\mathbf{q})} \quad (3.35)$$

where  $c_{v,\xi}(\mathbf{q})$  is the mode specific heat capacity at constant volume. The mode Grüneisen parameter can be calculated via Hellmann-Feynman theorem.

$$\gamma_{\xi}(\mathbf{q}) = -\frac{V}{2\omega_{\xi}^2(\mathbf{q})} \left\langle \mathbf{e}(\mathbf{q}, \xi) \left| \frac{\partial \mathbf{D}(\mathbf{q})}{\partial V} \right| \mathbf{e}(\mathbf{q}, \xi) \right\rangle \quad (3.36)$$

where  $\mathbf{D}(\mathbf{q})$  is the dynamical matrix with wave vector  $\mathbf{q}$  and  $\mathbf{e}(\mathbf{q}, \xi)$  is the eigenvector of the  $\xi^{th}$  normal mode at reciprocal lattice point  $\mathbf{q}$ . The first order derivative of  $\mathbf{D}(\mathbf{q})$  with respect to the volume can be approximately evaluated using the finite difference technique.

Typically thermodynamic properties, instead of thermodynamic potentials, are measurable quantities. The thermal properties of a system can be determined from certain thermodynamic potential according to the given ensemble, e.g., for a system with temperature and pressure as independent variables, the related potential is the Gibbs free energy.

At temperatures far below melting point, the total energy and free energy can be evaluated within the harmonic approximation, according to equation 3.26. However, some thermal properties, such as heat capacity at constant volume and entropy, are derived from the first order derivatives of the thermodynamic potentials with respect to temperature at constant volume. Other thermal properties that are not defined at constant volume, such as thermal expansion and isothermal bulk modulus, can be evaluated via the equation of state (EOS), which will be discussed in the next section.

Heat capacity is the first order derivative of the total energy with respect to temperature at constant volume (neglecting the temperature dependence of phonon frequency), and entropy can be derived in a very similar way as the first order derivative of free energy.

$$C_V = \left( \frac{\partial E}{\partial T} \right)_V = \frac{k_B}{N_{\mathbf{q}}} \sum_{\mathbf{q}\xi} \frac{\left( \frac{\hbar\omega_{\xi}(\mathbf{q})}{k_B T} \right)^2 e^{\frac{\hbar\omega_{\xi}(\mathbf{q})}{k_B T}}}{\left( e^{\frac{\hbar\omega_{\xi}(\mathbf{q})}{k_B T}} - 1 \right)^2} \quad (3.37)$$

$$S = - \left( \frac{\partial F}{\partial T} \right)_V = - \frac{k_B}{N_{\mathbf{q}}} \sum_{\mathbf{q}\xi} \left[ \ln \left( 1 - e^{-\frac{\hbar\omega_{\xi}(\mathbf{q})}{k_B T}} \right) + \frac{\frac{\hbar\omega_{\xi}(\mathbf{q})}{k_B T}}{1 - e^{-\frac{\hbar\omega_{\xi}(\mathbf{q})}{k_B T}}} \right] \quad (3.38)$$

At a fixed volume, these two quantities can be calculated directly from phonon frequencies and the corresponding phonon density of state. For the reason that it is impractical to perform first-principles calculations at a large number of volume points in order to numerically evaluate the derivatives, EOS is of special importance for interpolation with the limited number of volume points. With the adopted EOS, we are able to obtain the relation among pressure, volume and temperature. Thus we can predict the thermal expansion coefficient with the finite difference method.

$$\alpha = \frac{1}{V} \left( \frac{\partial V}{\partial T} \right)_P \quad (3.39)$$

With the adopted equation of states and previously calculated quantities, the Gibbs free energy, isothermal bulk modulus, isobaric heat capacity, and adiabatic bulk modulus



can be calculated as follow:

$$G(T, P) = F(T, V) + PV \quad (3.40a)$$

$$B_T = -V \left( \frac{\partial P}{\partial V} \right)_T \quad (3.40b)$$

$$C_P = T \left( \frac{\partial S}{\partial T} \right)_P \quad (3.40c)$$

$$B_S = \frac{C_P}{C_V} \cdot B_T \quad (3.40d)$$

The bulk Grüneisen parameter is related to the thermal expansivity, volume, bulk modulus and heat capacity:

$$\gamma = \frac{\alpha V B_T}{C_V} \quad (3.41)$$

### 3.3.2 Equation of State (EOS) Models

In previous sections, we have discussed the calculation of Helmholtz free energy at a given volume. The temperature effect is considered within the framework of QHA and a further correction from the lowest order anharmonic contribution is introduced in Appendix C. To predict the thermoelastic and thermodynamic properties such as bulk modulus, thermal expansion coefficient, Grüneisen parameter etc., equation of state (EOS) is necessary. From the experimental point of view, the EOS is usually the Pressure-Volume-Temperature ( $P - V - T$ ) relationship, but on the theory side, the Energy-Volume-Temperature ( $F - V - T$ ) relationship is often convenient. The roles that EOS plays are mainly in the following aspects

1. It extends the direct calculated free energies (high computational cost) from a few volume points to a continuous range.
2. The interpolation with EOS from directly calculated points may reduce the random type of numerical error.
3. It provides an analytical form of relationship which is helpful in deriving other quantities.

4. Some physical quantities, such as equilibrium volume, equilibrium energy, bulk modulus at zero pressure and its pressure derivative, can be extracted by fitting data to the EOS.

Although many EOS models have been proposed in the past, we confine our study to those most commonly adopted ones, namely the 2<sup>nd</sup>-order, 3<sup>rd</sup>-order Birch-Murnaghan EOS (BM-EOS)<sup>159,160</sup> and the Vinet EOS<sup>161,162</sup>.

Birch-Murnaghan EOS is derived from the finite strain theory based upon a Taylor expansion of the free energy in terms of powers of small volumetric strains. There are two types of strains that are differentiated from the definition of reference configuration. *Eulerian strain* takes the deformed state as the reference configuration, and *Lagrangian strain* chooses the undeformed state as the reference state. Both strains can be expressed as a function of the volume ratio.

$$\varepsilon = \frac{1}{2} \left[ 1 - \left( \frac{V_0}{V} \right)^{2/3} \right] \quad (3.42a)$$

$$\eta = \frac{1}{2} \left[ \left( \frac{V}{V_0} \right)^{2/3} - 1 \right] \quad (3.42b)$$

where  $\varepsilon$  and  $\eta$  are Eulerian and Lagrangian strains, respectively. Eulerian strain is employed in the BM-EOS for the reason of better convergence and the free energy is in the form of

$$F = \sum_{n=1}^{n_m} A_n \varepsilon^n \quad (3.43)$$

where  $A_n$  is the  $n^{\text{th}}$  power coefficient and  $n_m$  determines up to which order to terminate. With  $n_m = 2$ , equation 3.43 leads to the second order BM-EOS.

$$F(T, V) = F_0 + \frac{9}{8} K_0 V_0 \left[ \left( \frac{V_0}{V} \right)^{2/3} - 1 \right]^2 \quad (3.44)$$

where  $F_0$  and  $K_0$  are the equilibrium free energy and the bulk modulus at zero pressure condition. Note that  $F_0$ ,  $V_0$ , and  $K_0$  are temperature dependent implicitly. The hydrostatic

pressure can be derived as the negative of the first-order partial derivative of free energy with respect to volume.

$$P(T, V) = - \left( \frac{\partial F}{\partial V} \right) = \frac{3}{2} K_0 \left[ \left( \frac{V_0}{V} \right)^{7/3} - \left( \frac{V_0}{V} \right)^{5/3} \right] \quad (3.45)$$

Third order BM-EOS can be obtained from equation 3.43 with  $n_m = 3$ .

$$F(T, V) = F_0 + \frac{9}{8} K_0 V_0 \left[ \left( \frac{V_0}{V} \right)^{2/3} - 1 \right]^2 \cdot \left\{ 1 + \frac{1}{2} (4 - K'_0) \left[ 1 - \left( \frac{V_0}{V} \right)^{2/3} \right] \right\} \quad (3.46)$$

$$P(T, V) = \frac{3}{2} K_0 \left[ \left( \frac{V_0}{V} \right)^{7/3} - \left( \frac{V_0}{V} \right)^{5/3} \right] \cdot \left\{ 1 + \frac{3}{4} (4 - K'_0) \left[ 1 - \left( \frac{V_0}{V} \right)^{2/3} \right] \right\} \quad (3.47)$$

where  $K'_0$  is the pressure derivative of  $K_0$  at  $P = 0$  ( $K'_0 = \left( \frac{dK}{dP} \right)_{P=0}$ ). With  $K'_0 = 4$ , the third-order BM-EOS reduces to the second-order BM-EOS.

Vinet EOS is derived from an empirical interatomic potential and resulting in:

$$F(T, V) = F_0 + \frac{2K_0 V_0}{(K'_0 - 1)^2} \cdot \left\{ 2 - \left[ 5 + 3K'_0 \left( \left( \frac{V}{V_0} \right)^{1/3} - 1 \right) - 3 \left( \frac{V}{V_0} \right)^{1/3} \right] \cdot e^{\frac{3}{2}(K'_0 - 1) \left( \left( \frac{V}{V_0} \right)^{1/3} - 1 \right)} \right\} \quad (3.48)$$

$$P(T, V) = 3K_0 \left( \frac{V}{V_0} \right)^{-2/3} \left[ 1 - \left( \frac{V}{V_0} \right)^{1/3} \right] e^{\frac{3}{2}(K'_0 - 1) \left( 1 - \left( \frac{V}{V_0} \right)^{1/3} \right)} \quad (3.49)$$

Numerous studies have been done for comparing models of EOSs on all types of solids. Stacey *et al.*<sup>163</sup> and Anderson<sup>164</sup> have pointed out that the convergence of the BM-EOS from polynomial expansion terms may not be good for large strains if  $K'_0 \neq 4$ . This is due to the fact that the coefficient of the 4<sup>th</sup> order term is larger than that of the 3<sup>rd</sup> order term. In this sense, the second order BM-EOS is capable dealing with rather low pressures

where  $K'_0$  is close to 4 and does not vary much. At very high pressures up to several megabars, the third order BM-EOS will surpass the second order for better accounting the pressure dependence of  $K'$ . In the extremely high pressure case (of the order terapascals), the EOS models derived from finite strains will in general fail due to large compression. The Vinet EOS derived from an empirical potential is comparatively good in the low pressure conditions and it fits better with large compressions.

Temperature is another factor that introduces strains. It is convenient to separate the free energy into static and thermal part.

$$F(T, V) = E_0(V) + F_{vib} \quad (3.50)$$

where  $E_0(V)$  is the static energy and  $F_{vib}$  is the free energy due to lattice vibrations, which also includes the zero-point energy. Only the second term has temperature dependence and therefore we separate the overall fitting (to EOS) into two parts: fitting to static EOS and isothermal EOS. For the static energy part, considering the nature of studies in this dissertation, the pressures will not exceed 2 megabars and temperatures are typically well below the melting points, we adopt the BM-EOS over the Vinet EOS because of its wide acceptance and simplicity. In practical calculations, a set of our first-principles calculated  $E$ - $V$  data is fitted to the third order BM-EOS (equation 3.46) with least-square-fitting algorithm.  $E_0$ ,  $V_0$ ,  $K_0$  and  $K'_0$  can be obtained as fitting parameters. For a better result, the volume points are chosen to be evenly spaced with  $V_0$  (the minimum of the  $E$ - $V$  curve) around the middle.

For the thermal part, we usually choose the  $2^{nd}$  order BM-EOS which has been shown to be effective. Meanwhile we have done a case study in MgO to investigate several EOS models for fitting to the thermal free energies.

### 3.3.3 Case Study: MgO

MgO (periclase) is an important mineral of the Earth’s lower mantle and it has a very high melting point that allows us to study its thermal properties in a wide temperature range. The motivation of this study is to verify the influence of EOS model on the thermal expansion coefficient as a function of temperature, and to find the model that has a better agreement with published experimental data. Within the framework of QHA, we have calculated the thermal Helmholtz free energies ( $F_{vib}$ ) at 17 volume points. These volume points are evenly spaced and cover the pressure range at which our study is concerned. Based on equation 3.28, we evaluate the thermal free energy at a temperature step of 5 K from 0 K to 3000 K. Figure 3.3 shows our calculated data at temperatures of 0 K and 2000 K. At the first glance, two data sets almost resemble each other. However, the vertical scales are difference in these two plots, thus the temperature has more effect in lowering the free energy of larger volumes. Also, the numerical uncertainties in our calculation contributes to the unsmoothness of the curves.

Besides the 2<sup>nd</sup> and 3<sup>rd</sup> order BM-EOS, based on the appearance of the curve in Figure 3.3, we proposed a model which assumes linear volume dependence of  $F_{vib}$ . Furthermore, we add an additional term to our linear model to address the nonlinear effect for small volumes. This additional term has been tested with two variants: one with a  $\ln V$  dependence and the other with an inverse volume dependence. Next our data at each temperature point are fitted to these five EOS schemes using the least-square-fitting algorithm. As most of the discrepancies of thermal expansion happen at the high temperature region, we plot our fitting results from different models at  $T = 2000$  K and zero pressure in Figure 3.4. In the region where directly calculated data points are available, all models fit the data similarly well with minor differences, whereas the differences become apparent immediately outside data region. This indicates the necessity for providing data sets in a wide volume range.

With each thermal EOS model and the common 3<sup>rd</sup> order BM-EOS for static energy, we have calculated the thermal expansion and compared with experimental results, as shown in Figure 3.5. Most experimental data are measured from 300 K to 3000 K. At

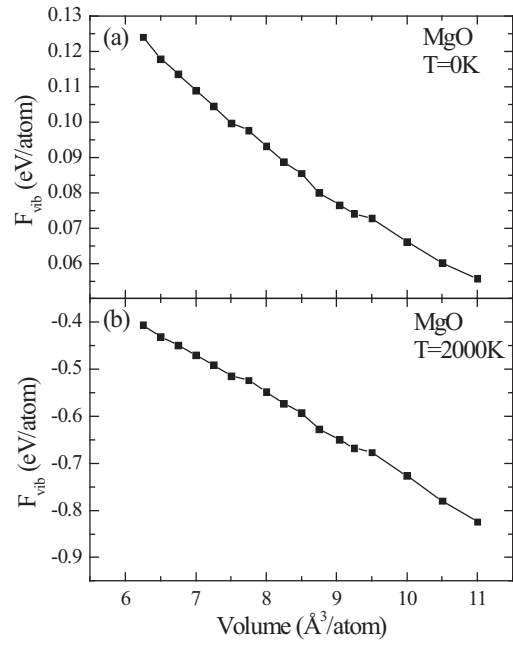


Figure 3.3: LDA calculated thermal free energy at several volume points. (a) At  $T = 0\text{ K}$ . (b) At  $T = 2000\text{ K}$ .

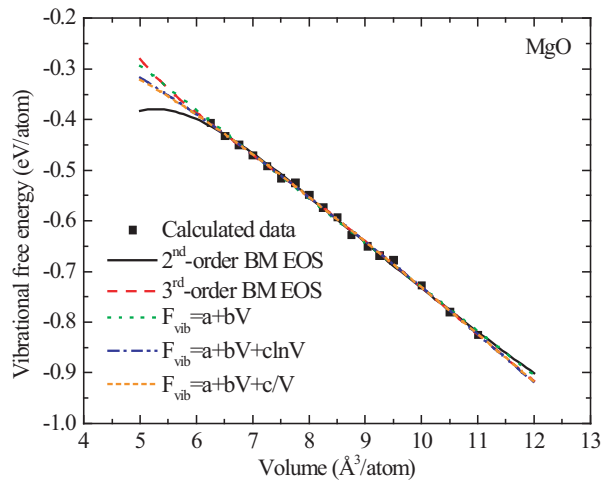


Figure 3.4: LDA calculated  $F_{\text{vib}} - V$  data at  $T = 2000\text{ K}$  are fitted to several EOS models.

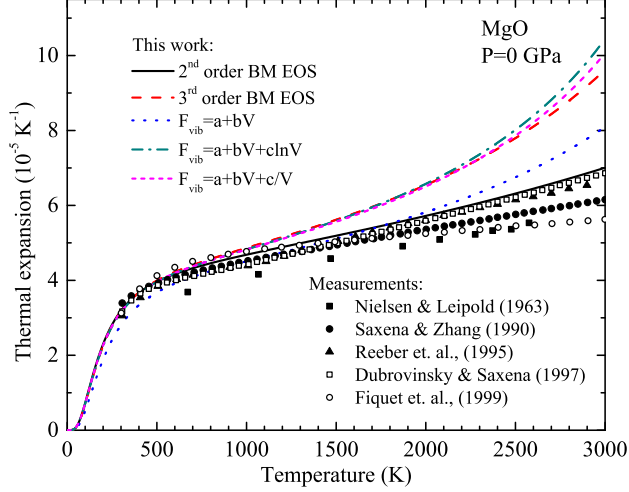


Figure 3.5: Thermal expansion of MgO at zero pressure. Lines represent this work from LDA calculation. Discrete symbols are reported measurements.

low temperatures from 300 K to 600 K, calculated thermal expansions of all models have a good agreement with most measurements except the linear model is slightly lower than the majority. At temperatures above 600 K, the 3<sup>rd</sup> BM-EOS and two modified linear models lead to an overestimation and have the tendency to diverge. Thermal expansion from the linear model at high temperatures does not diverge as much as those three models but is still apparently higher than all measured values. Considering its discrepancy at low temperatures, this model does not meet the satisfaction. Despite the differences among experimental data, the 2<sup>nd</sup> order BM-EOS is significantly better than the other models. Regarding the good fitting results in Figure 3.4, we attribute the discrepancies in thermal expansion to the its sensitivity to minor volume changes. Fiquet *et al.* has pointed out that a volume error of 1% translates into differences of up to 20% in thermal expansion coefficients<sup>21</sup>. This could explain why 3<sup>rd</sup> order BM-EOS is worse than 2<sup>nd</sup> order since it picks up more random errors from the data sets.

For the numerical error caused overestimation mentioned above, we also tried the Debye model to predict the thermal expansion since only one parameter, the Debye temperature, is needed to handle the temperature effect which may even out the previously magnified

unsmoothness at high temperatures (Figure 3.3). We first calculate the Debye temperatures for all volume points from vibrational free energy at zero temperature.

$$F_{vib}(T = 0K) = \frac{9}{8}k_B T_D \quad (3.51)$$

where  $T_D$  is the Debye temperature. Based on the appearance of  $(T_D, V)$  data sets, we fitted them to a  $T_D = a + b \ln V$  model using least square fitting algorithm. Thermal pressure as a function of  $T$  and  $V$  can be expressed in term of Debye temperature.

$$P_{th} = \left[ 27 \left( \frac{T}{T_D} \right)^4 \int_0^{T_D/T} \ln(1 - e^{-x}) x^2 dx - \frac{9}{8} - 9 \left( \frac{T}{T_D} \right) \ln(1 - e^{-T_D/T}) \right] \cdot k_B \frac{b}{V} \quad (3.52)$$

With equation 3.52 as our thermal EOS, we predict the thermal expansion coefficient as a function of temperature at zero pressure in Figure 3.6. Unfortunately result from Debye model diverges even faster at high temperatures. This, on one hand, reconfirms the sensitivity of thermal expansion to EOSs, and on the other hand implies that an accurate density of state can improve the result.



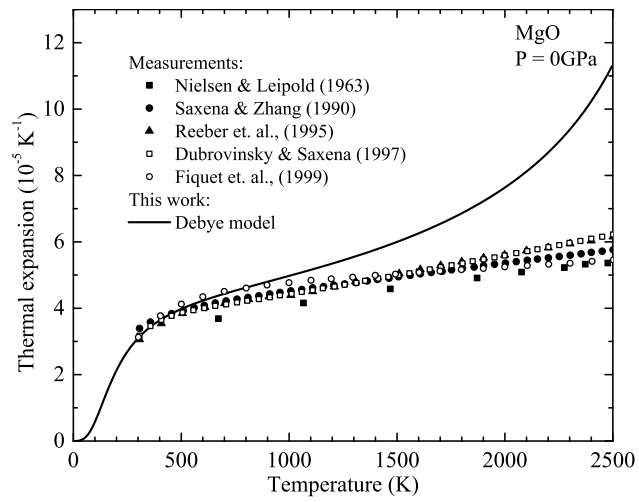


Figure 3.6: Thermal expansion of MgO at zero pressure. Solid line denotes our calculation with Debye model. Discrete symbols are reported measurements.

CHAPTER 4  
PRESSURE-INDUCED PHASE TRANSITIONS IN ALUMINIUM OXIDE AND  
ALUMINIUM NITRIDE

## 4.1 Aluminium Oxide: $\text{Al}_2\text{O}_3$

### 4.1.1 Introduction

Aluminium oxide ( $\text{Al}_2\text{O}_3$ ) is often referred to as alumina, sapphire or aloxite in the ceramic, mining and materials science communities. It is commonly used as an abrasive due to its hardness and as a refractory material due to its high melting point. The naturally-occurring crystalline form of  $\text{Al}_2\text{O}_3$  at ambient condition is primarily corundum. Rubies ( $\text{Cr}^{+3}$  doped) and sapphires are gem-quality forms of corundum. In high-pressure experiments, ruby usually serves as a standard pressure gauge (ruby scale) in diamond anvil cell (DAC)<sup>1</sup> and sapphire is used as window material in shock wave experiments<sup>2</sup>.  $\text{Al}_2\text{O}_3$  is also one of the major constituents of the Earth's lower mantle. High-pressure behaviors and thermal properties of alumina are important for both experimental research and better understanding of the interior of the earth.

At ambient conditions, The crystalline form of  $\text{Al}_2\text{O}_3$  is corundum ( $\alpha\text{-Al}_2\text{O}_3$ , space group  $R\bar{3}c$ ). This structure is known to exist over a wide range of pressure and temperature conditions. In the past twenty years theoretical<sup>3-7</sup> and experimental<sup>8-11</sup> studies showed that  $\alpha\text{-Al}_2\text{O}_3$  transforms into the  $\text{Rh}_2\text{O}_3(\text{II})$  structure (space group  $Pbcn$ ) around 90 GPa, and further transforms into the post-perovskite structure (space group  $Cmcm$ ) at  $\sim 130$  GPa. Several calculations predicted a transition from  $\text{Rh}_2\text{O}_3(\text{II})$  structure to the orthorhombic perovskite (PV) structure (space group  $Pbnm$ ) at even higher pressures<sup>5,12</sup>. However, it has never been observed in experiments. Recent calculations showed that  $Pbnm$  perovskite is not thermodynamically favored with respect to the corundum,  $\text{Rh}_2\text{O}_3(\text{II})$  and

post-perovskite phases<sup>6,7</sup>. Here we report our LDA calculated equilibrium  $T$ - $P$  phase diagram with both ultra-soft pseudopotentials (US-PP) and PAW method. The results are compared with other reported calculations<sup>3-6,6,7,13</sup>.

In the corundum $\rightarrow$ Rh<sub>2</sub>O<sub>3</sub>(II) transformation, *in situ* heating is found necessary. At room temperature, X-ray diffraction experiments showed that corundum phase is stable up to 175 GPa<sup>14,15</sup>, which implies the existence of a large kinetic barrier for this transition. On the other hand, Lin *et al.* found that the high-pressure Rh<sub>2</sub>O<sub>3</sub>(II) phase can be seen as low as 85 GPa on decompression after laser heating<sup>10</sup>, indicating the Rh<sub>2</sub>O<sub>3</sub>(II) $\rightarrow$ corundum transition is also sluggish. No experiment has recovered the Rh<sub>2</sub>O<sub>3</sub>(II) phase to ambient conditions upon decompression. Here We proposed a transformation pathway for the corundum $\rightarrow$ Rh<sub>2</sub>O<sub>3</sub>(II) transition and evaluate the kinetic barrier based on the proposed pathway. We further predict the meta-stability of two phases.

In addition to X-ray diffraction studies,  $\Gamma$ -point vibrational excitations are commonly used to identify the phase transformations. Their pressure dependencies also provide information on the structural stability under compression. Raman<sup>165-167</sup> and IR<sup>168-170</sup> spectra of the  $\alpha$ -Al<sub>2</sub>O<sub>3</sub> were subjected to several experimental studies. The dependence of Raman frequencies on uniaxial stress has also been measured<sup>171</sup>. Besides  $\Gamma$ -point phonons, the phonon dispersion curves along some high symmetry directions were measured using inelastic neutron scattering by Schober *et al.*<sup>172</sup>. On the theoretical side, Heid *et al.* calculated the dispersion curves and vibrational density of state by adopting LDA and norm-conserving pseudopotentials within the frame of density functional perturbation theory<sup>173</sup>. The phonon dispersion was also calculated from Łodziana *et al.* by means of DFT approach with GGA and ultrasoft pseudopotentials<sup>174</sup>. Montanari *et al.* investigated the  $\Gamma$ -point vibrational modes using all-electron Gaussian-type basis set with three different exchange-correlation functionals<sup>175</sup>. Presently no measurements has been reported for the two high-pressure phases: Rh<sub>2</sub>O<sub>3</sub>(II) and pPV. Ono *et al.* has computed Raman frequencies of the pPV-Al<sub>2</sub>O<sub>3</sub> at 130 GPa using LDA and non-local Troullier-Martins pseudopotentials with partial core corrections. We have calculated the phonon dispersion and the corresponding VDOS for the

four polymorphs. Phonon dispersion, vibrational density of state for  $\alpha$ -Al<sub>2</sub>O<sub>3</sub> and pressure dependence of  $\Gamma$ -point phonon frequencies for  $\alpha$ , Rh<sub>2</sub>O<sub>3</sub>(II) and pPV phases will be shown.

Thermodynamic properties, such as thermal expansion coefficient (TEC), heat capacity  $C_P$ , entropy and adiabatic bulk modulus have long been studied experimentally<sup>16–25</sup>. Almost a decade ago Hama *et al.* calculated the thermal properties of corundum phase by extending the formalism of Thomsen and combining the results with the Vinet model and the Debye model for lattice vibrations<sup>26</sup>. To date, no first-principles studies have been reported to predict the thermodynamic properties of Al<sub>2</sub>O<sub>3</sub>. And, both experimental and theoretical data of thermal properties of the high-pressure phases are lacking. We thus present our calculated high-pressure TEC and bulk modulus for Rh<sub>2</sub>O<sub>3</sub> (II) and pPV phases as a function of temperature up to 3000 K.

Before 2004, experimental elastic constants of  $\alpha$ -Al<sub>2</sub>O<sub>3</sub> were reported from as early as 1950s<sup>25,27–29</sup>. And many efforts of *ab initio* calculations were made to predict the elastic constants independently<sup>30,31</sup>. However, some calculations showed conflict in the sign of  $C_{14}$ <sup>32</sup>. In 2004, Gladden *et al.*<sup>33</sup> reported their reexamination of the elasticity of  $\alpha$ -Al<sub>2</sub>O<sub>3</sub> using resonance ultrasound spectroscopy (RUS) and confirmed that  $C_{14}$  is positive rather than negative. Gladden’s conclusion was later confirmed by both measurement with a different technique<sup>34</sup> and first-principles calculations<sup>35</sup>. Although measurements of  $C_{ij}$  for the high-pressure phases of Al<sub>2</sub>O<sub>3</sub> are still lacking, Duan *et al.*<sup>31</sup> and Stackhouse<sup>36</sup> have calculated the elastic constants of Rh<sub>2</sub>O<sub>3</sub>(II) (from 75 GPa to 300 GPa) and post-perovskite phases (at 136 GPa), respectively. Here we report our predicted  $C_{ij}$  of  $\alpha$ -, Rh<sub>2</sub>O<sub>3</sub>(II)- and pPV-Al<sub>2</sub>O<sub>3</sub> with pressure dependencies, which will be compared with other available results. Elastic properties of both corundum and Rh<sub>2</sub>O<sub>3</sub>(II) phases have been studied, but a direct comparison between the two phases is not accessible due to different crystal classes. Here we compare the elastic properties of corundum and Rh<sub>2</sub>O<sub>3</sub>(II) phase by treating both phases as the common-subgroup monoclinic lattices.

### 4.1.2 Crystal Structures, Total Energies and Vibrational Properties

The space group, formula units per primitive unit cell  $Z$  and Wyckoff sites of the above four polymorphs are summarized in Table 4.1. Their structures are shown in Figure 4.1. As a denser phase, high-pressure structure usually has a larger average coordination number than the low-pressure structure. However, for these four polymorphs of  $\text{Al}_2\text{O}_3$ , all the Al atoms are six coordinated and all the O atoms are four coordinated. Corundum has  $R\bar{3}c$  rhombohedral symmetry which can also be viewed as a hexagonal lattice with  $Z = 6$  formula units per cell. As illustrated in the ball-stick model of Figure 4.1(a), O atoms form a lightly distorted hexagonal close-packed (hcp) sublattice with Al atoms occupying 2/3 of the octahedral interstices. Each  $\text{AlO}_6$  octahedron has 1 face-sharing, 3 edge-sharing and 9 corner-sharing with other octahedra, as shown in Figure 4.1(a) (three figures on the right). The centered octahedron is highlighted in yellow color. Viewing from  $c$  axis, each figure shows the neighboring environment of the centered polyhedron with one octahedron layer (in the  $a$ - $b$  plane). For clarity purpose, the centered polyhedron is not shown in the last figure as it is overlapped with the octahedron underneath.  $\text{Rh}_2\text{O}_3$ -(II) structure (Figure 4.1(b)) is closely related to the corundum structure which will be shown later. Each octahedron in  $\text{Rh}_2\text{O}_3$ -(II) structure has 1 face-sharing, 2 edge-sharing and 11 corner-sharing with other octahedra. Different from corundum and  $\text{Rh}_2\text{O}_3$ -(II), two types of polyhedra are presented in the  $Pbnm$  perovskite structure (Figure 4.1(c)). Each Al atom still forms six bonds with neighboring O atoms, whereas the 4b and 4c Al atoms form  $\text{AlO}_6$  octahedra and triangular prism, respectively. Each octahedron is surrounded by 6 corner-sharing octahedra and 4 edge-sharing, 4 corner-sharing prisms. For the triangular prisms, each is neighboring with 2 edge-sharing, 2 corner-sharing prisms and 4 edge-sharing, 6 corner-sharing octahedra. The  $Cmcm$  post-perovskite structure also has both  $\text{AlO}_6$  octahedra (4a site Al) and triangular prisms (4c site Al). The octahedron shares edges with 2 octahedra and 2 prisms, also shares corners with 2 octahedra and 8 prisms. The prisms share their triangular faces with two neighboring prisms along the  $a$  axis, and has 2 edge-sharing, 8 corner-sharing octahedra neighbors.

Table 4.1: Space groups, formula units per primitive unit cell  $Z$  and Wyckoff sites of four polymorphs of  $\text{Al}_2\text{O}_3$ : Corundum,  $\text{Rh}_2\text{O}_3$ -(II),  $Pbnm$  perovskite and post-perovskite.

Phase	Space group	$Z$	Species	Wyckoff site
$\alpha$	$R\bar{3}c$	2	O	6e
			Al	4c
$\text{Rh}_2\text{O}_3$ -(II)	$Pbcn$	4	O	4c, 8d
			Al	8d
Perovskite	$Pbnm$	4	O	4c, 8d
			Al	4b, 4c
Post-perovskite	$Cmcm$	2	O	4c, 8f
			Al	4a, 4c

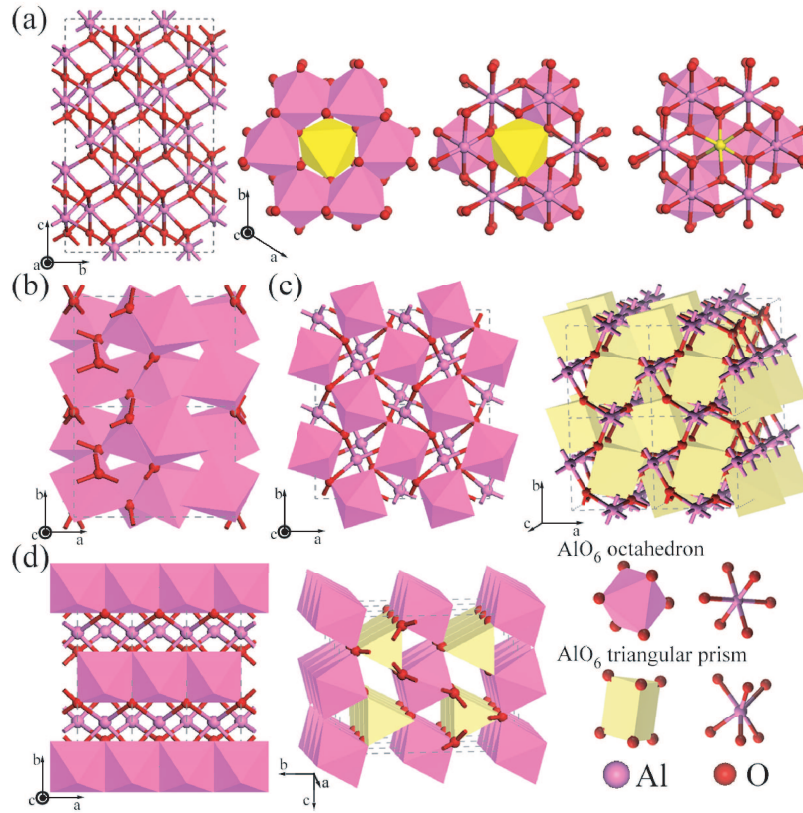


Figure 4.1: Crystal structures of four polymorphs of  $\text{Al}_2\text{O}_3$ : (a) Corundum, (b)  $\text{Rh}_2\text{O}_3$ -(II), (c)  $Pbnm$  perovskite and (d) post-perovskite.

Total energy calculations were performed for  $\alpha$ -, Rh<sub>2</sub>O<sub>3</sub>(II)-, PV- and pPV-Al<sub>2</sub>O<sub>3</sub> by imposing their symmetries. We adopted density functional theory (DFT) with a plane wave basis set and ultrasoft pseudopotentials (US-PP) (or PAW method), which is implemented in the VASP code<sup>139</sup>. The exchange and correlation functional is treated with local density approximation (LDA). The plane wave basis functions with energies up to 395.7 eV (or 400.0 eV) were used for US-PP (or PAW method). Total energy change of 10<sup>-9</sup> eV was chosen as the convergence criterion for the self-consistent iterations. The  $k$ -point sampling for Brillouin zone integration in our total energy calculations was carried out by the Monkhorst-Pack method with grids of  $6 \times 6 \times 6$ ,  $6 \times 8 \times 8$ ,  $6 \times 6 \times 4$  and  $6 \times 6 \times 4$  for  $\alpha$ -, Rh<sub>2</sub>O<sub>3</sub>(II)-, PV- and pPV-Al<sub>2</sub>O<sub>3</sub>, respectively.

The calculated static energy at various volumes are fitted to the 3<sup>rd</sup>-order Birch-Murnaghan EOS. Fitting parameters,  $E_0$ ,  $V_0$ ,  $K$  and  $K'$ , are listed in Table 4.2, together with reported experimental and theoretical results. As the measurements are usually made at room temperature, our predicted parameters at 300K from quasi-harmonic approximation are also listed. The present work is consistent with other calculations and experiments, and PAW method provides a slightly better agreement on bulk modulus than US-PP.

To calculate the phonon frequencies, we have constructed 120-atom, 160-atom, 80-atom and 120-atom supercells for  $\alpha$ -, Rh<sub>2</sub>O<sub>3</sub>(II)-, PV- and pPV-Al<sub>2</sub>O<sub>3</sub> respectively and adopted the real-space supercell force constant method. The size of the supercell is large enough to approximately neglect the interaction between one atom in the cell with its image outside the cell. Figure 4.2 shows the phonon spectra and VDOS of  $\alpha$ -Al<sub>2</sub>O<sub>3</sub> at zero pressure. Experimental data is also presented for comparison. As an ionic crystal, lattice vibrations of optic modes will induce dipole-dipole interactions which in turn affect the phonon frequencies around the  $\Gamma$  point ( $\mathbf{k} = 0$ ). The interaction causes the LO-TO splitting. However, this effect has not been taken into account in the VASP code. We thus manually calculate the LO-TO splitting from a correction to the dynamical matrix. The overall agreements for both US-PP and PAW are good and within the typical accuracy of *ab initio* calculations, but dispersion using PAW method fits the measured data slightly better.

Table 4.2: Third-order BM-EOS parameters for Al<sub>2</sub>O<sub>3</sub> polymorphs

Source	V <sub>0</sub> (Å <sup>3</sup> /atom)	B (GPa)	B'
Corundum			
Static calculation			
LDA+US-PP (this work)	8.430	249.1	3.540
LDA+PAW (this work)	8.357	259.9	3.967
Calculation <sup>5</sup>	8.441	258.9	4.01
Calculation <sup>7</sup>	8.10	248	4.13
Calculation <sup>6</sup>	8.486	252.6	4.237
300 K			
LDA+US-PP (this work)	8.519	241.3	3.540
LDA+PAW (this work)	8.454	250.4	3.999
Calculation <sup>13</sup>	8.498	251.0	4.04
Experiment <sup>176</sup>	8.484	254.4	4.275
Rh <sub>2</sub> O <sub>3</sub> (II)			
Static calculation			
LDA+US-PP (this work)	8.275	246.5	3.736
LDA+PAW (this work)	8.173	259.0	3.967
Calculation <sup>5</sup>	8.254	261.8	3.93
Calculation <sup>7</sup>	7.93	252	4.07
Calculation <sup>6</sup>	8.284	258.2	4.140
300 K			
LDA+US-PP (this work)	8.353	237.5	3.735
LDA+PAW (this work)	8.272	250.3	3.967
Perovskite			
Static calculation			
LDA+US-PP (this work)	8.292	217.2	4.030
LDA+PAW (this work)	8.206	236.3	3.963
Calculation <sup>5</sup>	8.322	235.0	3.98
Calculation <sup>7</sup>	7.986	223	4.22
Calculation <sup>6</sup>	8.324	229.2	4.286
300 K			
LDA+US-PP (this work)	8.404	207.8	4.031
LDA+PAW (this work)	8.304	229.8	3.963
Post-Perovskite			
Static calculation			
LDA+US-PP (this work)	8.056	225.3	4.189
LDA+PAW (this work)	7.975	239.6	4.185
Calculation <sup>7</sup>	7.756	231	4.38
Calculation <sup>6</sup>	8.058	241.6	4.464
Calculation <sup>13</sup>	7.985	251.6	4.11
300 K			
LDA+US-PP (this work)	8.171	214.6	4.190
LDA+PAW (this work)	8.086	230.6	4.185
Experiment <sup>11</sup>	7.92	249	4 (fixed)



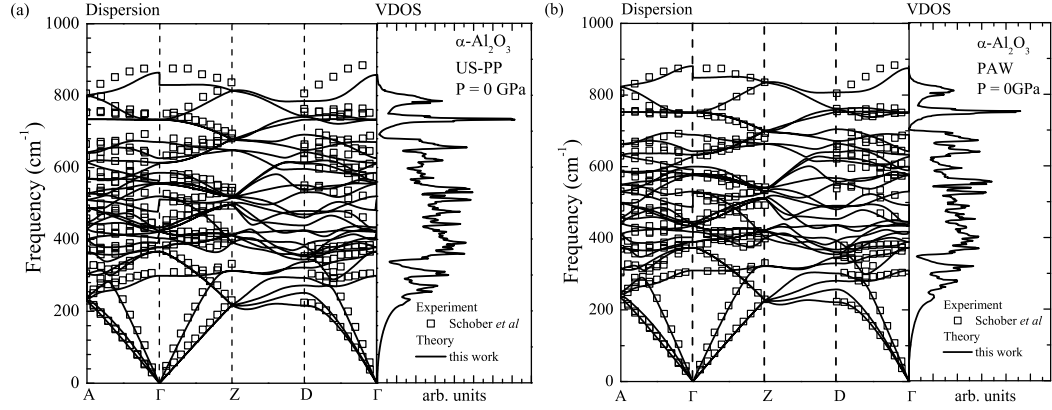


Figure 4.2: LDA calculated phonon dispersion curves and vibrational density of state of  $\alpha$ - $\text{Al}_2\text{O}_3$  at zero pressure using (a) US-PP and (b) PAW. Discrete squares denote experimental data<sup>172</sup>.

Among the calculated 30 phonon branches, the low-frequency ones have better agreement and the largest difference is given by the top branch which is 7% smaller for US-PP and 5% smaller for PAW. Heid *et al.*<sup>173</sup> pointed out two pseudogaps near 43 and 87 meV as well as a strong peak at about 92 meV in their calculated VDOS. In the VDOS we calculated, two pseudogaps are found to be 42, 86 meV for US-PP and 43, 87 meV for PAW, while the strong peak is located at 91 meV and 93 meV for US-PP and PAW, respectively. The agreement is excellent. Our calculation shows no soft phonon modes in  $\alpha$ - $\text{Al}_2\text{O}_3$  at least up to  $\sim 185$  GPa. And for  $\text{Rh}_2\text{O}_3(\text{II})$ , there is no soft phonon up to 212 GPa. However, the PV phase is dynamically unstable (soft phonon) below  $\sim 135$  GPa and the pPV phase shows the tendency of phonon softening at low pressure. The phonon instability of pPV- $\text{Al}_2\text{O}_3$  can be related to the fact that it is not quenchable to low pressures<sup>11</sup>.

$\Gamma$ -point phonon frequencies are of special interests since the measurable Raman and infrared (IR) spectra are commonly used to identify the phase transformations. And the pressure dependence can provide information on the structural instability. From group theory analysis, the irreducible representation for  $\Gamma$ -point phonons of  $\alpha$ - $\text{Al}_2\text{O}_3$  yields seven

Raman-active and six IR-active modes.

$$\Gamma_{Raman} = 2A_{1g} + 5E_g$$

$$\Gamma_{IR} = 2A_{2u} + 4E_u$$

Figure 4.3 shows our calculated Raman frequencies of  $\alpha$ -Al<sub>2</sub>O<sub>3</sub> as a function of pressure up to 40 GPa, for both US-PP and PAW. One can see that the frequency does not increase linearly with pressure in the range from 0 to 40 GPa. And the pressure dependencies reported from experiments are up to 1 GPa in Watson *et al.*<sup>166</sup> and Shin *et al.*'s<sup>171</sup> works, and up to 20 GPa in Xu *et al.*'s<sup>167</sup> work. In order to compare with the measurements, we perform linear fitting only to data sets which are below 20 GPa and expand the fitting lines to the full pressure range. It is clear that the high-pressure Raman modes exhibit decreasing slopes against pressure. However, the PAW result is more “linear” than the US-PP one. The experimental and our calculated zero-pressure Raman frequencies  $((\omega_i)_0)$  and pressure dependencies  $(\partial\omega_i/\partial P)$  of  $\alpha$ -Al<sub>2</sub>O<sub>3</sub> are listed in Table 4.3. For  $(\omega_i)_0$ , the PAW result reproduces the experimental data but the US-PP data has a constant underestimation of 3-4%. For  $\partial\omega_i/\partial P$ , PAW result is also in better agreement except two  $E_g$  modes.

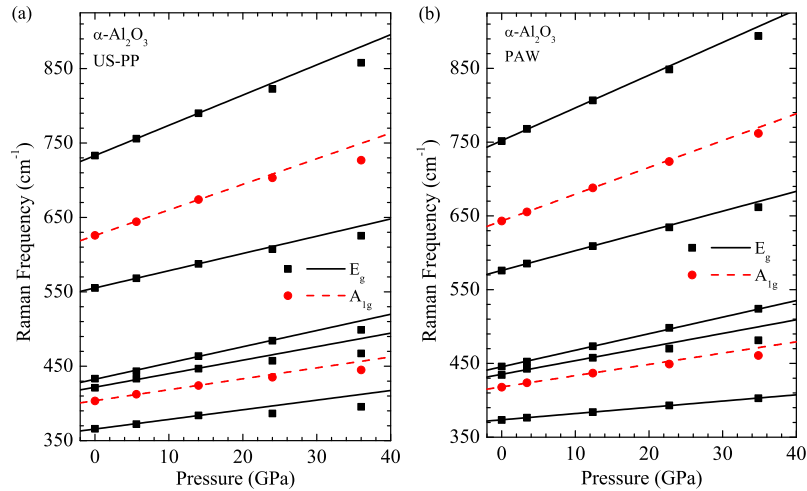


Figure 4.3: Calculated Raman-active frequencies of  $\alpha$ -Al<sub>2</sub>O<sub>3</sub> as a function of pressure. (a) US-PP, (b) PAW. Solid and dashed lines represent  $E_g$  and  $A_{1g}$  modes from linear fitting with data sets below 20 GPa.

Table 4.3: The theoretical data of Raman frequencies at zero pressure and their pressure dependencies, and comparison with other reported experimental results on corundum

Source	Modes ( $\text{cm}^{-1}$ for $(\omega_i)_0$ and $\text{cm}^{-1}/\text{GPa}$ for $\partial\omega_i/\partial P$ )						
	$A_{1g}$	$A_{1g}$	$E_g$	$E_g$	$E_g$	$E_g$	$E_g$
	$(\omega_i)_0$						
This work (US-PP)	403.4	625.9	366.0	421.1	433.3	555.1	733.2
This work (PAW)	417.8	643.1	373.4	434.4	445.8	575.9	751.5
Experiment <sup>165</sup>	418	645	378	432	451	578	751
Experiment <sup>166</sup>	417.4	644.6	378.7	430.2	448.7	576.7	750.0
	$\partial\omega_i/\partial P$						
This work (US-PP)	1.47	3.44	1.29	1.81	2.18	2.31	4.06
This work (PAW)	1.52	3.64	0.85	1.85	2.24	2.68	4.44
Experiment <sup>171</sup>	1.7±0.1	5.0±0.4	2.3±0.2	1.8±0.1	1.0±0.2	2.7±0.3	2.5±0.3
Experiment <sup>166</sup>	2.11±0.06	—	1.37±0.06	2.95±0.08	1.66±0.1	2.77±0.12	4.8±0.2
Experiment <sup>167</sup>	1.703	3.481	1.335	2.794	—	2.760	4.218

The calculated IR-active modes of  $\alpha\text{-Al}_2\text{O}_3$  as a function of pressure are shown in Figure 4.4. The TO and LO modes are plotted separately since they split at  $\Gamma$ -point. In general,  $(\omega_i)_0$  and  $\partial\omega_i/\partial P$  calculated using US-PP are smaller than the PAW data, which is consistent with the Raman results. And  $\partial\omega_i/\partial P$  also decreases with pressure for all the IR modes. No measurements have been done to obtain the pressure dependence of IR frequencies. Table 4.4 shows the IR frequencies at zero pressure from experiments and the present calculation. Again the PAW data shows better agreement than US-PP.

At present, no experimental data is available for the high-pressure phases of  $\text{Al}_2\text{O}_3$ . For  $\text{Rh}_2\text{O}_3(\text{II})\text{-Al}_2\text{O}_3$  there are thirty Raman-active modes ( $7A_g + 8B_{1g} + 7B_{2g} + 8B_{3g}$ ) and twenty IR-active modes ( $7B_{1u} + 6B_{2u} + 7B_{3u}$ ) out of the sixty  $\Gamma$ -point vibrational modes. Our predicted Raman frequencies of  $\text{Rh}_2\text{O}_3(\text{II})$  phase as a function of pressure up to 160 GPa is presented in Figure 4.5. One can see that  $\partial\omega_i/\partial P$  continuously decreases with respect to pressure for every mode. For pPV- $\text{Al}_2\text{O}_3$ , the  $\Gamma$ -point irreducible representation shows that there are twelve Raman modes ( $4A_g + 3B_{1g} + B_{2g} + 4B_{3g}$ ) and thirteen IR modes ( $5B_{1u} + 5B_{2u} + 3B_{3u}$ ). The calculated Raman frequencies of pPV phase are plotted from 70 GPa to 270 GPa, together with Ono *et al.*'s<sup>11</sup> theoretical data at 130 GPa. For each mode, Raman frequency increases with increasing pressure but the slope becomes smaller. Our PAW predicted frequencies are larger than the US-PP result, and agree with Ono *et*

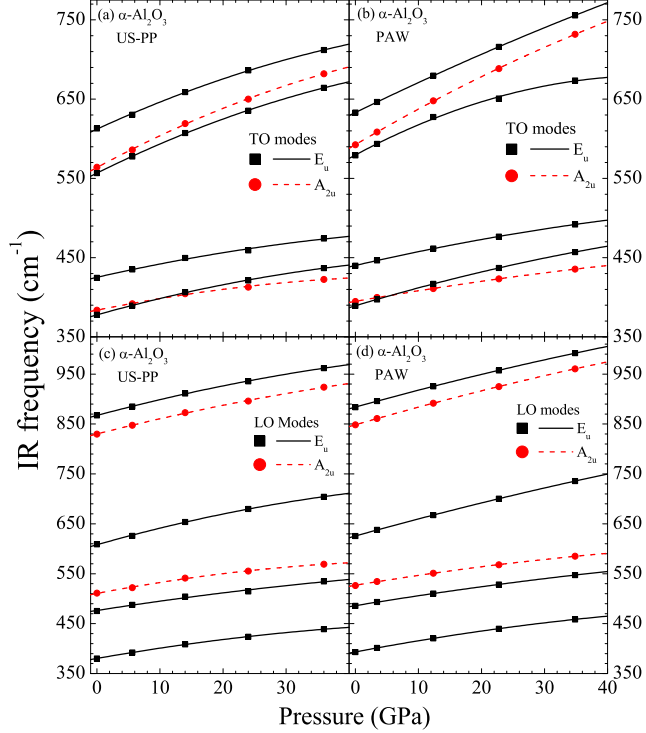


Figure 4.4: Calculated IR-active frequencies of  $\alpha\text{-Al}_2\text{O}_3$  as a function of pressure. (a) TO modes with US-PP, (b) TO modes with PAW, (c) LO modes with US-PP, (d) LO modes with PAW. Solid and dashed curves denote  $E_u$  and  $A_{2u}$  modes from  $2^{nd}$  order polynomial fitting.

Table 4.4: IR-active frequencies of corundum at zero pressure

Source	$(\omega_i)_0$ ( $\text{cm}^{-1}$ )					
	$A_{2u}$	$A_{2u}$	$E_u$	$E_u$	$E_u$	$E_u$
TO modes						
This work (US-PP)	384	564	378	425	557	613
This work (PAW)	395	593	389	440	579	633
Experiment <sup>168</sup>	400	583	385	442	569	635
Experiment <sup>169</sup>	399.5	584	384.6	439.3	569.5	635
Experiment <sup>170</sup>	397.5	582.4	385.0	439.1	569.0	633.6
LO modes						
This work (US-PP)	511	830	380	475	609	867
This work (PAW)	526	848	393	486	626	884
Experiment <sup>168</sup>	512	871	388	480	625	900
Experiment <sup>169</sup>	514	886.5	387.7	482	630.5	908
Experiment <sup>170</sup>	510.9	881.1	387.6	481.7	629.5	906.6

*al.*'s result very well. As better agreements are consistently obtained from calculation using PAW method by comparing with other calculations and experiments, we conclude that LDA calculation with PAW method is more suitable than using US-PP for predicting properties of  $\text{Al}_2\text{O}_3$ .

### 4.1.3 $T$ - $P$ Phase Diagram

Static enthalpies of four polymorphs (Figure 4.7) show the sequence of stable phases at increasing pressure, and the perovskite phase is unfavored at all pressures. The corundum-to- $\text{Rh}_2\text{O}_3(\text{II})$  transition pressure is predicted to be 93.8 GPa from US-PP and 84.0 GPa from PAW. Both of them are consistent with results from experiments<sup>8-10</sup> (79 – 100 GPa) and other calculations<sup>4-6</sup> (78 –105 GPa). Our calculated  $\text{Rh}_2\text{O}_3(\text{II})\rightarrow\text{pPV}$  transition pressure is 147.8 GPa (136.8 GPa) from US-PP (PAW), which is in accordance with reported calculations<sup>6,7,13</sup> (131 – 156 GPa) and Ono *et al.*'s observation (130 GPa)<sup>11</sup>.

Within the quasi-harmonic approximation, the  $T$ - $P$  phase diagram is calculated and shown in Figure 4.8. The corundum $\rightarrow\text{Rh}_2\text{O}_3(\text{II})$  transition pressure by US-PP (PAW) is 94.2 (82.9) GPa at 0 K, 94.5 (83.0) GPa at 300 K, 95.2 (82.2) GPa at 1000 K and 95.5 (79.6) GPa at 2000 K, which means the equilibrium  $P_t$  is not affected by the temperature. And for transformation from  $\text{Rh}_2\text{O}_3(\text{II})$  to post-perovskite phase, the calculated pressure by US-PP (PAW) is 146.9 (134.4) GPa at 0 K, 146.5 (133.7) GPa at 300 K, 143.4 (128.5) GPa at 1000 K and 136.3 (117.5) GPa at 2000 K. The  $\text{Rh}_2\text{O}_3(\text{II})\rightarrow\text{pPV}$  phase boundary has negative Clapeyron slope, i.e.,  $P_t$  decreases with increasing temperature. The phase diagram calculated by Oganov *et al.*<sup>6</sup> and Umemoto *et al.*<sup>13</sup> (LDA) show  $P_t$  of 79, 90 GPa at 0 K and 73, 88 GPa at 2000 K for the first transition, and 128, 133 GPa at 0 K and 114, 120 GPa at 2000 K for the second transition. These are consistent with this study. The stability zone of perovskite phase (bounded with dashed lines) is calculated based on the volume sets without soft phonon (above 135 GPa) and extrapolated to the low pressure region. However the PV phase only has the lowest Gibbs free energy below

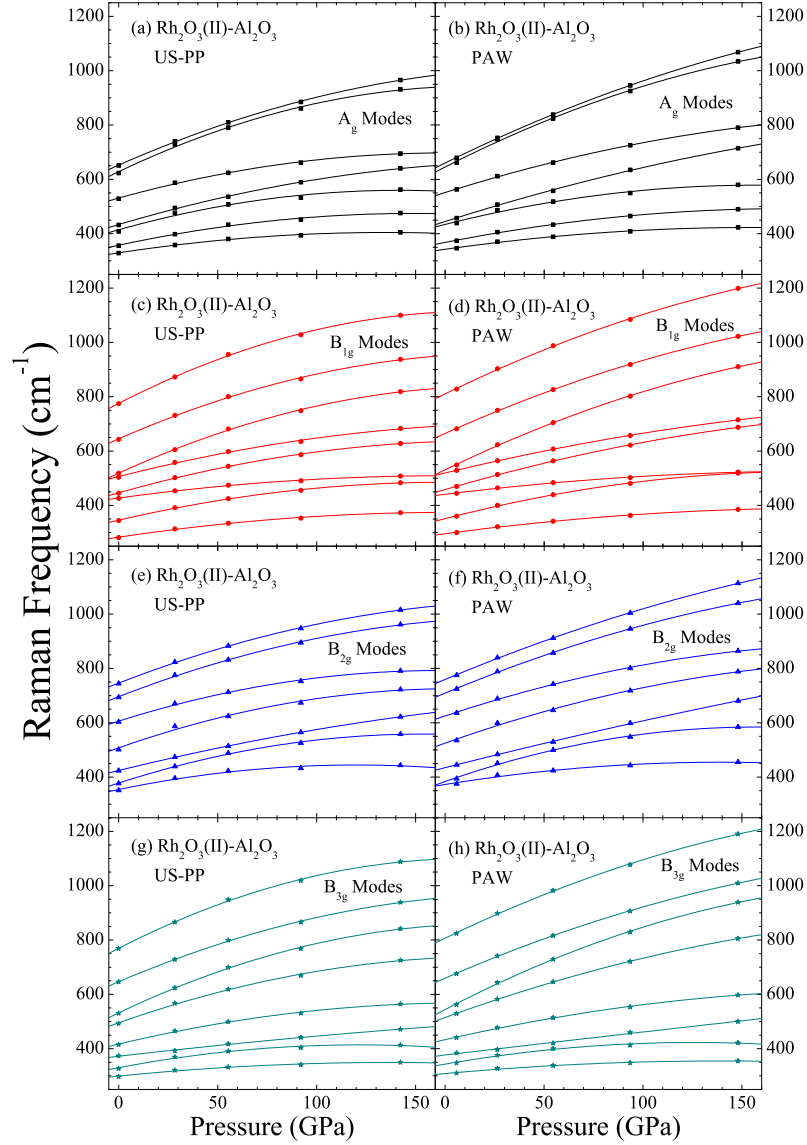


Figure 4.5: Calculated Raman-active frequencies of  $\text{Rh}_2\text{O}_3(\text{II})\text{-Al}_2\text{O}_3$  as a function of pressure. (a), (c), (e), (g) US-PP, (b), (d), (f), (h) PAW. Solid curves are from  $2^{\text{nd}}$  order polynomial fitting.

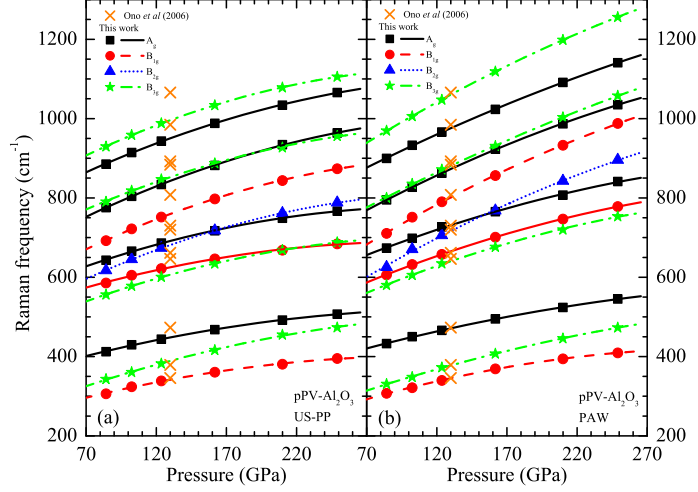


Figure 4.6: Calculated Raman-active frequencies of pPV-Al<sub>2</sub>O<sub>3</sub> as a function of pressure. (a) US-PP, (b) PAW. Solid, dashed, dotted and dash-dotted curves represent  $A_g$ ,  $B_{1g}$ ,  $B_{2g}$  and  $B_{3g}$  modes from 2<sup>nd</sup> order polynomial fitting.

135 GPa. Without taking the high temperature anharmonic effect into account, we think it is unlikely for the PV phase to be stable at the predicted conditions.

#### 4.1.4 Transition Pathways in the $\alpha$ -to-Rh<sub>2</sub>O<sub>3</sub>(II) Transition

In order to investigate the transformation pathway, we found that the rhombohedral corundum and the orthorhombic Rh<sub>2</sub>O<sub>3</sub>(II) structure are related by the common monoclinic lattice, which has 20 atoms per primitive unit cell. If we reinterpret the corundum structure (10-atom primitive unit cell) as this monoclinic lattice, it is a slightly distorted orthorhombic lattice, which is structurally close to the Rh<sub>2</sub>O<sub>3</sub>(II) structure. The 20-atom monoclinic cell can be derived from the rhombohedral setting in the following way. In terms of the 30-atom hexagonal lattice vectors, the unit vectors of the primitive rhombohedral cell can be expressed as:

$$\begin{pmatrix} \mathbf{a}_r \\ \mathbf{b}_r \\ \mathbf{c}_r \end{pmatrix} = \begin{pmatrix} \frac{1}{2}a_h & \frac{\sqrt{3}}{6}a_h & \frac{1}{3}c_h \\ -\frac{1}{2}a_h & \frac{\sqrt{3}}{6}a_h & \frac{1}{3}c_h \\ 0 & -\frac{\sqrt{3}}{3}a_h & \frac{1}{3}c_h \end{pmatrix} \quad (4.1)$$

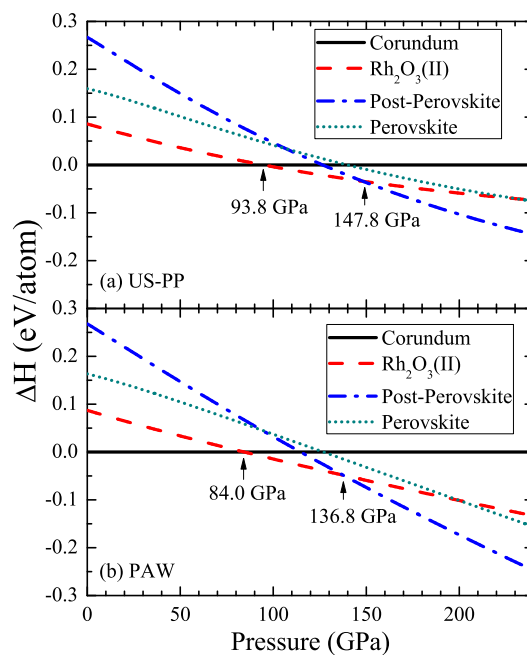


Figure 4.7: Static enthalpies of  $\text{Al}_2\text{O}_3$  polymorphs as a function of pressure relative to that of corundum phase using (a) US-PP and (b) PAW. The static  $\alpha \rightarrow \text{Rh}_2\text{O}_3(\text{II})$  and  $\text{Rh}_2\text{O}_3(\text{II}) \rightarrow \text{pPV}$  transition pressure are present. The PV phase is metastable at all pressures considered among the four polymorphs.



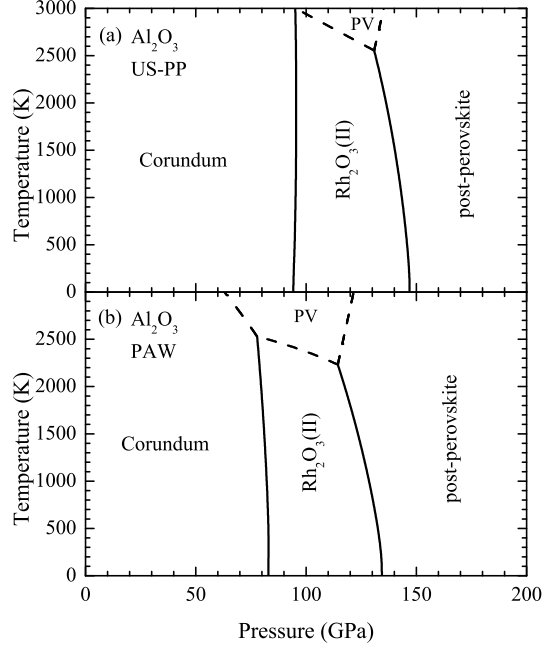


Figure 4.8: Calculated  $T$ - $P$  phase diagram of  $\text{Al}_2\text{O}_3$ . (a) US-PP, (b) PAW. Dashed lines denote possible phase boundaries.

where  $\mathbf{a}_r$ ,  $\mathbf{b}_r$  and  $\mathbf{c}_r$  are three unit vectors of the rhombohedral primitive cell,  $a_h$  and  $c_h$  are magnitudes of lattice vectors of the 30-atom hexagonal cell. The monoclinic cell can be obtained by applying the following transformation matrix

$$\begin{pmatrix} \mathbf{a}_m \\ \mathbf{b}_m \\ \mathbf{c}_m \end{pmatrix} = \begin{pmatrix} 1 & 1 & -1 \\ 1 & -1 & 0 \\ 0 & 0 & -1 \end{pmatrix} \begin{pmatrix} \mathbf{a}_r \\ \mathbf{b}_r \\ \mathbf{c}_r \end{pmatrix} \quad (4.2)$$

And the monoclinic lattice vectors can be written as

$$\begin{pmatrix} \mathbf{a}_m \\ \mathbf{b}_m \\ \mathbf{c}_m \end{pmatrix} = \begin{pmatrix} a_m & 0 & 0 \\ 0 & b_m & 0 \\ c_m \cdot \cos \beta & 0 & c_m \cdot \sin \beta \end{pmatrix} \quad (4.3)$$

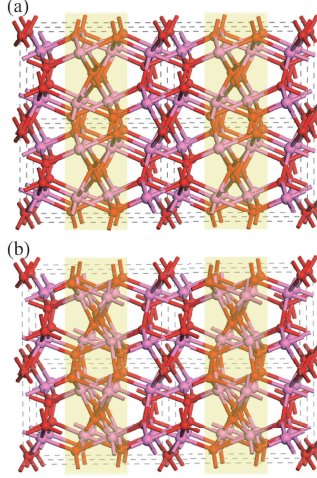


Figure 4.9: Comparison of structures of (a) corundum and (b) Rh<sub>2</sub>O<sub>3</sub>(II)-Al<sub>2</sub>O<sub>3</sub>. The corundum phase is viewed from an angle in which it appears “orthorhombic”-like. The differences between two polymorphs are highlighted.

here  $a_m = \sqrt{\frac{4}{3}a_h^2 + \frac{1}{9}c_h^2}$ ,  $b_m = a_h$ ,  $c_m = \sqrt{\frac{1}{3}a_h^2 + \frac{1}{9}c_h^2}$  and  $\beta = \cos^{-1} [(\frac{2}{3}a_h^2 - \frac{1}{9}c_h^2)/(a_m \cdot c_m)]$ .

The monoclinic unit cell has 20 atoms which is the same as the Rh<sub>2</sub>O<sub>3</sub>(II) phase. After this transformation, the two structures (Figure 4.9) are closely related and one-to-one correspondence of each atom can be found. The lattice parameters of the “monoclinic” corundum structure, taking the volume at transition pressure (84.0 GPa) as an example, are  $a_m = 6.481 \text{ \AA}$ ,  $b_m = 4.426 \text{ \AA}$ ,  $c_m = 4.732 \text{ \AA}$  and  $\beta = 95.26^\circ$ . For the orthorhombic Rh<sub>2</sub>O<sub>3</sub>(II) phase at this pressure,  $a_o = 6.475 \text{ \AA}$ ,  $b_o = 4.438 \text{ \AA}$ ,  $c_o = 4.599 \text{ \AA}$  and  $\beta = 90^\circ$ . The intermediate structures link the two end phases belong to monoclinic symmetry with space group  $P2/c$ , which is a common subgroup of  $R\bar{3}c$  (corundum phase) and  $Pbcn$  (Rh<sub>2</sub>O<sub>3</sub>(II) phase). The O atoms occupy 2e, 2f, <sup>I</sup>4g and <sup>II</sup>4g Wyckoff sites and Al atoms occupy <sup>I</sup>4g and <sup>II</sup>4g sites. During the phase transformation from corundum to Rh<sub>2</sub>O<sub>3</sub>(II) structure, besides the evolution of the external parameters ( $a$ ,  $b$ ,  $c$  and  $\beta$ ), the major changes on the internal coordinates are the  $z$  coordinates of <sup>I</sup>4g site O and <sup>I</sup>4g site Al, which are bonded to each other. Changes on other internal coordinates are relatively much smaller.

To transform from corundum to  $\text{Rh}_2\text{O}_3(\text{II})$  structure there are eighteen degrees of freedom for the intermediate phase, i.e.,  $a$ ,  $b$ ,  $c$ ,  $\beta$  and fourteen free parameters from internal coordinates. The complete information of the corundum-to- $\text{Rh}_2\text{O}_3(\text{II})$  transformation path can be revealed from a 18-dimensional potential-energy surface (PES). However, first-principles calculation of the 18D PES is not an easy task. Considering the similarity between corundum and  $\text{Rh}_2\text{O}_3(\text{II})$  structure, as can be seen from Figure 4.9, the phase transformation is mainly characterized by the displacements of the  $z$  coordinates of the  ${}^I4g$  O and Al atoms. Using the 20-atom unit cells, we constructed intermediate structures whose internal and external coordinates vary linearly from corundum to  $\text{Rh}_2\text{O}_3(\text{II})$  phase. Transition parameter ( $t_p$ ), which varies from 0 (corundum) to 1 ( $\text{Rh}_2\text{O}_3(\text{II})$ ), is defined to describe the intermediate state,  $z = z_i + (z_f - z_i) \cdot t_p$ . By fixing the  $z$  coordinates of the  ${}^I4g$  O atoms only, LDA total energy calculations were performed for 11  $t_p$  points and several volumes at each  $t_p$ , with all the other internal and external parameters being fully relaxed. Figure 4.10 shows the variation of Al-O bond lengths at the corundum-to- $\text{Rh}_2\text{O}_3(\text{II})$  transition pressure (84.0 GPa). For both corundum and  $\text{Rh}_2\text{O}_3(\text{II})$  structures, all the O atoms are four coordinated and all the Al atoms are six coordinated. Among the 12 distinct bonds, only one Al ( ${}^I4g$ )-O( ${}^I4g$ ) bond breaks and reforms during the transformation while the rest remain almost unchanged. We denote this one bond breaking and reforming mechanism simply as OB-BAR. The OB-BAR mechanism happens for 1/3 of the O atoms ( ${}^I4g$ ) and 1/2 of the Al atoms ( ${}^I4g$ ). The largest Al-O distance of the breaking bond corresponds to  $t_p = 1/2$ .

The volume variation during the transformation is investigated (Figure 4.11) at different pressures. At low pressure, if the transition could occur, the volume would expand slightly up to  $t_p = 0.5$  and monotonically decrease to the volume of  $\text{Rh}_2\text{O}_3(\text{II})$  phase. As pressure increases, the volume expansion is gradually depressed and the volume variation takes place mainly between  $t_p = 0.4$  and 0.8. Relative to the corundum phase, the volume variation during the transition is  $0.151 \text{ \AA}^3/\text{atom}$  (2.3% reduction) at 84.0 GPa and  $0.132 \text{ \AA}^3/\text{atom}$  (2.2% reduction) at 160 GPa.

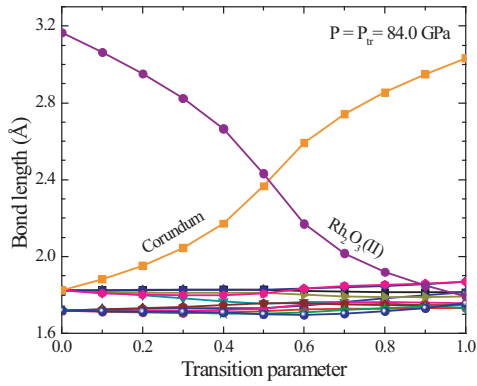


Figure 4.10: Al-O bond lengths as a function of the transition parameter at 84.0 GPa. As the transition parameter changes from 0 to 1, corundum structure transforms smoothly to the  $\text{Rh}_2\text{O}_3(\text{II})$  phase. There are 12 distinct bonds and only one bond breaks and reforms during the transformation.

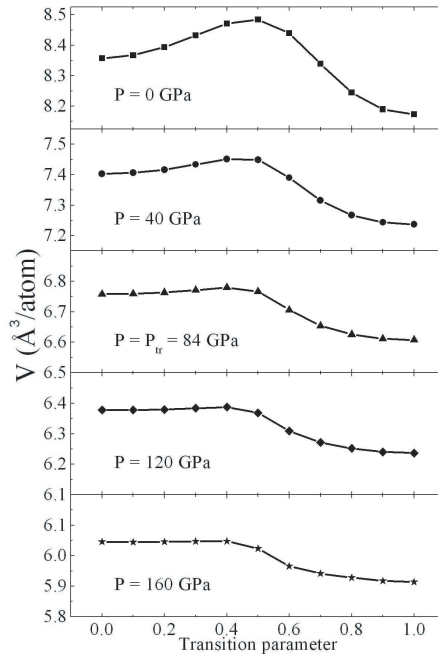


Figure 4.11: Volume per atom for the corundum  $\rightarrow$   $\text{Rh}_2\text{O}_3(\text{II})$  transformation at several pressures. Same volume ranges are used to illustrate the pressure effect.

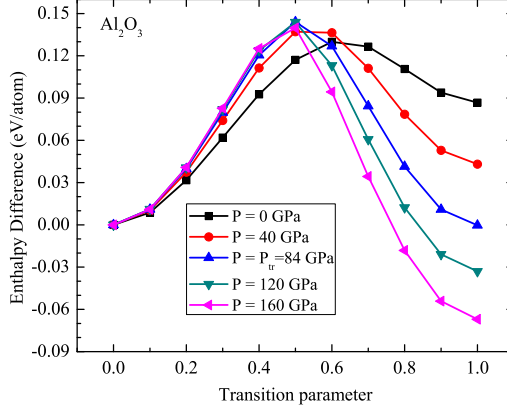


Figure 4.12: Enthalpies for the corundum $\rightarrow$ Rh<sub>2</sub>O<sub>3</sub>(II) transformation at several pressures.

For the corundum $\rightarrow$ Rh<sub>2</sub>O<sub>3</sub>(II) transition at room temperature (no heating in experiments), it is a good approximation to use enthalpy instead of Gibbs free energy to investigate the phase transition. We calculate the enthalpy along the transformation path at several pressures, as shown in Figure 4.12 (relative to the corundum phase). One can see that the forward barrier height (corundum $\rightarrow$ Rh<sub>2</sub>O<sub>3</sub>(II)) is not pressure sensitive (Figure 4.13), whereas the backward barrier height (Rh<sub>2</sub>O<sub>3</sub>(II) $\rightarrow$ corundum) decreases significantly on decompression. The forward barrier is about 140 meV/atom at and above  $P_t$ . The “constant” forward barrier height is in agreement with the observation that corundum phase is stable up to 175 GPa without heating. The backward barrier has a magnitude of 144 meV/atom at  $P_t$  and it drops to 43 meV/atom at 0 GPa. The decreasing backward barrier height is consistent with Lin’s findings that the high-pressure Rh<sub>2</sub>O<sub>3</sub>(II) phase is not quenchable to low pressures<sup>10</sup>. And, our estimated barrier height should be considered as an upper limit of the real barrier. It is very likely that the small backward barrier can be overcome by the room temperature thermal energy at low pressures.

We also calculated the full phonon spectra to investigate the dynamical stability of corundum phase at high pressure (Figure 4.14) and Rh<sub>2</sub>O<sub>3</sub>(II) phase at low pressure (Figure 4.15). Both are dynamically stable, which means that the meta-stability of each phase is due to kinetic reasons.

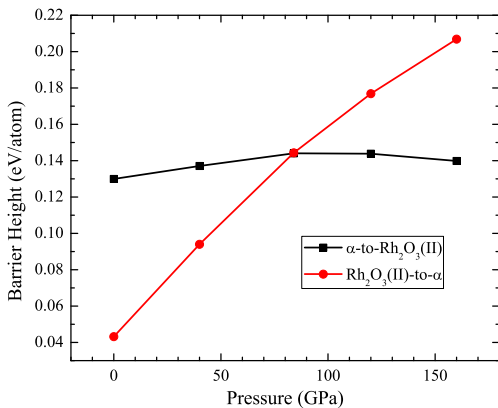


Figure 4.13: Enthalpy barrier height for the corundum $\rightarrow$ Rh<sub>2</sub>O<sub>3</sub>(II) and Rh<sub>2</sub>O<sub>3</sub>(II) $\rightarrow$ corundum transformations as a function of pressure.

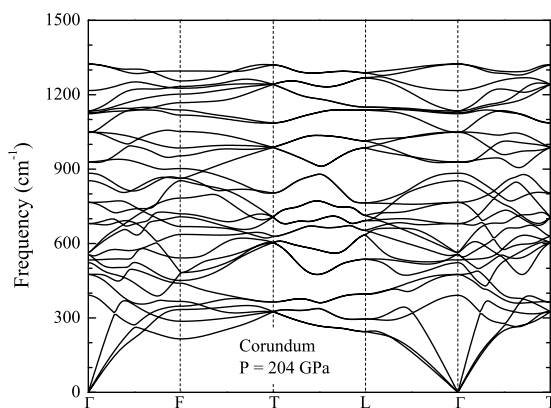


Figure 4.14: Calculated phonon dispersion curves of corundum-Al<sub>2</sub>O<sub>3</sub> at 204 GPa.

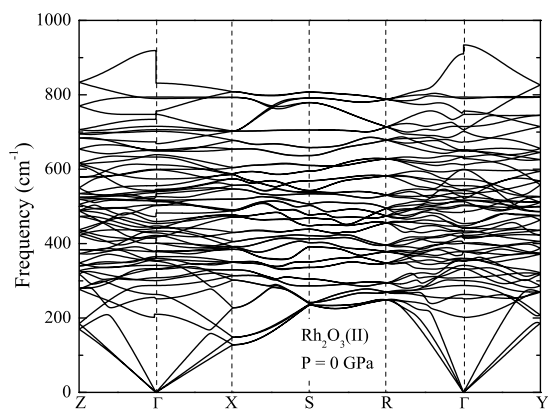


Figure 4.15: Calculated phonon dispersion curves of Rh<sub>2</sub>O<sub>3</sub>(II)-Al<sub>2</sub>O<sub>3</sub> at 0 GPa.

#### 4.1.5 Thermal Properties

Within the QHA, thermodynamic properties are calculated as described in Section 3.3. Here, in the case of  $\text{Al}_2\text{O}_3$ , the static energy is fitted to the 3<sup>rd</sup>-order Birch-Murnaghan equation of state (BM-EOS) and the thermal free energy is fitted to the 2<sup>nd</sup>-order BM-EOS.  $F(T, V) = E_{static}(V) + F_{vib}(T, V)$ . Our calculated zero pressure thermal expansion coefficient (TEC) of  $\alpha\text{-Al}_2\text{O}_3$  as a function of temperature using either US-PP or PAW method are compared with former measurements. First, no negative TEC is found at low temperatures which is consistent with the positive pressure dependencies of Raman and IR frequencies (Figure 4.3 and 4.4). Below 300 K, our US-PP and PAW results are coincident and both agree well with Wachtman *et al.*<sup>16</sup> and Schauer<sup>17</sup>, while slight underestimation appears with increasing temperature. Above 300 K, the experimental data are widely spread over the temperature range from 300 K to 2400 K. Our US-PP data is in good agreement with Amatuni *et al.*'s result<sup>18</sup> measured from 300 K to 2000 K, and with Aldebert *et al.*'s result<sup>20</sup> at temperatures above 1000 K. Our PAW calculation predict a slightly larger TEC than that from using US-PP above room temperature. Our PAW data lies in the middle of the experimental data and agrees with Schauer's data below 700 K and Wachtman *et al.*'s data above 1200 K. At 2500 K, our predicted TEC from US-PP is  $2.8 \times 10^{-5} \text{ K}^{-1}$ , and  $3.0 \times 10^{-5} \text{ K}^{-1}$  from PAW method.

At elevated pressures, the TEC decreases as shown in Figure 4.17. One can see that the TEC predicted by PAW method is larger than that from US-PP at any pressure. Presently no measurement is reported for TEC of corundum at high pressures. Hama and Suito<sup>26</sup> have calculated the thermal expansivity of corundum using empirical model for several pressures (same pressures as ours) as a function of temperature up to 2000 K. Their calculated TEC at 2000 K are  $3.0 \times 10^{-5} \text{ K}^{-1}$ ,  $2.5 \times 10^{-5} \text{ K}^{-1}$ ,  $2.1 \times 10^{-5} \text{ K}^{-1}$ ,  $1.6 \times 10^{-5} \text{ K}^{-1}$  and  $1.1 \times 10^{-5} \text{ K}^{-1}$  at 0, 10, 20, 50 and 100 GPa. The TEC we predict from US-PP (PAW) at the same temperature are  $2.7 \times 10^{-5} \text{ K}^{-1}$  ( $2.9 \times 10^{-5} \text{ K}^{-1}$ ),  $2.3 \times 10^{-5} \text{ K}^{-1}$  ( $2.5 \times 10^{-5} \text{ K}^{-1}$ ),  $2.1 \times 10^{-5} \text{ K}^{-1}$  ( $2.2 \times 10^{-5} \text{ K}^{-1}$ ),  $1.5 \times 10^{-5} \text{ K}^{-1}$  ( $1.6 \times 10^{-5} \text{ K}^{-1}$ ) and  $1.0 \times 10^{-5} \text{ K}^{-1}$  ( $1.1 \times 10^{-5} \text{ K}^{-1}$ )

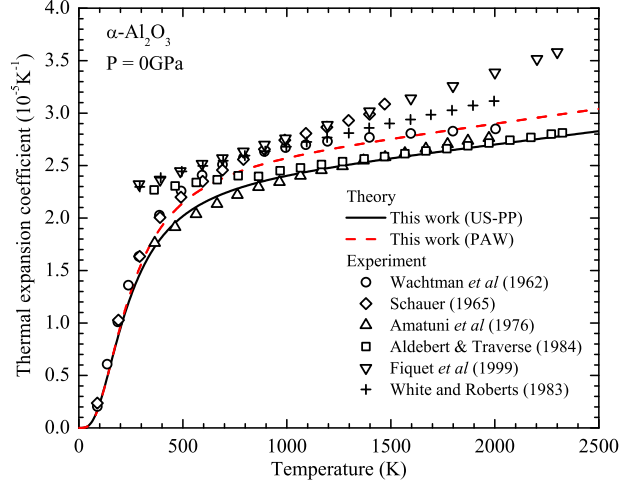


Figure 4.16: Comparison of the present theoretical calculation with measured thermal expansion coefficients of  $\alpha\text{-Al}_2\text{O}_3$  as a function of temperature at zero pressure. Solid and dashed lines represent our LDA calculations using US-PP and PAW method, respectively. Discrete symbols are reported experimental data.<sup>16–21</sup>

at 0, 10, 20, 50 and 100 GPa, respectively. Our PAW result is in very good agreement with Hama and Suito’s results.

In Figure 4.18, the calculated temperature dependence of adiabatic bulk modulus at zero pressure are compared with experimental values. Below 200 K,  $B_S$  does remains nearly unchanged with respect to temperature, which is the case for both calculation and measurements. Our PAW  $B_S$  at 0 K is in consistence with Chung *et al.*<sup>24</sup> and Teffet’s<sup>23</sup> data and our US-PP  $B_S$  at 0 K has an underestimation of about 4%. The temperature dependence predicted by US-PP and PAW are about -0.0122 GPa/K, which is larger than the experimental slope of -0.020 GPa/K. At 1800 K, the US-PP (PAW) calculated  $B_S$  overestimates about 1.8% (5.4%) compared with Goto *et al.*’s data<sup>25</sup>. As shown in Figure 4.19, our calculated isobaric hear capacity  $C_P$  and entropy  $S$  reproduce the zero pressure experimental result from Furukawa *et al.*<sup>22</sup> from 0 K to 1200 K. The  $C_P$  and  $S$  calculated using US-PP and PAW yield very similar values.

For the two high-pressure polymorphs, i.e.,  $\text{Rh}_2\text{O}_3(\text{II})$  and pPV, the TEC are calculated as a function of temperature at several pressures, as shown in Figure 4.20 and 4.21. US-PP



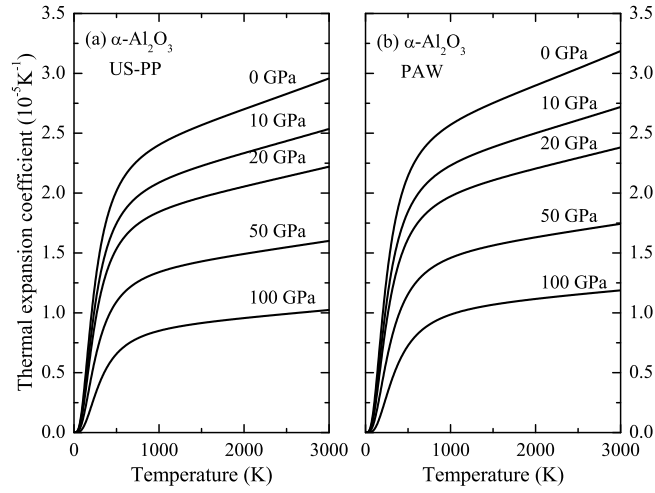


Figure 4.17: Theoretical thermal expansion coefficients of  $\alpha\text{-Al}_2\text{O}_3$  as a function of temperature at several pressures from using (a) US-PP, (b) PAW.

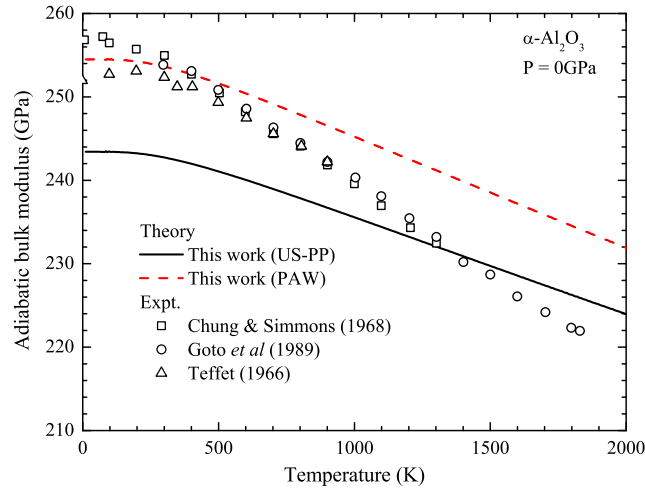


Figure 4.18: Comparison of the present LDA predicted adiabatic bulk modulus as a function of temperature of  $\alpha\text{-Al}_2\text{O}_3$  with Voigt-Ruess-Hill data by Teffet<sup>23</sup>, by Goto *et al.*<sup>25</sup> and the polycrystalline data by sound velocity measurements by Chung and Simmons<sup>24</sup>.

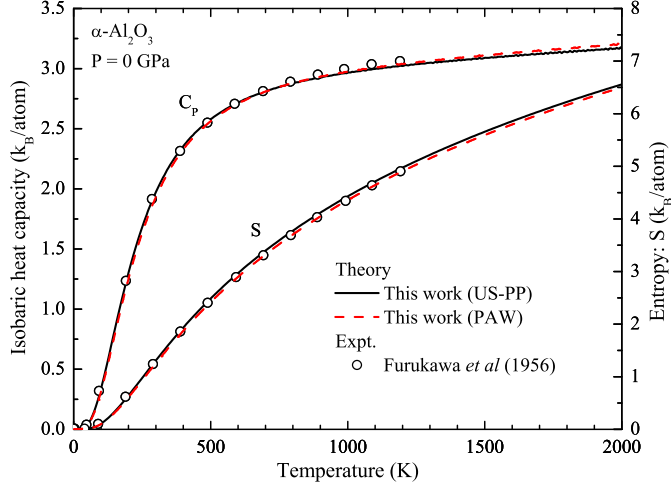


Figure 4.19: Comparison of calculated isobaric heat capacity and entropy as a function of temperature of  $\alpha$ - $\text{Al}_2\text{O}_3$  with experimental data at zero pressure. Discrete open circles denote measured data from Furukawa<sup>22</sup>.

and PAW provide comparable prediction at both low pressure and high pressure for the  $\text{Rh}_2\text{O}_3(\text{II})$  phase, whose calculated TEC are larger than those of corundum phase at any pressure. The TEC difference between two phases decreases with increasing pressure. Since the pPV phase is unstable at low pressures, the temperature dependence of TEC of pPV- $\text{Al}_2\text{O}_3$  is plotted at pressures from 80 GPa to 200 GPa. TEC from US-PP is smaller than that from PAW. Above 100 GPa, the TEC of corundum,  $\text{Rh}_2\text{O}_3(\text{II})$  and pPV are predicted to be comparable. Experimental data of TEC for the high-pressure phases are desired to make further comparison.

#### 4.1.6 High Pressure Elasticity

In this section, the athermal elastic constants of  $\alpha$ -,  $\text{Rh}_2\text{O}_3(\text{II})$ - and pPV- $\text{Al}_2\text{O}_3$  are determined from the strain-energy density relation, as described in Appendix B. The elasticity calculation adopted same models and settings as the static energy-volume calculation, i.e., primitive unit cells, same Brillouin zone  $\mathbf{k}$ -point samplings and plane-wave cut-off energies. Strain parameter  $\epsilon = 2.5\%$  is used for the trigonal corundum phase while  $\epsilon = 1.5\%$  for the orthorhombic  $\text{Rh}_2\text{O}_3(\text{II})$  and pPV phases.

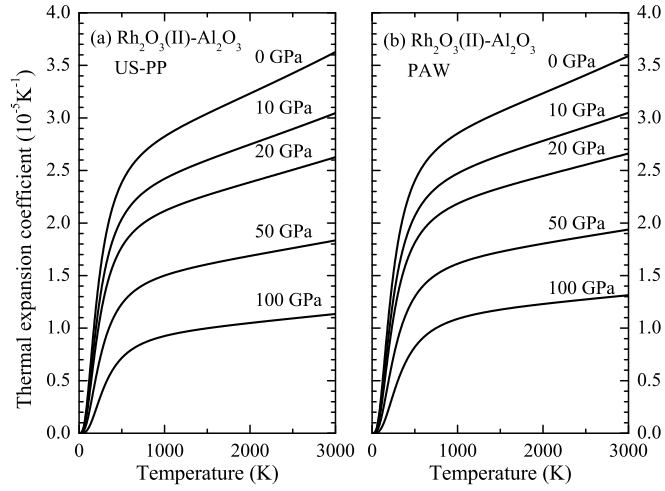


Figure 4.20: LDA calculated thermal expansion coefficients of  $\text{Rh}_2\text{O}_3(\text{II})\text{-Al}_2\text{O}_3$  at several pressures as a function of temperature up to 3000 K. (a) US-PP, (b) PAW

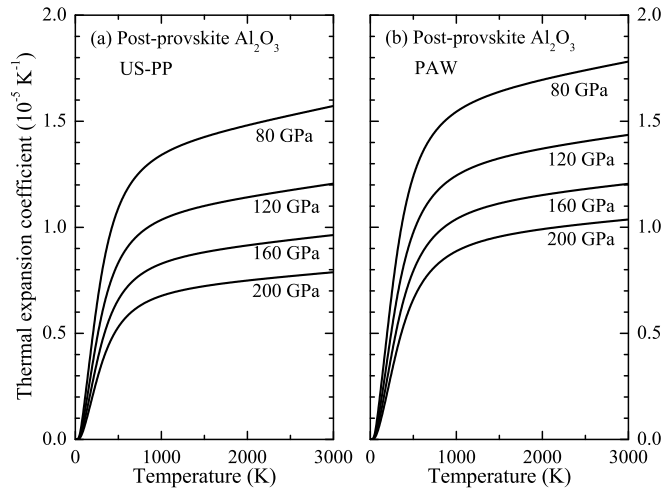


Figure 4.21: LDA calculated thermal expansion coefficients of  $\text{pPV-Al}_2\text{O}_3$  at several pressures as a function of temperature up to 3000 K. (a) US-PP, (b) PAW

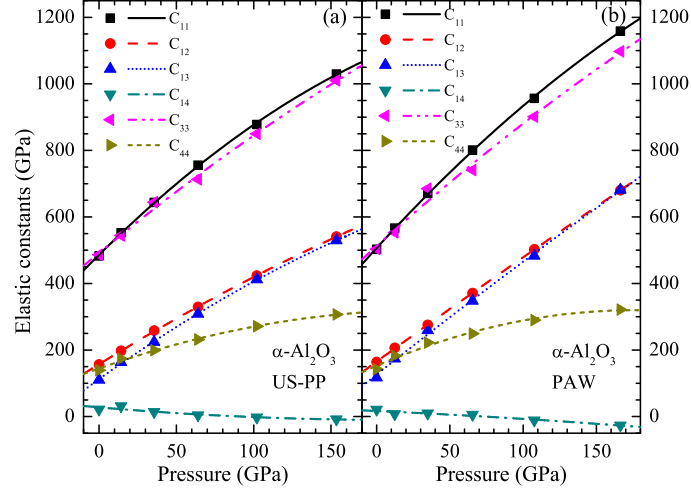


Figure 4.22: Pressure dependence of the elastic constants of corundum. (a) US-PP, (b) PAW. Discrete symbols represent directly calculated data. Curves are from the  $2^{nd}$ -order polynomial fitting.

There are six independent non-zero elastic constants for corundum, i.e.,  $C_{11}$ ,  $C_{33}$ ,  $C_{44}$ ,  $C_{12}$ ,  $C_{13}$ ,  $C_{14}$ .  $C_{ij}$  as a function of pressure using US-PP and PAW are shown in Figure 4.22. Second order polynomial fitting is applied since  $\partial C_{ij}/\partial P$  decreases with pressure. Our calculated zero pressure elastic moduli and their pressure derivatives at 0 GPa are listed in Table 4.5, together with previous calculations and experimental data. In 2004, Gladden *et al.*<sup>33</sup> corrected a long existing incorrect sign of  $C_{14}$ , which should be positive. Excellent agreement is obtained between our PAW results with the current accepted measured data, whereas the US-PP results show underestimation of 3-5%. The pressure dependence we predicted is in reasonable agreement with the measurement. PAW result is still better than US-PP but  $\partial C_{11}/\partial P$ ,  $\partial C_{33}/\partial P$  are noticeably smaller than the experimental values. This could be due to the fact that measurements were taken at room temperature and at pressures up to 1 GPa. We think  $\partial C_{14}/\partial P$  should be negative since the previous sign of  $C_{14}$  need to be reversed.  $C_{11}$  and  $C_{33}$  of corundum are comparable up to 160 GPa which indicate the crystal has similar compressibility along  $c$  axis and in the  $a$ - $b$  plane.  $C_{14}$  decreases with increasing pressure and changes sign at about 70 GPa (US-PP) or 84 GPa (PAW).

Table 4.5: Elastic constants of corundum at zero pressure and their pressure dependencies

Source	$C_{11}$	$C_{33}$	$C_{44}$	$C_{12}$	$C_{13}$	$C_{14}$
	$C_{ij}$ (GPa)					
This work (US-PP)	483	486	139	156	110	21
This work (PAW)	503	503	142	164	117	21
Calculation <sup>30</sup>	540	455	157	157	130	-48
Calculation <sup>31</sup>	502	501	157	161	125	-19
Calculation (LDA) <sup>35</sup>	497	493	154	165	130	19
Experiment <sup>28</sup>	497	498	147	164	111	-24
Experiment <sup>29</sup>	498	502	147	163	117	-23
Experiment <sup>33</sup>	498	503	147	163	116	23
	$\partial C_{ij}/\partial P$					
This work (US-PP)	4.62	3.83	1.64	2.86	3.34	-0.40
This work (PAW)	4.82	3.96	1.90	3.20	3.50	-0.20
Calculation <sup>30</sup>	5.78	4.36	1.62	3.44	3.56	0.18
Calculation <sup>31</sup>	5.52	5.10	2.03	3.09	3.57	0.19
Experiment <sup>29</sup>	6.17	5.00	2.24	3.28	3.65	0.13

Nine independent elastic constants exist for orthorhombic crystals, which are  $C_{11}$ ,  $C_{22}$ ,  $C_{33}$ ,  $C_{12}$ ,  $C_{13}$ ,  $C_{23}$ ,  $C_{44}$ ,  $C_{55}$ , and  $C_{66}$ . For  $\text{Rh}_2\text{O}_3(\text{II})$  phase, with increasing pressure (Figure 4.23), the relative magnitudes of  $C_{11}$  and  $C_{33}$  (largest) remain stable but  $C_{22}$  becomes smaller than  $C_{11}$  at high pressures. Consequently the  $c$  axis is the least compressible and the  $b$  axis is getting softer compared with  $a$  axis. The shear moduli are similar in their magnitudes at low pressure and diverge under compression. Again, our PAW result shows slightly better agreement with former LDA calculation from Duan *et al.*<sup>31</sup>.

In Section 4.1.4, we showed that corundum structure can be viewed as a monoclinic lattice which is closely related to the orthorhombic  $\text{Rh}_2\text{O}_3(\text{II})$  phase. To directly compare the elasticity between the corundum and  $\text{Rh}_2\text{O}_3(\text{II})$  phase, we calculated the elastic constants of both phases at 0, 84.0 GPa ( $P_t$ ) and 160 GPa and the results are listed in Table 4.6. Common 20-atom monoclinic unit cell with unique axis  $b$  was used and thirteen independent elastic constants  $C_{11}$ ,  $C_{22}$ ,  $C_{33}$ ,  $C_{12}$ ,  $C_{13}$ ,  $C_{23}$ ,  $C_{44}$ ,  $C_{55}$ ,  $C_{66}$ ,  $C_{15}$ ,  $C_{25}$ ,  $C_{35}$ ,  $C_{46}$  were calculated. At zero pressure,  $C_{ij}$  of corundum are similar to those of  $\text{Rh}_2\text{O}_3(\text{II})$  phase except  $C_{33}$ , which can be ascribed to the major difference between two structures (internal

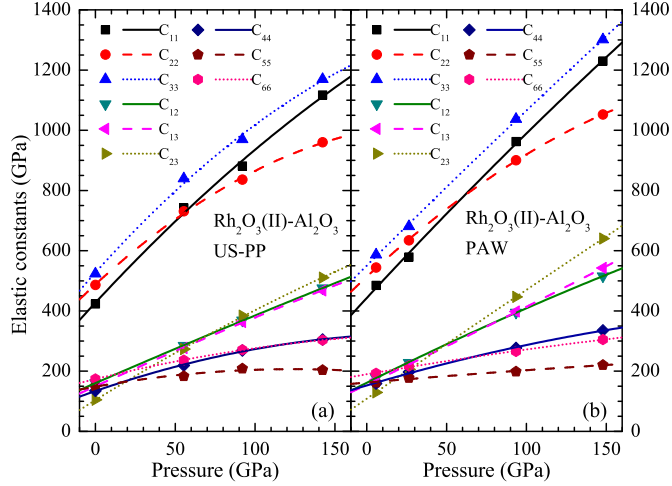


Figure 4.23: Pressure dependence of the elastic constants of  $\text{Rh}_2\text{O}_3(\text{II})\text{-Al}_2\text{O}_3$ . (a) US-PP, (b) PAW. Discrete symbols represent directly calculated data. Curves are from the  $2^{\text{nd}}$ -order polynomial fitting.

coordinates along  $c$  axis). At high pressures, the elastic constants of corundum are still differ with  $\text{Rh}_2\text{O}_3(\text{II})$  phase mostly by  $C_{33}$ . Larger  $C_{33}$  predicted from  $\text{Rh}_2\text{O}_3(\text{II})$  phase implies its less compressibility along the  $c$  axis.

Pressure dependence of  $C_{ij}$  of pPV phase using US-PP (PAW) are shown in Figure 4.24. Previous GGA calculated elastic constants by Stackhouse *et al.*<sup>36</sup> at 136 GPa is generally consistent with our predictions. They agree with our US-PP data except their  $C_{23}$  and  $C_{66}$  are larger, and their predicted  $C_{11}$ ,  $C_{22}$ ,  $C_{33}$ , and  $C_{23}$  are smaller when compared with our PAW result. Magnitudes of  $C_{ij}$  of pPV phase is not significantly larger than those of  $\alpha$  and  $\text{Rh}_2\text{O}_3(\text{II})$  phase. One major difference is that  $a$  axis is the least compressible in pPV phase. Currently no elastic properties have been measured for the high-pressure phases.

#### 4.1.7 Conclusions

We have systematically investigated the pressure-induced phase transformations of  $\text{Al}_2\text{O}_3$  using density functional theory within the local density approximation (LDA). The sequence of transitions under compression, i.e., corundum  $\rightarrow$   $\text{Rh}_2\text{O}_3(\text{II})$   $\rightarrow$  pPV, and  $T$ - $P$

Table 4.6: Comparison of elastic moduli between corundum and  $\text{Rh}_2\text{O}_3(\text{II})$  phase. The corundum phase is treated as a monoclinic crystal with 20 atoms per unit cell.

	0 GPa		84.0 GPa		160 GPa	
	corundum	$\text{Rh}_2\text{O}_3(\text{II})$	corundum	$\text{Rh}_2\text{O}_3(\text{II})$	corundum	$\text{Rh}_2\text{O}_3(\text{II})$
$C_{11}$	450	424	956	976	1235	1288
$C_{22}$	490	501	844	851	1073	1085
$C_{33}$	455	541	852	1013	1213	1320
$C_{12}$	180	170	420	369	639	541
$C_{13}$	161	163	358	374	566	571
$C_{23}$	125	109	412	418	680	692
$C_{44}$	126	134	246	261	303	331
$C_{55}$	185	170	230	218	207	204
$C_{66}$	184	182	226	260	234	287
$C_{15}$	-3	0	7	0	-5	0
$C_{25}$	16	0	19	0	10	0
$C_{35}$	9	0	21	0	24	0
$C_{46}$	2	0	-14	0	-25	0

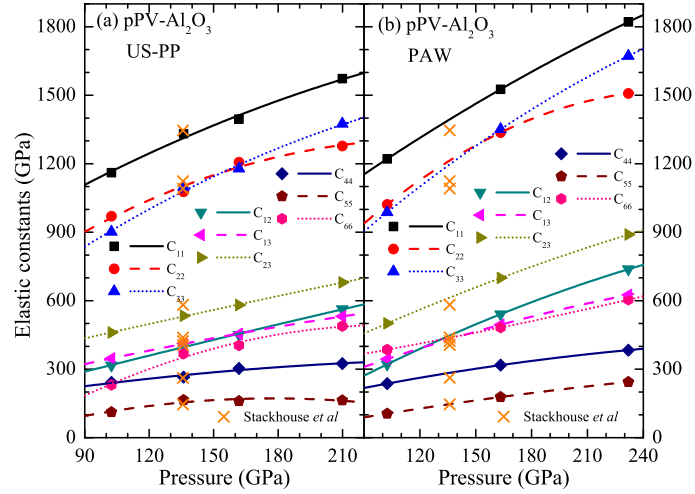


Figure 4.24: Pressure dependence of the elastic constants of  $\text{pPV-Al}_2\text{O}_3$ . (a) US-PP, (b) PAW. Discrete symbols (except crosses) represent directly calculated data from this work. Crosses denote GGA calculation from Stackhouse *et al.*<sup>36</sup> at 136 GPa. Curves are from the  $2^{\text{nd}}$ -order polynomial fitting.

phase diagram we obtained are consistent with previous theoretical and experimental studies. Zero pressure  $\Gamma$ -point phonon frequencies and their pressure dependencies are calculated for three stable polymorphs. Comparison with measured data of corundum and theoretical Raman frequencies of pPV phase suggest that, within LDA, predictions using PAW method is better than US-PP. This conclusion is also confirmed by the study of elastic properties.

We show that the rhombohedral corundum phase can also be interpreted as a slightly distorted orthorhombic structure with monoclinic symmetry, which is closely related to the  $\text{Rh}_2\text{O}_3(\text{II})$  phase. A microscopic transformation mechanism is proposed for the corundum-to- $\text{Rh}_2\text{O}_3(\text{II})$  transition, which is characterized by one bond breaking-and-reforming (OB-BAR) for 1/3 of the four-coordinated O atoms ( ${}^I4g$  site) and half of the six-coordinated Al atoms ( ${}^I4g$  site). Our calculated forward (C-to-R) enthalpy barrier height is 144 meV/atom at the equilibrium transition pressure and it is not pressure sensitive. On the other hand, the backward (R-to-C) barrier height decreases significantly under decompression, which indicates that the  $\text{Rh}_2\text{O}_3(\text{II})$  phase is unlikely to be quenchable to ambient conditions.

The temperature dependencies of thermal expansion coefficient from low to high pressures have been predicted for  $\alpha$ -,  $\text{Rh}_2\text{O}_3(\text{II})$ -, and pPV- $\text{Al}_2\text{O}_3$ . For corundum at zero pressure, our US-PP data is in good agreement with Amatuni *et al.*'s result measured from 300 K to 2000 K, and with Aldebert *et al.*'s result at temperatures above 1000 K. Our PAW data lies in the middle of the experimental data and agrees with Schauer's data below 700 K and Wachtman *et al.*'s data above 1200 K. Our calculated heat capacity  $C_P$ , entropy and adiabatic bulk modulus of corundum phase also agree well with measured results.

We have calculated the elastic constants and their pressure dependencies for corundum and two high-pressure phases. PAW calculated  $C_{ij}$  yield better agreement with accepted experimental data of  $\alpha$ - $\text{Al}_2\text{O}_3$ . We confirmed that the sign of  $C_{14}$  is positive. In addition, the elastic constants of the corundum and  $\text{Rh}_2\text{O}_3(\text{II})$  phase are found comparable, except for  $C_{33}$ . The larger  $C_{33}$  of  $\text{Rh}_2\text{O}_3(\text{II})$  phase means that its c axis is less compressible than that of corundum.



## 4.2 Aluminum Nitride: AlN

### 4.2.1 Introduction

AlN is an important semiconductor primarily due to its wide band-gap and thermal properties. The structural changes and properties at high pressures are well studied. Experiments<sup>37-40</sup> and calculations<sup>41-46</sup> have revealed that a pressure-induced first-order phase transition from wurtzite (B4) to rocksalt (B1) structure happens for AlN. On the experimental side, without heating, the lowest pressure at which the rocksalt structure started to show up is 14 GPa<sup>39</sup> and the B4-to-B1 transition was observed to complete at 20-31.4 GPa<sup>39,40</sup>. Xia *et al.* also found that the rocksalt phase is quenchable to ambient conditions<sup>39</sup>. On the other hand, theoretical calculations consistently predicted a transition pressure that is lower than the experimental values. Most of the recent first-principles predicted static  $P_t$  is less than 10 GPa<sup>43,46</sup>. The discrepancy implies the existence of a hysteresis for the forward and backward transitions that caused by a large kinetic barrier in this transition.

AlN is a good example material to study the microscopic mechanisms of the first-order solid-solid phase transformations with no group-subgroup relation. In its wurtzite to rocksalt transition, the coordination number changes from four to six. The wurtzite and rocksalt structures belong to the  $P6_3mc$  and  $Fm\bar{3}m$  symmetry, respectively. There are four atoms per primitive unit cell for wurtzite phase and two atoms for rocksalt phase. The B4-to-B1 transition has been studied intensively for many III-V and II-VI semiconductors, such as AlN, GaN, InN, ZnO, CdS, and CdSe, which crystallize in wurtzite (or zincblende) structure at ambient conditions and transform into the rocksalt structure at high pressures. Because of the interesting properties and applications of these semiconductors, numerous studies have been conducted from both experiments and calculations that are intended to understand the transition mechanism at the atomic level. Knowledge from these studies can help to predict and possibly control transitions and transition related properties.

Although the reconstructive phase transitions may involve nucleation processes, diffusionless collective atomic displacements can still characterize the transformation on a local

basis. The concept of transition pathway (TP) is then possible to describe the transformation from the starting phase to the ending phase in a continuous manner. Among the infinite number of ways for one structure to transform into another, the theoretical studies are restricted only to those most possible paths, e.g., preservation of bonds, less strains, etc. For the B4-to-B1 transition there has been, in principle, two different approaches to propose transition pathways. The first approach adopted a systematic procedure with certain restrictions to find the maximum number of pathways which belong to common subgroups of the two end structures. Using the computer program *COMSUBS*<sup>47</sup>, Stokes *et al.* proposed five paths (Figure 4.25 and 4.26) by preserving the nearest neighbors along the transition pathway and limiting the size of unit cell to no more than four different Wyckoff positions<sup>48</sup>. He also found a common bilayer sliding mechanism along five paths, which had been pointed out by Zahn *et al.*<sup>49</sup> and Sowa<sup>50</sup>. Another work adopted the systematic approach is from Capillas *et al.*<sup>51</sup>, which was performed using the databases and tools provided by the *Bilbao Crystallographic Server*<sup>52</sup>. They proposed eight possible paths with different orthorhombic and monoclinic symmetries by setting the maximum  $k$ -index equal to 4, strain tolerance  $S_{tol} < 0.15$  and maximum atomic displacement  $\Delta_{tol} < 2 \text{ \AA}$ . The intermediate structures along all the eight paths have eight atoms per unit cell. The difference between these two reports is that the nearest neighbors are not preserved along all the eight paths proposed by Capillas *et al.*

The second approach is less systematic and most of the proposed models can be summarized as two paths which are characterized by different intermediate structures, i.e., the “hexagonal” path and the “tetragonal” path. These two paths have been proposed and investigated intensively by experimental<sup>177–180</sup> and theoretical<sup>44,46,49,50,53–55,181–183</sup> works, and they both belong to the  $Cmc2_1$  path in the systematic approach. Cai *et al.* has studied the “hexagonal” and “tetragonal” paths with LDA calculations, and concluded that the “hexagonal” path is favored for AlN<sup>46</sup>. The  $Pna2_1$  and  $P2_1$  paths have also been described in previous works<sup>49,50,55</sup>.

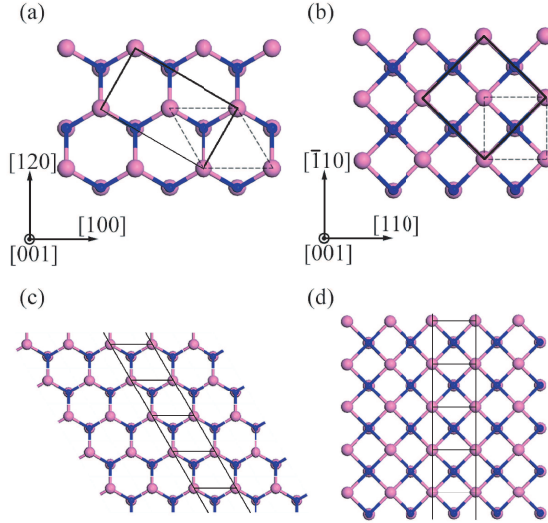


Figure 4.25: Phase transformation along TP1. (a) Unit cell of B4 structure, (b) Unit cell of B1 structure, (c), (d) Transformation pattern of “transition units” in B4 and B1 phases. Dashed lines denote primitive unit cell. (Origin shifted onto the position of an atom for better illustration of the unit cell.)

DFT calculations from Shimojo *et al.* showed that the enthalpy barrier of transformation is independent of the three paths ( $Cmc2_1$ ,  $Pna2_1$  and  $P2_1$ ) for CdSe. Cai suggested, without calculation, that the B4-to-B1 transition is characterized by the transformation of the four-atom “transition unit” (Figure 4.27), while the long-range pattern may be less important. On the other hand, using MD simulations, Zahn *et al.* pointed out that the favored paths have a tendency to avoid excess strains during the transformation.

It would be interesting to investigate the proposed TPs with another material via first-principles method. Previous studies<sup>53–55</sup> suggested that the energetically favored TPs are bond preserving. In this paper, we studied all five bond-preserving TPs proposed by Stokes *et al.* and one bond-breaking TP proposed by Capillas *et al.* from an energetic point of view for the B4-to-B1 transition in AlN. The correlation of the enthalpy barrier with different TPs and strains will be discussed. We also relate the bilayer sliding mechanism to the long-range patterns of “transition units”, and Cai’s hypothesis is examined.

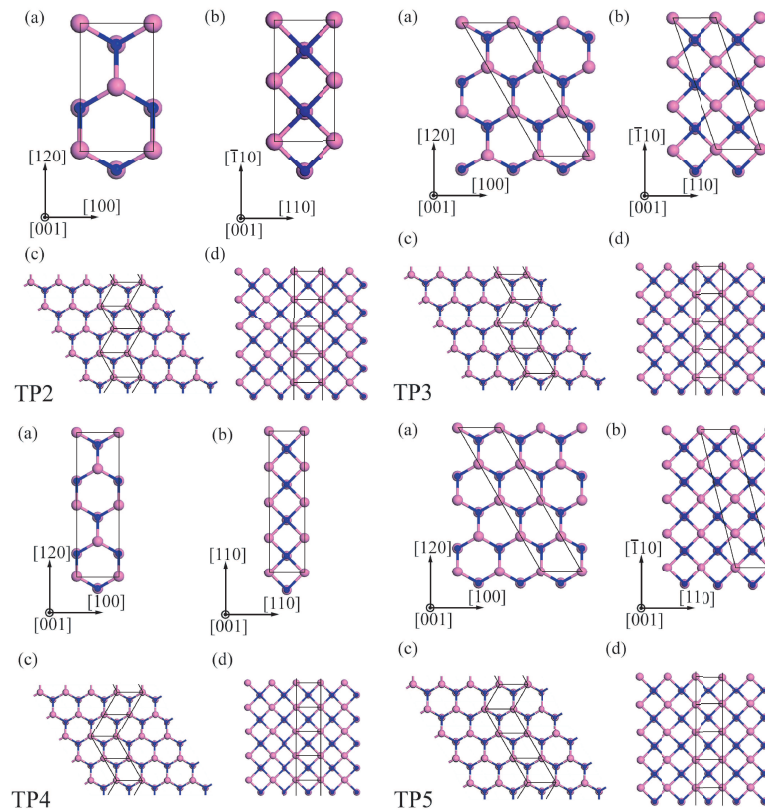


Figure 4.26: Phase transformation along TP2, TP3, TP4 and TP5. (a) Unit cell of B4 structure, (b) Unit cell of B1 structure, (c), (d) Transformation pattern of “transition units” in B4 and B1 phases. (Origin shifted onto the position of an atom for better illustration of unit cell.)

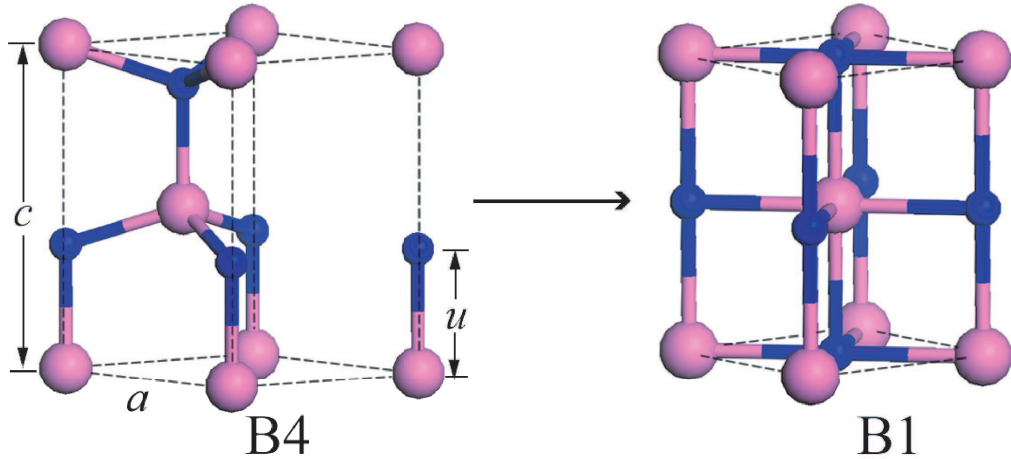


Figure 4.27: Four-atom “transition unit” from B4 to B1 structure.

#### 4.2.2 Total Energy and Equilibrium Phase Transition

We first calculated the total energies of the two end phases, i.e., wurtzite and rocksalt-AlN. The calculation was within the frame of density functional theory (DFT) and adopted Vanderbilt’s ultrasoft pseudopotentials (US-PP)<sup>121</sup>, as implemented in the VASP code<sup>139</sup>. The exchange and correlation functional is treated with local density approximation (LDA). Wave functions of valence electrons were expanded with plane-wave basis set up to the cut-off kinetic energy of 348 eV. Total energy change of  $10^{-9}$  eV was chosen as the convergence criterion for the self-consistent iterations. The  $k$ -point sampling for Brillouin zone integration in our total energy calculations was carried out by the Monkhorst-Pack method with grids of  $12 \times 12 \times 8$  and  $16 \times 16 \times 16$  for wurtzite and rocksalt-AlN, respectively.

The calculated static energies at various volumes are fitted to the 3<sup>rd</sup>-order Birch-Murnaghan EOS<sup>159,160</sup>. General agreement of fitting parameters,  $B_0$  and  $B'$ , and zero pressure structural parameters is achieved between our calculation with other reported values (Table 4.7). The zero pressure bulk modulus we predicted is slightly less than those from other LDA calculations (<3%). This could be caused by the different pseudopotentials adopted.

Table 4.7: Third-order BM-EOS parameters, zero pressure structural parameters for B4 and B1-AlN and B4-to-B1 transition pressure  $P_t$ . Parameters listed for B1 phase is for the 8-atom conventional cubic unit cell.

Source	$B_0$ (GPa)	$B'$	$a$ (Å)	$c/a$	$u$	$P_t$ (GPa)
Wurtzite (B4)						
This work	202	3.61	3.084	1.601	0.382	9.85
Calculation <sup>184</sup>	209	5.58	3.057	1.617	0.380	
Calculation <sup>43</sup>	209	3.7	3.061	1.600	0.382	9.2
Calculation <sup>185</sup>	208	3.87	3.100	1.6	0.382	21
Calculation <sup>46</sup>	—	—	3.06	1.606	0.382	9.8
Experiment <sup>38</sup>	207.9±6.3	6.3±0.9		1.60		22.9
Experiment <sup>39</sup>	185.0±5.0	5.7±1.0	3.19	1.626		14-20
Experiment <sup>40</sup>						20-31.4
Rocksalt (B1)						
This work	266	3.76	4.02			
Calculation <sup>43</sup>	272	3.8	3.978			
Calculation <sup>185</sup>	275	4.02	4.031			
Calculation <sup>46</sup>			4.02			
Experiment <sup>39</sup>	221.0±5.0	4.8±1.0	4.043			
Experiment <sup>40</sup>	295±17	3.5±0.4	4.046			

The static transition pressure can be determined from the common tangent of the  $E-V$  curves (Figure 4.28) of B4 and B1 phases, or equivalently from the intersection of the  $H-P$  curves, which gives  $P_t = 9.85$  GPa. Our prediction is consistent with most of the recent LDA calculations<sup>43,46</sup>, however, apparently less than those observed<sup>37-40</sup>. Despite of the uncertainty of DFT calculations, we attribute the discrepancy to the relatively large kinetic barrier along the phase transformation, which will be discussed in the next Section. The quenchable high-pressure B1 phase also indicates the existence of the backward (B1-to-B4) barrier at ambient conditions<sup>39</sup>.

### 4.2.3 Microscopic Mechanism for the Wurtzite-to-Rocksalt Transition

Five bond-preserving TPs proposed by Stokes *et al.* are summarized in Table 4.8.

Stokes *et al.* found that each TP is characterized by a sequence of bilayer sliding mechanism, as described in their paper<sup>?</sup>. Each bilayer moves  $\pm a/2$  (hexagonal lattice

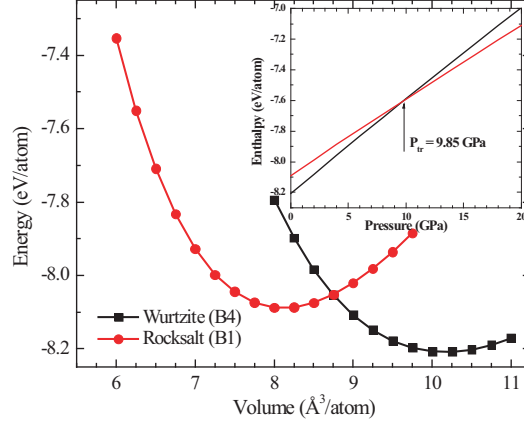


Figure 4.28: Cohesive energy per atom as a function of volume for B4 and B1-AlN. Enthalpy variation of both phases as a function of pressure is also shown.

Table 4.8: Bond-preserving TPs for the B4-to-B1 phase transition.  $G$  denotes the space group of two end structures and  $G'$  denotes the common subgroup.  $Z$  represents the number of formula units per unit cell along the TP. The transformation matrices are given with respect to the primitive unit cell lattice vectors and the fractional atomic coordinates are in terms of the setting of  $G'$ .  $u \approx 3/8$

TP	$G'$	$G$	$Z$	Transformation matrices	Coordinates (Al)	Coordinates (N)
1	$Cmc2_1$ (#36)	B4	4	(1, 1, 0), (-1, 1, 0), (0, 0, 1)	(0, 2/3, 0)	(0, 2/3, $u$ )
		B1	4	(1, -1, 1), (1, -1, -1), (1, 1, -1)	(0, 3/4, 0)	(0, 3/4, 1/2)
2	$Pna2_1$ (#33)	B4	4	(1, 2, 0), (-1, 0, 0), (0, 0, 1)	(1/3, 0, 0)	(1/3, 0, $u$ )
		B1	4	(-2, 2, 0), (0, 0, 1), (1, 1, -1)	(3/8, -1/4, 0)	(3/8, -1/4, 1/2)
3	$P2_1$ (#4)	B4	6	(-1, 0, 0), (0, 0, 1), (0, 3, 0)	(2/3, 0, 8/9)	(2/3, $u$ , 8/9)
				(1/3, 1/2, 7/9)	(1/3, $u+1/2$ , 7/9)	
		B1	6	(0, 0, 1), (1, 1, -1), (-3, 3, 1)	(2/3, 0, 5/9)	(2/3, $u$ , 5/9)
				(1/3, 0, 11/12)	(1/3, 1/2, 11/12)	
			(0, 1/2, 3/4)	(0, 1, 3/4)		
				(2/3, 0, 7/12)	(2/3, 1/2, 7/12)	
4	$Pna2_1$ (#33)	B4	8	(2, 4, 0), (-1, 0, 0), (0, 0, 1)	(19/24, 3/4, 0)	(19/24, 3/4, $u$ )
		B1	8	(-4, 4, 0), (0, 0, 1), (1, 1, -1)	(1/24, 1/4, 0)	(1/24, 1/4, $u$ )
				(13/16, 1/4, 0)	(13/16, 1/4, 1/2)	
				(1/16, 1/4, 0)	(1/16, 1/4, 1/2)	
5	$P2_1$ (#4)	B4	8	(-1, 0, 0), (0, 0, 1), (0, 4, 0)	(2/3, 0, 11/12)	(2/3, $u$ , 11/12)
				(1/3, 1/2, 5/6)	(1/3, $u+1/2$ , 5/6)	
		B1	8	(0, 0, 1), (1, 1, -1), (-4, 4, 1)	(2/3, 0, 5/12)	(2/3, $u$ , 5/12)
				(1/3, 1/2, 1/3)	(1/3, $u+1/2$ , 1/3)	
			(5/16, 0, 15/16)	(5/16, 1/2, 15/16)		
				(-1/16, 1/2, 13/16)	(-1/16, 1, 13/16)	
				(13/16, 0, 7/16)	(13/16, 1/2, 7/16)	
				(7/16, 1/2, 5/16)	(7/16, 1, 5/16)	

parameter) in the  $\pm[100]$  direction (in term of the B4 structure) relative to the adjacent bilayers. Besides the relative sliding of atomic bilayers, two other independent atomic displacements occur during the transformation, i.e., (1) N atoms with  $z = u \approx 3/8$  (and  $u - 1/2$ ) in the B4 phase displace in the  $[001]$  direction into the  $z = 1/2$  (and 0). (2) Spacings of bilayers increase until layers along  $[120]$  direction (in term of the B4 structure) are equally spaced apart. Illustration of five TPs listed in Table 4.8 are shown in Figure 4.25 and Figure 4.26. The small dark spheres represent N atoms and the large light spheres represent Al atoms. Referring to Stokes *et al.*'s description, the repeatable bilayer sliding patterns for the listed TPs are  $+$ ,  $+-$ ,  $++-$ ,  $++--$ , and  $++++-$  for TP1 through TP5, respectively. Where  $+$  means the bilayer slides  $+a/2$  relative to the previous bilayer and  $-$  means the bilayer slides  $-a/2$  relative to the previous bilayer.

We first examined the five bond-preserving TPs proposed by Stokes *et al.*<sup>48</sup>. The B4-to-B1 transformation along TP1 can be described by five independent parameters, i.e.,  $(a, b, c, u, v)$ . The parameters  $a$ ,  $b$ , and  $c$  are the orthorhombic cell edges,  $u$  is the relative position of two sublattices in  $[001]$  direction, and  $v$  is the relative displacements of atoms of alternating  $(\bar{1}10)$  planes in the direction of  $[\bar{1}10]$ . For TP2 and TP4, there are six degree of freedom, i.e.,  $(a, b, c, \delta, u, s)$ . Here  $\delta$  represents the relative displacements of atoms of alternating B4  $(010)$  planes in the  $[100]$  (unique-b axis) direction (in the setting of  $G'$ ), and  $s$  represents the atomic displacements in the sliding direction of bilayers. For TP3 and TP5, due to monoclinic symmetry, there is one more free parameter, angle  $\gamma$  between  $a$  and  $c$ . In Figure 4.25 and Figure 4.26, for clarity, we illustrate the unit cells with origins happen at the positions of atoms.

The complete information of the transition pathway requires computation of the potential energy as functions of all the degrees of freedom, i.e., a multi-dimension potential energy surface (PES). However, DFT calculation of 5-7 dimension PES is computationally expensive. In this dissertation, our main purpose is to obtain the activation barrier height for different TPs. And considering the hexagonal path suggested by Cai *et al.* for AlN<sup>46</sup>, we think the one dimensional PES can yield the correct kinetic barrier height. The only



parameter being controlled is  $v$  for TP1 or  $s$  for other TPs, which we believe is the parameter that characterizes for the structural transformation. Our calculated barrier height of TP1 will be compared with the 2D PES result of Cai *et al.* to ensure the validity of our simplified approach.

For the five TPs discussed above, we calculated the total energy as a function of the transition parameter. The transition parameter is defined to vary from 0 (B4 phase) to 1 (B1 phase) for the controlled free parameter, which is the  $y$  coordinates for TP1, TP2, TP4 and  $x$  coordinates for TP3, TP5. DFT calculation was performed by fixing the transition parameter and relaxing all the other external and internal coordinates. The initial structural parameters of the intermediate phases are generated from linear interpolation of the two end structures.  $x = x_i + (x_f - x_i) \cdot t_p$  where  $x$  denotes any internal or external parameter,  $x_i$  and  $x_f$  denote  $x$  values of the starting (B4) and ending (B1) structures, respectively. The  $k$ -point sampling for Brillouin zone integration was carried out by the Monkhorst-Pack method with grids of  $6 \times 4 \times 4$ ,  $4 \times 6 \times 4$ ,  $6 \times 4 \times 4$ ,  $4 \times 6 \times 6$  and  $6 \times 4 \times 4$  for TP1 through TP5, respectively. At each transition parameter, the calculation is made for several volumes which were later fitted to the  $2^{nd}$ -order BM-EOS in order to obtain the enthalpy-pressure relation.

The information of fractional coordinate  $u$  and angle  $\gamma$  (between  $a$  and  $b$ ) at 0 GPa and the transition pressure are extracted after the calculation of TP1. For  $\gamma$  larger than  $\sim 70^\circ$ ,  $u$  becomes 0.5 after relaxation, which is the value of B1 phase. So the enthalpy barrier we obtained is consistent with Cai *et al.*'s 2D PES. The calculated enthalpy as a function of the transition parameter for five TPs at different pressures from 0 to 30 GPa are shown in Figure 4.29. All five TPs yield comparable results, while the difference in the shape and position of the maximum enthalpy between TP1 and other TPs could be ascribed to the different transition parameters adopted. The discrepancies at  $t_p = 1$  should be due to the different size of unit cells and errors from fitting to equation of states. As can be seen from Figure 4.30, The forward (B4-to-B1) barrier height decreases with compression and the backward (B1-to-B4) barrier height decrease with decompression for all TPs. This can

explain the larger transition pressure observed in room temperature experiments compared with equilibrium transition pressure predicted by calculations. At 20 GPa, the forward activation barrier is about 80 meV/atom and continuously drops below 50 meV/atom upon compression up to 30 GPa. The low activation barrier height greatly increases the possibility of the occurrence of the B4-to-B1 phase transformation. On the other hand, the backward barrier height remains about 100 meV/atom even at 0 GPa. This is in agreement with the fact that the rocksalt phase can be quenchable to ambient conditions<sup>39</sup>. The activation barrier plot we obtained is very similar to the Figure 8 (a) of Cai *et al.*'s paper. Comparing our TP1 result with their calculation, the forward barrier heights we predicted are 0.199 eV/atom at 0 GPa, 0.128 eV/atom at 9.85 GPa, 0.102 eV/atom at 15 GPa and theirs are 0.219 eV/atom at 1 bar ( $10^{-4}$  GPa), 0.144 eV/atom at 9.8 GPa, 0.109 eV/atom at 15 GPa. We attribute the small discrepancy to the different symmetry and size of unit cell in both calculations. The volume sets used for fitting of EOS can also play a role. Considering the uncertainties involved in our calculation, the magnitudes of the barrier height of different TPs should be concluded as comparable at pressures from 0 to 30 GPa.

Since no apparent difference is found between TP1 and other TPs, we confirmed Cai *et al.*'s hypothesis, i.e., the four-atom "transition unit" is responsible for the B4-to-B1 transformation and different long-range arrangements of "transition units" are less important. From another point of view, Zahn *et al.*<sup>49</sup> pointed out that the favored TPs have a tendency to avoid excess strains during the transformation. TP2 and TP4, which have equal numbers of bilayer sliding in opposite directions, yield less strains. Our calculation show no clear preference of these two TPs over the rest. It is likely that the different strains involved in TPs may not be an important factor for the B4-to-B1 transformation.

We also calculated the #4 path proposed by Capillas *et al.*, which involves bond breaking during the phase transformation. The forward barrier heights are 0.956 meV/atom at 0 GPa and 0.976 meV/atom at 15 GPa, which are much larger than those calculated from the bond-preserving paths. So the bond-breaking path is less likely to be energetically favored if there are bond-preserving paths available.

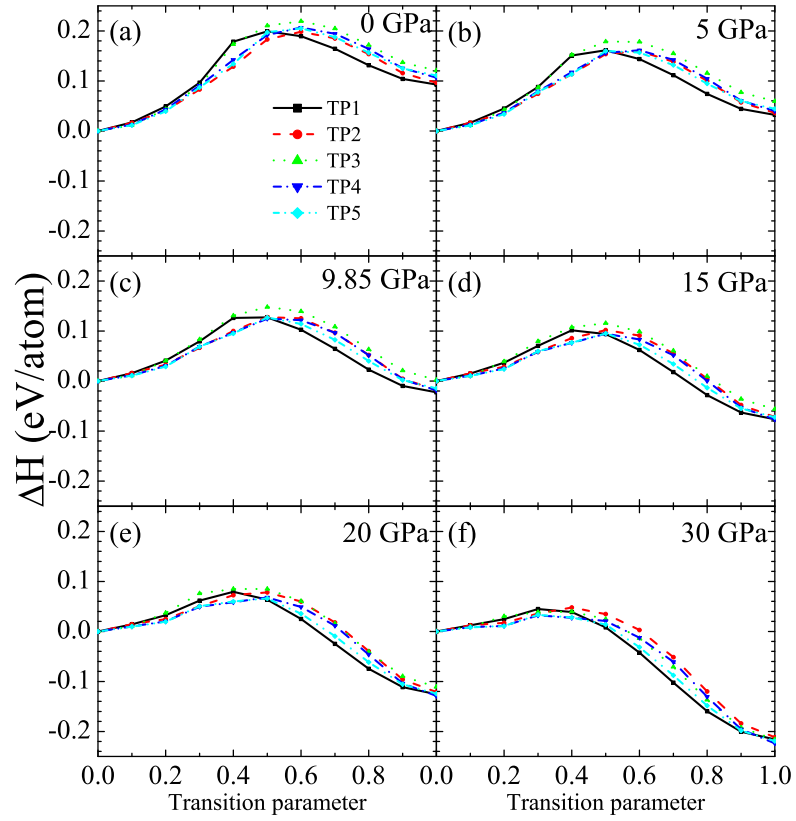


Figure 4.29: Enthalpy as a function of transition parameter relative to B4 phase for five TPs at six pressures. (a) at 0 GPa, (b) at 5 GPa, (c) at the predicted transition pressure 9.85 GPa, (d) at 15 GPa, (e) at 20 GPa and (f) at 30 GPa.

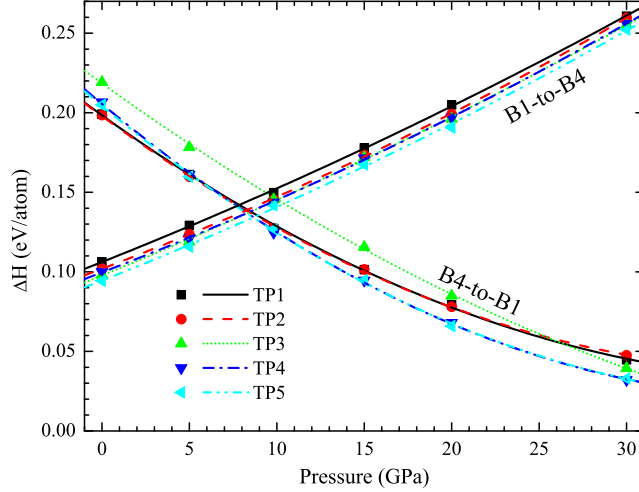


Figure 4.30: Forward (B4-to-B1) and backward (B1-to-B4) activation barrier height (enthalpy) as a function of pressure for five TPs.

#### 4.2.4 Conclusions

In summary, we show that the five bond-preserving paths can be interpreted as transformation of different long-range patterns of the “transition units” (two different orientations). The transformation of “transition unit” is equivalent to the path along TP1 (with  $Cmc2_1$  symmetry). Our calculated kinetic barriers are comparable for all five paths at pressures from 0 GPa to 30 GPa, which indicate that the wurtzite-to-rocksalt transition is characterized by the transformation of the “transition unit”, while the long-range pattern is less important. And the difference in strains of different TPs is not a major factor for at least the transition from wurtzite to rocksalt phase in AlN. In addition, the bond-breaking path is not energetically favored compared with the bond-preserving paths.

Besides the similarity from five bond-preserving TPs, our estimated forward and backward barrier heights are consistent with experimental observation and previous calculations.

## CHAPTER 5

### STUDY OF HIGH-PRESSURE PHASE TRANSITIONS IN SILICON NITRIDE

#### 5.1 Introduction

Silicon nitride ( $\text{Si}_3\text{N}_4$ ) is widely used in cutting tools and anti-friction bearings due to its excellent mechanical properties, low mass density, and thermal stability<sup>56</sup>. It is also used as an insulator layer or as an etch mask because of its dielectric properties and a better diffusion barrier against impurities in microelectronics<sup>57</sup>. For its technological importance, the mechanical and thermal properties of silicon nitride at ambient pressure has been investigated extensively by both experiment and theory<sup>56,57</sup>. In contrast, its properties at high-pressure is less known.

$\alpha$  ( $P3_1c$ ) and  $\beta$  ( $P6_3/m$ ) phases are the only two bulk polymorphs of  $\text{Si}_3\text{N}_4$  known at ambient pressure. Both phases can be synthesized by nitriding pure silicon. In 1999,  $\gamma$ - $\text{Si}_3\text{N}_4$  (or  $c$ - $\text{Si}_3\text{N}_4$ ,  $Fd\bar{3}m$ ) with the cubic spinel structure was synthesized at high pressure and high temperature<sup>58</sup>. Despite intensive research efforts in searching the “post-spinel” phases in Group-IV(B) nitrides, the spinel structured  $\gamma$  phase remains as the only experimentally identified high-pressure phase. The space groups and Wyckoff sites for these three phases are summarized in Table 5.1.

Table 5.1: Space groups, formula units per primitive unit cell and Wyckoff sites of hexagonal  $\alpha$ -,  $\beta$ - $\text{Si}_3\text{N}_4$  and cubic  $\gamma$ - $\text{Si}_3\text{N}_4$ .

Phase	Space group	Formula units per primitive unit cell	Species	Wyckoff site
$\alpha$	$P3_1c$	4	N Si	2a, 2b, 6c, 6c 6c, 6c
$\beta$	$P6_3/m$	2	N Si	2c, 6h 6h
$\gamma$	$Fd\bar{3}m$	2	N Si	32e 8a, 16d

Phase transitions in  $\text{Si}_3\text{N}_4$  have drawn extensive attention for more than a decade. The temperature-pressure ( $T$ - $P$ ) conditions for obtaining various observed and hypothesized polymorphs are sketched in Figure 5.1. The relative phase stability between  $\alpha$  and  $\beta$  phases has been a topic of investigation for many years. Direct measurements of energetics of  $\text{Si}_3\text{N}_4$  were reported by Liang *et al.*<sup>59</sup>. However, the difference in formation enthalpies between  $\alpha$ - and  $\beta$ - $\text{Si}_3\text{N}_4$  was founded to be less than the intrinsic experimental uncertainty of  $\pm 22$  kJ/mol ( $\pm 32.6$  meV/atom). Nevertheless, the  $\beta$  phase is believed to be the ground state in  $\text{Si}_3\text{N}_4$  because no  $\beta \rightarrow \alpha$  transition is ever observed. The stability condition for  $\alpha$  phase has been experimentally studied at temperatures of  $1300^\circ$ – $1800^\circ\text{C}$  and pressures up to 60 GPa<sup>60–67</sup>. A solution-precipitation mechanism was proposed for the  $\alpha \rightarrow \beta$  transformation<sup>67</sup>. Pure single-crystal  $\alpha$ - $\text{Si}_3\text{N}_4$  shows no sign of transformation at temperatures up to  $1820^\circ$ – $2200^\circ\text{C}$ <sup>67,186</sup>. Suematsu *et al.* discovered that the  $\alpha \rightarrow \beta$  transformation occurs with annealing in the presence of  $\text{Y}_2\text{O}_3$  or other oxides. The catalyst oxides first form a liquid phase with  $\text{Si}_3\text{N}_4$  on the surface at high temperatures. Then, through atomic transportation in the liquid, small particles of  $\beta$ - $\text{Si}_3\text{N}_4$  emerge. The observed liquid phase on the  $\alpha$ - $\text{Si}_3\text{N}_4$  surfaces was believed to lower the activation energy of atomic transportation. The stability of pristine  $\alpha$ - $\text{Si}_3\text{N}_4$  at high temperatures is ascribed to the extremely high value of the activation energy with clean surfaces. On the theory side, several studies confirmed that the static bonding energy of  $\alpha$  phase is slightly higher than that of  $\beta$  phase<sup>68–71</sup>. Wendel *et al.*<sup>70</sup> and Kuwabara *et al.*<sup>71</sup> carried out statistical QHA calculations, and they both found that the  $\alpha$  phase remains metastable in the temperature range from 0 to 2000 K at ambient pressure. Yet, pressure effects on the relative thermodynamic stability between  $\alpha$  and  $\beta$  phases was not addressed in previous studies. The first goal of the this chapter is to understand the relative thermodynamic stability at high pressures. The relative Gibbs free energies between two phases suggest that  $\beta$  phase, compared with  $\alpha$  phase, is thermodynamically stable at temperatures up to 2000 K and pressures up to 10 GPa. We further predicted the equilibrium phase boundaries for the  $\alpha \rightarrow \gamma$  and  $\beta \rightarrow \gamma$  transitions. The transition pressures for the  $\alpha \rightarrow \gamma$  transition is about 0.5 GPa lower than that of  $\beta \rightarrow \gamma$  transition.

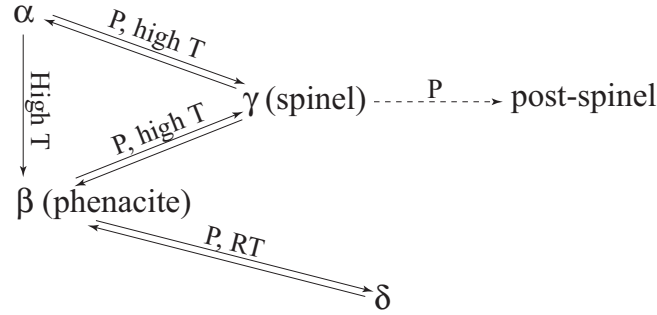


Figure 5.1: Polymorphs of Si<sub>3</sub>N<sub>4</sub> and synthesis conditions

The spinel structured  $\gamma$ -Si<sub>3</sub>N<sub>4</sub> was first synthesized by Zerr *et al.* with laser-heated diamond anvil cell (LH-DAC)<sup>58</sup>. Later experiments show that  $\gamma$ -Si<sub>3</sub>N<sub>4</sub> can be obtained from both  $\alpha$ - and  $\beta$ -Si<sub>3</sub>N<sub>4</sub> upon compression and simultaneous *in-situ* heating<sup>58,72–75</sup>. The  $\gamma$  phase is quenchable to the ambient condition, and it remains stable at temperatures ranging up to about 1670 K at ambient pressure<sup>76,77</sup>. When  $\gamma$ -Si<sub>3</sub>N<sub>4</sub> “decomposes” at ambient pressure upon heating, the samples may consist of both  $\alpha$ - and  $\beta$ -Si<sub>3</sub>N<sub>4</sub><sup>76</sup>. Previous *ab initio* studies also calculated the  $\beta \rightarrow \gamma$  transition pressure ( $P_t$ ) at adiabatic static condition<sup>58,79</sup>, as well as at high temperatures<sup>71,187</sup>. The Clapeyron slope is found to be positive and  $P_t$  varies only slightly over temperature. Furthermore, a new high-pressure post-spinel phase was proposed by first-principles method<sup>188,189</sup>. The new phase is predicted to be CaTi<sub>2</sub>O<sub>4</sub> type and the calculated  $P_t$  from  $\gamma$  to post-spinel phase is over 160 GPa. The predicted new phase has not yet been observed.

The *in-situ* heating to high temperature is found to be necessary to form the  $\gamma$ -Si<sub>3</sub>N<sub>4</sub> at high pressures. At room temperature the  $\beta \rightarrow \gamma$  transition is, however, by-passed. Zerr found that  $\beta$ -Si<sub>3</sub>N<sub>4</sub> exists up to 34 GPa and it then transforms into a new phase (labeled as  $\delta$ -phase) under further compression<sup>78</sup>. This phase transition was identified by Raman spectroscopy and energy dispersive X-ray powder diffraction (EDXD). But the structure of  $\delta$  phase was not fully determined. Zerr proposed three possible unit-cells based on the EDXD pattern: two tetragonal and one orthorhombic. The first hypothetical tetragonal unit-cell would have a density of 4.5 g/cm<sup>3</sup> at 42.6 GPa, which is smaller than that of  $\gamma$ -Si<sub>3</sub>N<sub>4</sub> (4.50

g/cm<sup>3</sup>). At the same pressure, the second tetragonal and the orthorhombic structures are proposed to have densities of 4.56 g/cm<sup>3</sup> and 5.16 g/cm<sup>3</sup>, respectively, which are larger than that of  $\gamma$  phase. The later two structures are considered as “post-spinel” phases. Zerr further suggested that the  $\delta$ -Si<sub>3</sub>N<sub>4</sub> should be considered as a metastable intermediate stage in the  $\beta \rightarrow \gamma$  transition. Kroll has proposed a metastable willemite-II-Si<sub>3</sub>N<sub>4</sub> phase which is an intermediate between  $\beta$ - and  $\gamma$ -Si<sub>3</sub>N<sub>4</sub> in both energetics and density<sup>79</sup>. However, the wII phase is unlikely to be the experimentally observed unknown phase at high pressure and room temperature. Because 1) the wII phase, which is structurally closely related to the spinel  $\gamma$ -Si<sub>3</sub>N<sub>4</sub>, has been shown to have a significantly lower activation barrier for the  $\gamma \rightarrow$ wII transformation, comparing to that of  $\gamma \rightarrow \beta$  transformation<sup>79</sup>. Although the activation barrier of the  $\beta \rightarrow$ wII transformation is unknown, it is more likely to be high enough to exclude the room temperature transition. 2) The calculated Raman frequencies of wII-Si<sub>3</sub>N<sub>4</sub> could not match many strong peaks appeared in the measurements, e.g., two observed peaks at about 500 cm<sup>-1</sup> and 550 cm<sup>-1</sup> are absent in the calculation. A recent experimental work from McMillan *et al.* reproduced Zerr’s findings on  $\delta$ -Si<sub>3</sub>N<sub>4</sub>, but excluded the wII cubic structure<sup>80</sup>.

Meanwhile,  $\beta$ -Ge<sub>3</sub>N<sub>4</sub> is found to transform into the metastable polymorph  $\delta$ -Ge<sub>3</sub>N<sub>4</sub> with hexagonal  $P3$  symmetry at room temperature by Soignard *et al.*<sup>81</sup>. *Ab initio* calculation from Dong *et al.* showed that a  $\beta \rightarrow \bar{P}\bar{6} \rightarrow P3$  transition sequence could occur in Ge<sub>3</sub>N<sub>4</sub> at the pressure of about 20 GPa and 28 GPa<sup>82</sup>, which are of second-order that driven by soft phonons. If  $\beta$ -Ge<sub>3</sub>N<sub>4</sub> directly transforms into the  $P3$  structure, the transition was predicted to be first-order and  $P_t = \sim 23$  GPa. Dong also pointed out that the  $\beta \rightarrow \bar{P}\bar{6}$  transition is originated from a soft silent  $B_u$  mode. Room temperature experimental study by Soignard *et al.* confirmed the direct  $\beta \rightarrow P3$  transition associated with a 5-7% volume reduction<sup>81</sup>. The Raman data they observed excludes the intermediate  $\bar{P}\bar{6}$  structure. Based on the density consideration, Soignard *et al.* suggested that the new polymorph is a “post-phenacite” phase, in stead of “post-spinel”. Comparison of the X-ray diffraction and Raman data between Ge<sub>3</sub>N<sub>4</sub> and Si<sub>3</sub>N<sub>4</sub> shows similarity which may suggest a  $P3$  structure for  $\delta$ -Si<sub>3</sub>N<sub>4</sub>. It is



still unclear whether there are intrinsic differences between the *HP-RT* behaviors of  $\text{Si}_3\text{N}_4$  and  $\text{Ge}_3\text{N}_4$ , or the experimental results may be interpreted differently. The second goal of our study is to theoretically investigate structural instabilities and possible metastable phase transitions in  $\alpha$ - and  $\beta$ - $\text{Si}_3\text{N}_4$  at high pressures and room temperature. We found no sign of dynamical instability in the  $\alpha$  phase at high-pressure. On the other hand, we predicted a phonon-softening related first-order phase transition at about 38.5 GPa in  $\beta$  phase. At this pressure, the density of the proposed high-pressure phase is 4.16 g/cm<sup>3</sup> which is larger than that of  $\beta$ - $\text{Si}_3\text{N}_4$  (3.71 g/cm<sup>3</sup>), yet smaller than that of  $\gamma$ - $\text{Si}_3\text{N}_4$  (4.53 g/cm<sup>3</sup>, calculated). We further estimated the kinetic barrier heights for our proposed  $\beta \rightarrow P3$  transition, which is only 67.23 meV/atom at 38.5 GPa. Despite being of first-order phase transition, the small barrier height suggests that the *P3* phase is unlikely to be recovered below 38.5 GPa.

Finally, we performed a series of systematical calculations of thermodynamic properties of  $\text{Si}_3\text{N}_4$ , such as thermal expansion coefficient (TEC), heat capacity and bulk Grüneisen parameter, and compared our results with available experimental data<sup>83–90</sup> and some previous calculations<sup>70,71,91,92</sup>. The overall good agreement with experiment validates the adopted statistical quasi-harmonic approximation (QHA) and the Birch-Murnagahn equation of states (EOS) models. Our results support the prediction of Kuwabara *et al.*<sup>71</sup> on the negative TEC of  $\alpha$  and  $\beta$  phases at temperatures below 100 K. We further attributed the origin of the negative TEC to the low-frequency phonon modes with the negative mode Grüneisen ratios in the two phases.

## 5.2 Crystal Structures, Static Binding Energies, and Vibrational Spectra

Atomic structures of  $\alpha$ -,  $\beta$ -, and  $\gamma$ - $\text{Si}_3\text{N}_4$  are shown in Figure 5.2. Both  $\alpha$  and  $\beta$ - $\text{Si}_3\text{N}_4$  have hexagonal symmetry, and they contain similar local bonding: each Si atom is tetrahedrally bonded to four N atoms ( $\text{Si-N}_4$ ) and each N atom has a threefold trigonal coordinates ( $\text{N-Si}_3$ ). All the  $\text{SiN}_4$  tetrahedra are slightly distorted and connected by corner-sharing. The difference between these two phases can be characterized by the stacking sequence along *c* axis. The periodicity of  $\alpha$ - and  $\beta$ - $\text{Si}_3\text{N}_4$  in that direction can be described

as ABCDABCD.... and ABAB.... stacking, respectively. From another point of view,  $\alpha$ - $\text{Si}_3\text{N}_4$  can be interpreted as a complex network formed with nonplanar six-membered (6-atom) rings, whereas  $\beta$ - $\text{Si}_3\text{N}_4$  is composed of non-planar six-, eight- and twelve-membered rings. There are two types of trigonal N-Si<sub>3</sub> units: those with N atoms at the 2a and 2b sites of  $\alpha$ - $\text{Si}_3\text{N}_4$  or the 2c site of  $\beta$ - $\text{Si}_3\text{N}_4$  locate at the basal plane perpendicular to the  $c$  axis, while the rest N-Si<sub>3</sub> units are in the vertical or near-vertical orientations. Most basal N-Si<sub>3</sub> units are perfectly planar with three equal-length bonds and three 120° Si-N-Si bond angles, except that the N-Si<sub>3</sub> units with N at the 2b sites of  $\alpha$ - $\text{Si}_3\text{N}_4$  form triangular pyramids (i.e. three bonds still have equal length, but the bond angles are less than 120°). The vertical N-Si<sub>3</sub> units are distorted in bond lengths and bond angles which yield distorted pyramidal units. The  $\gamma$  phase has a distinctively different structure, in which Si atoms occupy both tetrahedral (1/3 of Si atoms, 8a sites) and octahedral (2/3 of Si atoms, 16d sites) sites, and all the N atoms are tetrahedrally bonded. This is consistent with the fact that  $\gamma$ - $\text{Si}_3\text{N}_4$  is the high pressure phase which has a larger coordination number. The spinel structure is named after the mineral  $\text{MgAl}_2\text{O}_4$  which has a fcc lattice with space group  $Fd\bar{3}m$ . For  $\gamma$ - $\text{Si}_3\text{N}_4$ , there are two formula units in the primitive unit cell and eight units in the conventional cubic cell.

In this study, the equilibrium  $T$ - $P$  phase diagram and thermodynamic properties are predicted using the first-principles calculated thermodynamic potentials. As an insulator, the Helmholtz free energy of a bulk crystalline silicon nitride system consists of two parts:

$$F(T, V) = E_{static}(V) + F_{vib}(T, V) \quad (5.1)$$

where  $E_{static}(V)$  is the static binding energy of the system and  $F_{vib}(T, V)$  is the vibrational free energy. Free energy associated with the electronic thermal excitation is neglected.  $E_{static}(V)$  for  $\alpha$ -,  $\beta$ -, and  $\gamma$ - $\text{Si}_3\text{N}_4$  are calculated with unit-cell models of respective crystal symmetries. We adopted density functional theory (DFT) with a plane wave basis set and ultrasoft pseudopotentials (US-PP)<sup>121</sup>, which is implemented in the VASP code<sup>139</sup>. The

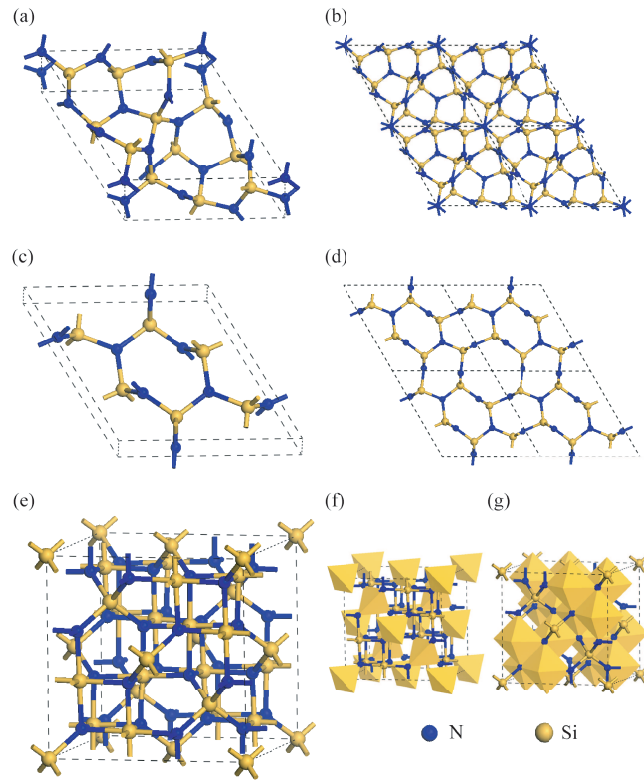


Figure 5.2: Crystal structures of (a),(b)  $\alpha$ -, (c),(d)  $\beta$ -, and (e),(f),(g)  $\gamma$ - $\text{Si}_3\text{N}_4$ . In the panel of  $\alpha$ - and  $\beta$ - $\text{Si}_3\text{N}_4$ , the first graph illustrates the unit-cell model and the second graph is the  $2 \times 2 \times 1$  supercell model viewed in the direction of  $c$  axis. In the panel of  $\gamma$ - $\text{Si}_3\text{N}_4$ , the first graph shows the conventional cubic cell of the spinel structure and the following two graphs show the fourfold and sixfold coordinated Si units( $\text{SiN}_4$  and  $\text{SiN}_6$ ) with tetrahedra and octahedra, respectively.

exchange and correlation functional is treated with local density approximation (LDA). The plane wave basis functions with energies up to 347.9 eV were used. Total energy change of  $10^{-9}$  eV per unit cell was chosen as the convergence criterion for the self-consistent iterations. The Brillouin zone integration in our total energy calculations was approximated with the Monkhorst-Pack method, with grids of  $4 \times 4 \times 6$ ,  $4 \times 4 \times 12$  and  $6 \times 6 \times 6$  for  $\alpha$ -,  $\beta$ - and  $\gamma$ -Si<sub>3</sub>N<sub>4</sub>, respectively. The calculated total energies at several chosen volumes were fitted to the third-order Birch-Murnaghan equation of state (BM-EOS)<sup>159,160</sup> by the least square fitting algorithm.

The calculated  $E$ - $V$  data sets of  $\alpha$ -,  $\beta$ - and  $\gamma$ -Si<sub>3</sub>N<sub>4</sub> are shown in Figure 5.3, and the corresponding fitting parameters from the third-order BM-EOS ( $E_0$ ,  $V_0$ ,  $B$  and  $B'$ ) are listed in Table 5.2, together with reported experimental and other theoretical results. As the measurements are usually made at room temperature, our predicted parameters at 300 K within QHA are also presented. Our calculation has a good overall agreement with other theoretical and experimental results. Compared to the experiments, our calculated static equilibrium volumes are consistently underestimated by about 1 to 3%, and the calculated bulk moduli are within the range of reported experimental data, which contain about 5 to 15% differences among different reports. The predicted thermal equation of states at 300 K are slightly closer to the measurement. Our results are within the typical accuracy of LDA calculation and they are consistent with the fact that LDA tends to slightly underestimate the equilibrium volume and overestimate the bulk modulus by a few percent.

Our static total energy calculation shows that  $\beta$  phase is only slightly energetically more stable (i.e., about 3 meV/atom lower) than  $\alpha$  phase at their respective static equilibrium volumes. Such a small energy difference is consistent with the fact that both  $\alpha$  and  $\beta$  phases are found to be co-exist during different synthesis routes. Also, in agreement with experiment, we find that the calculated  $\beta$  phase has larger density and lower compressibility comparing to the  $\alpha$  phase. This suggests that  $\alpha$  phase is even less favored thermodynamically at higher pressure relative to  $\beta$  phase. The relative stability between

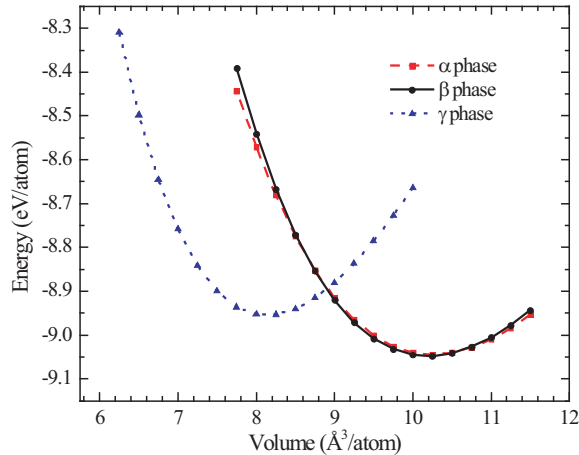


Figure 5.3: Energy-volume curves for  $\alpha$ -,  $\beta$ - and  $\gamma$ - $\text{Si}_3\text{N}_4$  in the scale of per atom.  $\beta$  phase has an equilibrium energy of 3 meV lower than that of  $\alpha$  phase.  $E_0$  of  $\gamma$  phase is 93 meV higher than  $\beta$  phase.

these two phases will be further examined in later text with the consideration of temperature and pressure effects. For the  $\gamma$  phase, our calculation yields a static equilibrium energy which is 93 meV/atom higher than that of the  $\beta$  phase, and a static equilibrium volume of  $2 \text{ \AA}^3/\text{atom}$  smaller than that of the  $\beta$  phase. These results agree with the fact that the spinel structured  $\gamma$  phase is a high pressure phase in  $\text{Si}_3\text{N}_4$ .

Figure 5.4 shows the phonon dispersion curves and VDOS plots of the  $\alpha$ -,  $\beta$ - and  $\gamma$ - $\text{Si}_3\text{N}_4$  at their respective static equilibrium volumes. All three phases studied here are dynamically stable, i.e., no soft phonon modes. The  $\alpha$  and  $\beta$  phases have very similar VDOS which reflects the similarity in their crystal structures and Si-N bonding. On the other hand, the spinel structured  $\gamma$ - $\text{Si}_3\text{N}_4$  shows some distinctively different characters in its VDOS, comparing with those of  $\alpha$  and  $\beta$  phases. High-pressure phases usually have higher vibration frequencies. Yet, we find that the top phonon branches in  $\gamma$  phase have frequencies which are significantly lower than those of  $\alpha$  or  $\beta$  phase.

Mode Grüneisen ratios along some high symmetry directions are shown in Figure 5.5. Although there are many similarities in the mode Grüneisen ratios between the  $\alpha$  and  $\beta$  phases, for example, their low-frequency phonon modes are found to have negative mode

Table 5.2: Summary of calculated and measured crystal parameters of  $\alpha$ -,  $\beta$ - and  $\gamma$ -Si<sub>3</sub>N<sub>4</sub>.  $V_0$  is the equilibrium volume per atom,  $B$  is the bulk modulus and  $B'$  is the first-order pressure derivative. Measurements were made at room temperature.

$\alpha$ -Si <sub>3</sub> N <sub>4</sub>			
Source	$V_0$ ( $\text{\AA}^3/atom$ )	$B$ (GPa)	$B'$
LDA (this work, static)	10.260	232	2.583
LDA (this work, 300K)	10.328	226	2.576
LDA <sup>71</sup>	10.325	240	4.0 (fixed)
LDA <sup>190</sup>	10.237	257	
OLCAO <sup>69</sup>	10.542	257	
Force fields (300K) <sup>70</sup>	10.806	246	
Experiment <sup>191</sup>	10.455		
Experiment <sup>192</sup>	10.445		
Experiment <sup>193</sup>	10.465	223.4 ( $\pm 15$ )	4.5 ( $\pm 1.3$ )
$\beta$ -Si <sub>3</sub> N <sub>4</sub>			
Source	$V_0$ ( $\text{\AA}^3/atom$ )	$B$ (GPa)	$B'$
LDA (this work, static)	10.199	241	3.439
LDA (this work, 300K)	10.267	237	3.440
LDA <sup>71</sup>	10.268	252	4.0 (fixed)
GGA <sup>194</sup>		237.2-241.5	
LDA <sup>190</sup>	10.183	225	
Force fields (300K) <sup>70</sup>	10.661	266	
Experiment <sup>195</sup>	10.396		
Experiment <sup>196</sup>	10.411	270 ( $\pm 5$ )	4.0 ( $\pm 1.8$ )
Experiment <sup>197</sup>	10.452	232.7	
Experiment <sup>68</sup>	10.356		
$\gamma$ -Si <sub>3</sub> N <sub>4</sub>			
Source	$V_0$ ( $\text{\AA}^3/atom$ )	$B$ (GPa)	$B'$
LDA (this work, static)	8.140	308	3.898
LDA (this work, 300K)	8.220	297	3.898
LDA <sup>71</sup>	8.137	320	4.0 (fixed)
OLCAO <sup>69</sup>	8.595	280	
Experiment <sup>198</sup>	8.270	290 ( $\pm 5$ )	4.9 ( $\pm 0.6$ )
Experiment <sup>74</sup>	8.286	308	4.0
Experiment <sup>76</sup>	8.261		
Experiment <sup>197</sup>		300 ( $\pm 10$ )	3.0 ( $\pm 0.1$ )
Experiment <sup>58</sup>	8.474 ( $\pm 0.26$ )		

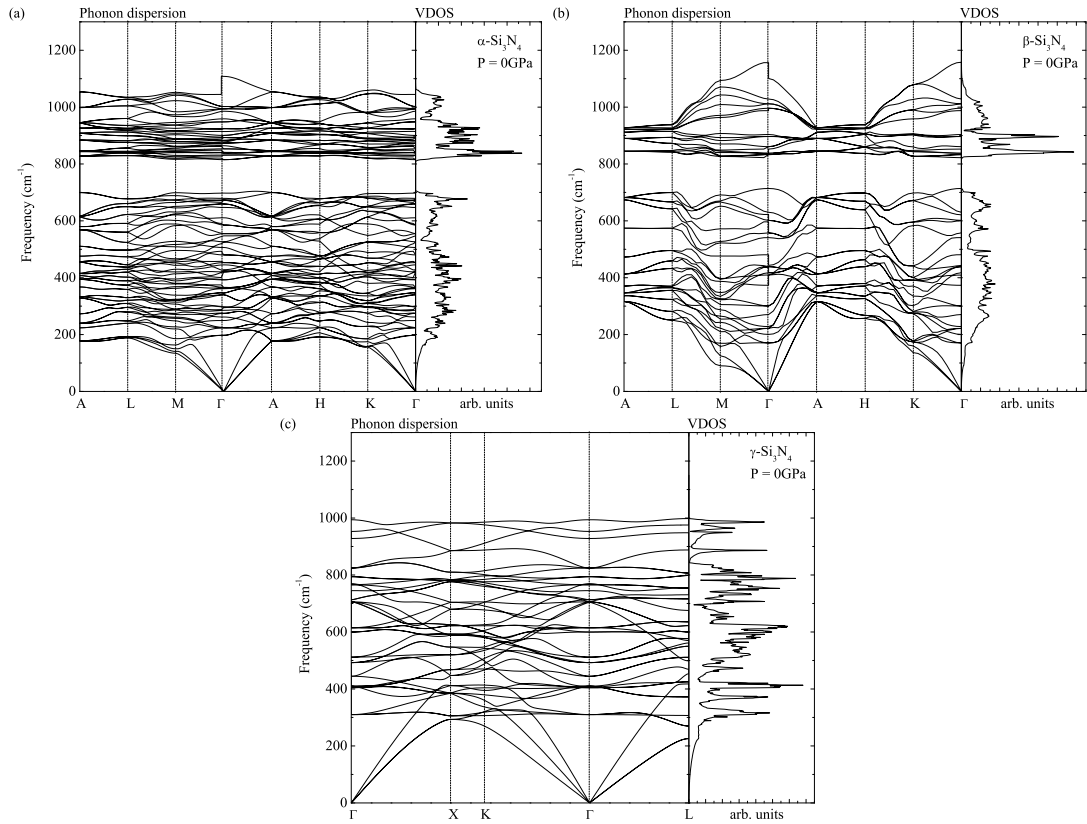


Figure 5.4: Phonon dispersion curves and vibrational density of states (VDOS) of (a)  $\alpha$ -, (b)  $\beta$ -, and (c)  $\gamma$ -Si<sub>3</sub>N<sub>4</sub> at zero pressure.

Grüneisen parameters while all the high-pressure modes have positive ratios with the upper limit of about 1.5, there are some noticeable differences for phonons around the M-point transverse acoustic (TA) mode and the  $\Gamma$ -point optic  $B_u$  mode. The phonons close to these two modes in  $\beta$  phase are found to have large negative Grüneisen ratios, which suggest possible structural instability of  $\beta$  phase upon compression. On the other hand, the  $\gamma$ - $\text{Si}_3\text{N}_4$  shows no negative mode Grüneisen ratios at all, and the values of its mode Grüneisen ratios range from 0.24 to 1.66 at zero pressure..

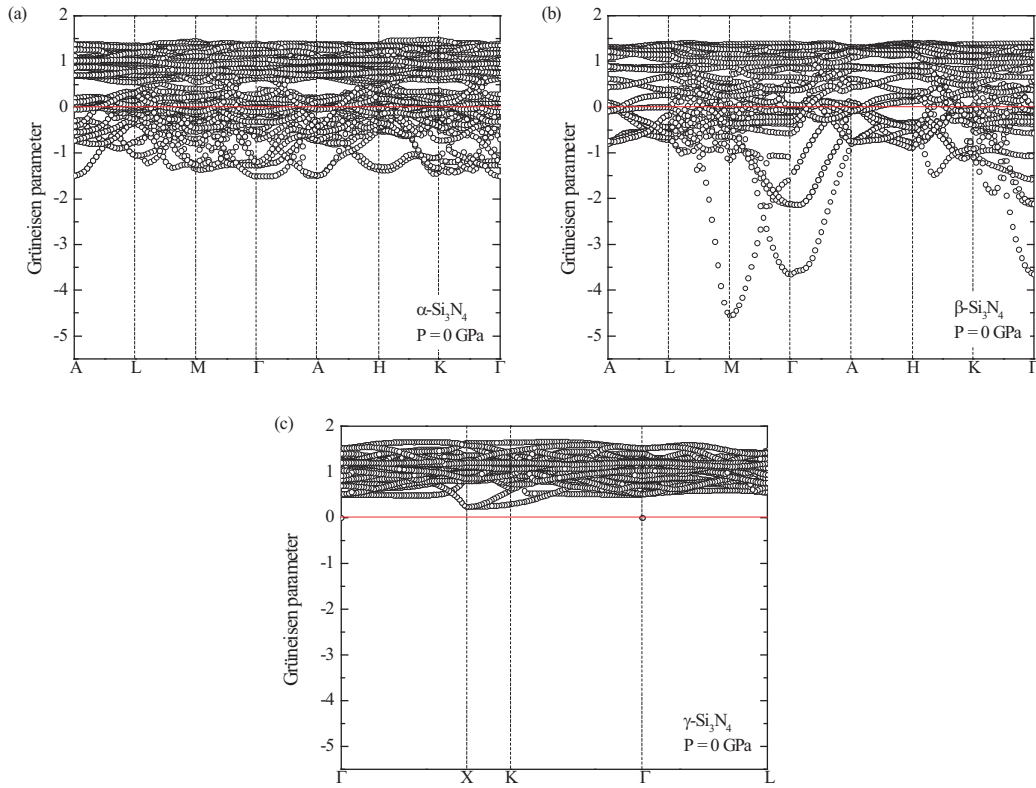


Figure 5.5: Calculated dispersion curves (scattered circles) of mode Grüneisen parameter of (a)  $\alpha$ -, (b)  $\beta$ -, and (c)  $\gamma$ - $\text{Si}_3\text{N}_4$  at zero pressure. Red horizontal line is present to separate the positive and negative values.



### 5.3 Equilibrium Thermodynamic Stability and Phase Transitions

To illustrate the relative thermodynamic stability between the  $\alpha$  and  $\beta$  phase, we plot the LDA calculated Gibbs free energy differences between the two phases at 0, 5 and 10 GPa in Figure 5.6. A positive value of  $\Delta G_{\alpha-\beta}$  means that  $\alpha$ -Si<sub>3</sub>N<sub>4</sub> is thermodynamically metastable. At isobaric conditions, the calculated  $\Delta G_{\alpha-\beta}$  are almost constant over the temperature range from 0 K to 2000 K. At zero pressure, our calculated  $\Delta G_{\alpha-\beta}$  is 2.8 meV/atom at 0 K which agrees with Kuwabara’s (DFT+PAW+LDA)  $\Delta F_{\alpha-\beta}$  of 2.6 meV/atom at 0 K. At 2000 K, our  $\Delta G_{\alpha-\beta}$  is 2.6 meV/atom, while Kuwabara’s  $\Delta F_{\alpha-\beta}$  decreases to 1.3 meV/atom. The results of Wendel *et al.* were based on empirical force field models and they gave opposite trend of temperature dependence, 0.1 meV/atom at 300 K and 0.7 meV/atom at 2000 K. At elevated pressures, we predict an increasing  $\Delta G_{\alpha-\beta}$ . At 5 GPa and 10 GPa,  $\Delta G_{\alpha-\beta}$  is about 4.6 meV/atom and 5.9 meV/atom, respectively. We do not predict  $\Delta G_{\alpha-\beta}$  at pressures higher than 10 GPa because the  $\beta$  phase starts to show signs of structural instability (see discussion in later text). We conclude that  $\alpha$  phase is metastable compared to  $\beta$  phase in the temperature range from 0 K to 2000 K and at least up to 10 GPa.

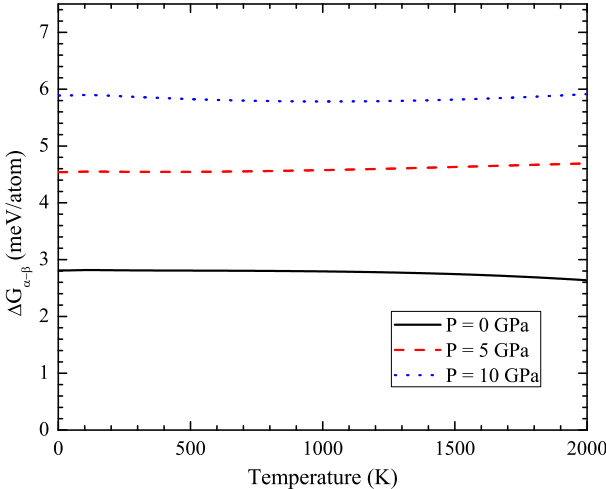


Figure 5.6: Gibbs free energy of  $\alpha$ -Si<sub>3</sub>N<sub>4</sub> relative to that of  $\beta$  phase as a function of temperature. Solid, dashed and dotted lines represent the pressure of 0, 5 and 10 GPa, respectively.

Upon compression, both the ground state  $\beta$  phase and meta-stable  $\alpha$  phase transform into the  $\gamma$  phase. Our predicted equilibrium  $T$ - $P$  phase boundaries are shown in Figure 5.7. The Clapeyron slopes for the  $\beta \rightarrow \gamma$  (solid line) and  $\alpha \rightarrow \gamma$  (dashed line) transitions are both positive, which suggests that the high-pressure  $\gamma$  phase has a lower vibrational entropy. Consequently, the transition pressure ( $P_t$ ) increases with temperature. The predicted  $P_t$  of the  $\beta \rightarrow \gamma$  transition is 7.5 GPa at 300 K, and it increases to 9.0 GPa at 2000 K. The  $P_t$  of the  $\alpha \rightarrow \gamma$  transition is about 0.5 GPa lower than that of  $\beta \rightarrow \gamma$  transition. Togo *et al.*<sup>187</sup> and Kuwabara *et al.*<sup>71</sup> also predicted a positive Clapeyron slope for the  $\beta \rightarrow \gamma$  transition. The large calculated Clapeyron slopes ( $dT/dP$ ) means that the transitions are primarily volume driven and the equilibrium  $P_t$  is not sensitive to the temperature. For example,  $P_t$  changes by less than 2 GPa when temperature rises from 300 K to 2000 K. On the experimental side, the transition pressures are scattered from 10 GPa to 36 GPa (Table 5.3). This could be ascribed to the different compositions/impurities of the starting samples being used. Nonetheless, *in situ* heating is required for the synthesis of  $\gamma$ -Si<sub>3</sub>N<sub>4</sub> in all experiments. This is a clear indication that large kinetic barriers exist. For better comparison between theory and experiment, we only list here the theoretical results at  $T = 2000$  K.

Table 5.3: Summary of phase transition pressure and temperature for synthesizing  $\gamma$ -Si<sub>3</sub>N<sub>4</sub>

Method	Starting material	$P_t$ (GPa)	Temperature (K)
Experiment			
diamond cell <sup>58</sup>	Si, amorphous Si <sub>3</sub> N <sub>4</sub> and poly-crystalline $\alpha + \beta$	15	2100
Shock compression <sup>73</sup>	$\beta + 2$ wt% (Nd <sub>2</sub> O <sub>3</sub> +Y <sub>2</sub> O <sub>3</sub> ) $\beta$	36	1990
Diamond anvil cell <sup>199</sup>	$\alpha + 1\%\beta$	17.5	-
Multi-anvil <sup>72</sup>	$\alpha + \beta$	17	2100
Shock wave <sup>75</sup>	$\beta$	10	2073
Theory			
PAW+GGA <sup>187</sup>	$\beta$	13	2000
PAW+LDA <sup>71</sup>	$\beta$	6.3	2000
USPP+LDA (this work)	$\alpha$	8.5	2000
USPP+LDA (this work)	$\beta$	9.0	2000

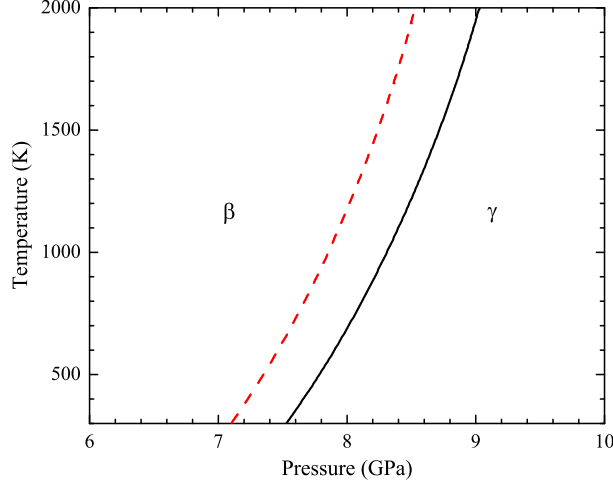


Figure 5.7:  $T$ - $P$  phase diagram of  $\text{Si}_3\text{N}_4$ . Solid curve denotes the phase boundary between  $\beta$ - and  $\gamma$ - $\text{Si}_3\text{N}_4$ . Dashed curve denotes the phase boundary between  $\alpha$ - and  $\gamma$ - $\text{Si}_3\text{N}_4$ .

#### 5.4 Phonon-Softening Induced Structural Instability in $\beta$ - $\text{Si}_3\text{N}_4$ at High Pressures

Although  $\beta$ - $\text{Si}_3\text{N}_4$  transforms into the  $\gamma$  phase at high pressures and temperatures, the  $\beta$  phase is stable at the room temperature up to at least 30 GPa. To investigate the structural stability of the  $\beta$  phase, we calculated the pressure dependence of lattice vibration. First, we examined the phonon modes at the zone center  $\Gamma$ -point. There are in total 42 vibrational modes for  $\beta$ - $\text{Si}_3\text{N}_4$  with space group  $P6_3/m$ . Using group theory, the irreducible representation for  $\Gamma$ -point phonon modes is

$$\Gamma_{acoustic} = A_u + E_{1u} \quad (5.2)$$

$$\Gamma_{optic} = 4A_g + 2A_u + 3B_g + 4B_u + 2E_{1g} + 5E_{2g} + 4E_{1u} + 2E_{2u} \quad (5.3)$$

For the optic modes, 11 modes ( $4A_g + 2E_{1g} + 5E_{2g}$ ) are Raman active, 6 modes ( $2A_{2u} + 4E_{1u}$ ) are infrared (IR) active, and the rest ( $3B_g + 4B_u + 2E_{2u}$ ) are silent modes, among which Raman and IR spectra can be detected in experiments. Figure 5.8 shows our calculated Raman, IR and silent modes of the  $\beta$  phase as a function of pressure up to 60 GPa. Experimental pressure dependencies up to 30 GPa are presented for comparison. For the measured

Raman modes from Zerr *et al.*<sup>200</sup>, one  $A_g$  mode is missing, possibly due to the weak intensity. The rest Raman modes match well with our calculation. Our prediction tends to underestimate the frequencies by about 2%-4% , which is typical for calculations of this type. The calculation shows a clear pattern that all low frequency modes (  $400 \text{ cm}^{-1}$  and below) have zero or negative pressure dependencies. The lowest  $B_u$  silent mode decreases much faster than the others and eventually vanishes at about 60 GPa. The predicted negative pressure dependence in these modes is consistent with the calculated negative mode Grüneisen ratios (Figure 5.5b). The calculated phonon softening pattern in  $\beta\text{-Si}_3\text{N}_4$  is in agreement with our previous results for  $\beta\text{-Ge}_3\text{N}_4$ <sup>82</sup>.

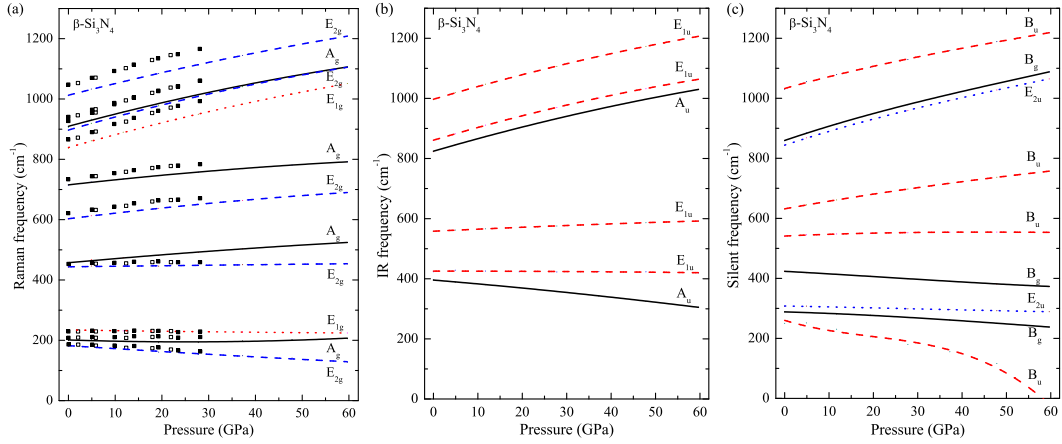


Figure 5.8: (a) Raman, (b) IR and (c) silent mode frequencies as a function of pressure up to 60 GPa for  $\beta\text{-Si}_3\text{N}_4$ . Experimental pressure dependence of Raman modes up to 30 GPa is also presented in discrete symbols as a comparison<sup>200</sup>. Solid squares denote measurements upon pressure increase and open squares denote measurements upon pressure decrease. Several low-frequency modes are found to decrease with increasing pressure. One  $B_u$  branch of silent modes is found dropping to zero at about 60 GPa.

Next, we extended our study to all the phonon modes in the reciprocal space. Our calculated phonon dispersion curve of  $\beta\text{-Si}_3\text{N}_4$  at 48 GPa (Figure 5.9) shows that two low-frequency branches decrease dramatically upon compression, i.e., one TA branch along the  $\Gamma$ -M direction and lowest optic  $B_u$  branch. The TA mode goes soft at the Brillouin zone boundary M point, i.e.  $\mathbf{k} = \frac{2\pi}{a} \left( \frac{1}{\sqrt{3}}, 0, 0 \right)$  and the optic mode goes soft at the zone center  $\Gamma$  point, i.e.  $\mathbf{k} = (0, 0, 0)$ . A vanishing phonon frequency results from the vanishing

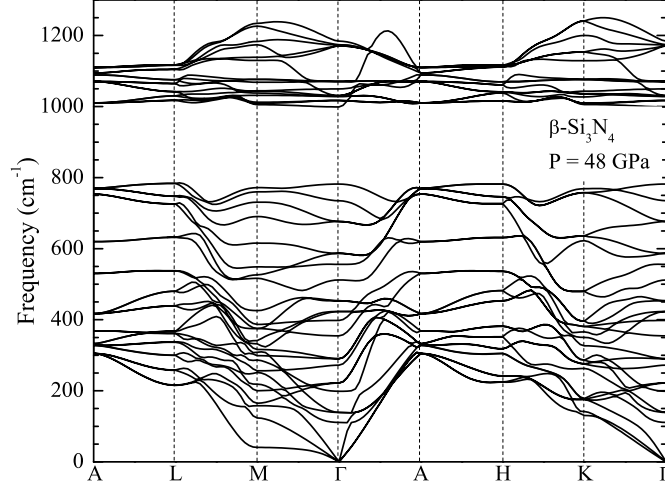


Figure 5.9: Phonon dispersion of  $\beta$ -Si<sub>3</sub>N<sub>4</sub> at a pressure of 48 GPa. Two competing soft phonon modes are found: one TA branch at M point and one optic branch at  $\Gamma$  point. No LOTO splitting correction is added for the interests of low-frequency modes only.

restoring force against the atomic displacement for the corresponding vibrational mode. Consequently, the crystal structure may undergo a displacive transition to reach a new minimal-energy configuration with lower symmetry. Our calculated  $\omega^2$  of the two most significant soft modes as a function of pressure are shown in Figure 5.10. The two  $\omega^2$  are found to exhibit linear pressure dependencies. Comparing to the M-point TA mode, the softening  $B_u$  mode has a higher frequency at ambient pressure, yet it decreases much faster with the increase of pressure. Phonon frequencies of both softening modes reach zero at  $\sim 60$  GPa. Although the frequency of the M-point TA phonon vanishes before the  $B_u$  branch, the predicted difference is, however, small. We thus consider both softening phonon modes as two competing mechanisms that may be responsible for the structural instability of  $\beta$ -Si<sub>3</sub>N<sub>4</sub> at high pressures. It is worth to point out that  $\alpha$ -Si<sub>3</sub>N<sub>4</sub> does not show any signs of structural instability in our calculation, which is consistent with the differences we have pointed out for the calculated mode Grüneisen ratios (Figure 5.5(a)).

The atomic displacements according to the soft M-point TA mode are in the  $x$ - $y$  plane and the symmetry of the unit-cell is reduced from hexagonal  $P6_3/m$  to monoclinic  $P2_1/m$  after the distortion. One vector of the  $P2_1/m$  primitive unit cell is about twice of the

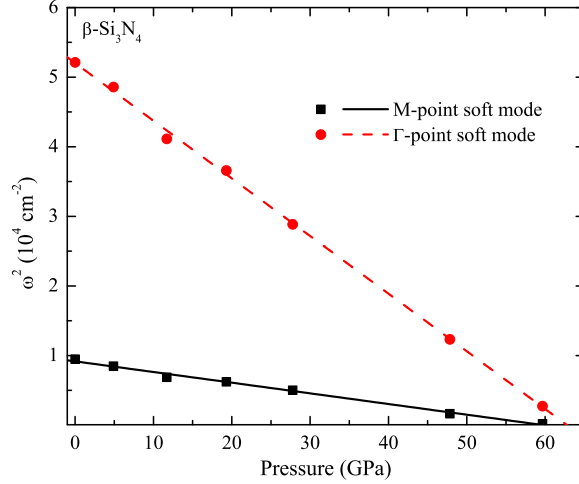


Figure 5.10: The square of vibration frequency ( $\omega^2$ ) as a function of pressure for two competing soft phonon branches: one TA branch at M point and one  $B_u$  branch at  $\Gamma$  point. Solid squares and circles represent data from calculation. Solid and dashed lines are from a linear fitting.

$\mathbf{a}$  vector of the original hexagonal unit-cell. Constrained with the  $P2_1/m$  symmetry, we calculated the total energies of the distorted structure for several volumes by allowing further relaxation of both unit-cell shapes and internal coordinates. The calculated  $E-V$  curve is shown in Figure 5.12. At volumes larger than  $8.75 \text{ \AA}^3/\text{atom}$ , the  $P2_1/m$  structure relaxes back to the original  $\beta$  structure with energy minimization calculation. Yet at volumes smaller than  $8.75 \text{ \AA}^3/\text{atom}$ , the  $P2_1/m$  phase yields a lower energy. The relaxed structure with a volume of  $8.25 \text{ \AA}^3/\text{atom}$  is shown in Figure 5.11(b). After relaxation, for volume  $8.25 \text{ \AA}^3/\text{atom}$ , the lattice parameters  $a = 13.912 \text{ \AA}$ ,  $b = 6.674 \text{ \AA}$  and  $c = 2.777 \text{ \AA}$ . The length of  $\mathbf{a}$  is slightly larger than twice that of  $\mathbf{b}$ . The angle between  $\mathbf{a}$  and  $\mathbf{b}$  becomes  $116.4^\circ$  from the original  $120^\circ$  in  $\beta$  phase. The  $c/b$  ratio is getting larger compared to that in  $\beta\text{-Si}_3\text{N}_4$ . This is consistent with the fact that it becomes more difficult to compress along  $\mathbf{c}$  axis than in the  $x-y$  plane after the structural distortion. The displacements of internal coordinates can be described in terms of N atoms. Around each  $2c$  N atom in  $\beta\text{-Si}_3\text{N}_4$  there are three nearest  $6h$  N atoms which are in the same basal plane. The displacements of those  $6h$  N atoms are in a way that it causes the previous planar vertical N-Si<sub>3</sub> units to pucker. The puckering pattern can be seen in Figure 5.11(b). In  $P2_1/m$  structure, two

of the nearest N atoms become closer to the “centered” 2c N atom (no longer 2c site in the  $P2_1/m$  symmetry, but it is convenient to label it consistently) but the third one moves away from it. Consequently the “centered” 2c N atom is “pushed” away by the two closer N atoms, which breaks the hexagonal symmetry and causes the three Si-N-Si bond angles to be distorted from the perfect  $120^\circ$ . More importantly, the interatomic distance between the Si atoms at the 2e site and one of their 2nd nearest neighbor decreases rapidly upon compression. At the volume of  $8.25 \text{ \AA}^3/\text{atom}$ , this distance is only  $1.988 \text{ \AA}$  which is slightly larger than that of previous Si-N bonds (less than  $1.7 \text{ \AA}$ ). This tendency of forming an extra bond may help to stabilize the distorted structure under high pressures. The new  $P2_1/m$  phase is dynamically stable at pressures up to 75 GPa.

A similar distortion calculation was performed for the soft  $B_u$  mode at  $\Gamma$  point. The atomic displacements based on the corresponding vibrational pattern yields a new structure which has a hexagonal  $P\bar{6}$  symmetry. The size of the primitive unit cell is the same as  $\beta$ - $\text{Si}_3\text{N}_4$  and the displacements are still within the  $x$ - $y$  plane. The  $E$ - $V$  curve and data points of  $P\bar{6}$  phase is shown in Figure 5.12 as the (red) dash line. Its structure returns to  $\beta$  phase after fully relaxation for volumes larger than  $8.75 \text{ \AA}^3/\text{atom}$ . Its energy is slightly lower than  $\beta$  phase at a smaller volume, however, it is higher than that of the  $P2_1/m$  phase. Figure 5.11(c) shows the relaxed  $P\bar{6}$  structure at the volume of  $8.25 \text{ \AA}^3/\text{atom}$ . The  $c/a$  ratio increase slightly compared to  $\beta$ - $\text{Si}_3\text{N}_4$  and this may again be ascribed to the less compressibility along  $c$  axis. The structure of  $P\bar{6}$  can be interpreted in terms of the puckering pattern of 6h N atoms. Unlike the  $P2_1/m$  structure, as shown in Figure 5.11(c), three “in-plane” 6h N atoms move clockwise and become closer to one of the “centered” 2c N atom, which has a  $z$  coordinate of  $\frac{3}{4}$  in term of  $c$  in our case. However, the other three 6h N atoms move counterclockwise and become away from the other “centered” 2c N atom ( $z = \frac{1}{4}$ ).

We further calculated the phonon spectrum of the  $P\bar{6}$  structure and discovered an optic soft phonon mode happens at its  $\Gamma$  point. Based on the corresponding eigenvector, we obtained a new structure with hexagonal  $P3$  symmetry. The primitive unit cell is in

the same size as the  $\beta$  phase, i.e., two formula  $\text{Si}_3\text{N}_4$  units per cell. The  $E$ - $V$  relation of  $P3$  phase is shown in Figure 5.12 as the (green) dash-dotted line. Its structure returns to  $\beta$  phase beyond a volume of  $8.75 \text{ \AA}^3/\text{atom}$  and remains stable at a smaller volume. The total energy of the  $P3$  phase is lower than the other three phases below the volume of  $8.37 \text{ \AA}^3/\text{atom}$ . Between  $8.37 \text{ \AA}^3/\text{atom}$  and  $8.75 \text{ \AA}^3/\text{atom}$ , the  $P2_1/m$  phase has the lowest energy. Structure model of  $P3$  phase at the volume of  $8.25 \text{ \AA}^3/\text{atom}$  is shown in Figure 5.11(d). The  $c/a$  ratio of  $P3$  structure is very close to that of  $\beta$  phase. This structure can be understood as a further distortion of the  $P\bar{6}$  phase. Relative to the  $P\bar{6}$  structure, the major difference in  $P3$  phase is the  $z$  coordinate of the “centered”  $2c$  N atom which is surrounded by three closer N atoms. This “centered”  $2c$  N atom, denoted thereafter as the puckering  $2c$  N, is “pushed” up or down by three approaching N atoms. As the volume getting smaller, the puckering  $2c$  N will be “pushed” by the three closer  $6h$  N atoms eventually to the middle of two “closer-N-atoms” layers ( $z = \frac{1}{4}$ ) and become six coordinated. The other “centered”  $2c$  N atom remains its  $z$  coordinate because there is no “push” effect. For volume between  $8.00 \text{ \AA}^3/\text{atom}$  and  $8.75 \text{ \AA}^3/\text{atom}$ , which is before the puckering  $2c$  N atom reach its final position ( $z = \frac{1}{4}$ ), the  $z$  coordinates of other atoms deviate slightly from their previous values. However, these  $z$  coordinates recover their previous values perfectly ( $z = \frac{1}{4}$  and  $\frac{3}{4}$ ) when the puckering  $2c$  N atom is stabilized at  $z = \frac{1}{4}$ . Using the same criterion to verify the formation of bonds, there are six extra bonds being formed within a primitive unit cell, i.e., 3 extra bonds per formula unit. And for  $P2_1/m$  phase, it is only  $\frac{1}{2}$  extra bonds per formula unit.

### 5.5 Room Temperature Metastable $P3$ Phase

Based on the  $E$ - $V$  curves shown in Figure 5.12, the transition from  $\beta$ - $\text{Si}_3\text{N}_4$  to one of the three candidates is determined by the common tangent line between them. The smallest magnitude of the slope (negative) is corresponding to the lowest transition pressure, and this is made by the  $P3$  phase. Both  $P2_1/m$  and  $P\bar{6}$  phases are likely bypassed. The transition pressure is estimated to be 38.5 GPa, which is comparable to the experimentally observed



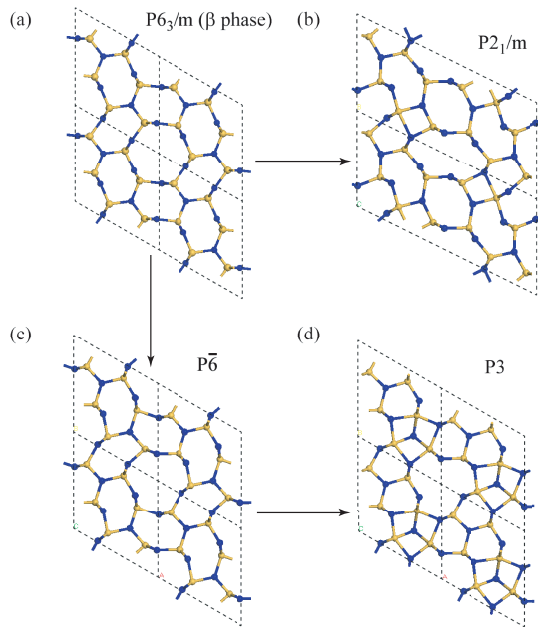


Figure 5.11: Ball-stick models of (a)  $P6_3/m$ , (b)  $P\bar{6}$ , (c)  $P2_1/m$  and (d)  $P3$  structures viewed along the  $c$  axis. Balls in dark color represent N atoms and Si atoms are in light color.

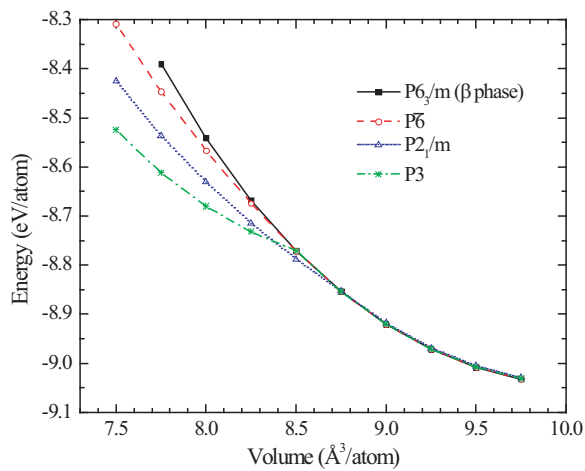


Figure 5.12: The total energy of  $P6_3/m$  ( $\beta$ ),  $P\bar{6}$ ,  $P2_1/m$  and  $P3$  structures as a function of volume.

35 GPa for the unidentified  $\delta$ -phase<sup>78</sup>. The transition pressure is much smaller than 60 GPa, at which one phonon frequency becomes zero in the  $\beta$ -Si<sub>3</sub>N<sub>4</sub>. The predicted  $\beta$ -to- $P3$  transition is a first-order phase transition, and the predicted volume reduction is about 10.8%.

To estimate the kinetic barrier height in the  $\beta \rightarrow P3$  transition, we calculated the enthalpy landscape in terms of the atomic displacements in the  $x$ - $y$  plane and of the  $z$  coordinate of the puckering 2c N atom. At the transition pressure, we took the  $\beta$  phase as the starting structure and the  $P3$  phase as the ending structure. Two transition parameters,  $f_{x-y}$  and  $f_z$ , are used to linearly interpret the phase transition. Initial internal coordinates of the intermediate structure can be expressed as

$$\begin{aligned} x &= x_i + (x_f - x_i) f_{x-y} \\ y &= y_i + (y_f - y_i) f_{x-y} \\ z &= z_i + (z_f - z_i) f_z \end{aligned} \tag{5.4}$$

where the subscript “ $i$ ” and “ $f$ ” denote the starting (initial) and ending (final) structures, respectively. Both  $f_{x-y}$  and  $f_z$  range from 0 to 1, and they can be set independently.  $10 \times 10$  uniform grids were adopted for the intermediate structures. In the total energy calculation of each structure, by fixing the internal coordinates, we allowed the external parameters to relax. Because this transition is observed to occur at room temperature, it is a good approximation to use enthalpy instead of Gibbs free energy to investigate the phase transition. The enthalpy landscape and its contour plot as functions of  $f_{x-y}$  and  $f_z$  at 38.5 GPa are shown in Figure 5.13. Two minimum points correspond to  $\beta$  (0,0) and  $P3$  (1,1) structures. The transition path is given by the gradient curve connecting the two minimum points. It will pass the saddle point which provides the transition barrier height. The pathway we predict is close to the linear path that  $f_{x-y}$  and  $f_z$  vary at similar paces. The calculated saddle point locates at (0.6,0.5) and the corresponding enthalpy barrier is 67.23 meV/atom. To overcome this barrier, certain activation temperature is necessary to

stimulate the atomic vibrations to a level that is comparable to  $\Delta H$ . Using Dulong and Petit law  $E = 3k_B T$ , the “threshold” activation temperature is estimated to be 260 K, which is lower than the room temperature. Since all the internal coordinates are fixed in our calculation, the activation temperature should be considered as an upper limit to its actual value. The  $\beta \rightarrow P3$  transformation should be interpreted as a low-barrier transition induced by softening phonon modes.

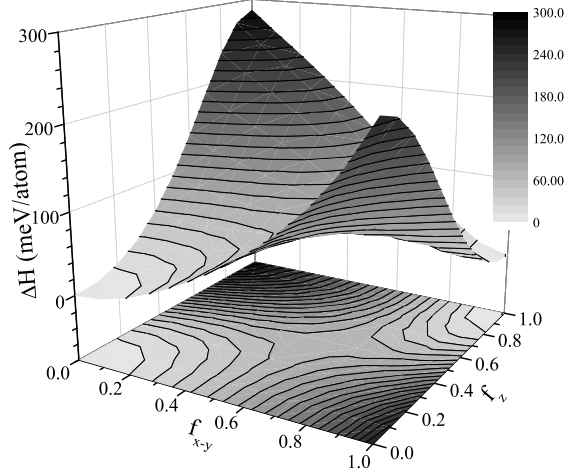


Figure 5.13: Enthalpy landscape and its contour plot as a function of  $f_{xy}$  and  $f_z$  at the transition pressure of 38.5 GPa.

It is interesting to point out that the new  $P3$  phase is dynamically stable above the transition pressure (i.e., 38.5 GPa). However, one of its TA branch shows a tendency to vanish at  $K$  point below the transition pressure. The atomic displacements according to the  $K$ -point softening mode suggest a structure which still belongs to  $P3$  symmetry, but the unit cell is three times larger than the previous  $P3$  phase, i.e., six formula units per primitive unit cell. To distinguish with the previous  $P3$ - $\text{Si}_3\text{N}_4$ , we will denote this second  $P3$  structure as  $P3'$  phase later on. Taking the  $P3'$  structure as the initial structure, we performed total energy calculations with both internal and external parameters being full relaxed.  $P3'$  phase is found to exist only between the volume of  $8 \text{ \AA}^3/\text{atom}$  and  $8.75 \text{ \AA}^3/\text{atom}$ . Its structure relaxes back to the  $\beta$  structure for volumes larger than  $8.75 \text{ \AA}^3/\text{atom}$  and becomes  $P3$  phase for volumes smaller than  $8 \text{ \AA}^3/\text{atom}$ . Its energy is slightly lower than

that of  $P3$  phase by merely a few meV/atom. The structure of  $P3'$  phase is very similar to  $P3$  phase except the  $z$  coordinates of each  $P3$  Wyckoff site split into three different values with small deviations. In another word, the  $P3$  phase is a special case of the  $P3'$  structure. As indicated in the calculated enthalpy landscape shown in Figure 5.13, the transition path is close to the linear path along which  $f_{xy}$  and  $f_z$  vary cooperatively. If we take  $P3'$  phase as an intermediate state connecting  $\beta$  and  $P3$  structures, the enthalpy barriers at 30 GPa and 38.5 GPa are shown in Figure 5.14 together with the barriers from direct  $\beta \rightarrow P3$  transition as a comparison. The barrier heights along two paths are very comparable. The  $\Delta H$  in  $\beta \rightarrow P3' \rightarrow P3$  path is lower than the  $\beta \rightarrow P3$  path by only 5.6 meV/atom at 38.5 GPa and 9.8 meV/atom at 30 GPa.

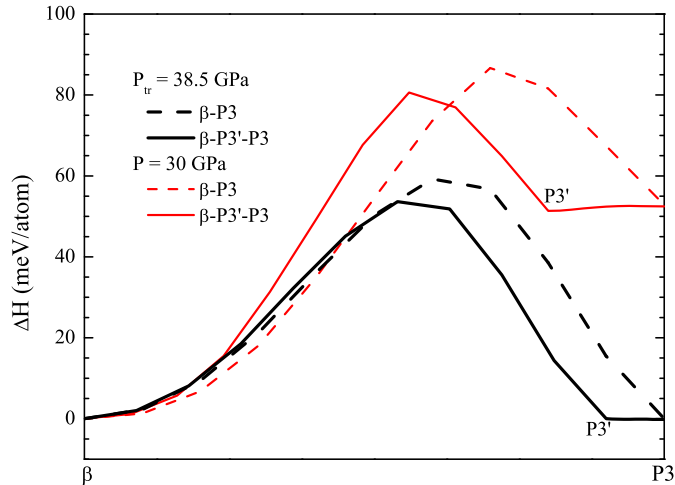


Figure 5.14: Enthalpy barrier (relative to  $\beta$  phase) as a function of linearly interpreted transition parameter at 30 GPa (thinner) and the transition pressure of 38.5 GPa (thicker). Solid curves denote the  $\beta \rightarrow P3' \rightarrow P3$  path and the dashed curves denote direct  $\beta \rightarrow P3$  path. Horizontal axis is defined as qualitative structural similarity. The left end represents  $\beta$  structure and the right end represent  $P3$  structure.

Our predicted  $P3$  phase has a hexagonal symmetry which is different from what Zerr proposed based on the EDXD pattern<sup>78</sup>. However, the interplanar spacings for the six peaks he observed could also be assigned to a crystal system with hexagonal symmetry. A supportive evidence is that Soignard *et al.*<sup>81</sup> observed a similar  $\beta \rightarrow P3$  metastable transition

in  $\text{Ge}_3\text{N}_4$ . They claimed that Zerr’s  $\delta$ - $\text{Si}_3\text{N}_4$  is likely to be analogous to their observed  $\delta$ - $\text{Ge}_3\text{N}_4$  based on comparison of the X-ray diffraction and Raman data. More experimental works are needed to confirm the structure of  $\delta$  phase.

## 5.6 Thermodynamic Properties

As a direct by-product of our thermodynamic potential calculation, we derived thermal properties for  $\alpha$ -,  $\beta$ -, and  $\gamma$ - $\text{Si}_3\text{N}_4$  over a wide  $T$ - $P$  range. In our vibrational Helmholtz free energy calculations, at each temperature, the data points of eight volumes (from 9.25 Å to 11.0 Å) were fitted to the second-order BM-EOS by the least square fitting algorithm. Note that the static EOS  $E_{static}(V)$  is fitted with the 3<sup>rd</sup>-order BM-EOS models. Figure 5.15 shows the temperature dependence of the volume thermal expansion of  $\beta$ - $\text{Si}_3\text{N}_4$  at zero pressure. The experimental data are widely scattered in both low  $T$  and high  $T$  regions which may be attributed to the lack of good-quality single crystal samples. Therefore first-principles calculated thermal properties of bulk  $\beta$ - $\text{Si}_3\text{N}_4$  can serve as a guide for interpretation of experiments. To illustrate the numerical uncertainties associated with the choices of different thermal BM-EOS models, we also include the results that are derived from the static energies fitted with 2<sup>nd</sup>-order BM-EOS. The two set of calculations both agree reasonably with experimental data. Below room temperature the two calculated curves are almost identical, and they gradually split as temperature increases. At  $T = 2000$  K, the TEC is  $1.19 \times 10^{-5} \text{ K}^{-1}$  for EOS-I ( $E_{static}$  fitted with 2<sup>nd</sup>-order BM-EOS and  $F_{vib}$  fitted with 2<sup>nd</sup>-order BM-EOS) and  $1.11 \times 10^{-5} \text{ K}^{-1}$  for EOS-II ( $E_{static}$  fitted with 3<sup>rd</sup>-order BM-EOS and  $F_{vib}$  fitted with 2<sup>nd</sup>-order BM-EOS). The thermal expansivity of EOS-I fits slightly better to the experimental results. For temperatures lower than 150 K our calculation shows negative thermal expansion, and this has also been pointed out by Kuwabara *et al.* in their calculations<sup>71</sup>. At low temperatures of  $T < 500$  K, our prediction agrees well to the measured data except Reeber’s, which is apparently different from the others. For temperatures  $T > 800$  K, Henderson’s data has a nearly linear temperature dependence which

is questionable. In most temperature range, our calculated thermal expansion coefficient from EOS-I is consistent with Bruls' results.

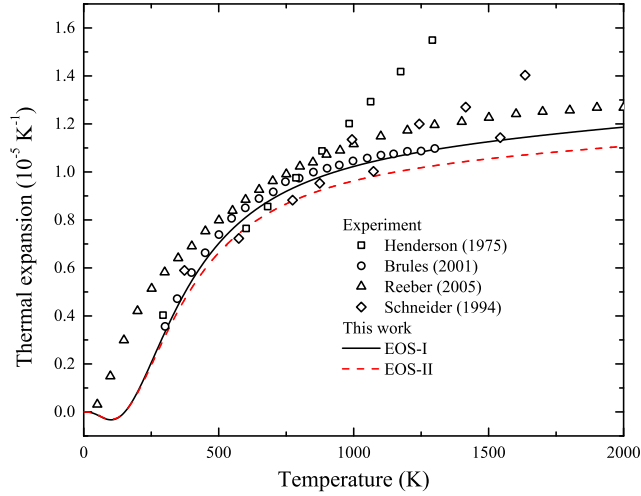


Figure 5.15: Temperature dependence of volume thermal expansion coefficient of bulk  $\beta$ - $\text{Si}_3\text{N}_4$  at zero pressure. Solid and dashed lines show present work with static energies fitted to the  $2^{\text{nd}}$ -order BM-EOS and  $3^{\text{rd}}$ -order BM-EOS, respectively, and both thermal free energies fitted to the  $2^{\text{nd}}$ -order BM-EOS. Discrete symbols denote experimental data<sup>83–86</sup>.

The negative thermal expansion coefficient below 150 K can be related to the negative bulk Grüneisen parameter  $\gamma$  in that temperature range.  $\alpha = \gamma C_V / (B_T V)$ . Figure 5.16 shows our calculated Grüneisen parameter of  $\beta$ - $\text{Si}_3\text{N}_4$  together with reported experimental data. The present temperature dependence of bulk Grüneisen parameter is in good agreement with Bruls' measured data in the temperature range between 300 K and 1300 K. The estimated percentage difference between experiment and calculation is within 10% for  $300 \text{ K} < T < 500 \text{ K}$  and the difference is gradually reduced to about 2% at  $T = 1300 \text{ K}$ . Also, one can notice that the Grüneisen parameter is not sensitive to the two EOS schemes we used. The EOS-I scheme yield a larger thermal expansivity and larger volume at high temperatures, while the EOS-II scheme yield a larger isothermal bulk modulus, and both EOS schemes give very similar  $C_V$  curves at all temperatures. The cancelation effect leads to the similarity in the bulk Grüneisen parameter.

The bulk Grüneisen parameter is the weighted average of mode Grüneisen ratios. At low temperature, only low-frequency phonons, which mostly have negative mode Grüneisen

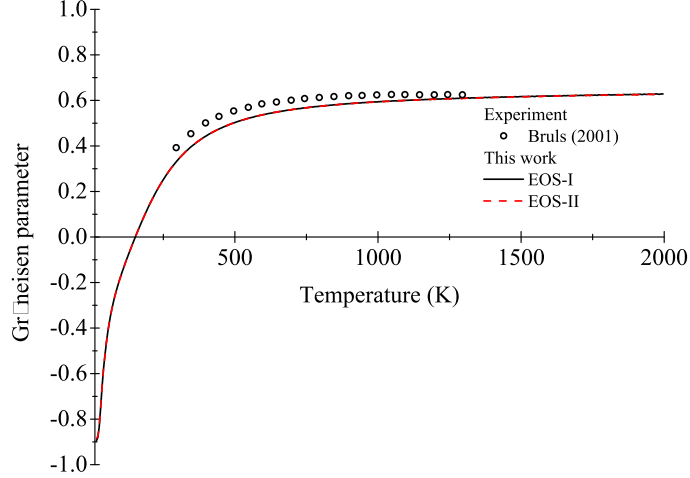


Figure 5.16: Temperature dependence of bulk Grüneisen parameter of  $\beta$ -Si<sub>3</sub>N<sub>4</sub> at zero pressure. Solid and dashed lines show present work with static energies fitted to the 2<sup>nd</sup>-order BM-EOS and 3<sup>rd</sup>-order BM-EOS, respectively, and both thermal free energies are fitted to the 2<sup>nd</sup>-order BM-EOS. Discrete symbols denote experimental data<sup>85</sup>.

ratios, are thermally excited. This yields the negative overall bulk Grüneisen parameters and consequently it leads to the negative thermal expansion coefficients. The two branches that corresponding to the most negative mode Grüneisen parameters are found to be the softening M-point TA and  $\Gamma$ -point B<sub>u</sub> modes, which are responsible for the instability of  $\beta$ -Si<sub>3</sub>N<sub>4</sub> at high pressures.

Figure 5.17 shows the calculated TEC of  $\beta$ -Si<sub>3</sub>N<sub>4</sub> based on EOS-II as a function of temperature at several pressures up to 30 GPa. As pressure increases from 0 to 30 GPa, the TEC decreases from  $1.11 \times 10^{-5}$  to  $0.69 \times 10^{-5}$  K<sup>-1</sup> at 2000 K temperature. The negative TEC range extends from below 150 K at 0 GPa to 220 K at 30 GPa. The most negative TEC value also decreases from  $-3.11 \times 10^{-7}$  to  $-5.09 \times 10^{-7}$  K<sup>-1</sup>. This pressure effect of TEC in  $\beta$ -Si<sub>3</sub>N<sub>4</sub> is in agreement with the calculated pressure effect on low frequency phonon modes and the soft-phonon associated structural instability discussed in earlier sections.

Isobaric heat capacity per atom as a function of temperature at zero pressure is shown in Figure 5.18. First, both EOS schemes yield very alike curves throughout the plotted temperature region, which implies that  $C_P$  is not sensitive to the equation of states adopted.

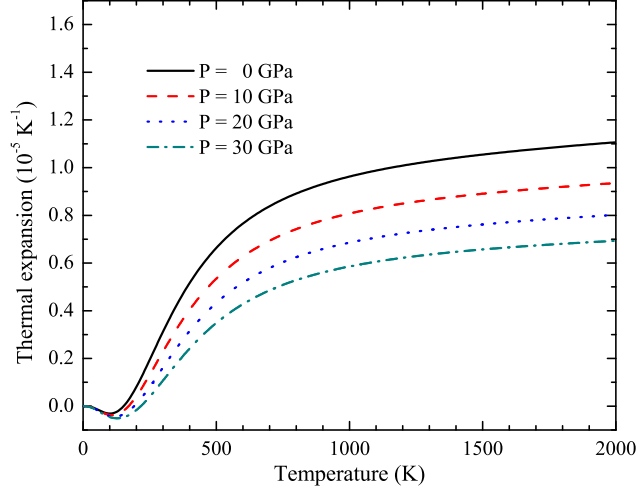


Figure 5.17: Temperature dependence of volume thermal expansion coefficient of bulk  $\beta$ - $\text{Si}_3\text{N}_4$  at pressures of 0, 10, 20 and 30 GPa.

Below room temperature our calculations are in excellent agreement with all shown experimental results, and the agreement is still good above room temperature except Reeber's data. Note that Reeber's data are considerably different from other experimental results and theoretical calculations in both thermal expansivity and isobaric heat capacity. At the same time, we find a persistent agreement with the Bruls' measurements for both  $C_P$  and TEC.

Figure 5.19 shows the temperature dependencies of TEC for  $\alpha$ -,  $\beta$ - and  $\gamma$ - $\text{Si}_3\text{N}_4$  at zero pressure. The equation of state scheme we adopted is EOS-II. We also present the experimental TEC of  $\gamma$ - $\text{Si}_3\text{N}_4$  in the same plot. Although the two experimental works do not agree well with each other, our prediction is consistent with Paszkowicz *et al.* below room temperature and the agreement is still reasonable in the temperature range from 300 K to 1000 K. More high quality measurements are required to assess the TEC of  $\gamma$ - $\text{Si}_3\text{N}_4$ . Thermal expansion coefficients of  $\alpha$ - and  $\beta$ - $\text{Si}_3\text{N}_4$  are similar in magnitude over all temperatures and their difference at 2000 K is less than  $2 \times 10^{-6} \text{ K}^{-1}$ . In Kuwabara *et al.*'s calculation, TEC of  $\alpha$  phase was predicted to be slightly smaller than that of  $\beta$  phase. This might be ascribed to the sensitive nature of TEC upon the numeric fluctuation of thermal data. Both  $\alpha$  and  $\beta$  phases present negative TEC at low temperature which is consistent



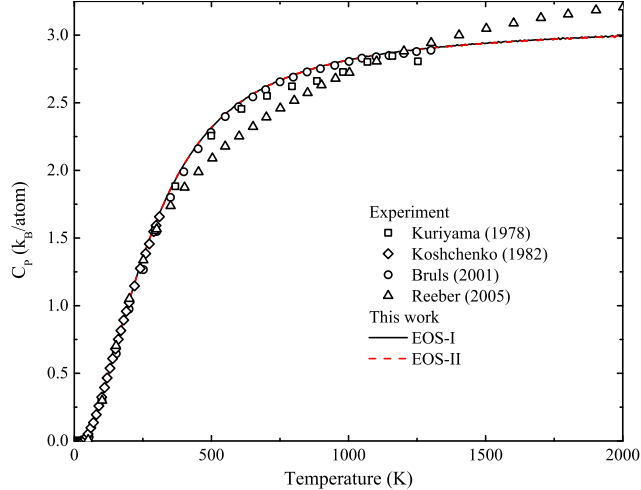


Figure 5.18: Temperature dependence of isobaric heat capacity of  $\beta$ - $\text{Si}_3\text{N}_4$  at zero pressure. Solid and dashed lines show present work with static energies fitted to the  $2^{\text{nd}}$ -order BM-EOS and  $3^{\text{rd}}$ -order BM-EOS, respectively, and both thermal free energies are fitted to the  $2^{\text{nd}}$ -order BM-EOS. Discrete symbols denote experimental data<sup>85–88</sup>.

with the first-principles calculation from Kuwabara *et al.* The lowest TEC for the  $\alpha$  phase is about  $-1.5 \times 10^{-7} \text{ K}^{-1}$  at 90 K, and for the  $\beta$  phase it is  $-3.1 \times 10^{-7} \text{ K}^{-1}$  at 100 K. Unlike  $\alpha$ - and  $\beta$ - $\text{Si}_3\text{N}_4$ , TEC of  $\gamma$  phase is about twice as large as the that of  $\alpha$ - or  $\beta$ - $\text{Si}_3\text{N}_4$  in the temperature range from room temperature to 2000 K. At 2000 K, we predict a TEC of  $2.3 \times 10^{-5} \text{ K}^{-1}$  which is in good agreement with Kuwabara *et al.*'s *ab initio* calculated  $2.2 \times 10^{-5} \text{ K}^{-1}$ . Paszkowicz *et al.* pointed out that their measured TEC tends to vanish for  $T < 100 \text{ K}$ <sup>90</sup>. However, our calculation is not clearly supportive. Similarly, two other first-principles calculations from Paszkowicz *et al.* and Kuwabara *et al.* do not show the negative or vanishing feature either.

## 5.7 Conclusions

In summary, we have theoretically studied phase transitions in silicon nitride ( $\text{Si}_3\text{N}_4$ ) at high pressure using a first-principles density functional theory method. We find that  $\alpha$ - $\text{Si}_3\text{N}_4$  remains as a metastable phase at temperatures up to 2000 K and pressures up to 10 GPa. The equilibrium  $\beta \rightarrow \gamma$  transition pressure is predicted as 7.5 GPa at 300K

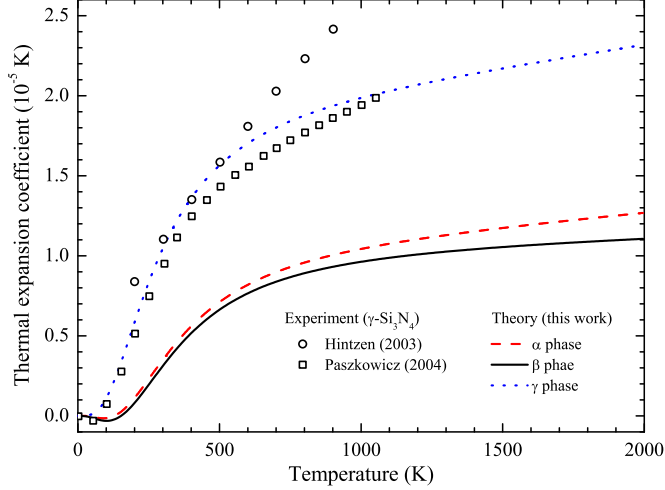


Figure 5.19: Temperature dependence of volume thermal expansion coefficient of  $\alpha$ -,  $\beta$ - and  $\gamma$ - $\text{Si}_3\text{N}_4$  at zero pressure. Discrete symbols represent experimental data<sup>89,90</sup>.

and it increases to 9.0 GPa at 2000K. Both  $\alpha$ - and  $\beta$ - $\text{Si}_3\text{N}_4$  are dynamically stable at low pressure. However, two competing phonon-softening mechanisms are found in the  $\beta$  phase at high pressures. At room temperature,  $\beta$ - $\text{Si}_3\text{N}_4$  is predicted to undergo a first-order  $\beta \rightarrow P3$  transition above 38.5 GPa, while  $\alpha$ - $\text{Si}_3\text{N}_4$  shows no signs of structural instability. The predicted metastable high-pressure  $P3$  phase is structurally related to  $\beta$ - $\text{Si}_3\text{N}_4$ . The enthalpy barrier height is estimated as only 67.23 meV/atom. Our LDA predicted thermal expansion coefficient, heat capacity and bulk Grüneisen parameter are in good agreement with Bruls' measured results. We find relatively large discrepancies between our calculation with experimental data from Reeber. And we attribute the cause of predicted negative TEC at low temperatures in  $\alpha$  and  $\beta$ - $\text{Si}_3\text{N}_4$  to the low-frequency phonon modes that have negative mode Grüneisen ratios.

CHAPTER 6  
FIRST-PRINCIPLES STUDY OF GALLIUM OXIDE AND GALLIUM  
OXYNITRIDE

## 6.1 Gallium Oxide: $\text{Ga}_2\text{O}_3$

### 6.1.1 Introduction

The oxides of group 13 elements (Al, Ga, In) are important solid-state compounds with applications in fields ranging from structural ceramics to catalysts and electronic materials<sup>201</sup>. Monoclinic gallium oxide ( $\text{Ga}_2\text{O}_3$ ) is usually known as a wide-band-gap semiconductor ( $E_g = 4.9$  eV) ; however, the conductivity can be varied from insulating to conducting behavior depending upon the preparation conditions<sup>93</sup>. Due to its tunable optical and electronic properties,  $\beta\text{-Ga}_2\text{O}_3$  is being developed for use in a wide variety of applications, for instance, as optical windows<sup>202</sup>, in high-temperature chemical gas sensors<sup>203</sup>, as a magnetic memory material<sup>204</sup>, and for dielectric thin films<sup>205</sup>. Recently, considerable effort has been devoted to the study of low-dimensional  $\text{Ga}_2\text{O}_3$  materials, and  $\beta\text{-Ga}_2\text{O}_3$  nanowires have been obtained through physical evaporation and arc-discharge methods<sup>101</sup>.  $\beta\text{-Ga}_2\text{O}_3$  has also attracted recent interest as a phosphor host material for applications in thin film electroluminescent displays<sup>206,207</sup>. Due to its chemical and thermal stability,  $\beta\text{-Ga}_2\text{O}_3$  may emerge as a useful alternative to sulfide based phosphors<sup>208</sup>.

It is well known that  $\text{Ga}_2\text{O}_3$  can exist in several forms, including  $\alpha$ ,  $\beta$ ,  $\gamma$ ,  $\delta$ , and  $\epsilon$  polymorphs that all have different structure types<sup>94</sup>. Of these, the most stable form at ambient conditions is determined to be  $\beta\text{-Ga}_2\text{O}_3$  (monoclinic  $C2/m$ , Figure 6.1)<sup>94</sup>. However, other metastable varieties can be prepared and they have been characterized at ambient pressure and temperature. This is an important observation, because the different forms have dramatically different optoelectronic properties. For example, the band gap of the  $\alpha\text{-Ga}_2\text{O}_3$

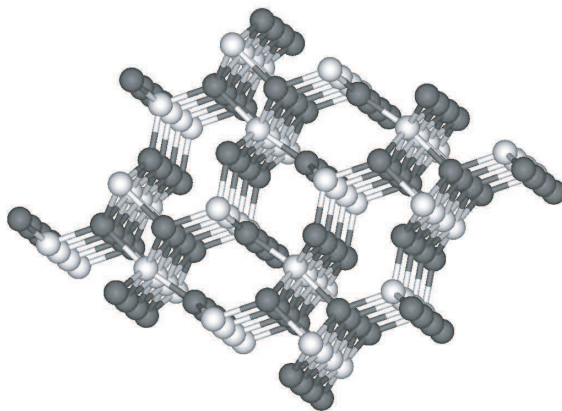


Figure 6.1: Crystal structure of monoclinic  $\beta$ -Ga<sub>2</sub>O<sub>3</sub> phase. Note that Ga<sup>3+</sup> cations (light color) occupy both tetrahedral and octahedral interstices within the ccp lattice of O<sup>2-</sup> ions (dark color).

polymorph that is isostructural with corundum ( $\alpha$ -Al<sub>2</sub>O<sub>3</sub>) is 2.41 eV, much narrower than that of  $\beta$ -Ga<sub>2</sub>O<sub>3</sub><sup>209</sup>.

It is of great interest to determine the pressure-induced phase transformations among Ga<sub>2</sub>O<sub>3</sub> polymorphs in order to establish the stable and metastable phase relations between different crystalline modifications, and to evaluate their production under different synthesis conditions. It is particularly important to understand the role of differential mechanical stresses that are present in creation of nanoparticles or nanowires, in promoting the formation of specific polymorphic forms.

The high-pressure behavior of Al<sub>2</sub>O<sub>3</sub> compounds has been studied extensively, particularly the corundum-structured  $\alpha$ -Al<sub>2</sub>O<sub>3</sub> phase, because of its importance as a mineral structure within the deep Earth and also due to the widespread use of ruby (Cr<sup>3+</sup>-doped  $\alpha$ -Al<sub>2</sub>O<sub>3</sub>) as a luminescent pressure gauge for *in situ* high-pressure experiments in the diamond anvil cell<sup>1</sup>. Cr<sup>3+</sup>-doped  $\beta$ -Ga<sub>2</sub>O<sub>3</sub> has likewise been proposed as a pressure gauge material. The R1 luminescence line in this phase shows a pressure shift nearly three times that of ruby, indicating that it would make a more sensitive pressure sensor that is especially

useful in the lower pressure range<sup>210</sup>. In situ high-pressure and high-temperature measurements on  $\alpha$ -Al<sub>2</sub>O<sub>3</sub> using synchrotron x-ray diffraction in a diamond anvil cell, combined with *ab initio* theory predictions, have now been used to characterize a transition into the Rh<sub>2</sub>O<sub>3</sub>-II structure occurring at  $P \sim 100$  GPa and  $T > \sim 1000$  K<sup>5,8</sup>.

The high-pressure behavior of Ga<sub>2</sub>O<sub>3</sub> has received much less attention. The various low-density Ga<sub>2</sub>O<sub>3</sub> structures encountered at low pressure contain the Ga<sup>3+</sup> cations in tetrahedral coordination (i.e., GaO<sub>4</sub> species). The thermodynamically stable  $\beta$ -Ga<sub>2</sub>O<sub>3</sub> polymorph is isomorphous with the metastable  $\theta$ -Al<sub>2</sub>O<sub>3</sub> structure, which represents a key phase achieved during metastable transformations among various partially dehydrated “transitional” aluminas as they evolve towards corundum<sup>211</sup>.  $\theta$ -Al<sub>2</sub>O<sub>3</sub> constitutes an intermediate structure between the cubic close packing of anions achieved within the low-temperature metastable aluminas, and hexagonally close-packed  $\alpha$ -Al<sub>2</sub>O<sub>3</sub> corundum (isomorphous with  $\alpha$ -Ga<sub>2</sub>O<sub>3</sub>).

In a recent study using synchrotron energy-dispersive x-ray diffraction techniques in the diamond anvil cell, it was reported that a sample of “ $\alpha$ -Ga<sub>2</sub>O<sub>3</sub>” transformed to a structure assigned to be tetragonal at a pressure of approximately 13.3 GPa.<sup>212</sup> However, the x-ray diffraction pattern of the starting material most strongly resembled that of  $\beta$ -Ga<sub>2</sub>O<sub>3</sub>, rather than the  $\alpha$ -form, and a mixture of phases was present. Commercial Ga<sub>2</sub>O<sub>3</sub> samples usually consist mainly of  $\beta$ -Ga<sub>2</sub>O<sub>3</sub>, along with some  $\alpha$ -Ga<sub>2</sub>O<sub>3</sub>; that phase can be removed by heat treatment<sup>94</sup>. The relative densities of  $\beta$ - and  $\alpha$ -Ga<sub>2</sub>O<sub>3</sub> are 5.94 and 6.48 g·cm<sup>-3</sup>, respectively<sup>95</sup>, indicating that a  $\beta \rightarrow \alpha$  transformation should occur at high pressure. Nanocrystalline  $\beta$ -Ga<sub>2</sub>O<sub>3</sub> particles embedded in a glassy matrix were also studied at high pressure using energy-dispersive x-ray diffraction<sup>96</sup>. In that work, a  $\beta$ -to- $\alpha$  phase transformation was found to be initiated at 6 GPa, but the process was not completed by 15 GPa, the highest pressure achieved in the study. However, it is known that the silica glass host matrix undergoes important structural and density changes within this pressure range<sup>97,98</sup>, so that it is not yet known if the structural changes are intrinsic to the  $\beta$ -Ga<sub>2</sub>O<sub>3</sub> material presumably influenced by the nanocrystalline nature of the sample, or

are promoted by anomalous densification among the  $\text{SiO}_2$  matrix. These results prompted us to theoretically investigate the high-pressure behavior of the phase-pure bulk  $\beta\text{-Ga}_2\text{O}_3$ , accompanied with an experimental study using Raman spectroscopy and high-resolution synchrotron x-ray diffraction angle dispersive techniques.

Recently, two further pressure-induced phase transitions have been confirmed from both first-principles calculations and high-pressure x-ray diffraction measurements using laser-heated diamond-anvil cell (LHDAC). The further transition sequence found in  $\text{Ga}_2\text{O}_3$  is the same as that in  $\text{Al}_2\text{O}_3$ , i.e.,  $\alpha \rightarrow \text{Rh}_2\text{O}_3(\text{II}) \rightarrow \text{postperovskite}$  ( $Cmcm$   $\text{CaIrO}_3$ -type). The experimentally determined  $P_t$  for these two transitions are  $\sim 37$  GPa at  $2000 \pm 100$  K and 164 GPa at  $1300 \pm 500$  K.

One-dimensional nanostructured forms of  $\beta$ -phase of gallium oxide ( $\beta\text{-Ga}_2\text{O}_3$ ) such as nanotubes, nanobelts, and nanowires, have attracted recent interest due to enhanced optical properties<sup>99,100</sup>. Recently, Choi *et al.*<sup>101</sup> synthesized  $\beta\text{-Ga}_2\text{O}_3$  nanowires (diameter range of 15–45 nm) with a [001] growth direction using an arc-discharge method. Gao *et al.*<sup>102</sup> synthesized  $[40\bar{1}]$   $\beta\text{-Ga}_2\text{O}_3$  nanowires with diameters ranging from  $\sim 10$ –100 nm in a vertical radio-frequency furnace. Interestingly, the Raman mode frequencies of the [001]  $\beta\text{-Ga}_2\text{O}_3$  nanowires coincide with the corresponding frequencies in bulk  $\beta\text{-Ga}_2\text{O}_3$ <sup>101</sup>. On the other hand<sup>102</sup>, the Raman mode frequencies of the  $[40\bar{1}]$   $\beta\text{-Ga}_2\text{O}_3$  nanowires are redshifted relative to corresponding frequencies in bulk  $\beta\text{-Ga}_2\text{O}_3$  by 4–23  $\text{cm}^{-1}$ . Using plasma-enhanced chemical vapor deposition, Rao *et al.* have synthesized  $\beta\text{-Ga}_2\text{O}_3$  nanowires whose growth is along the [110] direction<sup>103</sup>, and the Raman spectrum is significantly blueshifted in frequency<sup>104</sup>. Here we focus on the first-principles calculations of the Raman mode frequencies under internal strains. Our calculated Raman frequency shifts suggest that the observed shifts in the nanowires with the  $[40\bar{1}]$  and [110] growth directions can be explained in term of different internal strains, in contrast to the previously suggested quantum confinement effects and defect-induced effects.

Table 6.1: Third-order BM-EOS parameters for Ga<sub>2</sub>O<sub>3</sub> polymorphs

Source	Phase	$V_0$ (Å <sup>3</sup> /atom)	$B$ (GPa)	$B'$
This work	$\beta$	10.134	177	3.84
Calculation <sup>214</sup>		10.228	142	4.1
Experiment <sup>213</sup>			202(7)	2.4(6)
Experiment <sup>96</sup>			191(5)	8.3(9)
Experiment <sup>214</sup>		10.462	134(12)	4
This work	$\alpha$	9.375	226	3.971
Calculation <sup>214</sup>		9.448	243	4.0
Experiment <sup>213</sup>			~250	
Experiment <sup>214</sup>		9.632(1)	223(2)	4
This work	Rh <sub>2</sub> O <sub>3</sub> (II)	9.130	234	3.98
Calculation <sup>214</sup>		9.188	244	4.3
Experiment <sup>214</sup>		9.244(4)	271(10)	4

### 6.1.2 Total Energy and Vibrational Properties

During the course of the experimental studies from our collaborators<sup>104,213</sup>, we began a parallel theoretical investigation of the structures, relative energetics, and properties of Ga<sub>2</sub>O<sub>3</sub> phases. Our calculations are based on the first-principles density functional theory within the local density approximation (LDA). The calculations were carried out with the VASP codes<sup>139–142</sup>, using planewave basis sets and ultrasoft pseudopotentials (US-PP)<sup>121</sup>. In this study, both valence (4s4p) and semi-core (3d) electrons in Ga atoms were treated explicitly, while the core electrons were approximated with the US-PP. The energy cutoff of the plane-wave basis was chosen as 396 eV. The Brillouin zone integration of total energy of the unit cells was carried out using  $6 \times 6 \times 6$  grids for both phases.

Equilibrium volume  $V_0$ , bulk moduli  $B$  and  $B'$  for  $\beta$ ,  $\alpha$  and Rh<sub>2</sub>O<sub>3</sub>(II) phases are obtained from the least-square fitting to the 3<sup>rd</sup>-order Birch-Murnaghan equation of state. Fitting parameters  $V_0$ ,  $B$  and  $B'$ , are listed in Table 6.1. Our LDA results agree reasonably with other calculated and experimental data. Compared with the experimental values of  $V_0$ , our prediction has an underestimation of less than 3%. The static enthalpies of three polymorphs relative to the  $\alpha$  phase are plotted in Figure 6.2 as a function of pressure. It

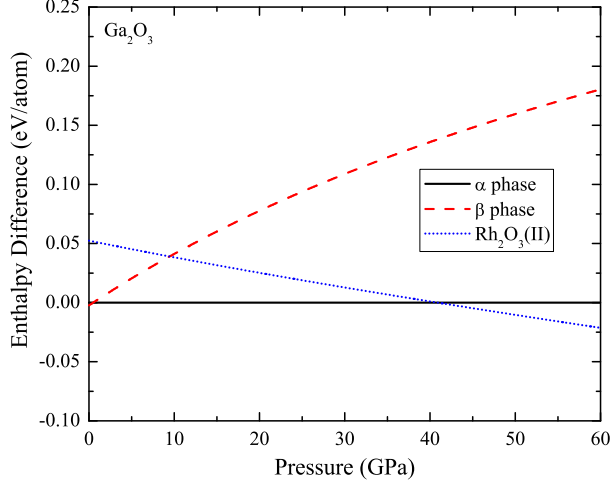


Figure 6.2: Enthalpy differences relative to  $\alpha$  phase for  $\alpha$ ,  $\beta$  and  $\text{Rh}_2\text{O}_3(\text{II})$ - $\text{Ga}_2\text{O}_3$  as a function of pressure up to 60 GPa. The  $\beta$  and  $\alpha$  curves cross at 0.5 GPa, the  $\alpha$  and  $\text{Rh}_2\text{O}_3(\text{II})$  curves cross at 40.9 GPa.

can be seen that  $\beta$  phase is predicted to transform into  $\alpha$  phase at 0.5 GPa and  $\alpha$  phase further transforms into  $\text{Rh}_2\text{O}_3(\text{II})$  phase at 40.9 GPa.

The phonon dynamical matrices  $D_{ij}(\mathbf{k})$  were constructed at the Brillouin zone center ( $\Gamma$ -point:  $\mathbf{k} = 0$ ) using a (realspace) force constant matrix  $\phi_{ij}(\mathbf{r})$  by calculating forces on each atom as it is slightly displaced from its equilibrium position (e.g., by 0.015 Å). Further approximations were adopted to calculate the  $D_{ij}(\mathbf{k})$  matrix at a general  $\mathbf{k}$ -point. In the case of  $\alpha$ - $\text{Ga}_2\text{O}_3$ , we first obtained the real space  $\phi_{ij}(\mathbf{r})$  matrix using a 120-atom supercell model. Because of the large size of the supercell model, and the fact that the material is insulating wide-gap semiconducting, we can safely neglect interatomic interactions between atoms separated by >50% of the supercell lattice constants, and thus obtain  $D_{ij}(\mathbf{k})$  by Fourier transformation of the real-space matrix elements  $\phi_{ij}(\mathbf{r})$ .

Fifteen Raman-active modes are expected for the  $\beta$ - $\text{Ga}_2\text{O}_3$  structure (point symmetry  $C_{2h}^3$ ) from symmetry analysis:

$$\Gamma_{\text{Raman}} = 10A_g + 5B_g \quad (6.1)$$



Table 6.2: Calculated and experimental zone-center Raman peak positions and Grüneisen parameter for the  $\beta$ -Ga<sub>2</sub>O<sub>3</sub> phase

Mode symmetry	Frequency (cm <sup>-1</sup> )				Grüneisen ratio	
	calculated		measured		This work (LDA)	This work (measured <sup>213</sup> )
	This work (LDA)	Empirical calculation <sup>215</sup>	Machon <i>et al.</i> <sup>213</sup>	Rao <i>et al.</i> <sup>104</sup>		
$A_g$	104	113	110.2		1.39	
$B_g$	113	114	113.6		-0.7	
$B_g$	149	152	144.7	144	1.53	1.97(8)
$A_g$	165	166	169.2	169	1.00	0.35(3)
$A_g$	205	195	200.4	200	1.30	0.98(2)
$A_g$	317	308	318.6	317	1.13	0.95(1)
$A_g$	346	353	346.4	344	1.83	1.52(1)
$B_g$	356	360			1.47	
$A_g$	418	406	415.7	416	0.58	0.78(4)
$A_g$	467	468		472	1.26	
$B_g$	474	474	473.5		1.14	1.27(9)
$A_g$	600	628		629	1.70	
$B_g$	626	644	628.7		0.8	1.54(3)
$A_g$	637	654	652.5	654	1.39	1.39(2)
$A_g$	732	760	763.9	767	1.23	1.11(1)

The calculated frequencies and their mode Grüneisen parameters are reported in Table 6.2. The Raman-active modes of  $\beta$ -Ga<sub>2</sub>O<sub>3</sub> can be classified into three groups: high-frequency stretching and bending of GaO<sub>4</sub> tetrahedra ( $\sim$ 770–500 cm<sup>-1</sup>), midfrequency deformation of Ga<sub>2</sub>O<sub>6</sub> octahedra ( $\sim$ 480–310 cm<sup>-1</sup>), and lowfrequency libration and translation (below 200 cm<sup>-1</sup>) of tetrahedra-octahedra chains<sup>215</sup>. The listed experimental values of Machon *et al.* are from an unpolarized Raman spectrum of  $\beta$ -Ga<sub>2</sub>O<sub>3</sub> recorded from powdered material obtained by annealing a commercial sample<sup>213</sup>. Our calculated frequencies agree well with the observed values, to within 0.1%–6%, which is typical for LDA calculations (Table 6.2). The  $B_g$  mode predicted at 356 cm<sup>-1</sup> was likely unresolved from the  $A_g$  mode at 346 cm<sup>-1</sup> in the measured Raman spectrum<sup>213</sup>; however, a weak peak at this frequency was recorded by Dohy *et al.*<sup>215</sup>. The band observed at 474 cm<sup>-1</sup> also likely contains contributions from the calculated  $A_g$  and  $B_g$  modes at 467 and 474 cm<sup>-1</sup>. Surprisingly, we found no experimental evidence for the predicted  $A_g$  mode at 600 cm<sup>-1</sup>. We have no explanation for that observation. Symmetry analysis indicates that seven Raman active modes ( $2A_{1g} + 5E_g$ ) are expected for the corundum structure. Our theoretically calculated frequencies agree to within 0.7%–5.5% with the observed values (Table 6.3).

Table 6.3: Calculated and experimental zone-center Raman peak positions for the  $\alpha$ -Ga<sub>2</sub>O<sub>3</sub>

Mode symmetry	Frequency (cm <sup>-1</sup> )	
	(calculated)	(measured)
$A_{1g}$	215	217.4
$E_g$	239	240.8
$E_g$	281	286.1
$E_g$	344	328.7
$E_g$	410	432.2
$A_{1g}$	551	573
$E_g$	680	688.1

### 6.1.3 $T$ - $P$ Phase Diagram

The monoclinic  $\beta$ -Ga<sub>2</sub>O<sub>3</sub> structure is the stable polymorph at ambient pressure and temperature. In this phase, the O<sup>2-</sup> anions form a slightly distorted fcc lattice and cations occupy tetrahedral and octahedral interstices (Figure 6.1). This structure is quite different from that of the  $\alpha$ -Ga<sub>2</sub>O<sub>3</sub> phase (corundum structure), which is based on a distorted hcp O<sup>2-</sup> sublattice with 2/3 of the octahedral interstices occupied by Ga<sup>3+</sup> ions. The  $\beta \rightarrow \alpha$  transition is expected to result from increasing the pressure, from the observed density relationships between the two phases. The transformation involves a change in the O<sup>2-</sup> packing from cubic to hexagonal, accompanied by a shift in Ga<sup>3+</sup> ions between tetrahedral and octahedral sites. The reconstructive nature of the transition indicates that it is thermodynamically of the first order, and it might be expected to involve a large activation energy, which gives rise to slow transformation kinetics at low temperature. In addition, the high-density structure has significant possibilities for disorder among the Ga<sup>3+</sup> positions on octahedral sites within the hcp O<sup>2-</sup> sublattice, which might not be readily detected by x-ray diffraction<sup>8</sup>.

$\beta$ - $\alpha$  and  $\alpha$ -Rh<sub>2</sub>O<sub>3</sub>(II) phase boundaries of Ga<sub>2</sub>O<sub>3</sub> are plotted in Figure 6.3. The calculated transition pressure from  $\beta$  to  $\alpha$  phase is 0.3 GPa at 0 K and 1.6 GPa at 2000 K. The Clapeyron slope for this transition is positive which has the value of about +0.6 MPa/K at 1000 K. Our predicted  $P_t$  is consistent with reported LDA calculation from Yusa *et al*<sup>214</sup>. On the experimental side,  $\alpha$ -Ga<sub>2</sub>O<sub>3</sub> was synthesized from  $\beta$ -Ga<sub>2</sub>O<sub>3</sub> at 4.4 GPa

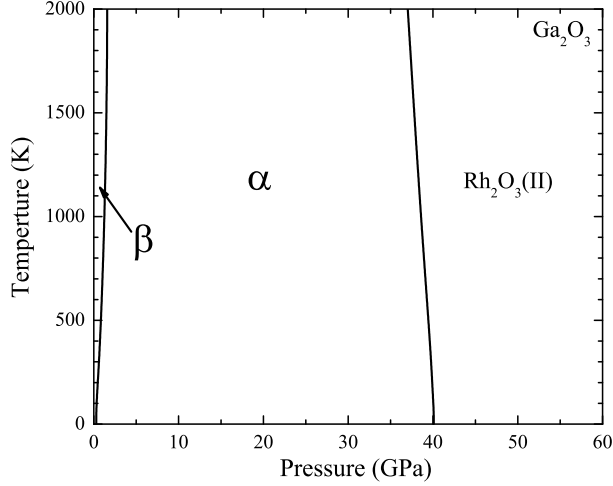


Figure 6.3:  $T$ - $P$  phase diagram for  $\beta$ ,  $\alpha$  and  $\text{Rh}_2\text{O}_3(\text{II})$ - $\text{Ga}_2\text{O}_3$  polymorphs.

and 1000 °C<sup>95,216</sup>. However, the room temperature compression experiments obtain much higher transition pressures. Tu *et al.* have reported a  $\beta$ -to- $\alpha$  phase transition in  $\text{Ga}_2\text{O}_3$  at 13.3 GPa<sup>212</sup>. But there is some uncertainty in the nature of the starting material used in that work. Recently, x-ray diffraction and Raman scattering results from Machon *et al.*<sup>213</sup> on  $\beta$ - $\text{Ga}_2\text{O}_3$  clearly indicate that a pressure-induced phase transformation occurs within the  $P = 20 - 22$  GPa range, and perhaps as low as  $P = 18.5$  GPa. Analysis of the x-ray diffraction data suggest that the high-density phase corresponds to corundum-structured  $\alpha$ - $\text{Ga}_2\text{O}_3$ . However, broadening observed both in the x-ray diffraction peaks and in the Raman spectra indicate that the material is structurally disordered. The large discrepancy on  $P_t$  may be caused by a large kinetic barrier, which is significantly lowered under compression. Our calculated  $\alpha$ -to- $\text{Rh}_2\text{O}_3(\text{II})$  transition pressure is 40 GPa at 0 K and 37 GPa at 2000 K, which is in excellent agreement with the experimental value (about 37 GPa at  $2000 \pm 100$  K)<sup>214</sup>. The phase boundary we predict shows negative Clapeyron slope which is about -1.65 MPa/K at 1000 K. Tsuchiya *et al.* reported their calculated Clapeyron slope of the  $\alpha$ - $\text{Rh}_2\text{O}_3(\text{II})$  boundary, which is -2.2 MPa/K at 1000 K<sup>217</sup>. The discrepancy may be ascribed to the adopted computational methodologies.

#### 6.1.4 Blue-Shifted Raman Scattering in Gallium Oxide Nanowires

Rao *et al.*<sup>104</sup> reported the Raman and Fourier transform infrared spectra of  $\beta$ -Ga<sub>2</sub>O<sub>3</sub> nanowires with [110] growth direction which is blueshifted relative to the bulk spectra by 10–40 cm<sup>-1</sup>. The blueshift in phonon frequencies of low-dimensional materials are often attributed to the size-confinement effect<sup>218,219</sup>. However, the average diameter of the  $\beta$ -Ga<sub>2</sub>O<sub>3</sub> nanowires is around 25 nm. It is unlikely that the quantum size confinement at this length scale is significant enough to cause the phonon shifts as large as 50 cm<sup>-1</sup>. Furthermore, three distinctly different shift patterns have been experimentally observed for the  $\beta$ -Ga<sub>2</sub>O<sub>3</sub> nanowires of different growth directions. In contrast to the blueshift in the Raman and FTIR spectra reported by Rao *et al.*, Choi *et al.* showed that their Fourier transform Raman spectrum of [001]  $\beta$ -Ga<sub>2</sub>O<sub>3</sub> nanowires is identical to that of bulk  $\beta$ -Ga<sub>2</sub>O<sub>3</sub><sup>101</sup>, while Gao *et al.* exhibited a *redshift* of 4–23 cm<sup>-1</sup> in the Raman peak frequencies of their [40 $\bar{1}$ ]  $\beta$ -Ga<sub>2</sub>O<sub>3</sub> nanowires relative to the corresponding Raman frequencies in bulk  $\beta$ -Ga<sub>2</sub>O<sub>3</sub><sup>102</sup>. The size confinement effect is clearly insufficient to explain the diversity of the observed shift patterns.

On the other hand, the redshift in the phonon frequencies has also been attributed to the presence of impurities and defects, such as point defects, twins, and stacking faults<sup>220</sup>. These defects are also likely to be responsible for additional vibrational modes observed in the Raman spectra (and to a small extent in the FTIR spectrum) of nanowires. From a detailed high-resolution transmission electron microscopy (HRTEM) study, Gao *et al.* confirmed the presence of twins and edge dislocations in their nanowires<sup>102</sup>. Dai *et al.*<sup>221</sup> also proposed that the O vacancies and the stacking faults caused an abnormality in the Ga–O bond vibration and led to redshift in the Raman frequencies. Although this simple hypothesis is plausible, there is one obvious weakness, i.e., lack of close correlation between defect types and the growth directions. Presumably, similar defects might exist in the nanowires with different growth directions. It is also not clear which types of defects will lead to a blueshift in vibrational frequencies. Moreover, different regions in the nanowires contain different defects which would imply that different shifts in the Raman and/or IR spectra

should be observed when different regions of the *same* nanowire are probed. However, this does not seem to be the case and instead overall distinct blueshifts or redshifts have been observed for a given nanowire. Therefore, alternative models that are capable of describing these diverse peak-shift patterns in a consistent fashion are needed.

Based on a first-principles calculation which we describe next, we propose that the phonon frequencies in different  $\beta$ -Ga<sub>2</sub>O<sub>3</sub> nanowires are shifted as a result of internal strains in the nanowire. The basic assumption of our model is the presence of non-negligible internal strains in the nanowires due to their large surface/volume ratio. Different growth directions will cause different surface reconstruction, and consequently lead to internal strains of different magnitudes and directions. This model provides a consistent explanation for all three aforementioned Raman spectra.

Direct first principles calculations of phonon frequencies of 25-nm-diam nanowires is a computationally challenging task as large supercell models (of at least tens of thousands of atoms) are needed. Instead, our current computation study focuses on providing a quantitative estimation of the internal strains which can account for the observed blue- and redshifts in the Raman frequencies for [110] and  $[40\bar{1}]$   $\beta$ -Ga<sub>2</sub>O<sub>3</sub> nanowires, respectively. We have calculated the strain dependencies of the *bulk*  $\beta$ -Ga<sub>2</sub>O<sub>3</sub> using a density functional theory (DFT) method. The internal strains of the nanowires were estimated based on the least-squares fitting of the experimentally observed Raman frequency shifts with theoretically predicted linear strain coefficients  $d\omega/d\varepsilon_{ij}$ , where  $\omega$  and  $\varepsilon_{ij}$  are Raman frequencies and components of strain tensors, respectively.

The  $\Gamma$ -point phonons of bulk  $\beta$ -Ga<sub>2</sub>O<sub>3</sub> were calculated with a real-space finite displacement technique<sup>129</sup>. Because of its  $C_{2h}$  space-group symmetry, the LO-TO splitting in the optic modes of  $\beta$ -Ga<sub>2</sub>O<sub>3</sub> only exist for the infrared ( $A_u$  and  $B_u$ ) phonon modes, not the Raman active ( $A_g$  and  $B_g$ ) phonon modes. Therefore, all our Raman frequency calculations of  $\beta$ -Ga<sub>2</sub>O<sub>3</sub> were carried out with 10-atom base-centered monoclinic unit-cell model without the correction for the macroscopic interaction. As shown in Table 6.2, the theoretical data for bulk  $\beta$ -Ga<sub>2</sub>O<sub>3</sub> matches well with 13 out of the 15 Raman active ( $10A_g + 5B_g$ ) modes

Table 6.4: Estimated internal strains

	[110]	[401]
Strain	nanowire	nanowire
$\varepsilon_{11}$	-0.0077	0.0029
$\varepsilon_{22}$	0.0180	-0.0064
$\varepsilon_{33}$	-0.0311	0.0106
$\varepsilon_{13}$	0.0233	-0.0256
$\Delta V/V$	-0.0208	0.0071

observed experimentally<sup>104</sup>, as well as those of the previous study of Dohy *et al*<sup>215</sup>. In both cases of the unobserved Raman modes, there is another Raman active mode in the close proximity. For example, our LDA calculations predicted two Raman modes at 469 and 474  $\text{cm}^{-1}$ , and two Raman modes at 601 and 629  $\text{cm}^{-1}$ . This suggests that it is possible that the two “missing” Raman modes are hidden by the stronger adjacent Raman modes.

The strain tensor of this monoclinic crystal has six independent elements,  $\varepsilon_{11}$ ,  $\varepsilon_{22}$ ,  $\varepsilon_{33}$ ,  $\varepsilon_{23}$ ,  $\varepsilon_{13}$  and  $\varepsilon_{12}$ . For simplicity, we restricted this study to linear effects, i.e.,  $\omega(\varepsilon) \approx \omega_0 + \sum (d\omega/d\varepsilon_{ij}) \times \varepsilon_{ij}$ . This approximation is valid for small strains. We further neglected the strain of  $\varepsilon_{23}$  or  $\varepsilon_{12}$  because their  $d\omega/d\varepsilon_{ij}$  coefficients are zeroes due to the monoclinic lattice symmetry. For each of four remaining types of strains ( $\varepsilon_{11}$ ,  $\varepsilon_{22}$ ,  $\varepsilon_{33}$ , and  $\varepsilon_{13}$ ), the Raman frequencies were calculated for five finite strain values between -0.02 and +0.02. The calculated frequencies were then fitted with a polynomial function to obtain the linear strain coefficients.

Fitting the experimental data within our strain-induced phonon shifts model, we predict the internal strains in nanowires which showed the three distinct Raman spectra. The results of the  $[40\bar{1}]$  and  $[110]$  nanowires are listed in Table 6.4, and our model predicts the strain tensor for the  $[001]$  nanowires contain non-negligible  $\varepsilon_{11}$ ,  $\varepsilon_{22}$ ,  $\varepsilon_{33}$ , and  $\varepsilon_{13}$  components. As shown in Table 6.5, we obtain overall excellent fits for both the redshifted and blueshifted Raman spectra, with exception of the 134  $\text{cm}^{-1}$   $B_g$  mode in the  $[40\bar{1}]$  nanowire (Gao *et al.*). Our calculation shows that the  $[110]$  nanowire is compressed along its  $a$  and  $c$  axis, and stretched along its  $b$  axis. The strain in the  $[40\bar{1}]$  nanowire exhibits a contrasting pattern and its strain magnitude is only about 1/3 of that evaluated for the  $[110]$  nanowire. In both

Table 6.5: Raman mode frequencies and frequency shifts in  $\beta$ -Ga<sub>2</sub>O<sub>3</sub> nanowires with the [40 $\bar{1}$ ] and [110] growth directions. Overall, excellent agreement between the observed and calculated shifts is seen for all mode frequencies except the one marked with an \*.

Gao <i>et al.</i> <sup>102</sup>				This work			
[40 $\bar{1}$ ] growth direction				[110] growth direction			
Bulk frequency (cm <sup>-1</sup> )	Nanowire frequency (cm <sup>-1</sup> )	Frequency shifts $\Delta\omega$ (cm <sup>-1</sup> )	Calculated frequency shifts (cm <sup>-1</sup> )	Bulk frequency (cm <sup>-1</sup> )	Nanowire frequency (cm <sup>-1</sup> )	Frequency shifts $\Delta\omega$ (cm <sup>-1</sup> )	Calculated frequency shifts (cm <sup>-1</sup> )
			-4.8				12.0
			1.7				-3.1
142	134	-8*	-1.0	144			3.8
167	160	-7	-7.2	169	180	+11	10.6
198	194	-4	-6.5	200	213	+13	13.5
320			-3.9	317			9.5
344	332	-12	-6.7	344			16.8
			-1.7				0.7
415	409	-6	-5.3	416	428	+12	12.3
473			-4.4	472	492	+20	21.1
			-6.2				18.5
627			-5.7	629	645	+16	17.8
			-0.3				3.6
651	641	-10	-14.8	654	697	+43	36.4
765	742	-23	-20.6	767	810	+43	47.0

cases, the  $a$  axis has the smallest change (Table 6.4). The strain-induced volume changes are predicted to be -2% and 0.7% for the [110] and [40 $\bar{1}$ ] nanowires, respectively. Seo *et al.*<sup>222</sup> studied the internal strains of GaN nanowires using x-ray measurements and they reported the strains of  $\varepsilon_{xx}=2.3\%$ ,  $\varepsilon_{yy}=-0.734\%$ , and  $\varepsilon_{zz}=-0.4\%$  based on their experimental x-ray measurement. The magnitudes of our predicted strains of  $\beta$ -Ga<sub>2</sub>O<sub>3</sub> are comparable to those of GaN nanowires.

### 6.1.5 Conclusions

For bulk Ga<sub>2</sub>O<sub>3</sub>, we have calculated the Raman frequencies and their mode Grüneisen parameters for  $\beta$  and  $\alpha$  phases. Good agreement is achieved between our results with experiments and other calculations. We also predict the equilibrium  $T$ - $P$  phase diagram of Ga<sub>2</sub>O<sub>3</sub> consists of  $\beta$ ,  $\alpha$  and Rh<sub>2</sub>O<sub>3</sub>(II) phases. Our LDA calculated transition pressure from  $\beta$  phase to  $\alpha$  phase is 0.3 GPa at 0 K and 1.6 GPa at 2000 K. The Clapeyron slope

for this transition is positive which has the value of about +0.6 MPa/K at 1000 K. This is consistent with previous calculations. However, the experimental  $P_t$  at room temperature is much larger (20–22 GPa). The discrepancy can be attributed to the existence of a large kinetic barrier, which may be significantly lowered under compression. Our calculated  $\alpha$ -to- $\text{Rh}_2\text{O}_3(\text{II})$  transition pressure is 40 GPa at 0 K and 37 GPa at 2000 K, which is in excellent agreement with the experimental value (about 37 GPa at about 2000 K).

In the case of nanowires, based on a comparison of the experimental Raman mode frequencies with our first-principles calculations, we find compelling evidence for growth direction induced internal strains in  $\beta\text{-Ga}_2\text{O}_3$  nanowires which significantly influence the vibrational mode frequencies. Within the linear model approximation, the observed blue and redshifts of peak frequencies in the micro-Raman spectra of the  $\beta\text{-Ga}_2\text{O}_3$  nanowires with different growth directions can be attributed to two small anisotropic internal strains: one compressive strain of 2% volume change, and the other tensile strain of 0.7% volume change. The overall high quality of the fitted models to available experimental data suggests a strong correlation between the shifts in Raman mode frequencies and the growth direction-induced internal strains in the  $\text{Ga}_2\text{O}_3$  nanowires.

## 6.2 Gallium Oxynitride: $\text{Ga}_3\text{O}_3\text{N}$

### 6.2.1 Introduction

Semiconducting materials with a wide bandgap are of interest for applications in high-temperature electronics and in optoelectronic devices, particularly when the gap is direct. The oxides and nitrides of gallium are wide-gap semiconductors that give rise to materials that are useful in the blue to UV range at short wavelength. The cubic (sphalerite) and hexagonal (wurtzite) forms of GaN have bandgap energies of 3.3<sup>223</sup> and 3.4 eV<sup>224</sup>, respectively. When alloyed with In and Al, hexagonal GaN-based materials with a direct gap have been developed for use in light-emitting diodes and lasers at wavelengths extending



from the blue to the ultraviolet range<sup>225</sup>. The thermodynamically stable  $\beta$ -Ga<sub>2</sub>O<sub>3</sub> polymorph has a direct gap of 4.7 eV, and it has also been proposed for development as a solid-state LED material for UV applications<sup>226</sup>. The group 13 oxynitride materials have other useful properties related to their electronic structure.  $\alpha$ -Ga<sub>2</sub>O<sub>3</sub> with the corundum structure is conveniently alloyed with Al<sub>2</sub>O<sub>3</sub> to provide selective reduction catalysts for gaseous NO<sub>x</sub><sup>105</sup>, and various other Ga<sub>2</sub>O<sub>3</sub> phases have been proposed as gas sensors, and in nanoscale structures as electron emitters and magnetic memory materials<sup>106</sup>. Within the Al<sub>2</sub>O<sub>3</sub>-AlN system, several important Al<sub>x</sub>O<sub>y</sub>N<sub>z</sub> ceramic alloys and compounds are known. At high AlN contents, layered forms based on hexagonal/cubic intergrowths are present. As the Al<sub>2</sub>O<sub>3</sub> content is increased, cubic spinel-structured materials begin to appear. A large family of defect spinels ( $\gamma$ -Al<sub>2</sub>O<sub>3</sub>, Al<sub>x</sub>O<sub>y</sub>N<sub>z</sub>) contain vacancies on both cation and anion sites<sup>107</sup>. A stoichiometric oxynitride spinel-structured compound is obtained at the Al<sub>3</sub>O<sub>3</sub>N composition, in which Al<sup>3+</sup> ions are present on the octahedral and tetrahedral sites, and O<sup>2-</sup> and N<sup>3-</sup> occupy tetrahedral anion sites<sup>108,109</sup>.

Among the related nitride compounds Si<sub>3</sub>N<sub>4</sub> and Ge<sub>3</sub>N<sub>4</sub>, high-pressure synthesis has recently resulted in formation of a new class of spinel structures, that contain Si<sup>4+</sup> and Ge<sup>4+</sup> cations on both tetrahedral and octahedral sites<sup>110-114</sup>. The new solid-state compounds are recoverable to ambient conditions, and they possess high hardness and low compressibility, comparable with materials such as Al<sub>2</sub>O<sub>3</sub>-corundum<sup>107</sup>. The new group 14 nitride spinels are also predicted to be wide direct band semiconductors, with band gaps calculated to lie within the range 2.2-4.0 eV<sup>82,227</sup>. The analogous spinel-structured compound Sn<sub>3</sub>N<sub>4</sub> has also been made at ambient pressure<sup>228,229</sup>, raising the possibility of future preparation of  $\gamma$ -(Si,Ge)<sub>3</sub>N<sub>4</sub> films via metastable synthesis routes, such as chemical vapor deposition, to yield materials compatible with optoelectronics applications, for example.

Gallium oxynitride (Ga<sub>3</sub>O<sub>3</sub>N) has been predicted to form a new spinel-structured compound within the Ga<sub>2</sub>O<sub>3</sub>-GaN system, with potentially useful electronic properties<sup>115,116</sup>. It is predicted to be a direct wide bandgap semiconductor, comparable with GaN<sup>115</sup>. There

has previously been an experimental report of a cubic gallium oxynitride phase with composition close to  $\text{Ga}_{2.8}\text{O}_{3.5}\text{N}_{0.5}$ , that formed metastably during GaN thin film synthesis from chemical precursors<sup>117,118</sup>. Here, we report our first-principles theoretical study of the formation energetics, stability, and electronic properties of the  $\text{Ga}_3\text{O}_3\text{N}$  spinel-structured phase, combined with experiments using a combination of high pressure-high temperature techniques to establish the formation and stability of spinel-structured  $\text{Ga}_3\text{O}_3\text{N}$  from  $\text{Ga}_2\text{O}_3+\text{GaN}$  mixtures, and to determine the chemical composition, structure and properties of the resulting materials.

### 6.2.2 Total Energy Calculations of GaN and $\text{Ga}_3\text{O}_3\text{N}$

In order to obtain the Gibbs free energy of formation of gallium oxynitride, Gibbs free energies of  $\text{Ga}_2\text{O}_3$ , GaN and  $\text{Ga}_3\text{O}_3\text{N}$  are required. As an approximation, assuming a cancellation effect on the vibrational entropies between  $\text{Ga}_2\text{O}_3+\text{GaN}$  and  $\text{Ga}_3\text{O}_3\text{N}$ , the static formation enthalpy  $\Delta H(P)$  is adopted as an estimation of  $\Delta G(T, P)$ . Enthalpies of  $\text{Ga}_2\text{O}_3$  polymorphs as a function of pressure has been shown in section 6.1.2. For GaN, previous studies showed that the ground wurtzite structure undergoes a phase transition into the rocksalt structure at high pressure. The experimentally observed transition pressure is at 37-52 GPa<sup>230-232</sup> and the theoretically calculated  $P_t$  is 35-52 GPa<sup>43,233-235</sup>. In this study, the synthesis pressure of  $\text{Ga}_3\text{O}_3\text{N}$  (several GPa) is much lower than the WZ-to-RS  $P_t$  of GaN. Therefore the only polymorph we considered for GaN is the wurtzite phase, which is one of the starting materials (99.99%  $\text{Ga}_2\text{O}_3$ , containing a mixture of  $\alpha+\beta$  phases, and 99.99% pure GaN) in the experimental work<sup>236</sup>. Here, we first present our total energy calculation of wurtzite-GaN and spinel- $\text{Ga}_3\text{O}_3\text{N}$ . The calculation was on the basis of first-principles density functional theory (DFT), implemented by the VASP code<sup>139-142</sup>. The many-electron exchange-correlation interaction was approximated within the local density approximation (LDA). For parts of the study that were associated with small energy differences, we compared the LDA results with calculations using the generalized gradient approximation (GGA). To improve numerical efficiency, core electrons were approximated

Table 6.6: Third-order Birch-Murnaghan EOS parameters, zero pressure structural parameters for wurtzite GaN

Source	$B_0$ (GPa)	$B'$	$a$ (Å)	$c/a$	$u$
This work (LDA)	198	4.01	3.144	1.631	0.376
This work (GGA)	175	4.15	3.187	1.633	0.375
Calculation <sup>43</sup>	196	4.3	3.180	1.632	0.376
Calculation <sup>184</sup>	172	5.11		1.632	0.376
Experiment <sup>230</sup>	245				0.377
Experiment <sup>231</sup>	188	3.2	3.191	1.626	
Experiment <sup>232</sup>	237	4.3	3.191	1.627	0.377

with ultrasoft pseudopotentials (US-PP)<sup>121</sup>, and only the s and p valence electrons in these elements and the semicore 3d electrons in Ga were treated explicitly. The wave functions of the valence and semi-core electrons were expanded using a planewave basis, with a kinetic energy cut-off set at 348 eV for GaN and 396 eV for Ga<sub>3</sub>O<sub>3</sub>N.

The calculated static energies at various volumes are fitted to the 3<sup>rd</sup>-order Birch-Murnaghan EOS. General agreement of fitting parameters,  $B_0$  and  $B'$ , and zero pressure structural parameters is achieved between our calculation with other reported values (Table 6.6). GGA calculated bulk modulus is about 12% less than that of the LDA value, which is also the case from other calculations. The experimental  $B_0$  is scattered from 188 to 245 GPa, as well. Despite of the underestimation of  $B_0$ , the lattice parameter  $a$  by GGA gives a better agreement with other reported values.

Results for Ga-O-N phases relevant to the synthesis of the spinel-structured Ga<sub>3</sub>O<sub>3</sub>N oxynitrides and the stability and properties of that compound are described below.

### 6.2.3 Theoretical Study of the Synthesis, Structure, and Stability of Ga<sub>3</sub>O<sub>3</sub>N Spinel

We performed *ab initio* calculations of the atomic structures and energetic properties of the Ga<sub>3</sub>O<sub>3</sub>N systems to understand the formation and thermodynamic stability of the spinel-structured phase. The ideal spinel crystal has an A<sub>3</sub>X<sub>4</sub> stoichiometry (A and X represent cations and anions, respectively) with two molecular equivalents per primitive unit

cell corresponding to the fcc structure. Assuming a Ga:O:N ratio of 3:3:1 that corresponds to the ideal stoichiometry, a solid of  $n$  Ga<sub>3</sub>O<sub>3</sub>N molecular units contains  $n$  tetrahedrally coordinated Ga atoms (labeled as <sup>IV</sup>Ga),  $2n$  octahedrally coordinated Ga atoms (<sup>VI</sup>Ga),  $3n$  O atoms, and  $n$  N atoms. The Gibbs free energy of formation of the oxynitride from a mixture containing the corresponding oxide and nitride is defined as

$$\Delta G_{formation}(T, P) = G_{Ga_3O_3N}(T, P) - [G_{Ga_2O_3}(T, P) + G_{GaN}(T, P)] \quad (6.2)$$

Here  $G$  represents the Gibbs free energies for each molecular unit, and a negative  $\Delta G_{formation}$  corresponds to a driving force for the formation of the oxynitride. Because the oxynitride spinel can have O or N atoms distributed among the anion sites, it is likely that there will be a large configurational entropy term contained within  $\Delta G_{formation}$ . A complete statistical modeling of the Gibbs free energy of Ga<sub>3</sub>O<sub>3</sub>N material that might contain such oxygen/nitrogen compositional disorder requires calculating a very large number of atomic configurations using supercell models. In the first stage of our theoretical investigation, we performed the *ab initio* energetic calculations with a limited number of atomic configurations using (pseudo) face-centered-cubic unitcell models. We interpreted our data using a simplified model that breaks the Gibbs energy into two terms:

$$G_{Ga_3O_3N}(T, P) = H_{ground}(P) + G_{alloy}(T, P) \quad (6.3)$$

Here  $H_{ground}$  is the temperature-independent enthalpy of the ground-state (lowest energy) configuration, which allows us to gain insights into the energetically favored local coordination states and their O/N ordering, and to study pressure effects on the Gibbs free energy of formation. The temperature effects are then described by the second term,  $G_{alloy}$ , which models the contributions related to the O/N disorder. In this study, we ignored the entropy contributions due to the lattice vibrations.

We first studied the pressure effects on formation of Ga<sub>3</sub>O<sub>3</sub>N by setting  $T = 0$  K; the Gibbs free energy of formation  $\Delta G_{formation}$  is thus identical to the enthalpy of formation

Table 6.7: Parameters of the third-order Birch-Murnaghan equation of states of three unit-cell-based atomic models of the spinel-structured  $\text{Ga}_3\text{O}_3\text{N}$  that have the lowest energy calculated within the LDA.

	$E_0$	$V_0$	$a_0$	$B_0$	$B'$
model	(eV/ $\text{Ga}_3\text{O}_3\text{N}$ )	( $\text{\AA}^3/\text{Ga}_3\text{O}_3\text{N}$ )	( $\text{\AA}$ )	(GPa)	
I	-48.109 (0.000)	69.5424	8.2246	210	4.13
II	-47.966 (0.143)	69.6928	8.2357	208	4.17
III	-47.854 (0.255)	69.6181	8.2275	209	4.14

$\Delta H(P) = \Delta E + P\Delta V$ . We first carried out a search for the lowest energy unit-cell configuration of the spinel-structured  $\text{Ga}_3\text{O}_3\text{N}$ . Among the  $8!/(6!2!) = 28$  configurations, there are three crystallographically distinct O/N arrangements for  $(\text{Ga}_3\text{O}_3\text{N})_2$ . We used the LDA to calculate lattice parameters at  $P = 1$  atm and also the  $V(P)$  relations for these three models: the calculated third-order Birch-Murnaghan equation of state parameters for each of these three unit-cell models are listed in Table 6.7. The configuration labeled as model I has a rhombohedral symmetry ( $R\bar{3}m$ ). This has the lowest equilibrium energy, and it is considered to provide the ground-state configuration of  $\text{Ga}_3\text{O}_3\text{N}$  in our theoretical study. The rhombohedral distortion from the ideal cubic structure is very small; i.e., the angles between the pseudocubic lattice vectors are  $89.33^\circ$  within the equilibrium configuration. The calculated equilibrium volume and the bulk modulus of this ground-state configuration compare favorably with the experimental measurements (see below). At zero pressure, our LDA calculations predict an endothermic enthalpy of formation, with  $\Delta H = +272$  meV per  $\text{Ga}_3\text{O}_3\text{N}$  unit (26.2 kJ/mol) with respect to  $\text{Ga}_2\text{O}_3$  (monoclinic  $\beta$  phase) + GaN (hexagonal wurtzite structure). The LDA calculations predict a negative  $d\Delta H/dP$  slope (solid line in Figure 6.4a), so the Gibbs free energy of formation becomes negative at  $P > 17$  GPa. However,  $\text{Ga}_2\text{O}_3$  does not always remain in the monoclinic  $\beta$  phase at high pressure. According to our (static) LDA calculations, a  $\beta$ -to- $\alpha$  phase transition in  $\text{Ga}_2\text{O}_3$  takes place at  $P \approx 0.5$  GPa. More importantly, the slope of  $d\Delta H/dP$  becomes positive when  $\text{Ga}_2\text{O}_3$  is in the  $\alpha$  phase (dashed line plot, Figure 6.4a). The experimental phase transition has been reported to occur between 0.1 MPa and 4.4 GPa<sup>237,238</sup>; however, a direct transition pressure was not recorded in those studies<sup>213</sup>. Recently, Tu *et al.* have reported a  $\beta$ -to- $\alpha$

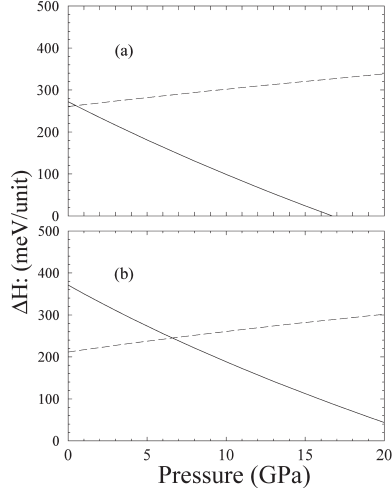


Figure 6.4: LDA-calculated formation enthalpy  $\Delta H$  (i.e., Gibbs free energy of formation  $\Delta G_{formation}$  at zero temperature) as a function of pressure using (a) LDA methods and (b) the GGA approach. The calculated positive  $\Delta H$  suggests an endothermic formation. The solid plots are calculated assuming the oxynitrides are synthesized from  $\beta$ - $\text{Ga}_2\text{O}_3$  and wurtzite GaN, and the dashed plots are calculated assuming the oxynitrides are synthesized from  $\alpha$ - $\text{Ga}_2\text{O}_3$  and wurtzite GaN. The solid plot and the dashed plot cross at the pressure of the  $\beta$ -to- $\alpha$  phase transition in  $\text{Ga}_2\text{O}_3$  (predicted to be 0.5 and 6.6 GPa by LDA and GGA methods, respectively).

phase transition in  $\text{Ga}_2\text{O}_3$  at 13.3 GPa<sup>212</sup>. However, there is some uncertainty in the nature of the starting material used in that work, and Machon *et al.* repeated the study: he found that the  $\beta$ -to- $\alpha$  transition occurs at  $P = 22$  GPa<sup>213</sup>, without heating. It is obvious that the nature of the  $\text{Ga}_2\text{O}_3$  starting material, and how it transforms under high- $P$ ,  $T$  conditions, will affect the energetics of the high-pressure synthesis experiment.

Within the present study, we repeated our calculations within the GGA (Figure 6.4b). The GGA calculations predict a phase transition pressure for  $\text{Ga}_2\text{O}_3$  of 6.6 GPa. The GGA formation enthalpy for the  $\text{Ga}_3\text{O}_3\text{N}$  synthesis reaction is predicted as +370 meV (35.6 kJ/mol) at  $P = 1$  atm, and this value is reduced to its minimum of +245 meV (23.6 kJ/mol) at the  $\text{Ga}_2\text{O}_3$  transition pressure. Despite the quantitative differences between the two sets of calculations, the GGA results agree qualitatively with the findings from the LDA calculations. Both the LDA and GGA studies predict that the optimal pressure for

synthesizing the spinel-structured  $\text{Ga}_3\text{O}_3\text{N}$  from  $\text{Ga}_2\text{O}_3$  and  $\text{GaN}$  mixtures is around that of the  $\beta$ -to- $\alpha$  phase transition in  $\text{Ga}_2\text{O}_3$  ( $P \approx 6.6$  GPa, according to GGA calculations).

Next, we investigated the temperature effects on the stability of the oxynitrides systems. A simple ideal solution model has been previously adopted to estimate the effects of O/N disorder in spinel-structured oxynitrides<sup>116,239</sup>. Such a simple statistical model is valid only in the cases where all the atomic configurations have very similar energies, and it approximates the additional Gibbs free energy term with a contribution due to the alloy disorder with a pure entropic term:

$$G_{\text{alloy}}(T, P) = -4k_B T [x \ln x + (1 - x) \ln (1 - x)] \quad (6.4)$$

(here the factor 4 is due to the presence of four possible different anion sites in the molecular unit that are assumed to be equally accessible). It is known that such simple models can significantly underestimate the alloy formation temperature if some of the atomic configurations are energetically inaccessible at the temperature of the experiment. To obtain a better estimate of the entropic contribution to the Gibbs free energy that is more relevant to the experimental results, we studied the correlation between the energetic properties of the oxynitride materials and their local atomic ordering schemes among the three unit-cell models (Table 6.8). The spinel structure is described as a packing of  $\text{AX}_4$  tetrahedra and  $\text{AX}_6$  octahedra present in a 1:2 ratio. In the case of  $\text{Ga}_3\text{O}_3\text{N}$ , there are five possible types of  $\text{AX}_4$  tetrahedra, i.e.,  ${}^{IV}\text{GaO}_4$ ,  ${}^{IV}\text{GaO}_3\text{N}$ ,  ${}^{IV}\text{GaO}_2\text{N}_2$ ,  ${}^{IV}\text{GaON}_3$ , and  ${}^{IV}\text{GaN}_4$ . Similarly, there exist seven types of  $\text{AX}_6$  octahedra:  ${}^{VI}\text{GaO}_6$ ,  ${}^{VI}\text{GaO}_5\text{N}$ ,  ${}^{VI}\text{GaO}_4\text{N}_2$ ,  ${}^{VI}\text{GaO}_3\text{N}_3$ ,  ${}^{VI}\text{GaO}_2\text{N}_4$ ,  ${}^{VI}\text{GaON}_5$ , and  ${}^{VI}\text{GaN}_6$ . The distribution of various types of  $\text{AX}_4$  and  $\text{AX}_6$  units within the three models studied is listed in Table 6.8. No  ${}^{IV}\text{GaON}_3$ ,  ${}^{IV}\text{GaN}_4$ ,  ${}^{VI}\text{GaON}_5$ , or  ${}^{VI}\text{GaN}_6$  species were considered to simplify the statistical analysis; such N-rich  $\text{AX}_4$  or  $\text{AX}_6$  species are expected to have low concentration because the average O:N ratio is 3:1. The LDA calculations show a clear energetic preference for the structure containing  ${}^{IV}\text{GaO}_3\text{N}$  sites over those with the combination 50%  ${}^{IV}\text{GaO}_4$  + 50%  ${}^{IV}\text{GaO}_2\text{N}_2$

Table 6.8: Analysis of local coordination ordering schemes within the three unit-cell models of the spinel-structured  $\text{Ga}_3\text{O}_3\text{N}$  in terms of the ratio of various types of  $\text{AX}_4$  tetrahedral and  $\text{AX}_6$  octahedral units.

model	tetrahedral Ga (%)			octahedral Ga (%)		
	${}^{IV}\text{GaO}_4$	${}^{IV}\text{GaO}_3\text{N}$	${}^{IV}\text{GaO}_2\text{N}_2$	${}^{VI}\text{GaO}_6$	${}^{VI}\text{GaO}_5\text{N}$	${}^{VI}\text{GaO}_4\text{N}_2$
I		100		25		75
II		100			50	50
III	50		50		50	50

and the 25%  ${}^{VI}\text{GaO}_6$  + 75%  ${}^{VI}\text{GaO}_4\text{N}_2$  combination over that with 50%  ${}^{VI}\text{GaO}_5\text{N}$  + 50%  ${}^{VI}\text{GaO}_4\text{N}_2$ .

We then constructed a three-energy-level model to investigate the consequences of this anion site ordering on the formation energetics of the oxynitride spinel, using the ground-state energies of the three lowest energy models found above (Table 6.7):

$$\Delta G_{formation}(T, P) = \Delta H(P) - \frac{1}{2}k_B T \ln \left[ 4 + 12e^{-2\Delta\epsilon_1/k_B T} + 12e^{-2\Delta\epsilon_2/k_B T} \right] \quad (6.5)$$

Here  $\Delta H(P)$  is the static formation enthalpy as discussed above, the values 4, 12, and 12 are the degeneracies of the levels corresponding to each model, and  $\Delta\epsilon_1$  and  $\Delta\epsilon_2$  are the energies of the two “excited” states (i.e., models II and III) compared to the ground-state energy (as listed in column 2 of Table 6.7). At a given pressure, the alloy formation temperature corresponds to that at which  $\Delta G_{formation}$  becomes zero. On the basis of our LDA calculations, this condition occurs at  $T_{alloy} = 2800$  K. This result means that, according to our model, a stoichiometric  $\text{Ga}_3\text{O}_3\text{N}$  spinel phase would become thermodynamically stabilized with respect to other ordering schemes and could be synthesized from  $\text{Ga}_2\text{O}_3 + \text{GaN}$  mixtures above  $P \approx 6 - 7$  GPa and  $T = 2800$  K. This temperature estimate is considerably higher than that used experimentally to synthesize an oxynitride spinel-structured material from the component oxides and nitrides (synthesis temperatures as low as 1200 °C at 5 GPa; see below). The main reasons for the discrepancy are that the oxynitride materials obtained experimentally contain vacancies on the  $\text{Ga}^{3+}$  and perhaps also on the anion sites and the O:N ratio obtained is larger than the ideal stoichiometry that was modeled. Both



considerations will have a large effect on the relative energies of ground-state and experimentally accessible “excited-state” models. Also, it is not yet clear that it is justified to exclude high-N-content environments such as  $V\text{GaON}_3$ ,  $IV\text{GaN}_4$ ,  $VI\text{GaON}_5$ , or  $VI\text{GaN}_6$  on purely statistical grounds from the thermodynamic treatment. Such species could have special stability due to local bonding environments, including bond valence constraints<sup>128</sup>. That will have to be tested in future investigations of local coordinations in  $\text{Ga}_x\text{O}_y\text{N}_z$  materials using appropriate experimental probes of the local structural environments (e.g., X-ray absorption spectroscopy/EXAFS, NMR, etc.).

#### 6.2.4 Electronic Properties

Using *ab initio* LDA methods, we calculated the electronic band structure within the LDA on the basis of our atomic model of the ground-state configuration of  $\text{Ga}_3\text{O}_3\text{N}$  (model I). The LDA-predicted band dispersion is plotted in Figure 6.5a from the center of the Brillouin zone (the  $\Gamma$  point) along three directions to the  $F$ ,  $T$ , and  $L$  points at the zone boundaries. The electronic density of states function is shown in (b). Our calculations indicate that spinel-structured gallium oxynitrides are direct wide band gap semiconductors, with optoelectronic properties that are similar to those of wurtzite- and sphalerite-structured GaN and gallium oxides. Because of well-known limitations of the LDA for such electronic structure calculations, the predicted magnitude of the band gap (2.1 eV) is likely to be underestimated in this study. The same LDA methods underestimate the band gaps of the GaN (wurtzite) and  $\beta\text{-Ga}_2\text{O}_3$  phases by 1.3 and 2.3 eV, respectively; we thus expect the experimental band gap of  $\text{Ga}_3\text{O}_3\text{N}$  (spinel) to lie around 4 eV. Our collaborator obtained room-temperature photoluminescence spectra of the  $\text{Ga}_{2.8}\text{N}_{0.64}\text{O}_{3.24}$  sample obtained by high- $P,T$  synthesis, using 325 nm laser excitation (Figure 6.6). The onset of the photoluminescence signal begins just below 2.5 and extends to 1.5 eV. Because the experimentally synthesized material contains a large quantity of defects on the  $\text{Ga}^{3+}$  sites, and also perhaps on the anion sites, along with O/N disorder, it is unlikely that the photoluminescence feature corresponds to excitations across the band gap. Instead, the observed PL band is

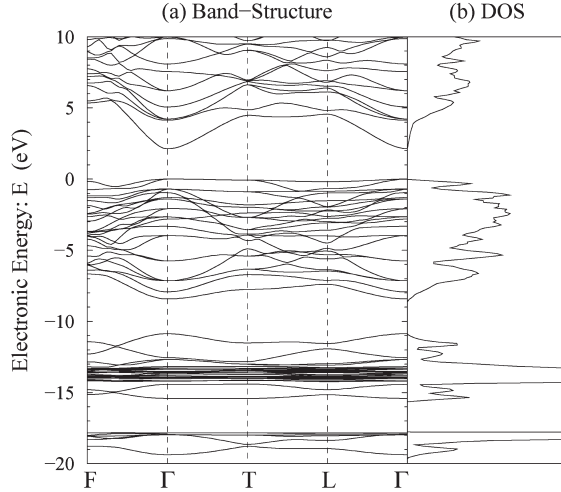


Figure 6.5: (a) Electronic band structure and (b) Electronic density of states for  $\text{Ga}_3\text{O}_3\text{N}$  calculated using first-principles (DFT) methods within the LDA.

likely to arise from defect related transitions between states mainly within the gap, so that the intrinsic band gap for a stoichiometric ordered material would lie considerably above 2.5 eV, as predicted by theory.

### 6.2.5 Phonon Spectrum

The Raman spectrum of the new oxynitride spinel phase contains several broad bands (Figure 6.7), indicating substantial disorder among the O and N atoms on the 32e sites in the spinel structure and/or the presence of cation ( $\text{Ga}^{3+}$ ) or anion vacancies. The broad bands have maxima near  $700$  and  $800\text{ cm}^{-1}$ , and also near  $300\text{ cm}^{-1}$ , that correspond generally to the positions of Raman-active modes within the analogous spinel-structured compound  $\gamma\text{-Ge}_3\text{N}_4$ <sup>240</sup>. To aid in the interpretation of our experimentally obtained Raman spectra of  $\text{Ga}_x\text{O}_y\text{N}_z$  phases, we calculated the  $\Gamma$  point phonon frequencies of the 14-atom rhombohedral unit cell of  $\text{Ga}_3\text{O}_3\text{N}$  (model I structure) using first-principles LDA methods. The same technique was previously used to predict the positions of the Raman-active vibrational modes in  $\gamma\text{-Ge}_3\text{N}_4$ <sup>114,240</sup>. The pseudocubic  $R\bar{3}m$  model structure for  $\text{Ga}_3\text{O}_3\text{N}$  is predicted to have nine Raman-active modes ( $4A_{1g} + 5E_g$ ), with zone-center frequencies calculated

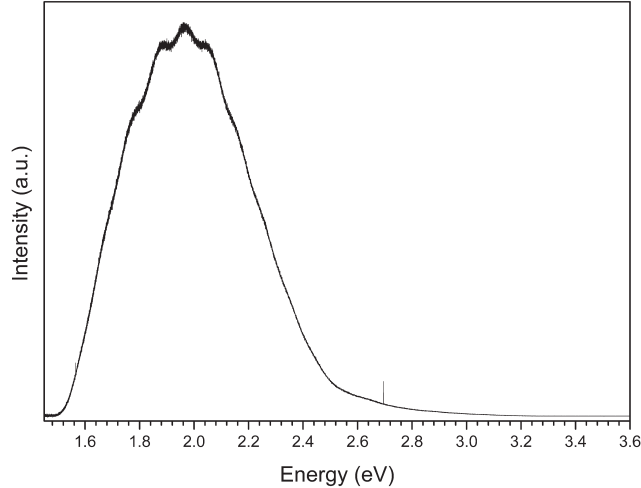


Figure 6.6: Photoluminescence spectrum of the Ga<sub>2.8</sub>N<sub>0.64</sub>O<sub>3.24</sub> sample obtained via high- $P,T$  synthesis in the multianvil experiments, using UV laser excitation (325 nm)

at 213, 219, 367, 379, 499, 512, 634, 647, and 782  $\text{cm}^{-1}$ . These calculated frequencies are denoted by dashed lines in Figure 6.7. Within an anion-disordered structure, as expected for the real Ga <sub>$x$</sub> O <sub>$y$</sub> N <sub>$z$</sub>  spinel, he predicted zone-center modes act as poles for interpreting the broadened spectra that approach the full vibrational density of states (VDOS). The expected mode frequencies are grouped around the five frequency values (i.e., 216, 373, 506, 640, and 782  $\text{cm}^{-1}$ ) that are associated with the ideal spinel structure. By analogy with the Raman spectrum of  $\gamma$ -Ge<sub>3</sub>N<sub>4</sub>, we expect the lowest frequency peak (216  $\text{cm}^{-1}$ ) and the two highest frequency peaks (640 and 782  $\text{cm}^{-1}$ ) to have the strongest intensities, whereas the two intermediate frequency peaks (373 and 506  $\text{cm}^{-1}$ ) are relatively weak. We cannot yet directly calculate the effects of the O/N disorder on the broadening patterns observed in our Raman spectra. However, it is likely that the observed Raman spectrum provides a first view of the VDOS functions of Ga<sub>3</sub>O<sub>3</sub>N and also  $\gamma$ -Ge<sub>3</sub>N<sub>4</sub> spinels.

To provide a semiquantitative estimation of the widths of the broad peaks, we calculated the full phonon dispersion using a 112-atom supercell model. The Born effective charge induced LO-TO splitting in the ionic compounds are corrected on the basis of the interplanar force constant model proposed by Kunc and Martin<sup>156</sup>. As shown in Figure 6.7,

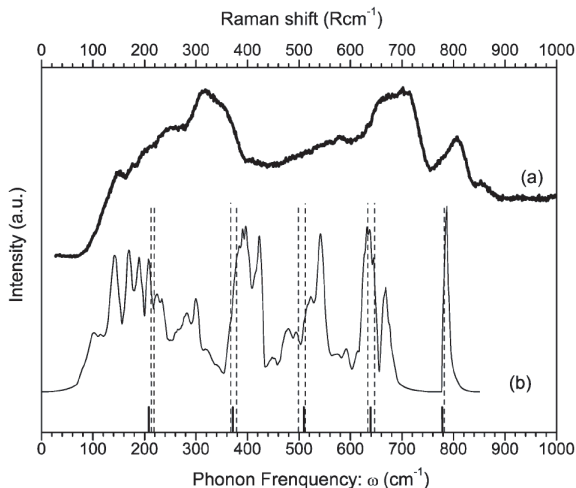


Figure 6.7: (a) Raman spectrum collected for the  $\text{Ga}_{2.8}\text{N}_{0.64}\text{O}_{3.24}$  sample at an excitation wavelength of 514.5 nm. The bold solid lines on the frequency scale below indicate the positions of the Raman bands for the analogous spinel form of  $\gamma\text{-Ge}_3\text{N}_4$ . (b) Phonon density of states (VDOS) calculated for the  $R\bar{3}m$  pseudocubic  $\text{Ga}_3\text{O}_3\text{N}$  phase, predicted as “model I” in the enthalpy calculations (Table 6.7). The dashed lines indicate the Raman-active modes for that phase.

the highest frequency strong Raman peak (i.e., the  $A_g$  mode near  $782\text{ cm}^{-1}$ ) is expected to be the sharpest one. The other strong peak near  $640\text{ cm}^{-1}$  is expected to have a broader width ( $40\text{-}60\text{ cm}^{-1}$ ).

### 6.2.6 Conclusions

Our theoretical study showed that the most stable structure for  $\text{Ga}_3\text{O}_3\text{N}$  corresponds to a rhombohedral distortion of the ideal spinel structure. The formation of  $\text{Ga}_3\text{O}_3\text{N}$  is endothermic at ambient pressure and low temperature, and the optimal synthesis pressure is predicted to lie close to that for the  $\beta$ -to- $\alpha$  phase transition in  $\text{Ga}_2\text{O}_3$  (around 6.6 GPa according to our GGA calculations). The calculated direct band gap energy for a stoichiometric oxynitride spinel was estimated to be around 4 eV. This value is larger than that obtained from photoluminescence data collected on the experimentally synthesized sample, which likely contains  $\text{Ga}^{3+}$  vacancies and other structural defects. The synthesis of this new Ga-O-N phase makes contact with the important optoelectronic materials known to exist

in the (Ga,Al,In)N system that provide light-emitting diodes and solid-state lasers in the blue to UV range. A cubic  $\text{Ga}_3\text{O}_3\text{N}$  material similar to the compound synthesized here has recently been prepared in thin film form via chemical precursor techniques<sup>241</sup>. That result indicates that the new materials could be developed for use within novel optoelectronic devices.

## CHAPTER 7

### CONCLUSIONS AND FUTURE WORK

In this dissertation, I have adopted and further developed a series of first-principles computational techniques to theoretically investigate the pressure-induced phase transitions and thermodynamic properties for several representative main-group oxides and nitrides.

For  $\text{Al}_2\text{O}_3$ , we have systematically investigated the pressure-induced phase transformations. The sequence of transitions under compression, i.e., corundum  $\rightarrow$   $\text{Rh}_2\text{O}_3(\text{II}) \rightarrow$  pPV, and the  $T$ - $P$  phase diagram we obtained are consistent with previous theoretical and experimental studies. Results using US-PP and PAW are presented. By finding a transition path that links the corundum and  $\text{Rh}_2\text{O}_3(\text{II})$  phases with monoclinic intermediate structures which has a space group  $P2/c$ , we proposed a single-bond breaking-and-reforming (SB-BAR) mechanism to describe the transformation between corundum and  $\text{Rh}_2\text{O}_3(\text{II})$  phase. Total energy calculation using PAW method shows that the enthalpy barrier height of the forward corundum-to- $\text{Rh}_2\text{O}_3(\text{II})$  transition is around 130 meV/atom and remains unchanged with varied pressures. However, the barrier height of the backward  $\text{Rh}_2\text{O}_3(\text{II})$ -to-corundum transition decreases significantly under decompression, which indicates that the  $\text{Rh}_2\text{O}_3(\text{II})$  phase may not be quenchable to ambient conditions. In addition, great similarity is found in the elastic constants between corundum and  $\text{Rh}_2\text{O}_3(\text{II})$  phase, except  $C_{33}$ . The larger  $C_{33}$  of  $\text{Rh}_2\text{O}_3(\text{II})$  phase means that its  $c$  axis is less compressible than that of corundum. Zero pressure  $\Gamma$ -point phonon frequencies and their pressure dependencies are calculated for three stable polymorphs. Comparison with measured data of corundum and theoretical Raman frequencies of pPV phase suggest that, within LDA, predictions using PAW method have better results than US-PP. This conclusion is also confirmed from the study of elastic properties. We have calculated the elastic constants and their pressure dependencies for corundum and two high-pressure phases. PAW calculated  $C_{ij}$  yield better

agreement with available experimental data of  $\alpha$ -Al<sub>2</sub>O<sub>3</sub>. The temperature dependencies of thermal expansion coefficient from low to high pressures have been predicted for  $\alpha$ -, Rh<sub>2</sub>O<sub>3</sub>(II)-, and pPV-Al<sub>2</sub>O<sub>3</sub>. For corundum at zero pressure, our US-PP data is in good agreement with Amatuni *et al.*'s result measured from 300 K to 2000 K, and with Aldebert *et al.*'s result at temperatures above 1000 K. Our PAW data lies in the middle of the experimental data and agrees with Schauer's data below 700 K and Wachtman *et al.*'s data above 1200 K. Our calculated heat capacity  $C_P$ , entropy and adiabatic bulk modulus of corundum phase also agree well with measured results.

For AlN, we presented our *ab initio* calculation of activation barriers of the B4-to-B1 transition for five TPs proposed by Stokes *et al.* We showed that the five bond-preserving paths can be interpreted as transformation of different long-range patterns of the "transition units" (two different orientations). The transformation of "transition unit" is equivalent to the path along TP1 (with  $Cmc2_1$  symmetry). Our calculated kinetic barriers are comparable for all five paths at pressures from 0 GPa to 30 GPa, which indicate that the wurtzite-to-rocksalt transition is characterized by the transformation of the "transition unit", while the long-range pattern is less important. And the difference in strains of different TPs is not a major factor for at least the transition from wurtzite to rocksalt phase in AlN. In addition, the bond-breaking path is not energetically favored compared with the bond-preserving paths. Besides the studies of different TPs, our estimated forward and backward barrier heights are consistent with experimental observation and previous calculations.

For Si<sub>3</sub>N<sub>4</sub>, in summary, we have theoretically studied phase transitions in silicon nitride (Si<sub>3</sub>N<sub>4</sub>) at high pressure using a first-principles density functional theory method. We find that  $\alpha$ -Si<sub>3</sub>N<sub>4</sub> remains as a metastable phase at temperatures up to 2000 K and pressures up to 10 GPa. The equilibrium  $\beta \rightarrow \gamma$  transition pressure is predicted as 7.5 GPa at 300K and it increases to 9.0 GPa at 2000K. Both  $\alpha$ - and  $\beta$ -Si<sub>3</sub>N<sub>4</sub> are dynamically stable at low pressure. However, two competing phonon-softening mechanisms are found in the  $\beta$  phase at high pressures. At room temperature,  $\beta$ -Si<sub>3</sub>N<sub>4</sub> is predicted to undergo a first-order  $\beta \rightarrow P3$  transition above 38.5 GPa, while  $\alpha$ -Si<sub>3</sub>N<sub>4</sub> shows no signs of structural instability.

The predicted metastable high-pressure  $P3$  phase is structurally related to  $\beta$ - $\text{Si}_3\text{N}_4$ . The enthalpy barrier height is estimated as only 67.23 meV/atom. Our LDA predicted thermal expansion coefficient, heat capacity and bulk Grüneisen parameter are in good agreement with Bruls' measured results. We find relatively large discrepancies between our calculation with experimental data from Reeber. And we attribute the cause of predicted negative TEC at low temperatures in  $\alpha$  and  $\beta$ - $\text{Si}_3\text{N}_4$  to the low-frequency phonon modes that have negative mode Grüneisen ratios.

For bulk  $\text{Ga}_2\text{O}_3$ , we have calculated the Raman frequencies and their mode Grüneisen parameters for  $\beta$  and  $\alpha$  phases. Good agreement is achieved between our results with experiments and other calculations. We also predict the equilibrium  $T$ - $P$  phase diagram of  $\text{Ga}_2\text{O}_3$  consists of  $\beta$ ,  $\alpha$  and  $\text{Rh}_2\text{O}_3(\text{II})$  phases. Our LDA calculated transition pressure from  $\beta$  to  $\alpha$  phase is 0.3 GPa at 0 K and 1.6 GPa at 2000 K. The Clapeyron slope for this transition is positive which has the value of about +0.6 MPa/K at 1000 K. This is consistent with previous calculations. However, the experimental  $P_t$  is much larger. The large discrepancy can be attributed to a large kinetic barrier, which may be significantly lowered under compression. Our calculated  $\alpha$ -to- $\text{Rh}_2\text{O}_3(\text{II})$  transition pressure is 40 GPa at 0 K and 37 GPa at 2000 K, which is in excellent agreement with experimental value (about 37 GPa at about 2000 K). In the case of nanowires, based on a comparison of the experimental Raman mode frequencies with our first-principles calculations, we find compelling evidence for growth-direction-induced internal strains in  $\beta$ - $\text{Ga}_2\text{O}_3$  nanowires which significantly influence the vibrational mode frequencies. Within the linear model approximation, the observed blue and redshifts of peak frequencies in the micro-Raman spectra of the  $\beta$ - $\text{Ga}_2\text{O}_3$  nanowires with different growth directions can be attributed to two small anisotropic internal strains: one compressive strain of 2% volume change, and the other tensile strain of 0.7% volume change. The overall high quality of the fitted models to available experimental data suggests a strong correlation between the shifts in Raman mode frequencies and the growth-direction-induced internal strains in the  $\text{Ga}_2\text{O}_3$  nanowires.



For gallium oxynitride, our theoretical study showed that the most stable structure for  $\text{Ga}_3\text{O}_3\text{N}$  corresponds to a rhombohedral distortion of the ideal spinel structure. The formation of  $\text{Ga}_3\text{O}_3\text{N}$  is endothermic at ambient pressure and low temperature, and the optimal synthesis pressure is predicted to lie close to that for the  $\beta$ -to- $\alpha$  phase transition in  $\text{Ga}_2\text{O}_3$  (around 6.6 GPa according to our GGA calculations). The calculated direct band gap energy for a stoichiometric oxynitride spinel was estimated to be around 4 eV. This value is larger than that obtained from photoluminescence data collected on the experimentally synthesized sample, which likely contains  $\text{Ga}^{3+}$  vacancies and other structural defects. The synthesis of this new Ga-O-N phase makes contact with the important optoelectronic materials known to exist in the (Ga,Al,In)N system that provide light-emitting diodes and solid-state lasers in the blue to UV range. A cubic  $\text{Ga}_3\text{O}_3\text{N}$  material similar to the compound synthesized here has recently been prepared in thin film form via chemical precursor techniques. That result indicates that the new materials could be developed for use within novel optoelectronic devices.

The above results show that DFT calculations within the frame of quasi-harmonic approximation (QHA) is successful in calculating the finite-temperature thermodynamic potentials for hard materials. However, to improve the prediction of thermodynamic properties for normal materials at high temperatures or strongly anharmonic crystals even at low temperatures, we are looking forward to developing and implementing an algorithm based on the perturbation theory to add anharmonic correction to the QHA vibrational free energy, as shown in Appendix C. The first order correction is contributed from the 3<sup>rd</sup> and 4<sup>th</sup> order lattice anharmonicity tensors. With these anharmonicity tensors, the temperature dependence of elasticity and phonon frequencies are also within the scope.

And, for the metastable  $P3$  phase we found in  $\text{Si}_3\text{N}_4$ , our collaborator who did experiments showed that there is a mismatch between the observed X-ray diffraction (XRD) pattern after phase transition at high pressure and the calculated XRD pattern from  $P3$  structure at the same pressure. But the unknown  $\delta$  phase is believed to be structurally close

to the  $P3$  phase. We will look at the low-frequency phonon modes with softening tendency for  $\beta$ ,  $P\bar{6}$ ,  $P3$  and  $P2_1/m$  phases, which may suggest other possible structures.

## BIBLIOGRAPHY

1. H. Mao, P. Bell, J. Shaner, and D. Steinberg, *J. Appl. Phys.* **49**, 3276 (1978).
2. W. Nellis and C. Yoo, *J. Geophys. Res.* **95**, 21749 (1990).
3. H. Cynn, D. Isaak, E. Cohen Ronald, M. Nicol, and O. Anderson, *Am. Mineral.* **75**, 439 (1990).
4. F. Marton and R. Cohen, *Am. Mineral.* **79**, 789 (1994).
5. K. Thomson, R. Wentzcovitch, and M. Bukowinski, *Science* **274**, 1880 (1996).
6. A. Oganov and S. Ono, *PNAS* **102**, 10828 (2005).
7. R. Caracas and R. Cohen, *Geophys. Res. Lett* **32**, L06303 (2005).
8. N. Funamori and R. Jeanloz, *Science* **278**, 1109 (1997).
9. T. Mashimo, K. Tsumoto, K. Nakamura, Y. Noguchi, K. Fukuoka, and Y. Syono, *Geophys. Res. Lett* **27**, 2021 (2000).
10. J. Lin, O. Degtyareva, C. Prewitt, P. Dera, N. Sata, E. Gregoryanz, H. Mao, and R. Hemley, *Nat. Mater.* **3**, 389 (2004).
11. S. Ono, A. Oganov, T. Koyama, and H. Shimizu, *Earth Planet. Sci. Lett.* **246**, 326 (2006).
12. S. Jahn, P. Madden, and M. Wilson, *Phys. Rev. B* **69**, 20106 (2004).
13. K. Umemoto and R. Wentzcovitch, *PNAS* **105**, 6526 (2008).
14. A. Jephcoat, R. Hemley, H. Mao, and K. Goettel, *Physica B* **150**, 115 (1988).

15. J. Mougin, T. Le Bihan, and G. Lucazeau, *J. Phys. Chem. Solids.* **62**, 553 (2001).
16. J. Wachtman, T. Scuderi, and G. Cleek, *J. Am. Ceram. Soc.* **45**, 319 (1962).
17. A. Schauer, *Can. J. Phys.* **43**, 523 (1965).
18. A. Amatuni, T. Malyutina, V. Chekhovskoi, and V. Petukhov, *High Temp-High Press* **8**, 565 (1976).
19. G. White and R. Roberts, *High Temp-High Press* **15**, 321 (1983).
20. P. Aldebert and J. Traverse, *High Temp-High Press* **16**, 127 (1984).
21. G. Fiquet, P. Richet, and G. Montagnac, *Phys. Chem. Miner.* **27**, 103 (1999).
22. G. Furukawa, T. Douglas, R. McCoskey, and D. Ginnings, *J. Res. Nat. Bur. Stand.* **57**, 67 (1956).
23. W. Tefft, *Natl Bur Stand* **70**, 277 (1966).
24. D. Chung and G. Simmons, *J. Appl. Phys.* **39**, 5316 (1968).
25. T. Goto, O. ANDERSON, I. Ohno, and S. Yamamoto, *J. Geophys. Res.* **94**, 7588 (1989).
26. J. Hama and K. Suito, *Phys. Chem. Miner.* **28**, 258 (2001).
27. W. Mayer and E. Hiedemann, *J. Acoust. Soc. Am.* **30**, 756 (1958).
28. J. Wachtman, W. Tefft, D. Lam, and R. Stinchfield, *J. Am. Ceram. Soc.* **43**, 334 (1960).
29. J. Gieske and G. Barsch, *Phys. Stat. sol. (b)* **29**, 121 (1968).
30. R. Cohen, *Geophys. Res. Lett.* **14**, 37 (1987).
31. W. Duan, B. Karki, and R. Wentzcovitch, *Am. Mineral.* **84**, 1961 (1999).

32. Y. Le Page, P. Saxe, and J. Rodgers, *Phys. Status Solidi C* **229**, 1155 (2002).
33. J. Gladden, J. So, J. Maynard, P. Saxe, and Y. Le Page, *Appl. Phys. Lett.* **85**, 392 (2004).
34. D. Hovis, A. Reddy, and A. Heuer, *Appl. Phys. Lett.* **88**, 13 (2006).
35. S. Shang, Y. Wang, and Z. Liu, *Appl. Phys. Lett.* **90**, 101909 (2007).
36. S. Stackhouse, J. Brodholt, and G. Price, *Geophys. Res. Lett.* **32**, 13305 (2005).
37. H. Vollstädt, E. Ito, M. Akaishi, S. Akimoto, and O. Fukunaga, *Proc. Jpn. Acad., B* **66**, 7 (1990).
38. M. Ueno, A. Onodera, O. Shimomura, and K. Takemura, *Phys. Rev. B* **45**, 10123 (1992).
39. Q. Xia, H. Xia, and A. Ruoff, *J. Appl. Phys.* **73**, 8198 (1993).
40. S. Uehara, T. Masamoto, A. Onodera, M. Ueno, O. Shimomura, and K. Takemura, *J. Phys. Chem. Solids* **58**, 2093 (1997).
41. P. E. Van Camp, V. E. Van Doren, and J. T. Devreese, *Phys. Rev. B* **44**, 9056 (1991).
42. N. E. Christensen and I. Gorczyca, *Phys. Rev. B* **50**, 4397 (1994).
43. J. Serrano, A. Rubio, E. Hernández, A. Muñoz, and A. Mujica, *Phys. Rev. B* **62**, 16612 (2000).
44. A. Saitta and F. Decremps, *Phys. Rev. B* **70**, 35214 (2004).
45. C. Silva, H. Leite Alves, L. Scolfaro, and J. Leite, *Phys. Status Solidi C* **2**, 2468 (2005).
46. J. Cai and N. Chen, *Phys. Rev. B* **75**, 134109 (2007).
47. H. Stokes and D. Hatch, *Isotropy Software Package* (2004), URL <http://stokes.byu.edu/isotropy.html>.

48. H. Stokes, J. Gunter, D. Hatch, J. Dong, H. Wang, and J. Lewis, *Phys. Rev. B* **76**, 012102 (2007).
49. D. Zahn, Y. Grin, and S. Leoni, *Phys. Rev. B* **72**, 64110 (2005).
50. H. Sowa, *Acta Crystallogr., Sect. A: Found. Crystallogr.* **61**, 325 (2005).
51. C. Capillas, J. Perez-Mato, and M. Aroyo, *J. Phys.: Condens. Matter* **19**, 275203 (2007).
52. M. Aroyo, J. Perez-Mato, C. Capillas, E. Kroumova, S. Ivantchev, G. Madariaga, A. Kirov, and H. Wondratschek, *Z. Kristallogr.* **221**, 15 (2006).
53. H. Sowa, *Acta Crystallogr., Sect. A: Found. Crystallogr.* **57**, 176 (2001).
54. S. Limpijumnong and W. Lambrecht, *Phys. Rev. Lett.* **86**, 91 (2001).
55. F. Shimojo, S. Kodiyalam, I. Ebbsjö, R. Kalia, A. Nakano, and P. Vashishta, *Phys. Rev. B* **70**, 184111 (2004).
56. K. Komeya and M. Matsui, *Materials Science and Technology*, vol. 11 (Wiley-VCH, Weinheim, 1994).
57. F. Schröder, *Gmelin Handbook of Inorganic and Organometallic Chemistry*, vol. Si Suppl. B 5c of *Silicon Nitride in Electronics* (Springer-Verlag, Berlin, 1991).
58. A. Zerr, G. Miehe, G. Serghiou, M. Schwarz, E. Kroke, R. Riedel, H. Fueß, P. Kroll, and R. Boehler, *Nature* **400**, 340 (1999).
59. J. Liang, L. Topor, A. Navrotsky, and M. Mitomo, *J. Mater. Res* **14**, 1959 (1999).
60. C. Greskovich and S. Prochazka, *J. Am. Ceram. Soc.* **60**, 471 (1977).
61. L. Bowen, R. Weston, T. Carruthers, and R. Brook, *J. Mater. Sci.* **13**, 341 (1978).
62. M. Shimada, N. Ogawa, M. Koizumi, F. Dacheille, and R. Roy, *Am. Ceram. Soc. Bull.* **58**, 519 (1979).

63. L. Gauckler, H. Hohnke, and T. Tien, *J. Am. Ceram. Soc.* **63**, 35 (1980).
64. K. Jack, *Progress in Nitrogen Ceramics*, Martinus Nijhoff, The Hague, Netherlands pp. 45–60 (1983).
65. J. Park, J. Kim, and C. Kim, *J. Am. Ceram. Soc.* **70**, 240 (1987).
66. H. Hirai and K. Kondo, *J. Am. Ceram. Soc.* **77**, 487 (1994).
67. H. Suematsu, M. Mitomo, T. Mitchell, J. Petrovic, O. Fukunaga, and N. Ohashi, *J. Am. Ceram. Soc.* **80**, 615 (1997).
68. R. Grün, *Structural Crystallography and Crystal Chemistry* **567**, 7408 (1979).
69. W. Y. Ching, L. Ouyang, and J. D. Gale, *Phys. Rev. B* **61**, 8696 (2000).
70. J. Wendel and W. Goddard, *J. Chem. Phys.* **97**, 5048 (1992).
71. A. Kuwabara, K. Matsunaga, and I. Tanaka, *Phys. Rev. B* **78**, 064104 (2008).
72. M. Schwarz, G. Miehe, A. Zerr, E. Kroke, B. Poe, H. Fuess, and R. Riedel, *Adv. Mater.* **12**, 883 (2000).
73. T. Sekine, H. He, T. Kobayashi, M. Zhang, and F. Xu, *Appl. Phys. Lett.* **76**, 3706 (2000).
74. E. Soignard, M. Somayazulu, J. Dong, O. Sankey, and P. McMillan, *J. Phys: Condens. Matter* **13**, 557 (2001).
75. Y. Zhang, A. Navrotsky, and T. Sekine, *J. Mar. Res.* **21**, 41 (2006).
76. J. Jiang, F. Kragh, D. Frost, K. Stahl, and H. Lindelov, *J. Phys: Condens. Matter* **13**, 515 (2001).
77. T. Sekine and T. Mitsuhashi, *Appl. Phys. Lett.* **79**, 2719 (2001).
78. A. Zerr, *Phys. Stat. sol. (b)* **227**, R4 (2001).

79. P. Kroll, *J. Solid State Chem.* **176**, 530 (2003).
80. P. McMillan, O. Shebanova, D. Daisenberger, R. Cabrera, E. Bailey, A. Hector, V. Lees, D. Machon, A. Sella, and M. Wilson, *Phase Transitions* **10**, 1003 (2007).
81. E. Soignard, P. McMillan, C. Hejny, and K. Leinenweber, *J. Solid State Chem.* **177**, 299 (2004).
82. J. Dong, O. Sankey, S. Deb, G. Wolf, and P. McMillan, *Phys. Rev. B* **61**, 11979 (2000).
83. C. M. B. Henderson and D. Taylor, *Trans. J. Brit. Ceramic Soc.* **74**, 49 (1975).
84. J. Schneider, F. Frey, N. Johnson, and K. Laschke, *Z. Kristallogr.* **209**, 328 (1994).
85. R. J. Bruls, H. T. Hintzen, G. de With, R. Metselaar, and J. C. van Miltenburg, *J. Phys. Chem. Solids.* **62**, 783 (2001).
86. R. R. Reeber, *Therm. Conduct.* **27**, 525 (2005).
87. M. Kuriyama, *Am. Ceram. Soc. Bull.* **57**, 1119 (1978).
88. V. Koshchenko and G. Ya, *Inorg. Mater. Inorg. Mater.* **18**, 903 (1982).
89. H. T. Hintzen, M. R. M. M. Hendrix, H. Wondergem, C. M. Fang, T. Sekine, and G. de With, *J. Alloys Compd.* **351**, 40 (2003).
90. W. Paszkowicz, R. Minikayev, P. Piszora, M. Knapp, C. Bahtz, J. M. Recio, M. Marques, P. Mori-Sanchez, L. Gerward, and J. Z. Jiang, *Phys. Rev. B* **69**, 52103 (2004).
91. C. Fang, G. de Wijs, H. Hintzen, et al., *J. Appl. Phys.* **93**, 5175 (2003).
92. L. Wang, J. Sun, W. Yang, and R. Tian, *Acta Phys. Pol., A* **114**, 807 (2008).
93. M. Fleischer and H. Meixner, *J. Mater. Sci. Lett.* **11**, 1728 (1992).
94. R. Roy, V. Hill, and E. Osborn, *J. Am. Chem. Soc.* **74**, 719 (1952).
95. J. Remeika and M. Marezio, *Appl. Phys. Lett.* **8**, 87 (1966).



96. K. Lipinska-Kalita, B. Chen, M. Kruger, Y. Ohki, J. Murowchick, and E. Gogol, *Phys. Rev. B* **68**, 035209 (2003).
97. M. Grimsditch, *Phys. Rev. Lett.* **52**, 2379 (1984).
98. C. Meade, R. Hemley, and H. Mao, *Phys. Rev. Lett.* **69**, 1387 (1992).
99. C. Liang, G. Meng, G. Wang, Y. Wang, L. Zhang, and S. Zhang, *Appl. Phys. Lett.* **78**, 3202 (2001).
100. G. Gundiah, A. Govindaraj, and C. Rao, *Chem. Phys. Lett.* **351**, 189 (2002).
101. Y. Choi, W. Kim, Y. Park, S. Lee, D. Bae, Y. Lee, G. Park, W. Choi, N. Lee, and J. Kim, *Adv. Mater.* **12**, 746 (2000).
102. Y. Gao, Y. Bando, T. Sato, Y. Zhang, and X. Gao, *Appl. Phys. Lett.* **81**, 2267 (2002).
103. S. Sharma and M. K. Sunkara, *J. Am. Chem. Soc.* **124**, 1228812293 (2002).
104. R. Rao, A. Rao, B. Xu, J. Dong, S. Sharma, and M. Sunkara, *J. Appl. Phys.* **98**, 094312 (2005).
105. M. Haneda, Y. Kintaichi, H. Shimada, and H. Hamada, *Chem. Lett.* **27**, 181 (1998).
106. E. Aubay and D. Gourier, *J. Phys. Chem.* **96**, 5513 (1992).
107. N. Corbin, *J. Eur. Ceram. Soc.* **5**, 143 (1989).
108. H. Willems, G. De With, R. Metselaar, R. Helmholdt, and K. Petersen, *J. Mater. Sci. Lett.* **12**, 1470 (1993).
109. V. Dravid, J. Sutliff, A. Westwood, M. Notis, and C. Lyman, *Philos. Mag. A* **61**, 417 (1990).
110. A. Zerr, G. Miehe, G. Serghiou, M. Schwarz, E. Kroke, and R. Riedel, *Nature* **400**, 340 (1999).

111. K. Leinenweber, M. O’Keeffe, M. Somayazulu, H. Hubert, P. McMillan, and G. Wolf, *Chem. Eur. J.* **5**, 3076 (1999).
112. G. Serghiou, G. Miehe, O. Tschauner, A. Zerr, and R. Boehler, *J. Chem. Phys.* **111**, 4659 (1999).
113. H. He, T. Sekine, T. Kobayashi, and K. Kimoto, *J. Appl. Phys.* **90**, 4403 (2001).
114. E. Soignard, P. McMillan, and K. Leinenweber, *Chem. Mater* **16**, 5344 (2004).
115. J. Lowther, T. Wagner, I. Kinski, and R. Riedel, *J. Alloys Compd.* **376**, 1 (2004).
116. P. Kroll, R. Dronskowski, and M. Martin, *J. Mater. Chem.* **15**, 3296 (2005).
117. S. Wolter, J. DeLucca, S. Mohny, R. Kern, and C. Kuo, *Thin Solid Films* **371**, 153 (2000).
118. M. Puchinger, D. Kisailus, F. Lange, and T. Wagner, *J. Cryst. Growth* **245**, 219 (2002).
119. P. Hohenberg and W. Kohn, *Phys. Rev* **136**, B864 (1964).
120. W. Kohn, L. Sham, et al., *Phys. Rev* **140**, A1133 (1965).
121. D. Vanderbilt, *Phys. Rev. B* **41**, 7892 (1990).
122. W. Frank, C. Elsässer, and M. Fähnle, *Phys. Rev. Lett.* **74**, 1791 (1995).
123. G. Kresse, J. Furthmüller, and J. Hafner, *Europhys. Lett* **32**, 729 (1995).
124. A. García and D. Vanderbilt, *Phys. Rev. B* **54**, 3817 (1996).
125. J. Dong, O. Sankey, and G. Kern, *Phys. Rev. B* **60**, 950 (1999).
126. J. Dong and O. Sankey, *J. Phys: Condens. Matter* **11**, 6129 (1999).
127. J. Dong, J. Tomfohr, and O. Sankey, *Phys. Rev. B* **61**, 5967 (2000).

128. J. Dong, J. Deslippe, O. Sankey, E. Soignard, and P. McMillan, Phys. Rev. B **67**, 94104 (2003).
129. Z. Feng, *Sic Power Materials: Devices and Applications* (Springer, 2004).
130. T. Hahn and C. A. J., *International Tables for Crystallography, Volume A: Space-group Symmetry* (Kluwer Academic Publishers, Dordrecht, 1992), 3rd ed.
131. V. Dmitriev, S. Rochal, Y. Gufan, and P. Toledano, Physical review letters **60**, 1958 (1988).
132. C. Mailhot and A. McMahan, Physical review. B, Condensed matter **44**, 11578 (1991).
133. A. Christy, Acta Crystallographica Section B: Structural Science **49**, 987 (1993).
134. M. O’Keeffe, B. Hyde, and W. Baur, *Crystal Structures I. Patterns and Symmetry* (Mineralogical Society of America Washington, DC, 1996).
135. H. Stokes, D. Hatch, J. Dong, and J. Lewis, J. Phys. Chem. Solids Phys Rev B **69**, 174111 (2004).
136. D. Hatch, H. Stokes, J. Dong, J. Gunter, H. Wang, and J. Lewis, Phys. Rev. B **71**, 184109 (2005).
137. M. Born and R. Oppenheimer, Ann. Phys. **389**, 457 (1927).
138. L. Thomas, in *Proc. Cambridge Philos. Soc* (1927), vol. 23, pp. 542–548.
139. G. Kresse and J. Furthmüller, Phys. Rev. B **54**, 11169 (1996).
140. G. Kresse and J. Hafner, Phys. Rev. B **47**, 558 (1993).
141. G. Kresse and J. Furthmüller, Comput. Mater. Sci **6**, 15 (1996).
142. G. Kresse and J. Hafner, J. Phys.: Condens. Matter **6**, 5 (1994).
143. P. Blöchl, Phys. Rev. B **50**, 17953 (1994).

144. G. Kresse and D. Joubert, Phys. Rev. B **59**, 1758 (1999).
145. D. M. Ceperley and B. J. Alder, Phys. Rev. Lett. **45**, 566 (1980).
146. J. Perdew and A. Zunger, Phys. Rev. B **23**, 5048 (1981).
147. D. Langreth and J. Perdew, Phys. Rev. B **21**, 5469 (1980).
148. D. Langreth and M. Mehl, Phys. Rev. B **28**, 1809 (1983).
149. J. Perdew, Phys. Rev. B **33**, 8822 (1986).
150. J. Perdew and W. Yue, Phys. Rev. B **33**, 8800 (1986).
151. J. Perdew, K. Burke, and M. Ernzerhof, Phys. Rev. Lett. **77**, 3865 (1996).
152. R. King-Smith and R. Needs, J. Phys.: Condens. Matter **2**, 3431 (1990).
153. K. Karch, P. Pavone, W. Windl, O. Schütt, and D. Strauch, Phys. Rev. B **50**, 17054 (1994).
154. O. Schütt, P. Pavone, W. Windl, K. Karch, and D. Strauch, Phys. Rev. B **50**, 3746 (1994).
155. M. Yin and M. Cohen, Phys. Rev. B **26**, 3259 (1982).
156. K. Kunc and R. Martin, Phys. Rev. Lett. **48**, 406 (1982).
157. G. Lehmann and M. Taut, Physica Status Solidi(b) **54**, 469 (1972).
158. P. Blöchl, O. Jepsen, and O. Andersen, Physical Review B **49**, 16223 (1994).
159. F. Birch, J. Appl. Phys. **9**, 279 (1938).
160. F. Birch, Phys. Rev. **71**, 809 (1947).
161. P. Vinet, J. Ferrante, J. Rose, and J. Smith, J. Geophys. Res. **92**, 9319 (1987).

162. P. Vinet, J. Rose, J. Ferrante, and J. Smith, *J. Phys.: Condens. Matter* **1**, 1941 (1989).
163. F. Stacey, B. Brennan, and R. Irvine, *Surv. Geophys.* **4**, 189 (1981).
164. O. Anderson, *Equations of State of Solids for Geophysics and Ceramic Science* (Oxford University Press, USA, 1995).
165. S. Porto and R. Krishnan, *J. Chem. Phys.* **47**, 1009 (1967).
166. G. Watson Jr, W. Daniels, and C. Wang, *J. Appl. Phys.* **52**, 956 (1981).
167. J. Xu, E. Huang, J. Lin, and L. Xu, *Am. Mineral.* **80**, 1157 (1995).
168. A. Barker, *Phys. Rev.* **132**, 1474 (1963).
169. F. Gervais and B. Piriou, *J. Phys. C* **7**, 2374 (1974).
170. M. Schubert, T. Tiwald, and C. Herzinger, *Phys. Rev. B* **61**, 8187 (2000).
171. S. Shin, F. Pollad, and P. Paccah, in *Proceedings of the third international conference on light scattering in solids*, edited by M. Balkanski, R. Leite, and S. Porto (Wiley, New York, 1976), pp. 401–405.
172. H. Schober, D. Strauch, and B. Dorner, *Z. Phys. B: Condens. Matter* **92**, 273 (1993).
173. R. Heid, D. Strauch, and K. Bohnen, *Phys. Rev. B* **61**, 8625 (2000).
174. Z. Łodziana and K. Parliński, *Phys. Rev. B* **67**, 174106 (2003).
175. B. Montanari, B. Civalleri, C. Zicovich-Wilson, and R. Dovesi, *Int. J. Quantum Chem.* **106**, 1703 (2006).
176. D. Schiferl, W. Denner, H. Schulz, and W. Holzapfel, *J. Appl. Phys.* **49**, 4411 (1978).
177. S. Tolbert and A. Alivisatos, *J. Chem. Phys.* **102**, 4642 (1995).
178. S. Sharma and Y. Gupta, *Phys. Rev. B* **58**, 5964 (1998).

179. M. Knudson and Y. Gupta, *Phys. Rev. Lett.* **81**, 2938 (1998).
180. M. Knudson, Y. Gupta, and A. Kunz, *Phys. Rev. B* **59**, 11704 (1999).
181. M. Wilson and P. Madden, *J. Phys: Condens. Matter* **14**, 4629 (2002).
182. S. Limpijumnong and S. Jungthawan, *Phys. Rev. B* **70**, 054104 (2004).
183. Y. Cai, S. Wu, R. Xu, and J. Yu, *Phys. Rev. B* **73**, 184104 (2006).
184. C. Stampfl and C. G. Van de Walle, *Phys. Rev. B* **59**, 5521 (1999).
185. S. Saib and N. Bouarissa, *Eur. Phys. J. B* **47**, 379 (2005).
186. H. Suematsu, J. Petrovic, and T. Mitchell, *Mater. Res. Soc. Symp. Proc.* **287**, 449 (1992).
187. A. Togo and P. Kroll, *J. Comput. Chem.* **29**, 2255 (2008).
188. P. Kroll and J. Von Appen, *Phys. Stat. sol. (b)* **226**, 6 (2001).
189. K. Tatsumi, I. Tanaka, H. Adachi, F. Oba, and T. Sekine, *J. Am. Ceram. Soc.* **85**, 7 (2002).
190. S. Ogata, N. Hirosaki, C. Kocer, and Y. Shibusaki, *Acta Mater.* **52**, 233 (2004).
191. M. Yashima, Y. Ando, and Y. Tabira, *J. Phys. Chem. B* **111**, 3609 (2007).
192. H. Toraya, *J. Appl. Cryst.* **33**, 95 (2000).
193. M. B. Kruger, J. H. Nguyen, Y. M. Li, W. A. Caldwell, M. H. Manghnani, and R. Jeanloz, *Phys. Rev. B* **55**, 3456 (1997).
194. R. F. Zhang, S. H. Sheng, and S. Veprek, *Appl. Phys. Lett.* **90**, 191903 (2007).
195. D. Du Boulay, N. Ishizawa, T. Atake, V. Streltsov, K. Furuya, and F. Munakata, *Acta Crystallogr., Sect. B: Struct. Sci.* **60**, 388 (2004).

196. Y. Li, M. Kruger, J. Nguyen, W. Caldwell, and R. Jeanloz, *Solid State Commun.* **103**, 107 (1997).
197. H. He, T. Sekine, T. Kobayashi, H. Hirosaki, and I. Suzuki, *Phys. Rev. B* **62**, 11412 (2000).
198. A. Zerr, M. Kempf, M. Schwarz, E. Kroke, M. Goken, and R. Riedel, *J. Am. Ceram. Soc.* **85**, 86 (2002).
199. J. W. Swegle, *J. Appl. Phys.* **68**, 1563 (1990).
200. A. Zerr, G. Miehe, G. Serghiou, M. Schwarz, E. Kroke, R. Riedel, and R. Boehler, *Science and Technology of High Pressure AIRAPT-17*, 914 (2000).
201. G. Schmitz, P. Gassmann, and R. Franchy, *J. Appl. Phys.* **83**, 2533 (1998).
202. M. Passlack, E. Schubert, W. Hobson, M. Hong, N. Moriya, S. Chu, K. Konstadinidis, J. Mannaerts, M. Schnoes, and G. Zydzik, *J. Appl. Phys.* **77**, 686 (1995).
203. M. Fleischer and H. Meixner, *Sens. Actuators B* **4**, 437 (1991).
204. E. Aubay and D. Gourier, *Phys. Rev. B* **47**, 15023 (1993).
205. M. Passlack, N. Hunt, E. Schubert, G. Zydzik, M. Hong, J. Mannaerts, R. Opila, and R. Fischer, *Appl. Phys. Lett.* **64**, 2715 (1994).
206. T. Xiao, A. Kitai, G. Liu, A. Nakua, and J. Barbier, *Applied Physics Letters* **72**, 3356 (1998).
207. T. Miyata, T. Nakatani, and T. Minami, *J. Lumin.* **87**, 1183 (2000).
208. J. Hao and M. Cocivera, *J. Phys. D: Appl. Phys.* **35**, 433 (2002).
209. H. Kim and W. Kim, *J. Appl. Phys* **62**, 2000 (1987).
210. T. Beales, C. Goodman, and K. Scarrott, *Solid State Commun.* **73**, 1 (1990).

211. R. Zhou and R. Snyder, *Acta Crystallographica Section B: Structural Science* **47**, 617 (1991).
212. B. Tu, Q. Cui, P. Xu, X. Wang, W. Gao, C. Wang, J. Liu, and G. Zou, *J. Phys.: Condens. Matter* **14**, 10627 (2002).
213. D. Machon, P. McMillan, B. Xu, and J. Dong, *Phys. Rev. B* **73**, 094125 (2006).
214. H. Yusa, T. Tsuchiya, N. Sata, and Y. Ohishi, *Physical Review B* **77**, 064107 (2008).
215. D. Dohy, G. Lucazeau, and A. Revcolevschi, *J. Solid State Chem.* **45**, 180 (1982).
216. M. Marezio and J. Remeika, *J. Chem. Phys.* **46**, 1862 (1967).
217. T. Tsuchiya, H. Yusa, and J. Tsuchiya, *Phys. Rev. B* **76**, 174108 (2007).
218. J. Rubio, H. Van Der Meulen, N. Mestres, J. Calleja, K. Wang, P. Ils, A. Forchel, N. Gippius, and S. Tikhodeev, *Solid-State Electron.* **40**, 707 (1996).
219. A. Arora, T. Ravindran, G. Reddy, A. Sikder, and D. Misra, *Diamond Relat. Mater.* **10**, 1477 (2001).
220. S. Zhang, B. Zhu, F. Huang, Y. Yan, E. Shang, S. Fan, and W. Han, *Solid State Communications* **111**, 647 (1999).
221. L. Dai, X. Chen, X. Zhang, A. Jin, T. Zhou, B. Hu, and Z. Zhang, *J. Appl. Phys.* **92**, 1062 (2002).
222. H. Seo, S. Bae, J. Park, H. Yang, K. Park, and S. Kim, *J. Chem. Phys.* **116**, 9492 (2002).
223. H. Okumura, K. Ohta, K. Ando, W. Rühle, T. Nagatomo, and S. Yoshida, *Solid-State Electron.* **41**, 201 (1997).
224. H. Maruska and J. Tietjen, *Appl. Phys. Lett.* **15**, 327 (1969).
225. S. Mohammad, A. Salvador, and H. Morkoc, *Proc. IEEE* **83**, 1306 (1995).



226. H. Tippins, Phys. Rev. **140**, 316 (1965).
227. S. Mo, L. Ouyang, W. Ching, I. Tanaka, Y. Koyama, and R. Riedel, Phys. Rev. Lett **83**, 5046 (1999).
228. N. Scotti, W. Kockelmann, J. Senker, S. Trassel, and H. Jacobs, Z. Anorg. Allg. Chem **625**, 1435 (1999).
229. M. Shemkunas, G. Wolf, K. Leinenweber, and W. Petuskey, J. Am. Ceram. Soc. **85**, 101 (2002).
230. P. Perlin, C. Jauberthie-Carillon, J. Itie, A. San Miguel, I. Grzegory, and A. Polian, Phys. Rev. B **45**, 83 (1992).
231. H. Xia, Q. Xia, and A. Ruoff, Phys. Rev. B **47**, 12925 (1993).
232. M. Ueno, M. Yoshida, A. Onodera, O. Shimomura, and K. Takemura, Phys. Rev. B **49**, 14 (1994).
233. A. Munoz and K. Kunc, Phys. Rev. B **44**, 10372 (1991).
234. P. Van Camp, V. Van Doren, and J. Devreese, Solid State Commun. **81**, 23 (1992).
235. R. Pandey, J. Jaffe, and N. Harrison, J. Phys. Chem. Solids **55**, 1357 (1994).
236. E. Soignard, D. Machon, P. McMillan, J. Dong, B. Xu, and K. Leinenweber, Chem. Mater **17**, 5465 (2005).
237. L. Foster and H. Stumpf, J. Am. Chem. Soc. **73**, 1590 (1951).
238. J. Remeika and M. Marezio, Appl. Phys. Lett. **8**, 87 (1966).
239. C. Fang, R. Metselaar, H. Hintzen, and G. With, J. Am. Ceram. Soc. **84**, 2633 (2001).
240. S. Deb, J. Dong, H. Hubert, P. McMillan, and O. Sankey, Solid State Commun. **114**, 137 (2000).

241. I. Kinski, G. Miehe, G. Heymann, R. Theissmann, R. Riedel, and H. Huppertz, *Z. Naturforsch., B: Chem. Sci.* **60**, 831 (2005).
242. URL <http://cms.mpi.univie.ac.at/vasp/vasp/vasp.html>.
243. T. H. K. Barron and M. L. Klein, *Dynamical Properties of Solids*, vol. 1 (North-Holland Publishing Company American Elsevier Publishing Company, Inc., 1974).

## APPENDICES

## APPENDIX A

### TOTAL ENERGY CALCULATION WITH VASP

The VASP package<sup>242</sup> that we adopt in our study is implemented with ultra-soft pseudopotentials (US-PP) or the projector-augmented wave (PAW). The four essential input files needed for a VASP calculation are INCAR, POTCAR, KPOINTS and POSCAR. The INCAR file contains a large number of parameters and most of these parameters should be left at their default values in our calculations. One important parameter worth mentioning here is the ISIF-tag. ISIF controls which degree of freedom (ions, cell volume, cell shape) are allowed to change. With different crystal symmetries and purposes of calculations, one can choose a proper value. Table A.1 shows the meaning of each ISIF tag. Taking B1 NaCl as an example, which has cubic symmetry, if we are interested in a constant-volume total energy calculation, ISIF=0 is the choice. The POTCAR file contains the pseudopotential of each type of atoms. The KPOINTS file contains the k-point sampling scheme. And the POSCAR file basically includes information of cell geometry and the atomic coordinates.

Table A.1: Value and meaning of ISIF tag

ISIF	calculate force	calculate stress tensor	relax ions	change cell shape	change cell volume
0	yes	no	yes	no	no
1	yes	trace only	yes	no	no
2	yes	yes	yes	no	no
3	yes	yes	yes	yes	yes
4	yes	yes	yes	yes	no
5	yes	yes	no	yes	no
6	yes	yes	no	yes	yes
7	yes	yes	no	no	yes

Although VASP allows relaxation of cell volume, it is not recommended in an energy-volume calculation. The incompleteness of the plane wave basis set with respect to changes of volume will cause Pulay stress, which will underestimate the equilibrium volume unless a large plane wave cutoff is used. Nonetheless, if only volume conserving relaxations are carried out, the Pulay stress can often be neglected. Furthermore, errors from Pulay stress can also be reduced and reliable lattice constant, bulk modulus and other elastic properties can be yielded by doing calculations at different volumes with the same energy cutoff for each calculation and then fitting the total energies to an equation of state. But the interval of volume changes should be in the order of 5%-10% to average out the errors due to the basis set incompleteness.

APPENDIX B  
ELASTICITY CALCULATION

A solid responds to stress by changing its shape. Elasticity is the physical property to represent the ability of a material to recover when the stress is released. “Elastic” implies that the solid will restore to its original equilibrium shape if the stress is released.

$$\epsilon_{ij} = S_{ijkl}\sigma_{kl} \quad (\text{B.1a})$$

$$\sigma_{ij} = C_{ijkl}\epsilon_{kl} \quad (\text{B.1b})$$

where  $\epsilon_{ij}$  and  $\sigma_{kl}$  are strain and stress tensors,  $S_{ijkl}$  and  $C_{ijkl}$  are called the elastic compliance constants and elastic stiffness constants (or simply called elastic constants, stiffness constants).  $\epsilon_{ij}$  is dimensionless.  $\sigma_{ij}$  has the dimension of [force]/[area] or [energy]/[volume]. Because each suffix runs from 1 to 3 (x, y, z), there are totally 81 elastic constants or compliance constants. Elastic constants are measurable and characteristic properties of a solid.

Without considering any temperature effect (entropy is zero), the change of the internal energy density (energy per unit volume) purely caused by strain is a quadratic function of  $\epsilon_{ij}$ :

$$E/V = \frac{1}{2} \sum_{ijkl} C_{ijkl}\epsilon_{ij}\epsilon_{kl} \quad (\text{B.2})$$

Since  $\epsilon_{ij}$  and  $\epsilon_{ji}$  always appear together, we can define a symmetrical strain tensor  $\eta$  as follows:

$$\eta_{ij} = \frac{1}{2}(\epsilon_{ij} + \epsilon_{ji}) \quad (\text{B.3})$$

where  $\eta_{ij} = \eta_{ji}$  and the energy density is still in the previous form.

$$E/V = \frac{1}{2} \sum_{ijkl} C_{ijkl}\eta_{ij}\eta_{kl} \quad (\text{B.4})$$

From the above equation it is easy to prove that  $C_{ijkl} = C_{ijlk}$  and  $C_{ijkl} = C_{jikl}$ . These two conditions reduce the number of independent elastic constants from 81 to 36. However, it is cumbersome to deal with a fourth-rank tensor. Fortunately, the symmetry makes it possible to use a matrix form. The most commonly accepted way of translation is Voigt’s notation, by reducing the first two suffixes to one and the last two suffixes in the same way. Accordingly, the stress and strain tensor (second-order) components will be represented

with a single suffix.

$$\begin{pmatrix} \sigma_{11} & \sigma_{12} & \sigma_{13} \\ \sigma_{21} & \sigma_{22} & \sigma_{23} \\ \sigma_{31} & \sigma_{32} & \sigma_{33} \end{pmatrix} \rightarrow \begin{pmatrix} \sigma_1 & \sigma_6 & \sigma_5 \\ \sigma_6 & \sigma_2 & \sigma_4 \\ \sigma_5 & \sigma_4 & \sigma_3 \end{pmatrix} \quad (\text{B.5a})$$

$$\begin{pmatrix} \eta_{11} & \eta_{12} & \eta_{13} \\ \eta_{21} & \eta_{22} & \eta_{23} \\ \eta_{31} & \eta_{32} & \eta_{33} \end{pmatrix} \rightarrow \begin{pmatrix} \epsilon_1 & \frac{1}{2}\epsilon_6 & \frac{1}{2}\epsilon_5 \\ \frac{1}{2}\epsilon_6 & \epsilon_2 & \frac{1}{2}\epsilon_4 \\ \frac{1}{2}\epsilon_5 & \frac{1}{2}\epsilon_4 & \epsilon_3 \end{pmatrix} \quad (\text{B.5b})$$

The purpose of introducing a factor of  $\frac{1}{2}$  to the off-diagonal strain components is to keep equation B.4 in the same format. Besides the suffixes abbreviation, the elastic compliance constants are changed by a factor of 1, 2, or 4 in the following way:

$$\begin{cases} S_{ijkl} = S_{mn} & \text{if } m \text{ and } n \text{ are } 1, 2 \text{ or } 3 \\ 2S_{ijkl} = S_{mn} & \text{if either } m \text{ or } n \text{ are } 4, 5 \text{ or } 6 \\ 4S_{ijkl} = S_{mn} & \text{if both } m \text{ and } n \text{ are } 4, 5 \text{ or } 6 \end{cases} \quad (\text{B.6})$$

While at the same time, for  $C_{ijkl}$  there are no such factors changes.

$$C_{ijkl} = C_{mn} \quad (\text{B.7})$$

where  $i, j, k, l = 1, 2, 3$  and  $m, n = 1, \dots, 6$ . And the energy density due to strain is written as:

$$E/V = \frac{1}{2} \sum_{ij} C_{ij} \epsilon_i \epsilon_j \quad (\text{B.8})$$

In equation B.8, exchanging of suffix  $i$  and  $j$  does no effect, which leads to  $C_{ij} = C_{ji}$ . Thus the number of independent  $C_{ij}$  is further reduced to 21, and this is the case for a crystal with triclinic symmetry, which is the lowest symmetry of all. Any material with higher symmetry has even less number of independent elastic constants. Results for all the crystal classes are given in table B.1.

Table B.1: Independent components of  $C_{ij}$  for all the crystal classes

Crystal class	Independent $C_{ij}$
Triclinic	All 21
Monoclinic    unique axis b	$C_{11}, C_{22}, C_{33}, C_{12}, C_{13}, C_{23}, C_{44}, C_{55}, C_{66}, C_{15}, C_{25}, C_{35}, C_{46}$
unique axis c	$C_{11}, C_{22}, C_{33}, C_{12}, C_{13}, C_{23}, C_{44}, C_{55}, C_{66}, C_{16}, C_{26}, C_{36}, C_{45}$
Orthorhombic	$C_{11}, C_{22}, C_{33}, C_{12}, C_{13}, C_{23}, C_{44}, C_{55}, C_{66}$
Cubic	$C_{11}, C_{12}, C_{44}$
Tetragonal    Classes 4, $\bar{4}$ , $4/m$	$C_{11}, C_{33}, C_{12}, C_{13}, C_{44}, C_{66}, C_{16}$
Classes $4mm, \bar{4}2m, 422, 4/mmm$	$C_{11}, C_{33}, C_{12}, C_{13}, C_{44}, C_{66}$
Trigonal        Classes 3, $\bar{3}$	$C_{11}, C_{33}, C_{12}, C_{13}, C_{44}, C_{14}, C_{15}$
Classes $32, \bar{3}m, 3m$	$C_{11}, C_{33}, C_{12}, C_{13}, C_{44}, C_{14}$
Hexagonal	$C_{11}, C_{33}, C_{12}, C_{13}, C_{44}$
Isotropic	$C_{11}, C_{12}$

Equation B.8 is the foundation for evaluating the elastic constants. The procedure of our calculation can be summarized as three steps. 1) Based on the symmetry of the material, we generate a series of strained POSCAR files. 2) We calculate the total energy for each strained POSCAR. 3) Obtain the independent elastic constants.

Diagonal and off-diagonal terms of  $C_{ij}$  are treated differently. Taking cubic system for illustration, there are three independent elastic constants:  $C_{11}$ ,  $C_{12}$  and  $C_{44}$ . For  $C_{11}$  and  $C_{44}$ , we introduce single strain  $\epsilon_1$  and  $\epsilon_4$ , respectively, to the unstrained system. Then total energies of the strained systems are calculated. Because  $C_{11}$  and  $C_{44}$  are both diagonal terms, they are obtained in exactly the same way. Let's take  $C_{11}$  as an instance. First, assuming optimized CONTCAR file at a given volume is acquired in previous static total energy calculations, it serves as the unstrained POSCAR in the elasticity calculation. When single strain is applied to the system, the total energy will be changed due to strain and can be expanded as a Taylor's series of strain, provided the strain is small (usually between 0.5% and 1.5%).

$$E = a + b\epsilon + \frac{1}{2}c\epsilon^2 + \frac{1}{6}d\epsilon^3 + \frac{1}{24}e\epsilon^4 + \dots \quad (\text{B.9})$$

where  $a$ ,  $b$ ,  $c$ ,  $d$  and  $e$  are coefficients of the first five terms in Taylor's series. We keep up to the fifth term as a good approximation.

$$C_{11} = c \quad (\text{B.10})$$

$C_{11}$  is the coefficient of the quadratic term because the elastic energy due to strain  $\epsilon_1$  is  $U = \frac{1}{2}C_{11}\epsilon_1^2$ . We have implemented a "six-point" method to get this coefficient. Six single  $\epsilon_1$ -strains with the amount of  $3\epsilon$ ,  $2\epsilon$ ,  $\epsilon$ ,  $-\epsilon$ ,  $-2\epsilon$ ,  $-3\epsilon$  are applied to the original POSCAR and total energy calculations are carried out for each of them.

$$\begin{cases} E_1 = a + 3b\epsilon + \frac{9}{2}c\epsilon^2 + \frac{9}{2}d\epsilon^3 + \frac{27}{8}e\epsilon^4 \\ E_2 = a + 2b\epsilon + 2c\epsilon^2 + \frac{4}{3}d\epsilon^3 + \frac{2}{3}e\epsilon^4 \\ E_3 = a + b\epsilon + \frac{1}{2}c\epsilon^2 + \frac{1}{6}d\epsilon^3 + \frac{1}{24}e\epsilon^4 \\ E_4 = a - b\epsilon + \frac{1}{2}c\epsilon^2 - \frac{1}{6}d\epsilon^3 + \frac{1}{24}e\epsilon^4 \\ E_5 = a - 2b\epsilon + 2c\epsilon^2 - \frac{4}{3}d\epsilon^3 + \frac{2}{3}e\epsilon^4 \\ E_6 = a - 3b\epsilon + \frac{9}{2}c\epsilon^2 - \frac{9}{2}d\epsilon^3 + \frac{27}{8}e\epsilon^4 \end{cases} \quad (\text{B.11})$$

By canceling the terms of no interests, we have

$$C_{11} = c = \frac{-3E_1 + 16E_2 - 13E_3 - 13E_4 + 16E_5 - 3E_6}{24\epsilon^2} \quad (\text{B.12})$$

For  $C_{12}$ , we introduce two strains  $\epsilon_1$  and  $\epsilon_2$ , at the same time, to the unstrained system. The related elastic energy is

$$U = C_{12}\epsilon_1\epsilon_2 + C_{11}\epsilon_1^2 + C_{22}\epsilon_2^2 \quad (\text{B.13})$$

$C_{12}$  is the coefficient in the front of the  $\epsilon_1\epsilon_2$  term. With pair strains, the total energy of the system can also be expressed in a Taylor's series, being cut at the fourth-order terms



as an approximation.

$$\begin{aligned}
E = & a + b\epsilon_1 + c\epsilon_2 + d\epsilon_1\epsilon_2 + \frac{1}{2}e\epsilon_1^2 + \frac{1}{2}f\epsilon_2^2 + \frac{1}{6}g\epsilon_1^3 + \frac{1}{2}h\epsilon_1^2\epsilon_2 + \frac{1}{2}i\epsilon_1\epsilon_2^2 \\
& + \frac{1}{6}j\epsilon_2^3 + \frac{1}{24}k\epsilon_1^4 + \frac{1}{6}l\epsilon_1^3\epsilon_2 + \frac{1}{4}m\epsilon_1^2\epsilon_2^2 + \frac{1}{6}n\epsilon_1\epsilon_2^3 + \frac{1}{24}o\epsilon_2^4
\end{aligned} \tag{B.14}$$

where  $C_{12} = d$ . To eliminate the unrelated coefficients, an ‘‘eight-point’’ algorithm is implemented. The eight pair strains for  $(\epsilon_1, \epsilon_2)$  we apply are:  $(2\epsilon, 2\epsilon)$ ,  $(2\epsilon, -2\epsilon)$ ,  $(-2\epsilon, -2\epsilon)$ ,  $(-2\epsilon, 2\epsilon)$ ,  $(\epsilon, \epsilon)$ ,  $(\epsilon, -\epsilon)$ ,  $(-\epsilon, -\epsilon)$  and  $(-\epsilon, \epsilon)$ .

$$\left\{ \begin{aligned}
E_1 &= a + 2b\epsilon_1 + 2c\epsilon_2 + 4d\epsilon_1\epsilon_2 + 2e\epsilon_1^2 + 2f\epsilon_2^2 + \frac{4}{3}g\epsilon_1^3 + 4h\epsilon_1^2\epsilon_2 + 4i\epsilon_1\epsilon_2^2 \\
&+ \frac{4}{3}j\epsilon_2^3 + \frac{2}{3}k\epsilon_1^4 + \frac{8}{3}l\epsilon_1^3\epsilon_2 + 2m\epsilon_1^2\epsilon_2^2 + \frac{8}{3}n\epsilon_1\epsilon_2^3 + \frac{2}{3}o\epsilon_2^4 \\
E_2 &= a + 2b\epsilon_1 - 2c\epsilon_2 - 4d\epsilon_1\epsilon_2 + 2e\epsilon_1^2 + 2f\epsilon_2^2 + \frac{4}{3}g\epsilon_1^3 - 4h\epsilon_1^2\epsilon_2 + 4i\epsilon_1\epsilon_2^2 \\
&- \frac{4}{3}j\epsilon_2^3 + \frac{2}{3}k\epsilon_1^4 - \frac{8}{3}l\epsilon_1^3\epsilon_2 + 2m\epsilon_1^2\epsilon_2^2 - \frac{8}{3}n\epsilon_1\epsilon_2^3 + \frac{2}{3}o\epsilon_2^4 \\
E_3 &= a - 2b\epsilon_1 - 2c\epsilon_2 + 4d\epsilon_1\epsilon_2 + 2e\epsilon_1^2 + 2f\epsilon_2^2 - \frac{4}{3}g\epsilon_1^3 - 4h\epsilon_1^2\epsilon_2 - 4i\epsilon_1\epsilon_2^2 \\
&- \frac{4}{3}j\epsilon_2^3 + \frac{2}{3}k\epsilon_1^4 + \frac{8}{3}l\epsilon_1^3\epsilon_2 + 2m\epsilon_1^2\epsilon_2^2 + \frac{8}{3}n\epsilon_1\epsilon_2^3 + \frac{2}{3}o\epsilon_2^4 \\
E_4 &= a - 2b\epsilon_1 + 2c\epsilon_2 - 4d\epsilon_1\epsilon_2 + 2e\epsilon_1^2 + 2f\epsilon_2^2 - \frac{4}{3}g\epsilon_1^3 + 4h\epsilon_1^2\epsilon_2 - 4i\epsilon_1\epsilon_2^2 \\
&+ \frac{4}{3}j\epsilon_2^3 + \frac{2}{3}k\epsilon_1^4 - \frac{8}{3}l\epsilon_1^3\epsilon_2 + 2m\epsilon_1^2\epsilon_2^2 - \frac{8}{3}n\epsilon_1\epsilon_2^3 + \frac{2}{3}o\epsilon_2^4 \\
E_5 &= a + b\epsilon_1 + c\epsilon_2 + d\epsilon_1\epsilon_2 + \frac{1}{2}e\epsilon_1^2 + \frac{1}{2}f\epsilon_2^2 + \frac{1}{6}g\epsilon_1^3 + \frac{1}{2}h\epsilon_1^2\epsilon_2 + \frac{1}{2}i\epsilon_1\epsilon_2^2 \\
&+ \frac{1}{6}j\epsilon_2^3 + \frac{1}{24}k\epsilon_1^4 + \frac{1}{6}l\epsilon_1^3\epsilon_2 + \frac{1}{4}m\epsilon_1^2\epsilon_2^2 + \frac{1}{6}n\epsilon_1\epsilon_2^3 + \frac{1}{24}o\epsilon_2^4 \\
E_6 &= a + b\epsilon_1 - c\epsilon_2 - d\epsilon_1\epsilon_2 + \frac{1}{2}e\epsilon_1^2 + \frac{1}{2}f\epsilon_2^2 + \frac{1}{6}g\epsilon_1^3 - \frac{1}{2}h\epsilon_1^2\epsilon_2 + \frac{1}{2}i\epsilon_1\epsilon_2^2 \\
&- \frac{1}{6}j\epsilon_2^3 + \frac{1}{24}k\epsilon_1^4 - \frac{1}{6}l\epsilon_1^3\epsilon_2 + \frac{1}{4}m\epsilon_1^2\epsilon_2^2 - \frac{1}{6}n\epsilon_1\epsilon_2^3 + \frac{1}{24}o\epsilon_2^4 \\
E_7 &= a - b\epsilon_1 - c\epsilon_2 + d\epsilon_1\epsilon_2 + \frac{1}{2}e\epsilon_1^2 + \frac{1}{2}f\epsilon_2^2 - \frac{1}{6}g\epsilon_1^3 - \frac{1}{2}h\epsilon_1^2\epsilon_2 - \frac{1}{2}i\epsilon_1\epsilon_2^2 \\
&- \frac{1}{6}j\epsilon_2^3 + \frac{1}{24}k\epsilon_1^4 + \frac{1}{6}l\epsilon_1^3\epsilon_2 + \frac{1}{4}m\epsilon_1^2\epsilon_2^2 + \frac{1}{6}n\epsilon_1\epsilon_2^3 + \frac{1}{24}o\epsilon_2^4 \\
E_8 &= a - b\epsilon_1 + c\epsilon_2 - d\epsilon_1\epsilon_2 + \frac{1}{2}e\epsilon_1^2 + \frac{1}{2}f\epsilon_2^2 - \frac{1}{6}g\epsilon_1^3 + \frac{1}{2}h\epsilon_1^2\epsilon_2 - \frac{1}{2}i\epsilon_1\epsilon_2^2 \\
&+ \frac{1}{6}j\epsilon_2^3 + \frac{1}{24}k\epsilon_1^4 - \frac{1}{6}l\epsilon_1^3\epsilon_2 + \frac{1}{4}m\epsilon_1^2\epsilon_2^2 - \frac{1}{6}n\epsilon_1\epsilon_2^3 + \frac{1}{24}o\epsilon_2^4
\end{aligned} \right. \tag{B.15}$$

To solve for  $C_{12}$ , we do addition or subtraction with these equations and find that

$$C_{12} = d = \frac{-E_1 + E_2 - E_3 + E_4 + 16E_5 - 16E_6 + 16E_7 - 16E_8}{48\epsilon^2} \tag{B.16}$$

So far we have discussed the derivation and computation procedure of the elastic constants for an unstressed solid. However, elastic constants will change under stress. Here we follow Barron & Klein’s derivation and care only about the case of isotropic stress (hydrostatic pressure). When pressure is applied to the solid, Barron showed that the strain-energy density relation becomes:

$$C_{ijkl} = \frac{1}{V} \frac{\partial E}{\partial \epsilon_{ij} \partial \epsilon_{kl}} + \frac{1}{2} P (2\delta_{ij} \delta_{kl} - \delta_{il} \delta_{jk} - \delta_{ik} \delta_{jl}) \tag{B.17}$$

where  $V$  is the volume at that pressure,  $P$  is the pressure and  $\delta_{ij}$  is the Kronecker delta ( $\delta_{ij} = 1$  when  $i = j$ ;  $\delta_{ij} = 0$  when  $i \neq j$ ). The first term in equation B.17 is obtained from the strain-energy density relation as if the solid is not under stress. The second term is a correction because of pressure. In Voigt’s notation, the correction terms for each elastic constant is shown in table B.2.

Table B.2: Correction term to  $C_{ij}$  due to pressure

$C_{ij}$	Correction term	$C_{ij}$	Correction term	$C_{ij}$	Correction term
$C_{11}$	0	$C_{13}$	$P$	$C_{26}$	0
$C_{22}$	0	$C_{14}$	0	$C_{34}$	0
$C_{33}$	0	$C_{15}$	0	$C_{35}$	0
$C_{44}$	$-\frac{1}{2}P$	$C_{16}$	0	$C_{36}$	0
$C_{55}$	$-\frac{1}{2}P$	$C_{23}$	$P$	$C_{45}$	0
$C_{66}$	$-\frac{1}{2}P$	$C_{24}$	0	$C_{46}$	0
$C_{12}$	$P$	$C_{25}$	0	$C_{56}$	0

Again, if we use cubic crystal as an example, and let  $\tilde{C}$  represent the first term in equation B.17, the three independent elastic constants are:

$$\begin{cases} C_{11} = \tilde{C}_{11} \\ C_{12} = \tilde{C}_{12} + P \\ C_{44} = \tilde{C}_{44} - \frac{1}{2}P \end{cases} \quad (\text{B.18})$$

At the current stage, we only calculate the elastic constant and its pressure dependence at zero temperature condition.

## APPENDIX C

### BEYOND HARMONIC APPROXIMATION: PERTURBATION THEORY OF LATTICE ANHARMONICITY

The quasi-harmonic approximation (QHA) has achieved a great success in predicting thermodynamic properties for many hard materials at temperatures not too close to the melting point. However, to improve the prediction of thermodynamic properties of normal materials at high temperatures or strongly anharmonic crystals even at low temperatures, it is desired to add the anharmonicity contribution to the free energy as a next level approximation. This correction is usually small compare to the harmonic contribution. With the third and fourth order anharmonicity, we can evaluate the lowest order of anharmonic contribution to the harmonic free energy via perturbation theory. Within this theory, we treat the anharmonic terms in the hamiltonian as perturbations. The total hamiltonian can be written as:

$$\begin{aligned} H &= H_H + H_A \\ &= H_0 + H_2 + H_3 + H_4 + \dots \end{aligned} \tag{C.1}$$

where  $H_H = H_0 + H_2$  which is the harmonic part and  $H_A = \sum_{n=3}^{\infty} H_n$  is the anharmonic part.  $H_n$  is the  $n^{\text{th}}$  order term in the expansion of hamiltonian. As the anharmonic effect is more important at high temperatures, we deal this problem within the classical limit. Then the partition function of the system is:

$$\begin{aligned} Z &= h^{-3N} \int dx_1 \dots \int dx_{3N} \int dp_1 \dots \int dp_{3N} \cdot e^{-\beta(H_H + H_A)} \\ &= Z_H \cdot \frac{\int dx_1 \dots \int dx_{3N} \int dp_1 \dots \int dp_{3N} \cdot e^{-\beta H_H} \cdot e^{-\beta H_A}}{\int dx_1 \dots \int dx_{3N} \int dp_1 \dots \int dp_{3N} \cdot e^{-\beta H_H}} \\ &= Z_H \cdot Z_A \end{aligned} \tag{C.2}$$

where  $Z_H = h^{-3N} \int dx_1 \dots \int dx_{3N} \int dp_1 \dots \int dp_{3N} \cdot e^{-\beta H_H}$  is the partition function of the harmonic hamiltonian and  $Z_A$  is the ensemble average of the quantity  $e^{-\beta H_A}$  over the

unperturbed harmonic system. Expanding  $e^{-\beta H_A}$  into Taylor series, we have

$$\begin{aligned}
Z_A &= \langle e^{-\beta H_A} \rangle_0 \\
&= \left\langle 1 + \sum_{n=1}^{\infty} \frac{(-1)^n}{n!} \beta^n \cdot H_A^n \right\rangle \\
&= 1 + \sum_{n=1}^{\infty} \frac{(-1)^n}{n!} \beta^n \cdot \langle H_A^n \rangle_0
\end{aligned} \tag{C.3}$$

Since we have expressed the total partition function as a product of the harmonic partition function and  $Z_A$ , the anharmonic contribution to the Helmholtz free energy is:

$$\begin{aligned}
F_A &= -k_B T \ln Z_A \\
&= -\beta^{-1} \ln \left( 1 + \sum_{n=1}^{\infty} \frac{(-1)^n}{n!} \beta^n \cdot \langle H_A^n \rangle_0 \right)
\end{aligned} \tag{C.4}$$

Assuming the anharmonic terms are small compared to unity, the logarithm function in equation C.4 can be expanded into series following  $\ln(1+x) = x - \frac{x^2}{2} + \frac{x^3}{3} - \dots$  when  $-1 < x < 1$ . The expansion is expressed in terms of the  $\frac{(-\beta)^n}{n!}$  and the coefficient of  $\frac{(-\beta)^n}{n!}$  is called the  $n^{\text{th}}$  cumulant  $\langle H_A^n \rangle_{0,C}$

$$F_A = -\beta^{-1} \sum_{n=1}^{\infty} \frac{(-1)^n}{n!} \beta^n \cdot \langle H_A^n \rangle_{0,C} \tag{C.5}$$

Comparing equation C.5 with equation C.4, we have

$$\langle H_A \rangle_{0,C} = \langle H_A \rangle_0 \tag{C.6a}$$

$$\langle H_A^2 \rangle_{0,C} = \langle H_A^2 \rangle_0 - (\langle H_A \rangle_0)^2 \tag{C.6b}$$

$$\langle H_A^3 \rangle_{0,C} = \langle H_A^3 \rangle_0 - 3 \langle H_A^2 \rangle_0 \langle H_A \rangle_0 + 2 (\langle H_A \rangle_0)^3 \tag{C.6c}$$

According to pairing theorem<sup>243</sup>, the lowest order anharmonic contribution from  $\langle H_A \rangle_{0,C}$  term is  $\langle H_A \rangle_0$ . The lowest order anharmonic contribution from  $\langle H_A^2 \rangle_{0,C}$  term is  $\langle H_A^2 \rangle_0 - (\langle H_A \rangle_0)^2$ . Other higher order terms are ignored as an approximation. The anharmonicity correction to the free energy under this approximation is:

$$F_A = \langle H_A \rangle_0 - \frac{\beta}{2} \left[ \langle H_A^2 \rangle_0 - (\langle H_A \rangle_0)^2 \right] \tag{C.7}$$

Using normal coordinates, the third and fourth order anharmonic terms of hamiltonian can be written as:

$$H_3 = \sum_{\mathbf{q}, \mathbf{q}', \mathbf{q}''} \sum_{\xi, \xi', \xi''} W_3 \left( \begin{array}{c} \mathbf{q}, \mathbf{q}', \mathbf{q}'' \\ \xi, \xi', \xi'' \end{array} \right) Q_\xi(\mathbf{q}) Q_{\xi'}(\mathbf{q}') Q_{\xi''}(\mathbf{q}'') \quad (\text{C.8a})$$

$$H_4 = \sum_{\mathbf{q}, \mathbf{q}', \mathbf{q}'', \mathbf{q}'''} \sum_{\xi, \xi', \xi'', \xi'''} W_4 \left( \begin{array}{c} \mathbf{q}, \mathbf{q}', \mathbf{q}'', \mathbf{q}''' \\ \xi, \xi', \xi'', \xi''' \end{array} \right) Q_\xi(\mathbf{q}) Q_{\xi'}(\mathbf{q}') Q_{\xi''}(\mathbf{q}'') Q_{\xi'''}(\mathbf{q}''') \quad (\text{C.8b})$$

where  $W_3$  and  $W_4$  are defined as

$$W_3 \left( \begin{array}{c} \mathbf{q}, \mathbf{q}', \mathbf{q}'' \\ \xi, \xi', \xi'' \end{array} \right) = \frac{1}{6} \sum_{\alpha\beta\gamma} \sum_{ijk} N^{-\frac{1}{2}} \delta_{\mathbf{q}+\mathbf{q}'+\mathbf{q}'', \mathbf{G}} \cdot A_{\alpha i, \beta j, \gamma k}(\mathbf{q}', \mathbf{q}'') \cdot e_{\alpha, i}(\mathbf{q}, \xi) e_{\beta, j}(\mathbf{q}', \xi') e_{\gamma, k}(\mathbf{q}'', \xi'') \quad (\text{C.9a})$$

$$W_4 \left( \begin{array}{c} \mathbf{q}, \mathbf{q}', \mathbf{q}'', \mathbf{q}''' \\ \xi, \xi', \xi'', \xi''' \end{array} \right) = \frac{1}{24} \sum_{\alpha\beta\gamma\lambda} \sum_{ijkl} N^{-1} \delta_{\mathbf{q}+\mathbf{q}'+\mathbf{q}''+\mathbf{q}''', \mathbf{G}} \cdot B_{\alpha i, \beta j, \gamma k, \lambda l}(\mathbf{q}', \mathbf{q}'', \mathbf{q}''') \cdot e_{\alpha, i}(\mathbf{q}, \xi) e_{\beta, j}(\mathbf{q}', \xi') e_{\gamma, k}(\mathbf{q}'', \xi'') e_{\lambda, l}(\mathbf{q}''', \xi''') \quad (\text{C.9b})$$

In equation C.9,  $A_{\alpha i, \beta j, \gamma k}(\mathbf{q}', \mathbf{q}'')$  is the third order anharmonic dynamical tensor, which can be derived from the real-space third order force-constant tensor through a Fourier transformation.  $B_{\alpha i, \beta j, \gamma k, \lambda l}(\mathbf{q}', \mathbf{q}'', \mathbf{q}''')$  is the fourth order anharmonic dynamical tensor.

$$A_{\alpha i, \beta j, \gamma k}(\mathbf{q}', \mathbf{q}'') = \frac{1}{\sqrt{m_i m_j m_k}} \sum_{\mathbf{h}, \mathbf{h}'} A_{\alpha i, \beta j, \gamma k}(0, \mathbf{h}, \mathbf{h}') \cdot e^{i(\mathbf{q}' \cdot \mathbf{h} + \mathbf{q}'' \cdot \mathbf{h}')} \quad (\text{C.10a})$$

$$B_{\alpha i, \beta j, \gamma k, \lambda l}(\mathbf{q}', \mathbf{q}'', \mathbf{q}''') = \frac{1}{\sqrt{m_i m_j m_k m_l}} \sum_{\mathbf{h}, \mathbf{h}', \mathbf{h}''} B_{\alpha i, \beta j, \gamma k, \lambda l}(0, \mathbf{h}, \mathbf{h}', \mathbf{h}'') \cdot e^{i(\mathbf{q}' \cdot \mathbf{h} + \mathbf{q}'' \cdot \mathbf{h}' + \mathbf{q}''' \cdot \mathbf{h}'')} \quad (\text{C.10b})$$

With the pairing theorem we can evaluate the averaged hamiltonian over the unperturbed canonical ensemble.

$$\langle H_4 \rangle_0 = \frac{3}{\beta^3} \sum_{\mathbf{q}_1, \mathbf{q}_2} \sum_{\xi_1, \xi_2} \frac{W_4 \left( \begin{array}{c} \mathbf{q}_1, -\mathbf{q}_1, \mathbf{q}_2, -\mathbf{q}_2 \\ \xi_1, \xi_1, \xi_2, \xi_2 \end{array} \right)}{\omega_{\xi_1}^2(\mathbf{q}_1) \omega_{\xi_2}^2(\mathbf{q}_2)} \quad (\text{C.11a})$$

$$\begin{aligned} \langle H_3^2 \rangle_0 &= \frac{6}{\beta^3} \sum_{\mathbf{q}_1, \mathbf{q}_2, \mathbf{q}_3} \sum_{\xi_1, \xi_2, \xi_3} \frac{W_3 \left( \begin{array}{c} \mathbf{q}_1, \mathbf{q}_2, \mathbf{q}_3 \\ \xi_1, \xi_2, \xi_3 \end{array} \right) W_3 \left( \begin{array}{c} -\mathbf{q}_1, -\mathbf{q}_2, -\mathbf{q}_3 \\ \xi_1, \xi_2, \xi_3 \end{array} \right)}{\omega_{\xi_1}^2(\mathbf{q}_1) \omega_{\xi_2}^2(\mathbf{q}_2) \omega_{\xi_3}^2(\mathbf{q}_3)} \\ &+ \frac{9}{\beta^3} \sum_{\mathbf{q}_1, \mathbf{q}_2, \mathbf{q}_3} \sum_{\xi_1, \xi_2, \xi_3} \frac{W_3 \left( \begin{array}{c} \mathbf{q}_1, -\mathbf{q}_1, \mathbf{q}_3 \\ \xi_1, \xi_1, \xi_3 \end{array} \right) W_3 \left( \begin{array}{c} \mathbf{q}_2, -\mathbf{q}_2, -\mathbf{q}_3 \\ \xi_2, \xi_2, \xi_3 \end{array} \right)}{\omega_{\xi_1}^2(\mathbf{q}_1) \omega_{\xi_2}^2(\mathbf{q}_2) \omega_{\xi_3}^2(\mathbf{q}_3)} \end{aligned} \quad (\text{C.11b})$$

where  $\omega_\xi(\mathbf{q})$  is the phonon frequency of the  $\xi^{th}$  normal mode at reciprocal lattice point  $\mathbf{q}$ .

We have proposed an algorithm to evaluate the third order force-constant tensor  $A_{\alpha i, \beta j, \gamma k}(\ell, \ell', \ell'')$ . In order to get all the tensor elements, we apply a pair of displacements to the system. Here we keep up to the 4<sup>th</sup> order term of the hamiltonian and the amount of each displacement is  $\Delta$  which is much smaller than the interatomic distance. The pair-displacement scheme we adopt is to deviate the  $j^{th}$  atom in  $\beta$  direction and the  $k^{th}$  atom in  $\gamma$  direction by  $(\Delta, \Delta)$ ,  $(\Delta, -\Delta)$ ,  $(-\Delta, \Delta)$ , and  $(-\Delta, -\Delta)$ , respectively. The  $\alpha$  component of the H-F forces on the  $i^{th}$  atom are:

$$\begin{aligned}
F_{\alpha, i}^{++}(\ell) &= -[\Phi_{\alpha i, \beta j}(\ell, \ell') + \Phi_{\alpha i, \gamma k}(\ell, \ell'')] \cdot \Delta \\
&\quad - \frac{1}{2} [A_{\alpha i, \beta j, \beta j}(\ell, \ell', \ell') + A_{\alpha i, \gamma k, \gamma k}(\ell, \ell'', \ell'') + 2A_{\alpha i, \beta j, \gamma k}(\ell, \ell', \ell'')] \cdot \Delta^2 \\
&\quad - \frac{1}{6} \left[ \begin{array}{l} B_{\alpha i, \beta j, \beta j, \beta j}(\ell, \ell', \ell', \ell') + B_{\alpha i, \gamma k, \gamma k, \gamma k}(\ell, \ell'', \ell'', \ell'') \\ + 2B_{\alpha i, \beta j, \beta j, \gamma k}(\ell, \ell', \ell'', \ell''') + 2B_{\alpha i, \beta j, \gamma k, \gamma k}(\ell, \ell', \ell'', \ell''') \end{array} \right] \cdot \Delta^3
\end{aligned} \tag{C.12a}$$

$$\begin{aligned}
F_{\alpha, i}^{+-}(\ell) &= -[\Phi_{\alpha i, \beta j}(\ell, \ell') - \Phi_{\alpha i, \gamma k}(\ell, \ell'')] \cdot \Delta \\
&\quad - \frac{1}{2} [A_{\alpha i, \beta j, \beta j}(\ell, \ell', \ell') + A_{\alpha i, \gamma k, \gamma k}(\ell, \ell'', \ell'') - 2A_{\alpha i, \beta j, \gamma k}(\ell, \ell', \ell'')] \cdot \Delta^2 \\
&\quad - \frac{1}{6} \left[ \begin{array}{l} B_{\alpha i, \beta j, \beta j, \beta j}(\ell, \ell', \ell', \ell') - B_{\alpha i, \gamma k, \gamma k, \gamma k}(\ell, \ell'', \ell'', \ell'') \\ - 2B_{\alpha i, \beta j, \beta j, \gamma k}(\ell, \ell', \ell'', \ell''') + 2B_{\alpha i, \beta j, \gamma k, \gamma k}(\ell, \ell', \ell'', \ell''') \end{array} \right] \cdot \Delta^3
\end{aligned} \tag{C.12b}$$

$$\begin{aligned}
F_{\alpha, i}^{-+}(\ell) &= -[-\Phi_{\alpha i, \beta j}(\ell, \ell') + \Phi_{\alpha i, \gamma k}(\ell, \ell'')] \cdot \Delta \\
&\quad - \frac{1}{2} [A_{\alpha i, \beta j, \beta j}(\ell, \ell', \ell') + A_{\alpha i, \gamma k, \gamma k}(\ell, \ell'', \ell'') - 2A_{\alpha i, \beta j, \gamma k}(\ell, \ell', \ell'')] \cdot \Delta^2 \\
&\quad - \frac{1}{6} \left[ \begin{array}{l} -B_{\alpha i, \beta j, \beta j, \beta j}(\ell, \ell', \ell', \ell') + B_{\alpha i, \gamma k, \gamma k, \gamma k}(\ell, \ell'', \ell'', \ell'') \\ + 2B_{\alpha i, \beta j, \beta j, \gamma k}(\ell, \ell', \ell'', \ell''') - 2B_{\alpha i, \beta j, \gamma k, \gamma k}(\ell, \ell', \ell'', \ell''') \end{array} \right] \cdot \Delta^3
\end{aligned} \tag{C.12c}$$

$$\begin{aligned}
F_{\alpha, i}^{--}(\ell) &= +[\Phi_{\alpha i, \beta j}(\ell, \ell') + \Phi_{\alpha i, \gamma k}(\ell, \ell'')] \cdot \Delta \\
&\quad - \frac{1}{2} [A_{\alpha i, \beta j, \beta j}(\ell, \ell', \ell') + A_{\alpha i, \gamma k, \gamma k}(\ell, \ell'', \ell'') + 2A_{\alpha i, \beta j, \gamma k}(\ell, \ell', \ell'')] \cdot \Delta^2 \\
&\quad + \frac{1}{6} \left[ \begin{array}{l} B_{\alpha i, \beta j, \beta j, \beta j}(\ell, \ell', \ell', \ell') + B_{\alpha i, \gamma k, \gamma k, \gamma k}(\ell, \ell'', \ell'', \ell'') \\ + 2B_{\alpha i, \beta j, \beta j, \gamma k}(\ell, \ell', \ell'', \ell''') + 2B_{\alpha i, \beta j, \gamma k, \gamma k}(\ell, \ell', \ell'', \ell''') \end{array} \right] \cdot \Delta^3
\end{aligned} \tag{C.12d}$$

From equation C.12, simple derivation yields

$$A_{\alpha i, \beta j, \gamma k}(\ell, \ell', \ell'') = \frac{-F_{\alpha, i}^{++}(\ell) + F_{\alpha, i}^{+-}(\ell) - F_{\alpha, i}^{-+}(\ell) + F_{\alpha, i}^{--}(\ell)}{4\Delta^2} \tag{C.13}$$

For a  $3N \times 3N \times 3N$  tensor, there are  $C_{6N}^2 + 6N = 18N^2 + 6N$  H-F forces required. This number can be reduced by noticing that when  $(\beta, j, \ell') = (\gamma, k, \ell'')$ ,  $A_{\alpha i, \beta j, \beta j}(\ell, \ell', \ell')$  can be obtained from the single-displacement calculations which have been done when acquiring

the second order force-constant matrix.

$$A_{\alpha i, \beta j, \beta j}(\ell, \ell', \ell'') = \frac{F_{\alpha, i}^+(\ell) + F_{\alpha, i}^-(\ell) - F_{\alpha, i}^{2+}(\ell) - F_{\alpha, i}^{2-}(\ell)}{3\Delta^2} \quad (\text{C.14})$$

However, there are still  $C_{6N}^2$  forces needed which is not an easy task to calculate for a supercell. Again, the crystal symmetry plays an important role to greatly reduce the number of direct calculations. A code named as *Moves\_Analysis.x* has been implemented to figure out the irreducible number of pair-moves. Let us take the 120-atom supercell of  $\alpha\text{-Al}_2\text{O}_3$  as an example. The total number of pair-moves is 258840 initially. After the symmetry analysis, the number of independent pair-moves is reduced to 5168. Although this number has been greatly deducted, it is still impractical to carry out first-principles calculations for such a large number. At this stage, an approximation could be made that the tensor element is typically around zero if two atoms in the atomic indices of  $A_{\alpha i, \beta j, \gamma k}(\ell, \ell', \ell'')$  are far away from each other. If we drop all the calculations involving the distance between the  $j^{\text{th}}$  and  $k^{\text{th}}$  atoms that beyond the second nearest neighbor, we can reduce the number of direct pair-move calculations down to 632, which is now a feasible job.

After the direct calculations, other tensor elements can be either reconstructed from the irreducible ones or equal to zero.